MAPPING MOHO UNDULATIONS BENEATH THE GRAND BANKS OF NEWFOUNDLAND USING GRAVITY FIELD DATA

B. JANET MORRISSEY

Mapping Moho Undulations Beneath the Grand Banks of Newfoundland Using Gravity Field Data

by

B. Janet Morrissey

A thesis submitted to the
School of Graduate Studies
in partial fulfilment of the
requirements for the degree of
Master of Earth Sciences
(Geophysics)

Department of Earth Sciences

Memorial University of Newfoundland

April, 2001

St. John's Newfoundland

ABSTRACT

The Avalon terrane of Newfoundland has been the subject of considerable study, especially in relation to the other tectono-stratigraphic terranes of the Appalachian Orogen. The Grand Banks of Newfoundland in particular, located within the Avalon terrane, has been intensely investigated on both a local and crustal scale.

Gravity data is available for the Avalon terrane. A number of processing techniques, in both the space and frequency domains, was applied to the data in an effort to extract the topography of the Moho for the Grand Banks region. The data were passed through a series of low-pass filters, each having progressively lower cut-off frequencies to isolate the long-wavelength signal from Moho.

To ensure that the observed long-wavelength signal was due primarily to sources at Moho depth and not from intervening sources, the gravity field of the Mesozoic rift basins of the Grand Banks, also long-wavelength in character, was modelled and subtracted from the observed field.

Using an average depth to Moho derived from spectral analysis of the field and from seismic data for the region as well as a density contrast obtained from direct (seismic refraction results) and indirect (inferred geology) sources, the data was inverted to obtain a map of depth to Moho. Profiles along selected seismic reflection line locations were extracted and the Mohos compared.

The broad Moho relief obtained from the inverted gravity data agreed with that of the seismic Moho, however, the amplitude of the topography generated by the

inversion is significantly reduced. In light of the sparse deep seismic coverage within the study area, the inversion results give a good first approximation to a comprehensive map of Moho topography for the region.

ACKNOWLEDGEMENTS

I wish to thank Hugh Miller for providing me with the data for this project and for all the help he has given throughout the course of my research. I would also like to thank Tony Kocurko for his assistance during the development of the FORTRAN modelling program.

This research was funded in part by a Newfoundland Offshore Career Development Award to Janet Morrissey.

TABLE OF CONTENTS

LIST OF TABLES

LIST OF FIGURES

CHAPTER 1: INTRODUCTION

The objective of this thesis is to use available gravity data to produce a three-dimensional map of the Mohorovičić discontinuity (M-discontinuity or Moho) beneath the Avalon terrane of the Appalachian Orogen onshore and offshore in Newfoundland and beneath the Grand Banks. Seismic refraction and reflection profiling samples isolated regions of the subsurface and can only provide two-dimensional or cross-sectional images of the Moho. Thick layers of sediment and the presence of strong multiples sometimes obscure signals from the deep crust (see, for example, Figures 1.1(a) through 1.1(d)). Moreover, inferences of Moho topography from seismic refraction and reflection surveys are dependent on the accuracy of velocity information derived for the deep crust by the seismic processors and interpreters. Magnetic field data cannot be used to 'see' the Moho since temperatures at Moho depths would demagnetize any potentially magnetic source rock. For these reasons, areal gravity data is a good candidate for providing a continuous, three-dimensional representation of the topography of the Moho.

Knowledge of Moho topography can be applied to many areas of earth sciences. Maps of Moho topography are suitable for the study of isostasy. Here, they can be used to investigate how the shape of the Moho has been redefined in response to isostatic adjustment of the crust to extensional and compressional tectonics as well as to deficiencies and excesses of mass within the crust.

Studies of extensional tectonics examine the various aspects of extension including the mechanics of how crust thins and separates. Ancient planes of detachment show up on deep seismic profiles but it is sometimes unclear whether or not these fault planes extend to Moho depths or sole out above the Moho. Seismic profiling gives a two-dimensional view of décollement zones and detachment faults within the crust but three-dimensional maps of the Moho can be more illustrative. This is especially significant for the passive margin of eastern Canada, which was formed by rifting and extension. In particular, reliable maps of Moho topography across passive margins can be applied to the investigation of conjugate margins, such as those of western Europe and eastern Canada.

The long-wavelength signal from the sedimentary basins on the Grand Banks may interfere with the long-wavelength signal from sources at Moho depths. Therefore, the gravity effect of the Mesozoic basins was modelled and the modelled field subtracted from the original gravity field. Modelling of the basins was carried out by approximating them as stacked series of horizontal, polygonal laminae (Talwani and Ewing, 1960) using a published depth to basement contour map and density information derived from industry well logs. Once the effect of the basins was removed, the gravity field data were passed through a series of low-pass filters with progressively lower cut-off frequencies to isolate the long-wavelength features generally associated with Moho topography. Analysis of the energy spectrum of the filtered field gave an ensemble average depth (Spector and Grant, 1970) to these long-wavelength sources. The gravity data were then

inverted to obtain Moho relief using constraints on density from borehole data and average depth derived from seismic refraction data and the energy spectra. The results were then compared with the data from seismic reflection transects across the Grand Banks.

Deep crustal seismic coverage over the Grand Banks is moderate but is restricted mainly to the periphery of the region covered by the available gravity data (the majority of the deep seismic transects are situated normal to the ocean-continent boundary). The continuous, three-dimensional image of the Moho derived from the gravity data supplements the seismic data and provides information over a greater geographic area.

1.1 GEOLOGY

The following geological summary is based largely on the work of Grant and McAlpine (1990).

The Grand Banks of Newfoundland form the continental shelf to the south and east of the island. They are bounded by the northeast Newfoundland Shelf and Slope (DeSilva, 1999). To the south and east, the Grand Banks terminate at the continental slope and rise. They are separated from Flemish Cap, a positive continental fragment of Hadrynian age (King et al., 1985), by Flemish Pass Basin and from the Scotian Shelf to the southwest by the Laurentian Channel. Water depths on the Grand Banks are generally less than 500 m except at Flemish Pass, a bathymetric trough where water depths exceed 1100 m. Figure 1.2

shows the bathymetry of the region. The Pass is underlain by the Flemish Pass Basin (DeSilva, 1999).

The present structure of the Grand Banks results from a series of complex rifting episodes during the Mesozoic that migrated northward along the margin of eastern Canada. The Grand Banks are underlain by rocks of the Appalachian Orogen, specifically those of the Avalon and Meguma terranes, and contain basins, typically half-grabens formed by Mesozoic rifting events (Tankard and Welsink, 1988; Enachescu, 1987) separated by basement highs. The basins contain Mesozoic and older sediments and are roughly parallel to the structural trend of terranes of the Appalachian Orogen exposed on the island (Grant and McAlpine, 1990), therefore they may be related to the reactivation of pre-existing Paleozoic and Precambrian structures.

1.1.1 Pre-Mesozoic Geology

Beginning in the late Precambrian, rifting of Grenvillian basement accompanied by profuse igneous activity initiated the development of the Iapetus Ocean margin. This ancient margin is recorded in the rocks of western Newfoundland. In the late Early Ordovician, the destruction of the margin was precipitated by the closure of the Iapetus Ocean. This led to the development of the Appalachian Orogen, a succession of accretionary episodes that continued throughout the Paleozoic (Haworth, et al., 1994). The orogen in Newfoundland and on the Grand Banks is composed of five terranes (Williams, 1979; Williams, et al.,

1988). From west to east they are the Humber, Dunnage, Gander, Avalon, and Meguma terranes (Figure 1.3).

The majority of the Grand Banks is underlain by rocks of the Avalon terrane which is the largest of the tectono-stratigraphic zones into which the rocks of the Appalachian Orogen are divided (Figure 1.3). The Avalon terrane is composed primarily of belts of unmetamorphosed and undeformed late Precambrian volcanic and sedimentary rocks separated by faults. These are overlain by white quartzite which, in turn, is overlain by lower Cambrian fossiliferous shales exhibiting Atlantic trilobite faunas (Williams, 1979). The southern Avalon terrane is underlain by Precambrian mafic and ultramafic units (Miller, 1987). The Avalon terrane may be an amalgam of several terranes which were joined together before being accreted to the Gander terrane (Keppie, 1985; Keppie, et al., 1989). During the Precambrian, faults between the sedimentary and volcanic belts were active. These faults were reactivated during the Paleozoic and Mesozoic. The Mesozoic basins of the Grand Banks formed within these pre-existing Precambrian sedimentary basins (Haworth, et al., 1994).

The Meguma terrane on the Grand Banks occupies a smaller area south of the Collector Anomaly, a prominent magnetic feature on the southern Grand Banks. It consists of the Meguma Group, which is a conformable, 13 km thick sequence of Cambrian-Ordovician sediment, consisting of a greywacke unit overlain by shale. The Meguma Group is then overlain by an assemblage of undated volcanic and sedimentary rocks and covered by Devonian sediments (Williams, 1979).

1.1.2 Mesozoic and Cenozoic Geology

Figure 1.4 illustrates the stratigraphic relationships between major units and unconformities in key regions of the study area as well as their chronologic relationship to major tectonic events.

In the Early Jurassic, rifting between Nova Scotia and Africa (Figure 1.5(a)) initiated the development of northeast-southwest trending basins on the southern Grand Banks. Sediments deposited within the basins over pre-Mesozoic basement at this time include red clastics of the Eurydice Formation, evaporites such as halite of the Osprey and Argo Formations, and carbonates such as oolitic limestones and anhydritic dolomite of the Iroquois Formation (Figure 1.4).

Occurrences of basalt in drill cores on the Grand Banks and diabase dykes located on the Avalon Peninsula of Newfoundland that are about 200 Ma old (Hodych and Hayatsu, 1980) suggest that there was volcanic activity related to the tensional stresses between Nova Scotia and Africa and to the imminent sea floor spreading in the central North Atlantic (Pe-Piper and Jansa, 1986). Rifting between Nova Scotia and Africa was terminated north of the Newfoundland Fracture Zone at the southwest margin of the Grand Banks (Figure 1.6).

Between the Early and Late Jurassic, the region underwent epeirogenic subsidence during which shallow marine shales and limestones were deposited in a series of regionally gradational formations. Shale of the Downing Formation was deposited in this low-energy epeiric sea environment and is conformably

overlain by fine- to medium-grained quartzose sandstone with secondary amounts of shale, coal, and oolitic limestone of the Voyager Formation - marginal marine sediments with low accumulation rates, indicative of a shallowing of the epeiric sea. The Rankin Formation, consisting of Upper Jurassic oolitic limestone and minor amounts of fine-grained quartz sandstone rests conformably upon the Voyager Formation (Figure 1.4).

During the Late Jurassic, upwarping of the Grand Banks, referred to as the Avalon Uplift (Figure 1.6), initiated rifting between Iberia and North America at the southeastern Grand Banks (Figure 1.5(b)). The deposition of rift-related clastic sediments replaced that of epeirogenic carbonates and shales. Medium- to coarse-grained brown and red sandstones and conglomerates of the Eider Formation were deposited in this rifting environment while toward the northern Grand Banks, shallow water shales and siltstones of the Nautilus Shale were deposited. Volcanic activity associated with continental breakup formed the strongly magnetic Newfoundland Ridge (Figure 1.2) and the Newfoundland Seamounts southeast of the Grand Banks (Figure 1.6) (Sullivan and Keen, 1977). Hot-spot volcanism formed the J-Anomaly Ridge (Tucholke and Ludwig, 1982; Figure 1.2), also called Anomaly M0. North American-Iberian separation was completed to the stage of sea floor spreading by the late Early Cretaceous.

Rifting between western Europe and North America at the northern Grand Banks (Figure 1.5(c)) terminated at the Charlie-Gibbs Fracture Zone (Figure 1.6) northeast of Newfoundland and culminated in their separation about the mid-Cretaceous. There is evidence of volcanism on the southern Grand Banks along

the Avalon-Meguma contact around this time (Gradstein et al., 1977; Jansa and Pe-Piper, 1986). By the end of the Early Cretaceous, igneous activity on the Grand Banks had ended, indicating that tensional stresses in the area had relaxed. Stratigraphically, there is a transition from rift to drift sediments (Figure 1.4). Turonian and Cenomanian sediments consisting predominantly of shale with lesser amounts of siltstone and sandstone are found in the Dawson Canyon Formation. After the separation of Europe and the northern Grand Banks, sediment supply was irregular. When the rate of thermal subsidence overtook that of sedimentation, deep water chalky limestones such as those of the Wyandot Formation and the Petrel Member of the Dawson Canyon Formation were deposited.

Subsequent to the formation of the eastern Canadian margin, the Grand Banks experienced constant subsidence with some disruption of Tertiary sediments by the migration of subsurface salt. During the Tertiary, however, subsidence was extensive, particularly in the northern Grand Banks (Keen, et al., 1987a). Sediment supply had once again declined by the Eocene. Throughout the Tertiary, deep water shales of the Banquereau Formation were deposited. During the Middle to Late Miocene, the Grand Banks may have been subaerially exposed due to a drop in sea level prior to the widespread glaciation of the Pleistocene.

Progressing northward, the sedimentary basins of the Grand Banks exhibit a change in trend from northeast-southwest (e.g. Whale, Horseshoe, Carson and southern Jeanne d'Arc Basins) to north-south (e.g. northern Jeanne d'Arc and

Flemish Pass Basins). The change in trend reflects the change in rift strike from the northeast-southwest trending rift zone between the southern Grand Banks and Iberia to the north-south trending rift zone between the northern Grand Banks and Europe (Figure 1.6). Separating pre-rift metasediments of Paleozoic and Precambrian age and syn-rift sediments of Mesozoic age from post-rift sediments within these basins and across the Grand Banks is the Avalon Unconformity (Jansa and Wade, 1975), a prominent geological feature of the region associated with the Mesozoic Avalon Uplift. The Avalon Unconformity is a principal seismic marker (Keen and de Voogd, 1988) covered by Upper Cretaceous and Cenozoic sediments which thin landward but become very thick toward the northeast, particularly in the East Newfoundland Basin. Over the Carson, Horseshoe, southern Jeanne d'Arc and Whale Basins, and surrounding platformal areas, depth to the Avalon Unconformity stays fairly constant. Its depth over the Jeanne d'Arc Basin depocentre, though, is increased. Progressively younger sediments are found beneath the subsurface peneplain to the southwest and northeast representing 50 to 60 Ma of uplift, deformation and erosion. The Avalon Unconformity is actually several unconformities associated with no less than four Late Jurassic to early Late Cretaceous erosional events. They include the Kimmeridgian, Barremian, Aptian, and Cenomanian unconformities (Figure 1.4).

The deep crust in the study area is relatively homogeneous (Haworth, et al., 1994). Results from seismic refraction surveys reveal that the continental crust below the southern Grand Banks has a fairly uncomplicated structure, which

consists of a main crustal layer that thins toward the southwestern margin. Studies of syn- and post-rift subsidence (Keen and Dehler, 1993; Dehler and Keen, 1993) show that the crust of the Grand Banks has been thinned and stretched, severely in some regions. Crust of the northeastern Grand Banks has undergone considerable extension, forming the broad Orphan Basin. Values for the stretching parameter β (i.e. the amount of stretching or thinning, where $\beta = 1$ indicates no stretching while increasingly large values of β tend toward infinite stretching) in this region are approximately 2.0. In the central Grand Banks region, i.e. west of Flemish Cap and including the northern Jeanne d'Arc Basin, the crust has been moderately thinned with β about 1.35 (Enachescu, 1988). Toward the southern Grand Banks, $\beta = 1.59$ (Enachescu, 1988). East-dipping deep crustal faults alongside Whale and southern Jeanne d'Arc Basins seen on deep multichannel seismic lines have been suggested by Keen, et al. (1987a) to be planes of extension extending to Moho depths (e.g. simple shear; Wernicke, 1985) that facilitated the development of these basins.

1.2 PREVIOUS GEOPHYSICS

In the 1950s potential field, seismic refraction and *in situ* sampling surveys of the North American margin were conducted by both Canadian and American governments as well as by university research teams (Grant and McAlpine, 1990). The discovery of large quantities of sediments on the Grand Banks interested the petroleum industry. To date, more than 700 000 km of exploration

seismic data have been acquired and at least 158 wells have been drilled (DeSilva, 1999).

In 1964 the Earth Physics Branch carried out the first published gravity survey of Newfoundland (Weaver, 1967, 1968). The Atlantic Geoscience Centre has carried out marine gravity measurements on the Grand Banks for a number of years (see Figure 1.7). Comprehensive gravity surveys were restricted to the southern and central Grand Banks as well as the Gulf of St. Lawrence during the latter half of the 1960s. From 1982 to 1984 surveys concentrated on the continental shelves and margins of Newfoundland and Nova Scotia. The National Gravity data base, maintained by the Geological Survey of Canada, contains edited and adjusted gravity values from the offshore region of Newfoundland as well as from the rest of the country. Memorial University researchers collected gravity data on land and led several underwater gravity surveys in the near shore area (Miller, 1982a; Miller, 1987).

Deep crustal seismic data have been collected and interpreted on the Grand Banks and across the margin (Keen et al., 1987a; Keen et al., 1989; Marillier et al., 1994). Figures 1.8 and 1.9 illustrate the deep seismic reflection and refraction coverage, respectively, across the Grand Banks and around Newfoundland. The Geological Survey of Canada and the Lithoprobe Project have gathered 2400 km of deep multichannel seismic reflection data (Keen et al., 1989). In 1984, more than 1000 km of data were recorded northeast of Newfoundland as part of Lithoprobe East (Keen et al., 1987a), as were wide-angle reflection and refraction data across the Appalachian orogen in 1991

(Marillier et al., 1994). As part of the Frontier Geoscience Project, the Geological Survey of Canada collected over 6800 km of deep reflection seismic data off the coast of eastern Canada between 1984 and 1990. DeChassy et al. (1990) presented a compilation of deep seismic profiles across conjugate margins of the North Atlantic, which were used here for comparison with resultant gravity models. Reid and Keen (1990) and Reid (1993, 1994) investigated the deep crustal structure of the Grand Banks using seismic refraction techniques.

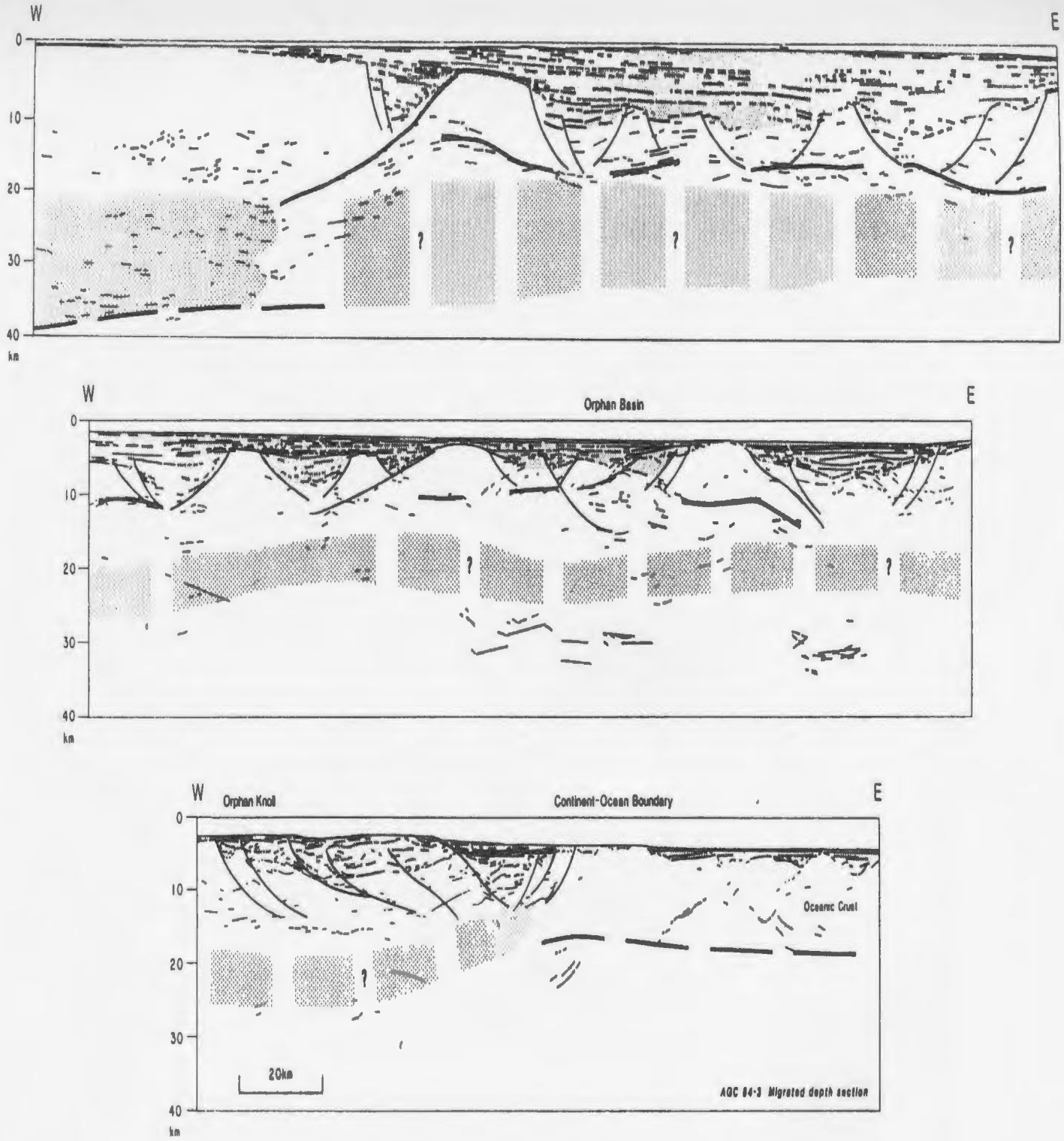

Figure 1.1(a). Migrated depth section along Reflection Line 84-3. Location shown in Figure 1.7. From DeChassy, et al. (1990).

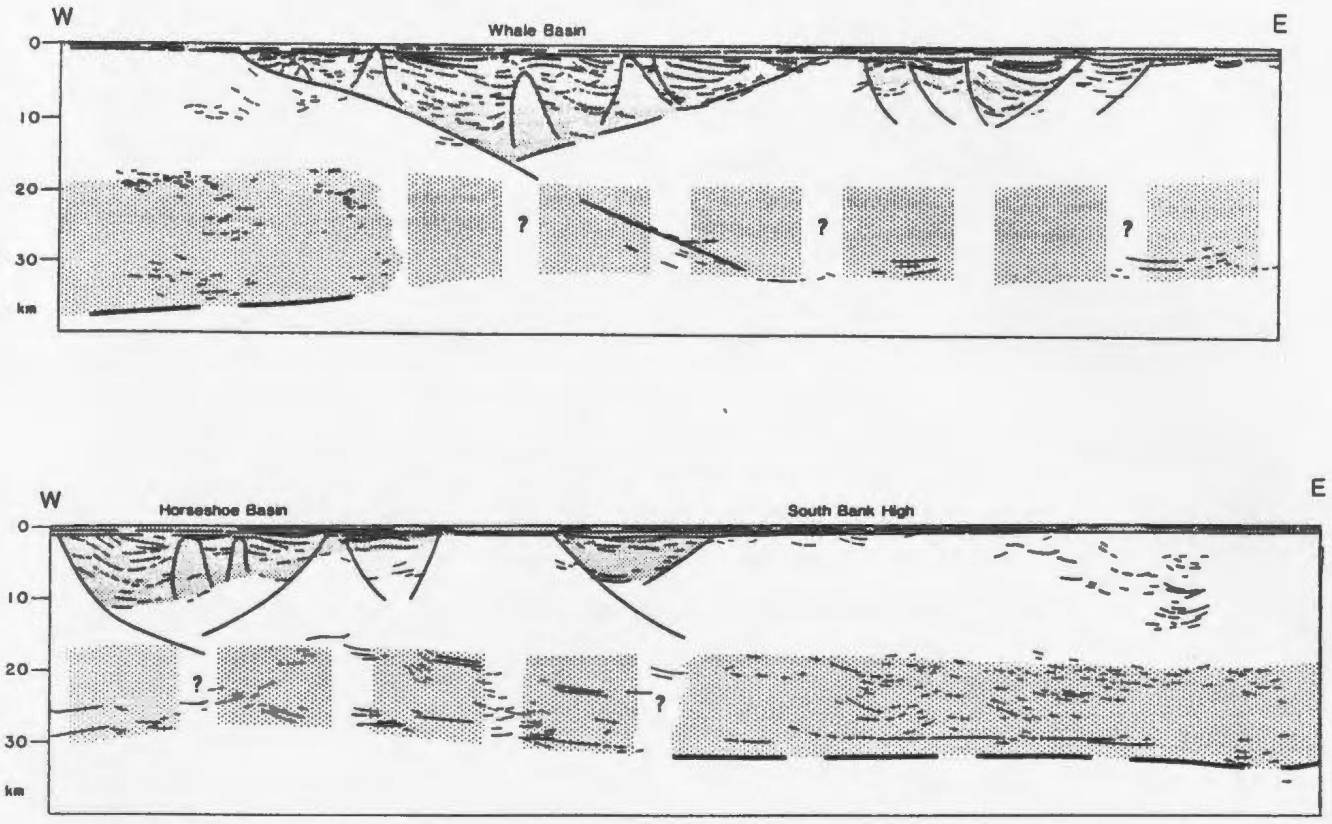

Figure 1.1(b). Migrated depth section along Reflection Line 85-1. Location shown in Figure 1.7. From DeChassy, et al. (1990).

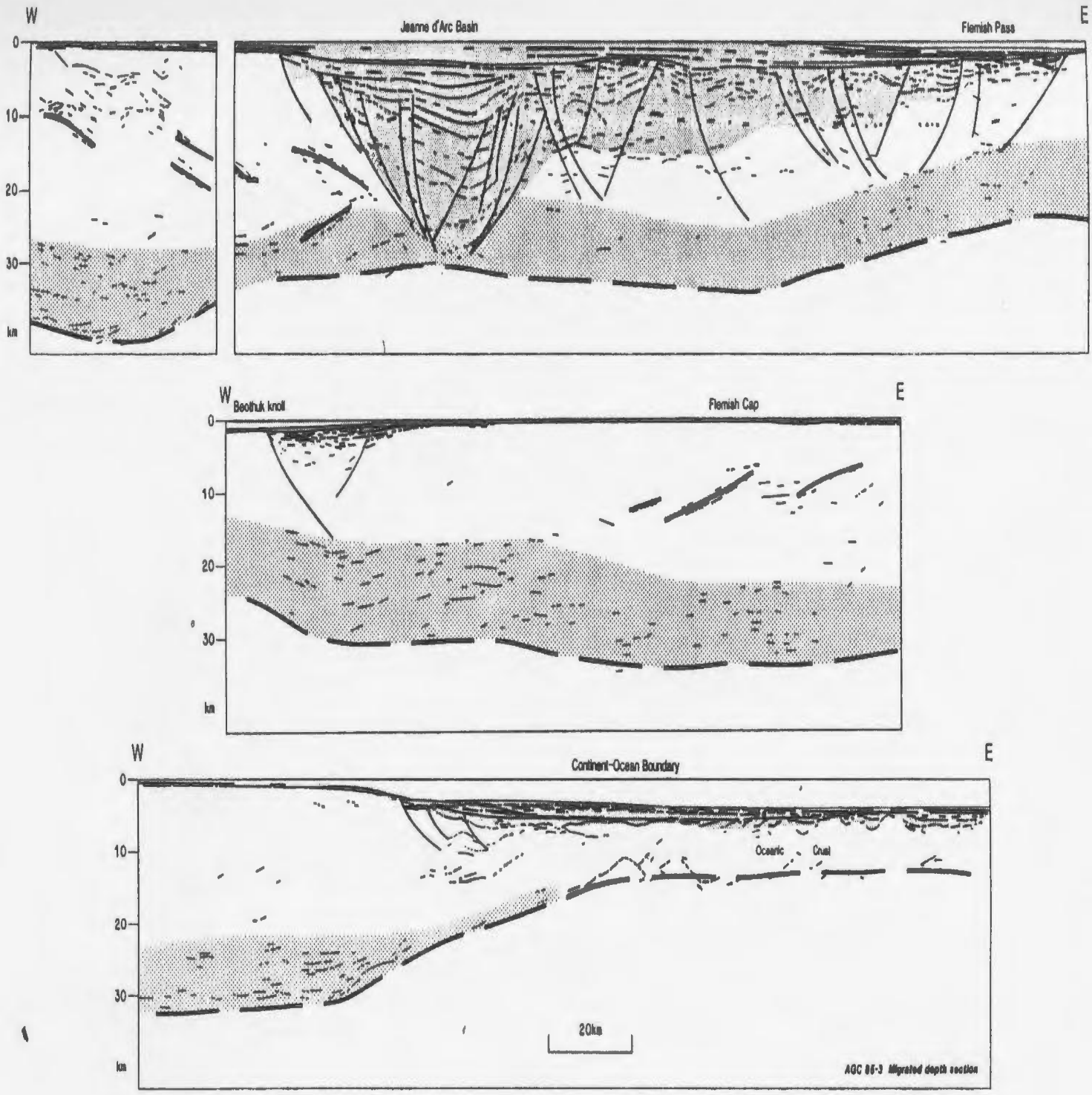

Figure 1.1(c). Migrated depth section along Reflection Line 85-3. Location shown in Figure 1.7. From DeChassy, et al. (1990).

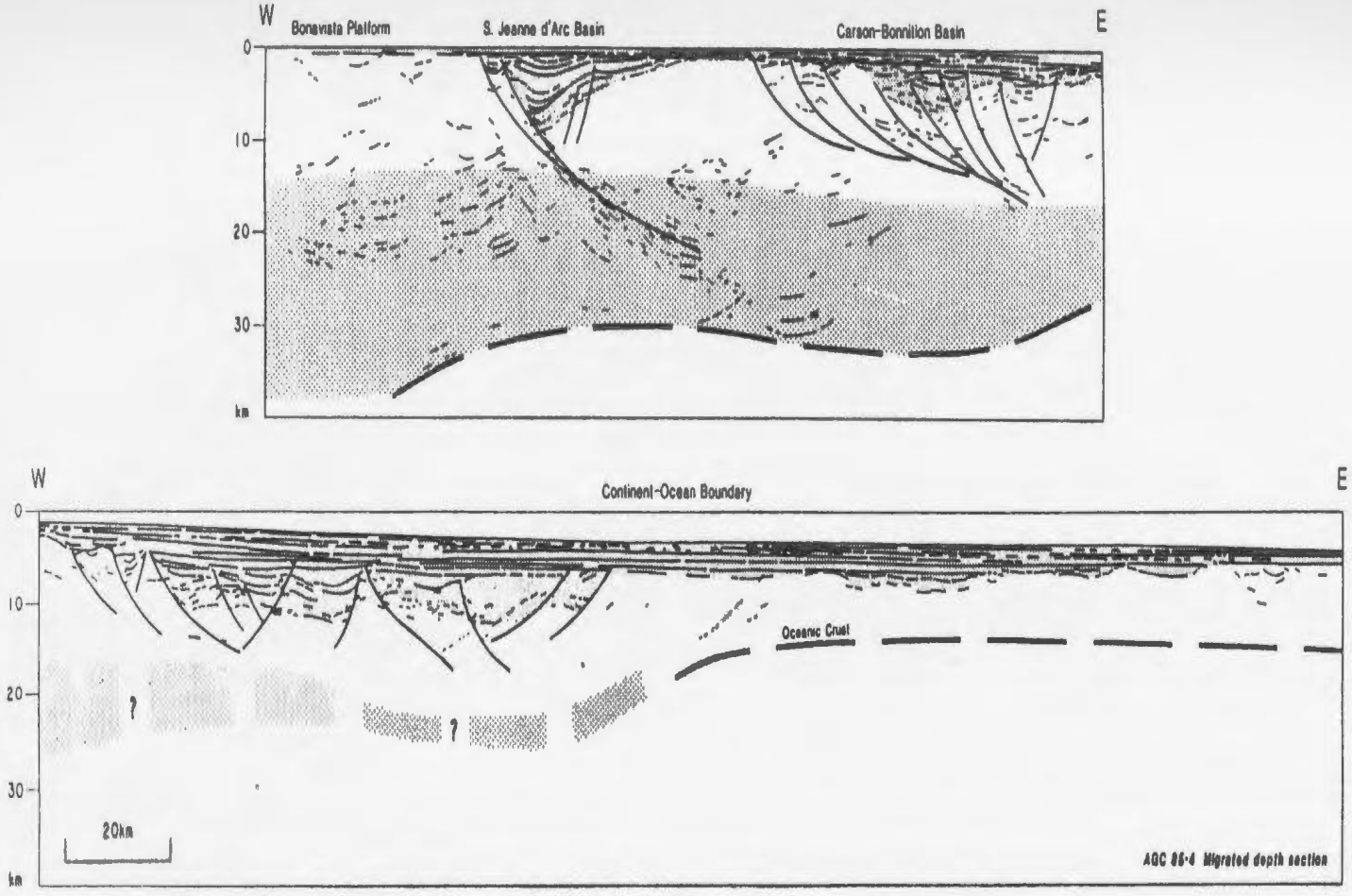

Figure 1.1(d). Migrated depth section along Reflection Line 85-4. Location shown in Figure 1.7. From DeChassy, et al. (1990).

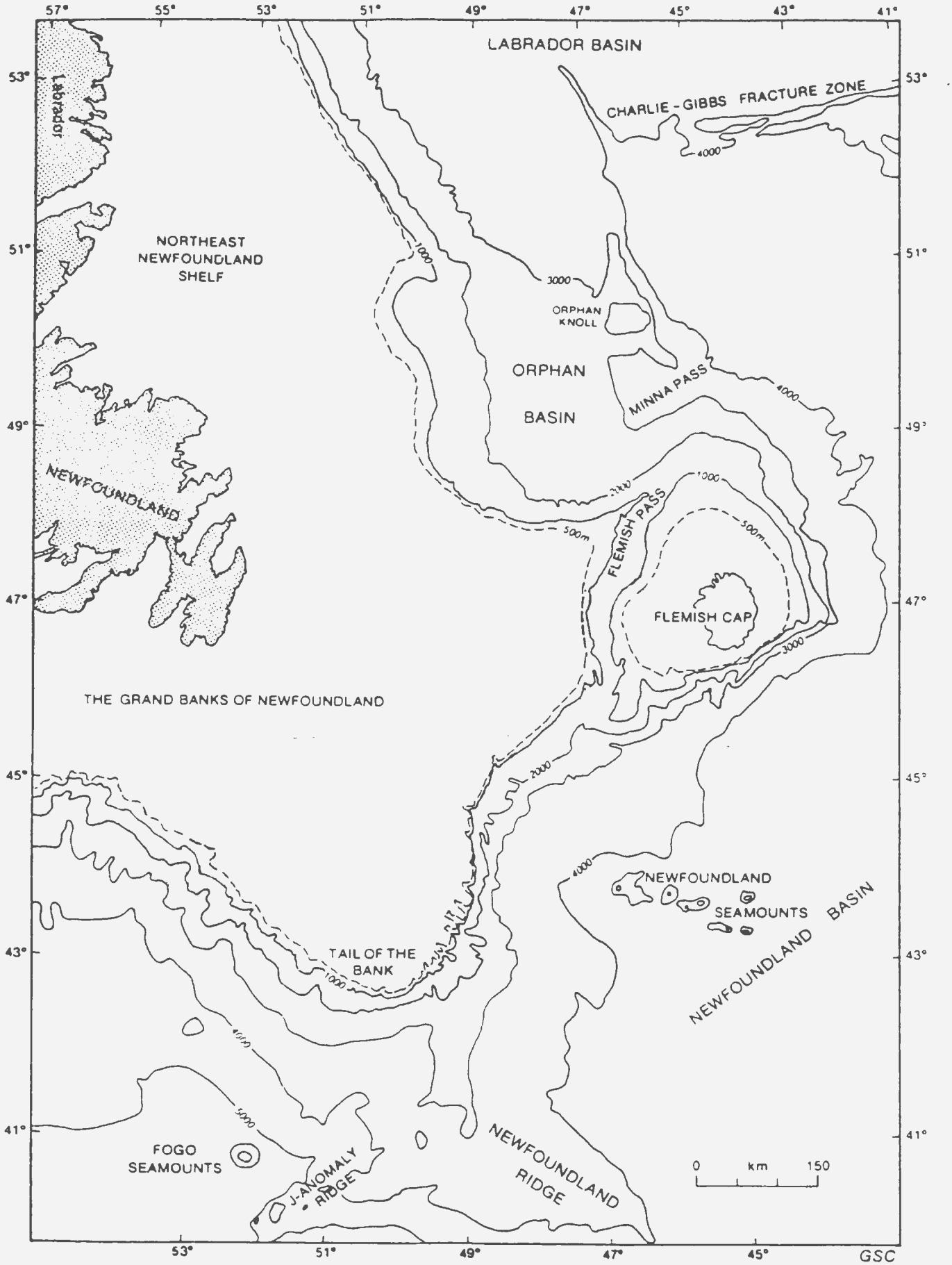

Figure 1.2. Bathymetry of the Newfoundland continental margin. Contours in metres. Dashed line is the 500 m water depth contour. (From Grant and McAlpine, 1990).

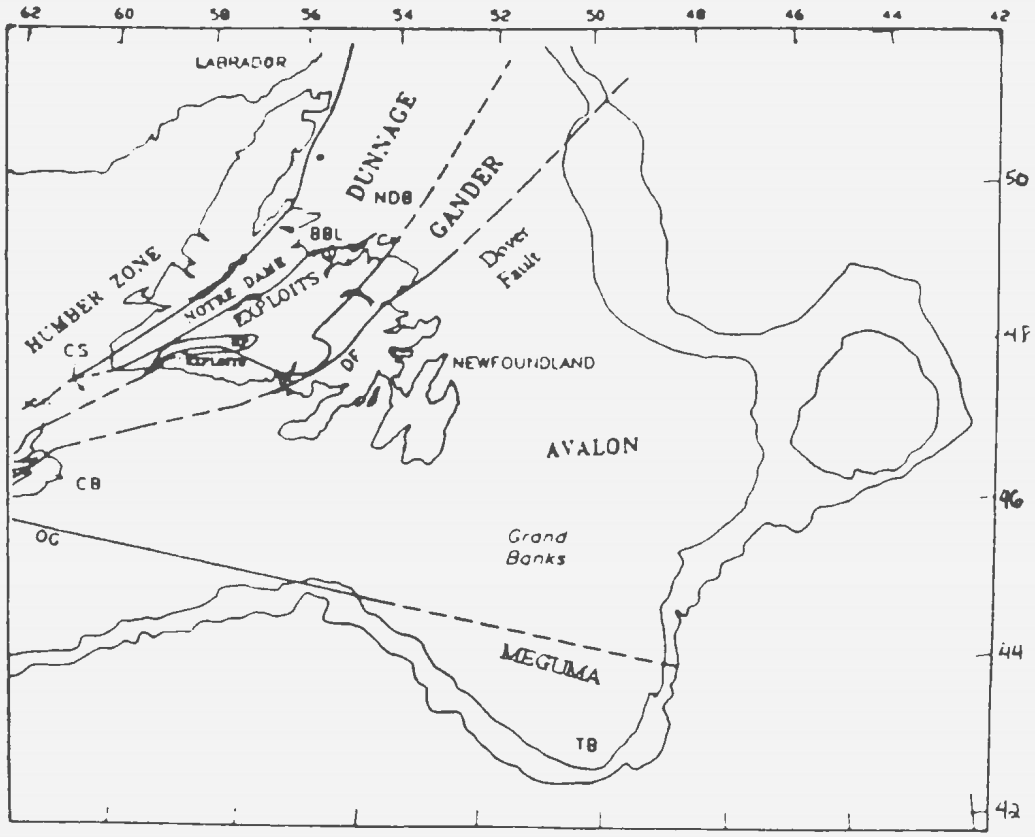

Figure 1.3. Tectono-stratigraphic terranes of eastern Canada. BBL – Baie Verte-Brompton Line: CB – Cape Breton; CS – Cabot Strait; DF – Dover Fault; MP – Meelpaeg Terrane; NDB – Notre Dame Bay; OG – Orpheus Graben; TB – Tail of the Banks. (From Miller, 1990).

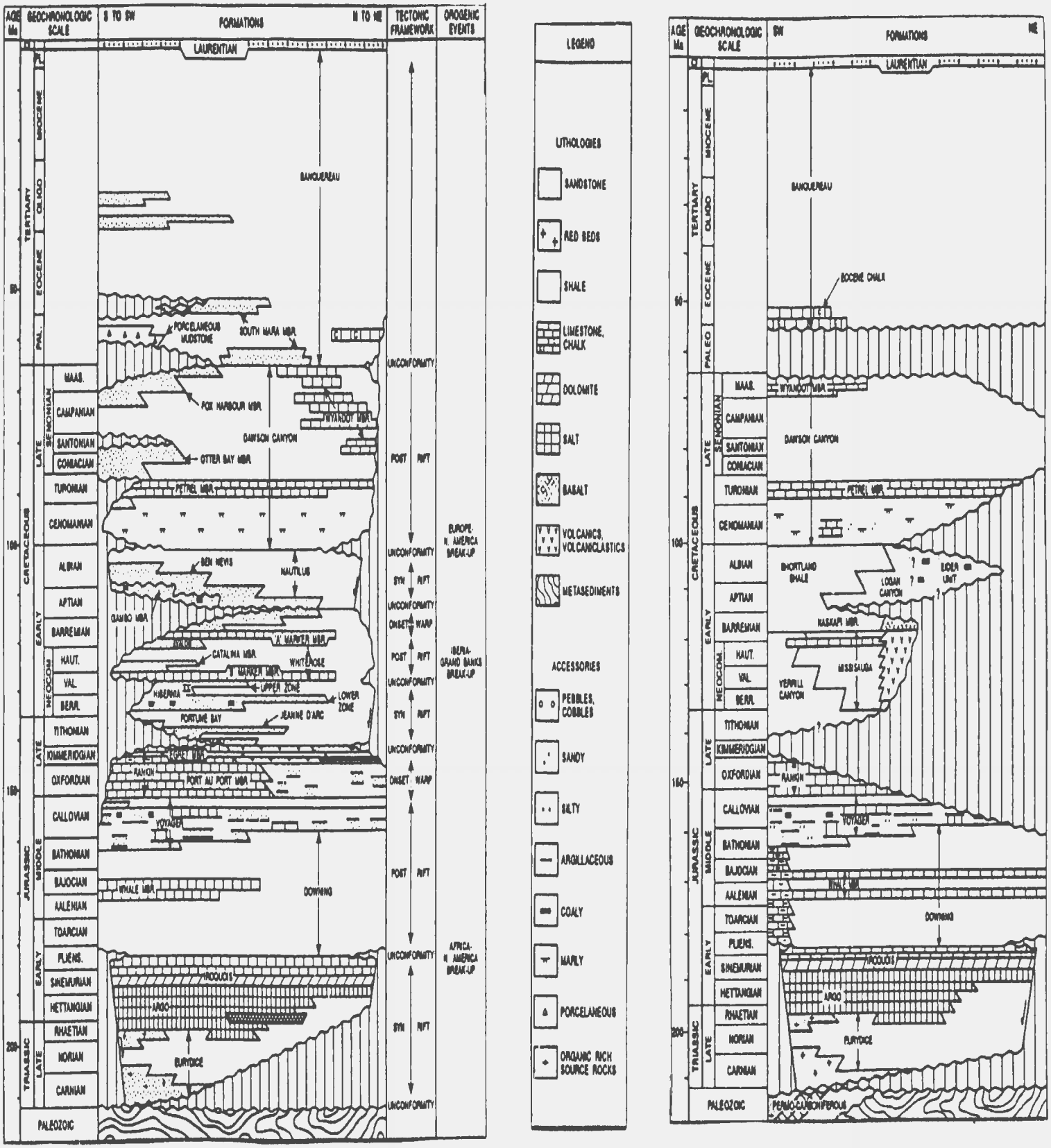

Figure 1.4. Lithostratigraphic chart for the Jeanne d'Arc Basin and the southern Grand Banks showing the relative locations of major unconformities and the timing of important tectonic events including the phases of continental breakup affecting eastern Canada. (From C-NOPB, Schedule of Wells, Newfoundland Offshore Area, 1995).

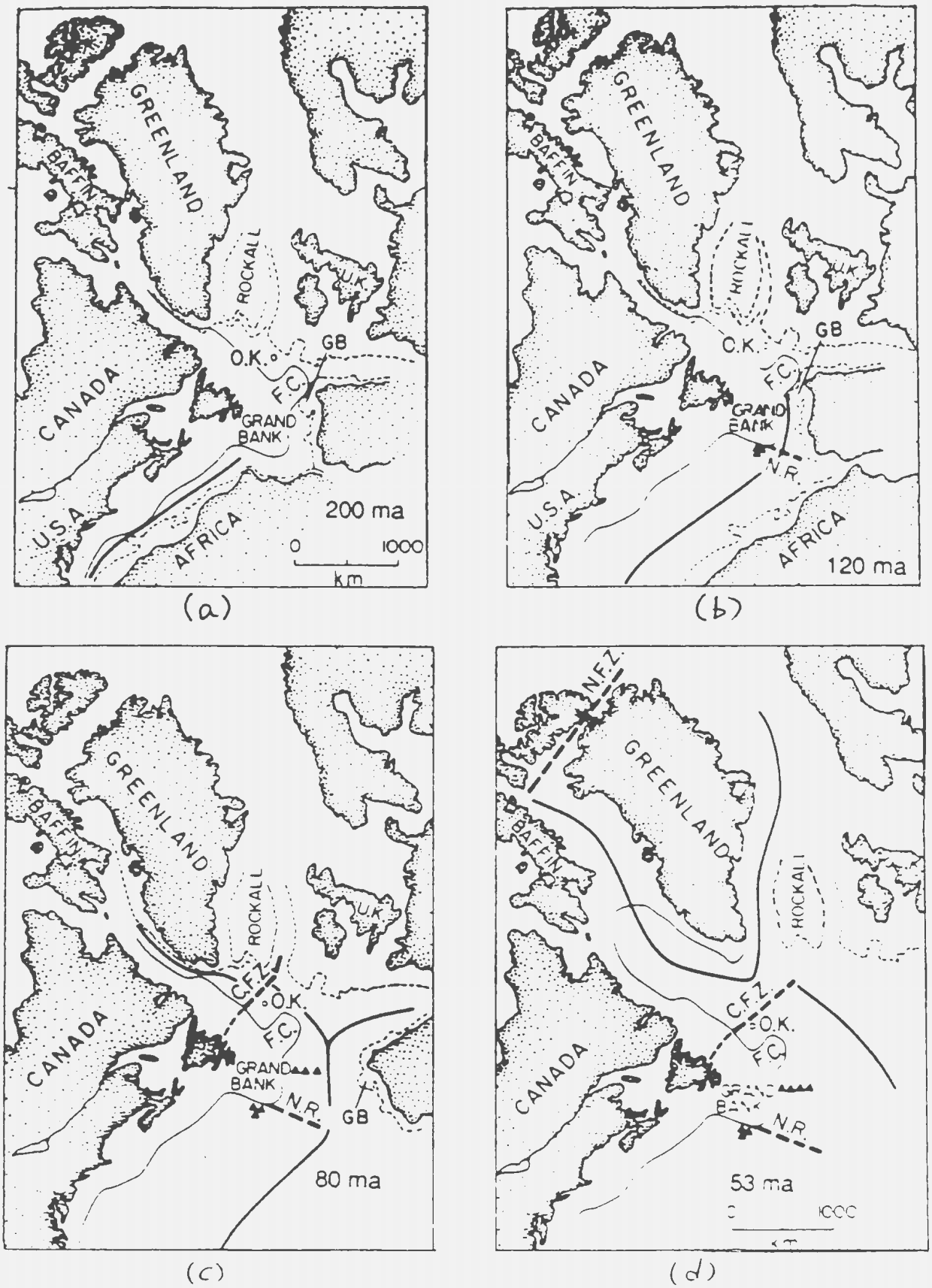

Figure 1.5. Continental breakup off eastern Canada during the Mesozoic and Early Cenozoic. The heavy solid lines are incipient or active mid-ocean ridges. The dashed lines are fracture zones. The triangles are seamounts. Lighter solid and dashed lines denote the shelf edge of each landmass. N.R. – Southeast Newfoundland Ridge; F.C. – Flemish Cap; O.K. – Orphan Knoll; C.F.Z. – Charlie Fracture Zone; GB – Galicia Bank; N.F.Z. – Nares Strait Fracture Zone (From Haworth, et al., 1994).

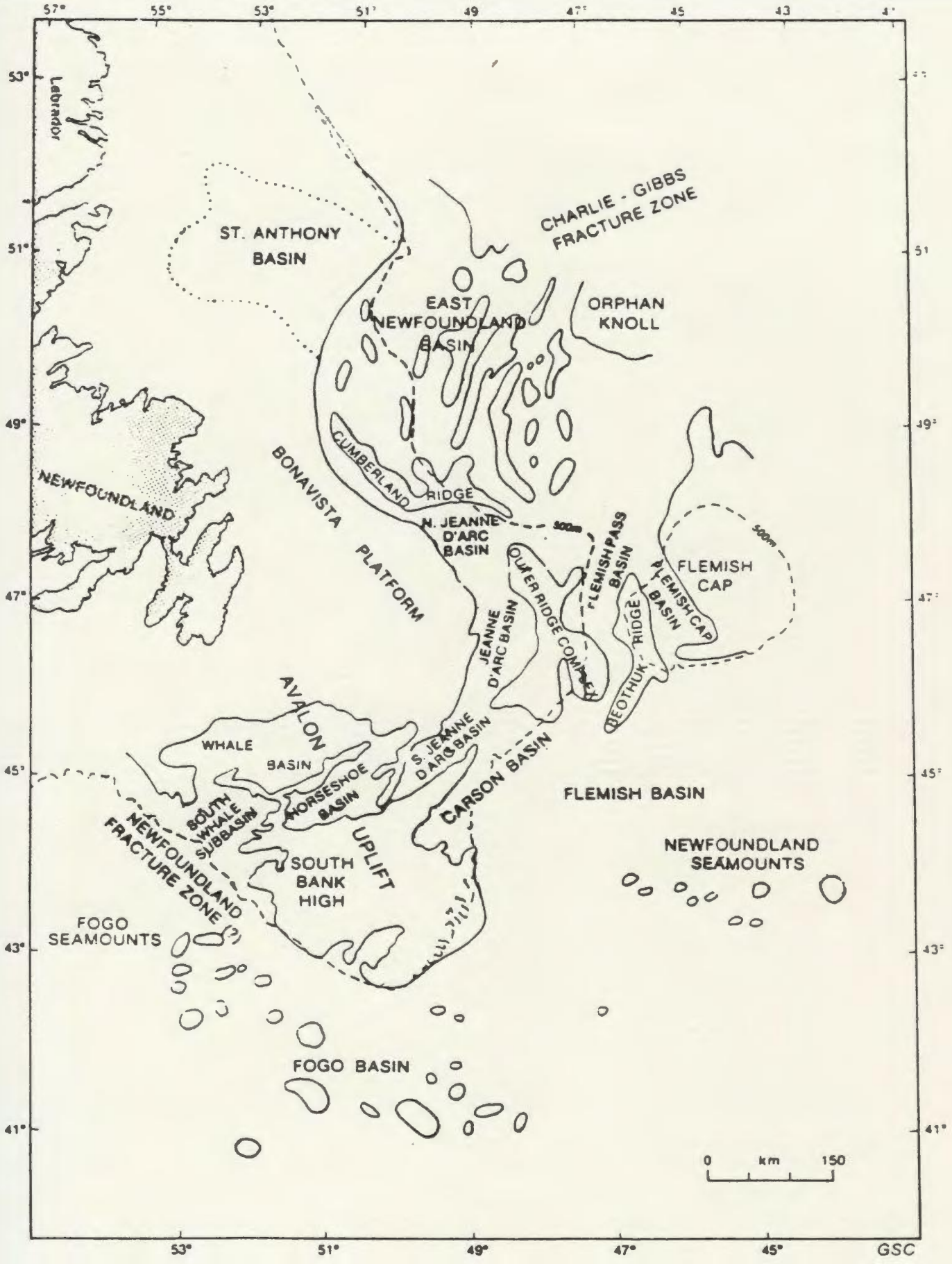

Figure 1.6. Map showing the primary structural elements of the continental margin of Newfoundland. The dashed line is the 500 metre bathymetric contour. (From Grant and McAlpine, 1990).

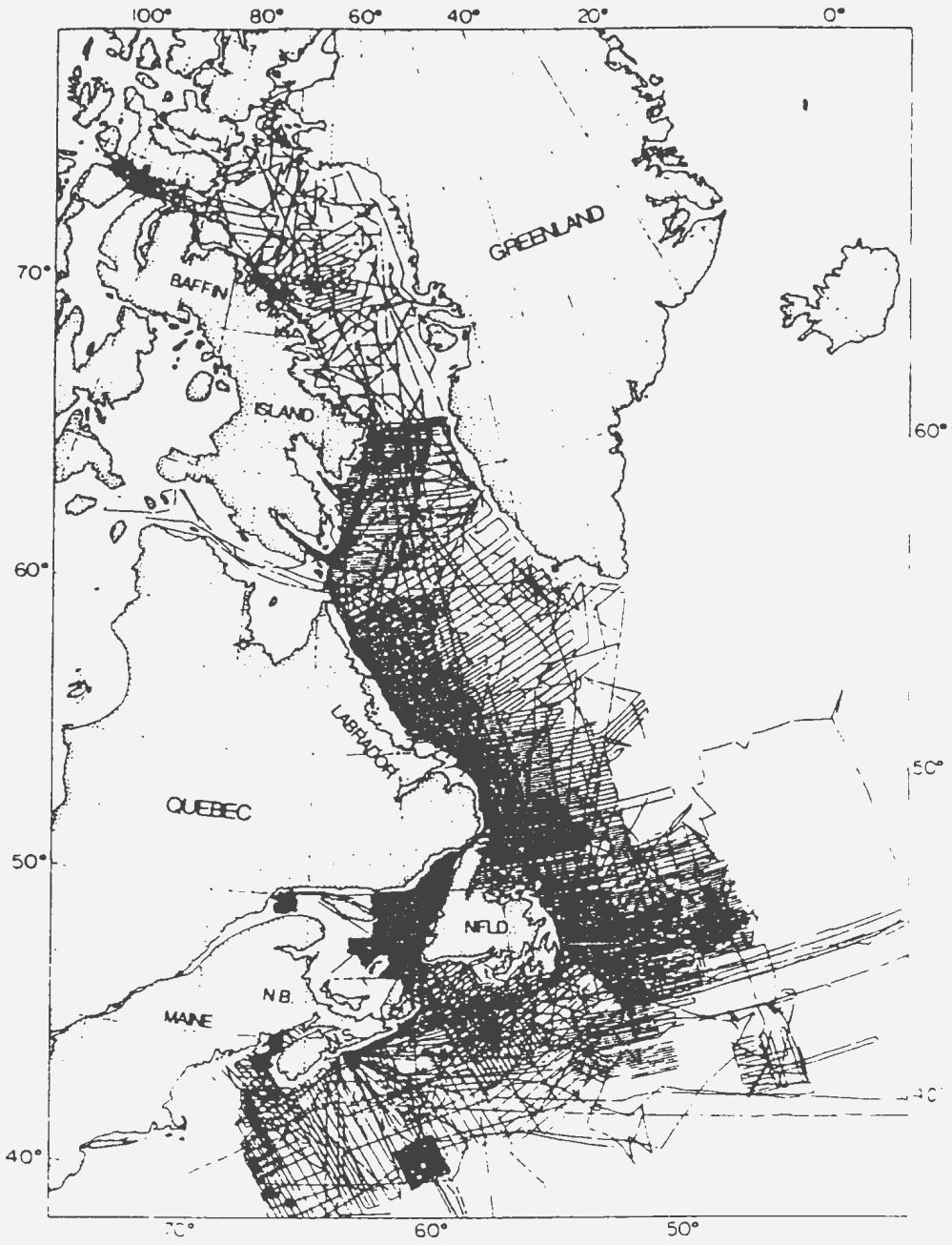

Figure 1.7. Track plot showing the coverage of marine gravity measurements off the coast of eastern Canada. (From Verhoef, et al., 1987).

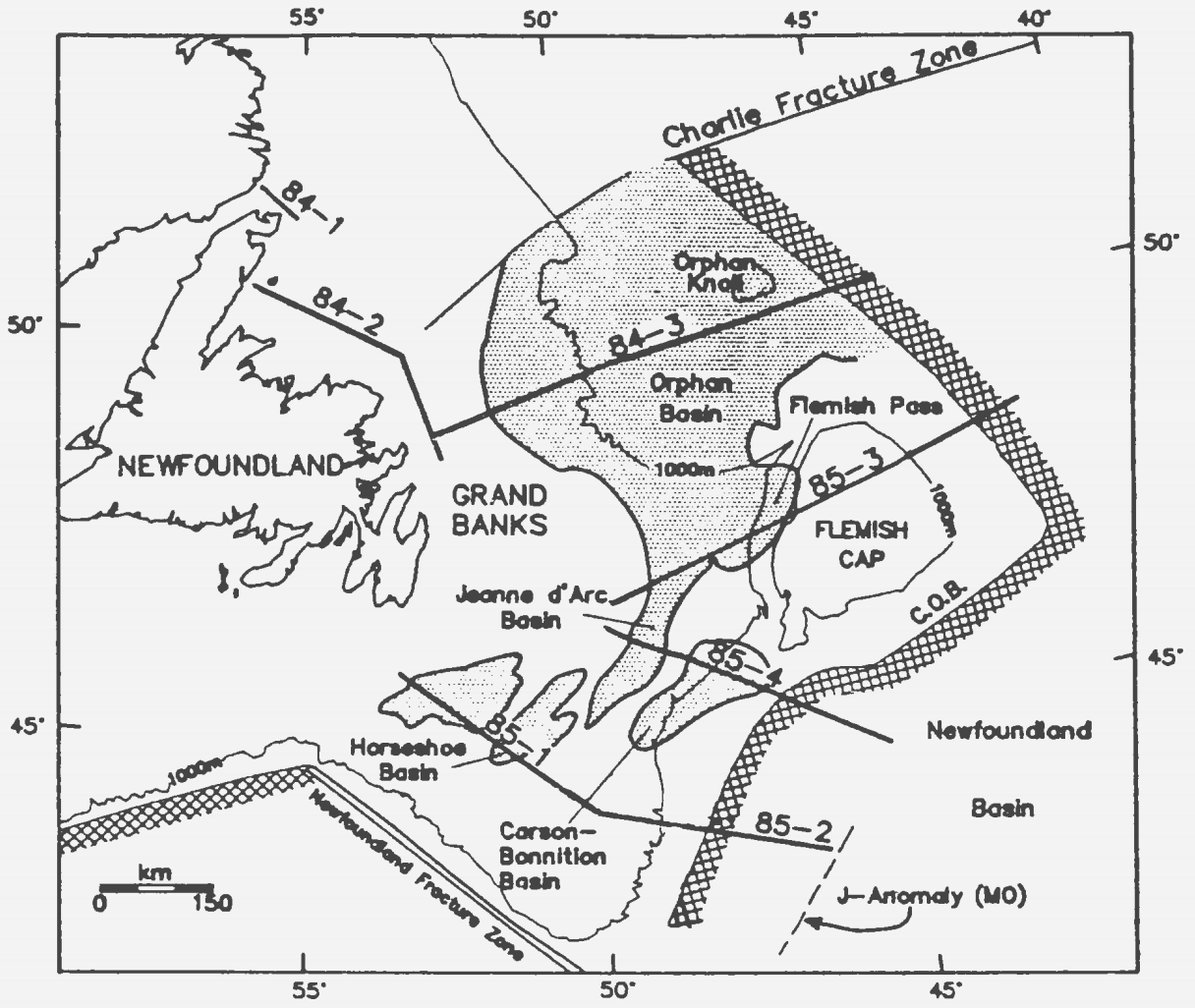

Figure 1.8. Deep multichannel seismic reflection profiles in the Grand Banks region. Shaded regions are major Mesozoic rift basins. Cross-hatched areas indicate the location of the inferred ocean-continent boundary (C.O.B.). (From Keen and de Voogd, 1988).

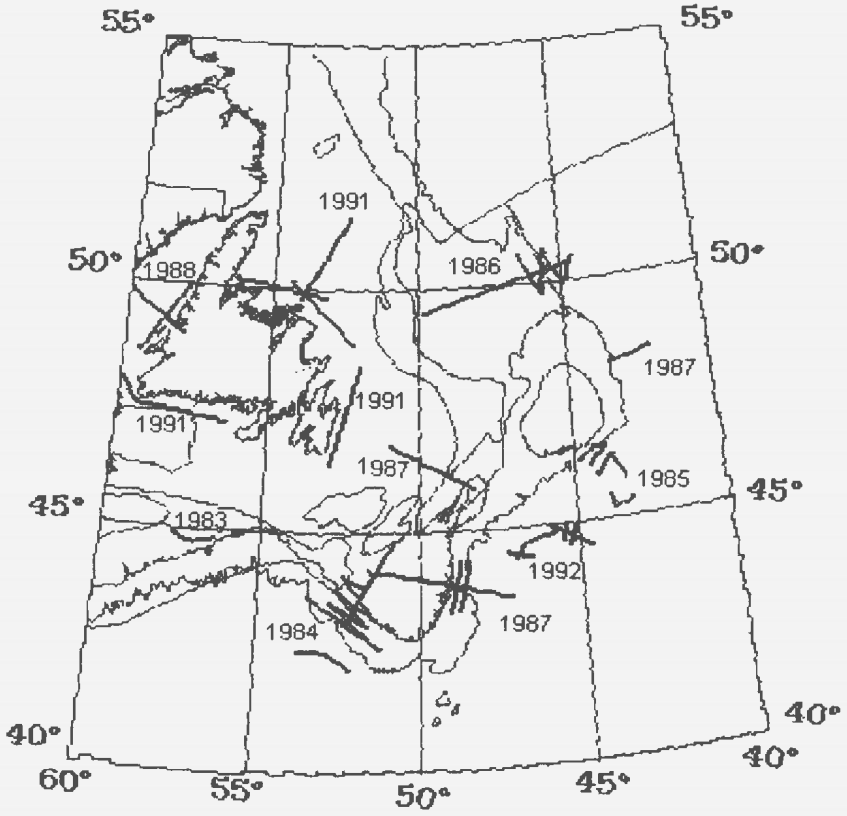

Figure 1.9. Location of deep seismic refraction lines in the Grand Banks region. (Modified from a Geological Survey of Canada web page containing an East Coast of Canada Refraction Catalogue for surveys between 1983 and 1992 inclusive; http://agc.bio.ns.ca/pubprod/ecref/index.html).

CHAPTER 2: DATA PROCESSING SEQUENCE

The Bouger anomaly data for the onshore-offshore portion of the Avalon terrane beneath eastern Newfoundland and the Grand Banks were subjected to a sequence of processing techniques discussed in this chapter to determine Moho topography. The gridding, display techniques and preparatory processing of the data for Fourier transformation are also discussed.

Since the long-wavelength (100 – 200 km) signal of the Grand Banks sedimentary basins may interfere with the long-wavelength (>100 km) signal from sources at Moho depths, the gravitational effect of these basins was modelled and the modelled field subtracted from the observed gravity field. This was accomplished using a three-dimensional modelling procedure devised by Talwani and Ewing (1960) with density information obtained from well logs and geometry information obtained from depth to basement contour maps.

The resultant gravity field was low-pass filtered in an effort to determine an ensemble average depth to Moho. This depth, along with other external information regarding Moho depth and crustal density derived mainly from seismic data and well logs was subsequently used to invert the data to derive a contoured map of Moho topography.

Each of these processing steps is discussed in detail in the following sections.

2.1 THE DATA

Figure 2.1 shows the Bouger gravity anomaly map for the Grand Banks and Avalon Peninsula region. The data are comprised of land, underwater, and shipborne gravity measurements. On land, gravity data were collected by the Dominion Observatory during the 1960s (Weaver, 1967, 1968). The data were collected at a spacing of approximately 13 km using the G74 and G9 LaCoste and Romberg gravimeters and two Wallace and Tiernan altimeters. Uncertainty in the Bouger anomaly values is approximately ±2 mGal with the greatest uncertainty attributed to the large error in elevation measurements (corresponding to ±0.9 mGal; Weaver, 1967).

From 1979 to 1986, Memorial University of Newfoundland, in collaboration with the Geological Survey of Canada, collected land gravity observations along the roads of the Avalon Peninsula with a mean spacing of 2.5 km, and by helicopter with a spacing of 5 km. Gravity measurements were made with a Sharpe CG2 gravimeter, while elevation measurements were made using Wallace and Tiernan altimeters (Miller, et al., 1985). The data were tied to the ISGN71 base system by base readings at St. John's. At each station, the Bouger anomaly was calculated using the 1967 International Gravity Formula with a crustal density of 2.67 g/cm^3. Uncertainties in the elevation measurements of ±2 m and in the horizontal position of ±50 m produce an associated uncertainty in the Bouger anomalies of ±0.4 mGal (Miller, et al., 1985; Miller, 1987).

Underwater gravity measurements were made within the major bays of the Avalon Peninsula (within 30 km of the coast) as part of a joint survey of Memorial University of Newfoundland and the Geological Survey of Canada from 1982 to 1986. The data were collected at a spacing of approximately 6 km using two LaCoste and Romberg underwater gravimeters (Miller, et al., 1985). Water depths were determined using the ship's depth sounder and horizontal positions were determined using a Mini-Ranger system consisting of three transponders located on shore. The Bouger anomalies were calculated in the same way as for the aforementioned land gravity data but a water density of 1.03 g/cm^3 was incorporated. The data were tied to the ISGN71 base network using St. John's, Newfoundland and Dartmouth, Nova Scotia base stations. Uncertainty in the water depth is approximately ±1 m while uncertainties in the horizontal positions of (i) the ship's antenna, and (ii) the underwater gravimeter with respect to the ship's antenna are approximately ±25 m each, giving a cumulative uncertainty in the horizontal position of the gravimeter of ±50 m. Therefore, the Bouger anomalies have an associated uncertainty of ±0.2 mGal.

Dynamic shipboard gravity data were collected by the Atlantic Geoscience Centre and the Geological Survey of Canada under the auspices of the Department of Energy, Mines and Resources (see Figure 1.7). From Davis Strait, east of Baffin Island, to the Gulf of Maine, the Atlantic Geoscience Centre and the Geological Survey of Canada have recorded approximately 2.3 million observations on 73 cruises spanning 21 years (Verhoef, et al., 1987; Woodside and Verhoef, 1989). Initially, the position of the ship was determined using

Survey Decca in the ranging mode which has an accuracy of 50-150 m. Long Range Navigation-C (LORAN-C) in the ranging mode replaced the Survey Decca after 1972. With the use of the Navy Navigation Satellite System (NNSS) and the Bedford Institute of Oceanography Integrated Navigation System (BIONAV), the accuracy of the ship's position was about 200 m (Verhoef, et al., 1987). Prior to 1981, the gravity measurements were made with the Graf-Askania Gss2 sea gravimeter. It was replaced with the Bodenseewerk Geosystem Kss30 gravimeter. The LaCoste and Romberg S and SL sea gravimeters and the Graf-Askania Gss3 have also been used on occasion (Verhoef, et al., 1987).

All the data were added to the National Gravity data base maintained by the Geological Survey of Canada. Crossovers, numbering over 21 000, were adjusted using a least squares network adjustment. The resulting data set has an accuracy of approximately 2.5 mGal (Verhoef, et al., 1987; Woodside and Verhoef, 1989).

National gravity data base information for eastern Canada including the offshore study area (up to the late 1980s) was obtained by Hugh Miller from the Geological Survey of Canada in the late 1980s (H. Miller, pers. comm., 2000). A polygon containing the study area was defined and the individual gravity data (i.e. Bouger and free-air anomalies, position) extracted for each gravity observation point located within the polygon. This resulted in a working data base of approximately 60 000 points. To facilitate processing, these were interpolated onto a regular 5 km grid using a simple inverse distance weighting procedure in the Geosoft Oasis Montaj geophysical software package. The

resulting gridded data were used by Miller and Singh (1995) and provided for use in this thesis.

The data extends from UTM 320000 E (59° 20' W) in the west to UTM 1365000 E (45° 30' W) in the east and from UTM 4935000 N (44° 20' N) in the south to UTM 5750000 N (51° 45' N) in the north. Before being used in this thesis, Miller clipped the data tens of kilometres landward of the inferred ocean-continent boundary, which is delineated by a strong seaward positive gravity gradient (H. Miller, pers. comm., 2000). The data are bounded as follows: west of the ocean-continent boundary from about UTM 1250000 E, 5250000 N (approximately 47° N, 47° 08' W) to about UTM 1100000 E, 4950000 N (approximately 44° 30' N, 49° 30' W); north of the Collector Anomaly, from about UTM 1100000 E, 4950000 N (approximately 44° 30' N, 49° 30' W) in the east to UTM 325000 E, 5125000 N (approximately 46° 15' N, 59° 15' W) in the west; near the Gander-Avalon Terrane boundary, i.e. from about UTM 325000 E, 5125000 N (approximately 46° 15' N, 59° 15' W) in the south to about UTM 875000 E, 5750000 N (approximately 51° 45' N, 51° 30' W) in the north; and around the western edge of the East Newfoundland Basin in the north. This clipping was undertaken to remove the gravitational edge effect due to the transition from continental to oceanic crust and to ensure only the Avalon terrane was considered.

The data were projected onto the map using the Universal Transverse Mercator (UTM) Zone 21 North projection method using the North American Datum (1927) (NAD 27).

The data covers the onshore-offshore region underlain by the Avalon Terrane of the Appalachian Orogen. The negative Bouger gravity anomalies in the offshore region are associated with sedimentary basins. In particular, the Jeanne d'Arc Basin on the northeastern Grand Banks is identified by an extreme gravity low (approximately -39 mGal) located near UTM 1125000 E, 5150000N (Figure 2.1). Generally, basins that have developed within continental crustal fabric exhibit negative gravity anomalies whereas basins that developed over the edge of the continental shelf generally exhibit positive anomalies, occasionally with flanking lows (Woodside and Verhoef, 1989) suggestive of a locally uncompensated load. The small areas of positive gravity anomaly on the interior of the Grand Banks correspond to platform regions. The Flemish Cap is identified by a large positive anomaly (40 to 50 mGal) centred on UTM 1333000 E, 5275000 N. Immediately east of the Avalon Peninsula is an elongate negative (approximately –22 mGal) Bouger anomaly (extending from about 850000 E, 5200000 N UTM to 825000 E, 5300000 N UTM) likely produced by a sedimentary basin comprised of Precambrian to Siluro-Devonian sedimentary rocks (Miller, et al., 1985). The boundary between the Gander and Avalon Terranes is expressed as the linear gravity anomaly in the western portion of the field extending from approximately UTM 875000 E, 5650000 N in the northeast to UTM 625000 E, 5350000 N in the southwest.

2.2 PRE-PROCESSING AND DISPLAY

Advances in imaging software and computational efficiency have made processing and presentation of potential field data much simpler. Computers with larger memories can store and process enormous amounts of data. The increased speed and imaging capability of contemporary computers allow the user to immediately view the effects of processing on data sets. Dynamic links between software packages allow different geophysical data to be integrated smoothly for a more comprehensive interpretation.

A limitation of computer-aided processing is that the data must be regularly spaced on a two-dimensional grid to perform such operations as Fourier transformation. The irregularly spaced nature of gravity field data requires that it be interpolated onto a regularly spaced grid.

All gravity field and topography maps displayed here were created using the GEOSOFT Oasis Montaj Data Processing and Analysis software package on a Windows platform. The gravity data were interpolated onto a regular grid with 5 km cell size in both horizontal directions using the minimum curvature algorithm of Oasis Montaj which fits a smooth minimum curvature surface to the observed values. A two-dimensional cubic spline is fitted to the data by solving its equivalent differential equation. The solution is constrained by forcing the surface to adopt the observed values at the observation points and by minimizing the total squared minimum curvature. This is accomplished by setting the partial derivatives of the total squared curvature equal to zero. A set of finite difference

equations expressed in terms of grid spacing and grid point values is produced that relate all of the surrounding grid points within a specified search radius, weighted by their inverse distance from the central grid point. The set of equations is solved iteratively until the smoothest possible surface is determined (Briggs, 1974). The advantage of the algorithm is that it readily accepts randomly spaced data sets. However, it is limited by the fact that the gridded values are interpolated estimates rather than precise values.

There are several variations on the presentation of potential field maps. The data may be contoured with lines drawn at selected intervals or at multiple intervals. Data ranges may be assigned specific colours to produce colour-contoured maps. The colour tables available in Oasis Montaj for application to gridded data sets range from grey-scale to full colour spectrum. Colour scaling can be linear or equal area. In linear colour scaling data values are divided linearly and each division is assigned a colour. With equal-area scaling the statistical histogram of data values is equalized so that each colour occupies equal area on the map. While equal-area colour scaling is useful for displaying data sets with large dynamic ranges, linear colour scaling gives a more accurate representation of the distribution of the data values.

2.3 MODELLING

The main concern in the interpretation of potential fields is identification of the source producing the observed field. A given potential field can be generated by

an infinite number of source distributions making interpretation of the field ambiguous. Modelling the potential field data is a key approach to interpretation. Three methods of modelling potential field data are two-dimensional (2-D) modelling, two-and-a-half-dimensional (2½-D) modelling, and three-dimensional (3-D) modelling.

Two-dimensional modelling is applied in situations where the geological structure of interest is linear. For example, dykes, continental margins, and fracture zones are typically longer than they are wide and produce lineated magnetic and gravity anomalies (Blakely, 1995). For two-dimensional modelling to produce reliable results, the length to width ratio of the anomaly should be significantly large. Peters (1949) suggested a ratio of 3:1 as a suitable prerequisite for two-dimensionality in estimating depth to magnetic sources. Miller (1982b) used a length to width ratio of 5:1 to model the thickness of the Holyrood Pluton in Newfoundland, while Haworth and Miller (1982) used a 6:1 ratio to model oceanic rocks beneath Notre Dame Bay, Newfoundland. Grant and West (1965) suggested that a ratio of 20:1 was needed to model near-surface ribbon-like structures. If the structure is sufficiently linear then it is treated as infinite in the direction parallel to length. In the plane perpendicular to length, the body is often modelled as an n-sided polygon (Talwani, Worzel, and Landisman, 1959; Won and Bevis, 1987) but can also be represented by rectangles of various size (Tanner, 1967) or triangular facets (Pedersen, 1978).

For structures that do not have an appropriate length to width ratio but are still roughly linear, end corrections can be applied (Rasmussen and Pedersen, 1979)

to accommodate their finite extent. This is two-and-a-half-dimensional modelling, which is applied in situations where the conditions of two-dimensionality cannot be adhered to.

For structures that do not meet the criteria of two- or two-and-a-half-dimensionality, three-dimensional modelling is used. An areal array of data values is required for three-dimensional modelling. The source distribution can be approximated by stacked horizontal laminae (Talwani and Ewing, 1960; Jacobi, 1967), cubical blocks (Mufti, 1975), rectangular prisms (Nagy, 1966; Cordell and Henderson, 1968), or polyhedra (Paul, 1974; Coggon, 1976; Barnett, 1976).

2.3.1 MODELLING THE GRAVITY FIELD OF THE SEDIMENTARY BASINS

The primary geological features of interest on the Grand Banks are the Mesozoic rift basins, half-grabens resulting from the extension and continental breakup that precipitated the formation of the Atlantic Ocean. Examination of the gravity anomaly map of the region (Figure 2.1) reveals that the gravity anomalies associated with the sedimentary basins have wavelengths on the order of 100 to 200 km. Since the purpose of this study is to isolate the long-wavelength (>100 km) effects of Moho topography, considerable problems can arise in attempting to distinguish Moho-related effects from basin effects. Therefore, the gravity effect of the sedimentary basins was modelled and subtracted from the observed gravity field. The model effect was calculated at each data point using the

method of Talwani and Ewing (1960), i.e. using stacked polygonal laminae, since depth to basement contour maps that outline the approximate shape of the basins were readily available. The FORTRAN program used is given in Appendix A. It was modified from an existing program provided by Hugh Miller (1970).

The underlying premise is that any three-dimensional body can be defined by a set of contours. Each contour defining the body is replaced with a horizontal, n-sided irregular polygonal lamina (Figure 2.2) and the gravity anomaly of the lamina may be calculated at any external location.

A three-dimensional body M bounded vertically at z_{top} and z_{bottom} is shown in Figure 2.2 with respect to a left-handed Cartesian coordinate system. The origin of the coordinate system, P, is the point at which the gravity anomaly is to be calculated. Letting the polygonal lamina $ABCDEFGH$ of infinitesimal thickness dz replace a contour on the surface of M at a depth z below the origin, the gravity anomaly at P due to $ABCDEFGH$ is (after Talwani and Ewing, 1960)

$$\Delta g = V dz, \qquad \ldots(2.1)$$

where V is the gravity anomaly caused by the lamina per unit thickness. V is expressed as a surface integral over the surface of $ABCDEFGH$ but can be rewritten as two line integrals along the boundary of the lamina: (after Talwani and Ewing, 1960)

$$V = G\rho\left[\oint d\psi - \oint \frac{z}{\sqrt{r^2 + z^2}} d\psi\right]$$

...(2.2)

where $z, \psi,$ and r are the cylindrical coordinates describing the boundary of the lamina. As illustrated in the second part of Figure 2.2, V can be expressed in terms of the geometry of $ABCDEFGH$: (after Talwani and Ewing, 1960)

$$V = G\rho\left[\sum_{i=1}^{n}\left\{\psi_{i+1} - \psi_i - \sin^{-1}\frac{z\cos\theta_i}{\sqrt{p_i^{\,2} + z^2}} + \sin^{-1}\frac{z\cos\phi}{\sqrt{p_i^{\,2} + z^2}}\right\}\right].$$

...(2.3)

Integration from z_{bottom} to z_{top} gives the total gravity anomaly caused by body M : (after Talwani and Ewing, 1960)

$$\Delta g_{tot} = \int_{z_{bottom}}^{z_{top}} V dz.$$

...(2.4)

For processing by computer, V can be expressed in terms of the coordinates of two consecutive vertices of the polygonal lamina, i.e. (x_i, y_i, z) and (x_{i+1}, y_{i+1}, z): (after Talwani and Ewing, 1960)

$$V = G\rho \sum_{i=1}^{n} \left\{ W \cos^{-1}\left[\frac{x_i}{r_i}\frac{x_{i+1}}{r_{i+1}} + \frac{y_i}{r_i}\frac{y_{i+1}}{r_{i+1}} \right] - \sin^{-1}\left[\frac{zq_iS}{\sqrt{p_i^2 + z^2}} \right] + \sin^{-1}\left[\frac{zf_iS}{\sqrt{p_i^2 + z^2}} \right] \right\}$$

...(2.5)

where ρ is the volume density of the lamina,

$$P_i = \frac{y_i - y_{i+1}}{r_{i,i+1}} x_i - \frac{x_i - x_{i+1}}{r_{i,i+1}} y_i,$$

$$q_i = \frac{x_i - x_{i+1}}{r_{i,i+1}} \cdot \frac{x_i}{r_i} + \frac{y_i - y_{i+1}}{r_{i,i+1}} \cdot \frac{y_i}{r_i},$$

$$f_i = \frac{x_i - x_{i+1}}{r_{i,i+1}} \cdot \frac{x_{i+1}}{r_{i+1}} + \frac{y_i - y_{i+1}}{r_{i,i+1}} \cdot \frac{y_{i+1}}{r_{i+1}},$$

$$m_i = \frac{y_i}{r_i} \cdot \frac{x_{i+1}}{r_{i+1}} - \frac{y_{i+1}}{r_{i+1}} \cdot \frac{x_i}{r_i},$$

$$r_i = +\sqrt{x_i^2 + y_i^2},$$

$$r_{i+1} = +\sqrt{x_{i+1}^2 + y_{i+1}^2},$$

$$r_{i,i+1} = +\sqrt{(x_i - x_{i+1})^2 + (y_i - y_{i+1})^2}\ ,$$

$S = +1$ if P_i is positive,

$S = -1$ if P_i is negative,

$W = +1$ if m_i is positive, and

$W = -1$ if m_i is negative.

...(2.6)

The computer program calculates V for each of the laminae. The gravitational attraction due to the entire body is obtained by numerical integration of the effect of each lamina. Letting $V_1, V_2, \text{and} V_3$ denote V at depths $z_1, z_2, \text{and} z_3$, respectively, then (after Talwani and Ewing, 1960)

$$\int_{z_1}^{z_3} V dz = \frac{1}{6}\left[V_1 \frac{(z_1 - z_3)}{(z_1 - z_2)}(3z_2 - z_3 - 2z_1) + V_2 \frac{(z_1 - z_3)^3}{(z_2 - z_3)(z_2 - z_1)} + V_3 \frac{(z_1 - z_3)}{(z_3 - z_2)}(3z_2 - z_1 - 2z_3) \right]$$

...(2.7)

The effect of the entire body is obtained by integrating over successive groups of three depths. This process is repeated for all constituent bodies of the model. In this way, the gravitational attraction of all the bodies in the model can be calculated at any external location.

Therefore, the information required by the program to calculate Δg is: (i) the coordinates of the points that define each contour of the body; (ii) the density of

the body; and (iii) the coordinates of the external points at which the anomaly is calculated. With these data, the program will output the calculated anomaly at each of the external input locations.

The closeness of fit between the polygons and the contours of the body, as well as the precision of the numerical integration over all polygons, determines the accuracy of the modelling procedure. The shape of any contour can be more closely approximated by increasing the number of sides in the representative polygon. Likewise, the shape of any three-dimensional body can be more closely approximated by increasing the number of constituent laminae. The greater the number of sides per lamina and/or the more closely spaced the laminae are, the more accurate the resultant anomaly will be. Increasing the number of sides in a polygon, however, will increase the computation time. Taking into consideration the speed of computers available at the time of publication of this method (1960) as compared to the speed of those presently available, the problem of computing time becomes less critical.

Talwani and Ewing (1960) compared the calculated anomaly due to a circular lamina with that of a 72-sided polygon (inscribed within the lamina) and found that the maximum difference occurred at the location of minimum separation between the lamina and the point of calculation. Even then, the difference amounted to less than one third of one percent of the total anomaly. Therefore, the closeness of fit between the contour and its polygon only becomes significant if the boundary of the polygon is near the point at which the anomaly is being calculated and, even then, only minimally so.

The accuracy of the numerical integration depends on the contour interval. The assumption that V is smoothly continuous between the contours is based on the assumption that the depth of the surface of the body is also smoothly continuous between the contours. Therefore, adding more contours between existing contours does not necessarily increase the accuracy of the method in determining the anomaly and only proves to be more labour intensive. However, the selected contour interval should be selected to ensure that the depth of the contours or the distances between them does not inordinately affect the calculated anomaly.

2.4 FREQUENCY DOMAIN PROCESSING

The application of frequency domain processing techniques to potential fields first appeared in a paper on the use of Fourier series in gravity interpretation by Tsuboi and Fuchida in 1937.

Processing in the frequency domain has many applications in the interpretation of gravity anomaly data. They include enhancement or attenuation of features of the gravity field through analytic continuation, delineation of the extent of the source body via first and second vertical derivatives, and estimating source depth and geometry from spectral analysis of the potential field. Potential field data is processed more easily and efficiently in the frequency domain.

2.4.1 Fourier Transformation

Conversion of a function from the space, or time, domain to the frequency, or wavenumber, domain is via the integral Fourier transform. Given a two-dimensional function $f(x,y)$, its Fourier transform is expressed as

$$F(k_x, k_y) = \int_{-\infty}^{\infty}\int_{-\infty}^{\infty} f(x,y)\exp[-2\pi i(k_x x + k_y y)]\,dy\,dx \qquad \ldots(2.8)$$

where $k_x = 2\pi/\lambda_x$ and $k_y = 2\pi/\lambda_y$ are wavenumbers of the function in units of radians per unit distance and $F(k_x, k_y)$ and $f(x,y)$ form a transform pair, i.e. $F(k_x, k_y) \leftrightarrow f(x,y)$. (In one dimension, given the function $f(x)$, its Fourier transform is

$$F(k) = \int_{-\infty}^{\infty} f(x)\exp(-2\pi ikx)\,dx \qquad \ldots(2.9)$$

and $F(k) \leftrightarrow f(x)$.)

Conversely, the inverse Fourier transform allows for conversion from the frequency domain to the space domain, i.e. given the function $F(k_x, k_y)$,

$$f(x,y) = 1/4\pi^2 \int_{-\infty}^{\infty}\int_{-\infty}^{\infty} F(k_x,k_y)\exp[2\pi i(k_x x + k_y y)]dk_x dk_y$$

...(2.10)

Transformations between the frequency and space domains are exact; that is, there is no loss of information during the conversion. This is a useful property since calculations performed in the frequency domain are more efficient. Operations such as continuation of the field (Bhattacharyya, 1967) and vertical and horizontal derivatives (Blakely, 1995) are simple linear relationships in the frequency domain. Convolution in the space domain corresponds to straightforward multiplication in the frequency domain.

The integral Fourier transform is obtained from the integration over infinite space of a continuous, non-periodic function whose flanks asymptotically approach zero (Cordell and Grauch, 1982). If a function or its derivatives are discontinuous then the fit between it and its Fourier transform is poor approaching the discontinuity. As the order of the Fourier series increases, the area of misfit becomes increasingly large and is referred to as Gibb's phenomenon (Sheriff, 1973). However actual data sets are not infinite in extent so the discrete form of the Fourier transform (also referred to as the fast Fourier transform, FFT) is used. By convolving a function $f(x,y)$ with a Dirac comb, a periodic function is generated. This function is then discretely sampled at evenly spaced intervals to form a sequence, $\hat{f}_j$, $j = 0,1,\ldots,N-1$ where **N** is the number

of discrete samples. The fast Fourier transform is obtained by summing the sequence over the number of samples, i.e. (after Cordell and Grauch, 1982)

$$\hat{F}_k = \sum_{j=0}^{N-1} \hat{f}_j \exp[-2\pi i(k_j / N)], \qquad j,k = 0,1,\ldots,N-1$$

...(2.11)

Formulae relating geologic parameters of the source to the field function are derived using the integral Fourier transform but, in practice, use the discrete Fourier transform. While the discrete transform is more practical for the manipulation of real, finite data sets, its use generates a new set of difficulties.

At zero wavenumber (i.e. the dc level), the value of the discrete transform is lower than that of the integral transform. Since the dc term of the integral transform, $F(k=0)$, is used to obtain the total anomalous Gaussian mass, M, in the case of gravity field interpretation (i.e. $F(0) = 2\pi GM$), underestimation of this value will result in an underestimate of the total anomalous mass. This problem is resolved by the convolution of the original function with a Dirac comb to produce a periodic function as described previously since this phenomenon is most apparent when the function is simply sampled periodically (i.e., multiplied by a Dirac comb rather than convolved with it).

A problem inherent in the discrete Fourier transform is the presence of a high-frequency tail (Cordell and Grauch, 1982) in the spectrum of the function at large wavenumbers, which becomes more pronounced as wavenumber increases.

The tail is caused by sampling the actual data set only a finite number of times and is evidenced by the divergence of the discrete transform from the integral transform at large wavenumbers. Due to the inherence of the tail in discrete Fourier transformation, it is invariably found in the discrete spectra of real data sets. The problem is remedied to some extent by convolution of the function with a Dirac comb, which swings the tail closer to the value of the integral transform. In practical situations, however, the high-frequency tail is best treated as noise and, as such, should be filtered out. This is particularly important in processing applications that tend to amplify the signal at large wavenumbers, such as downward continuation and differentiation.

2.4.2 Wavelength Filtering

A filter is an operator that acts on an input data set in such a way as to produce a modified output data set. Filtering simply separates data into its component parts in an effort to distinguish valuable information from irrelevant information, i.e. noise. When the observed signal and the attendant noise can be differentiated in some fundamental sense, e.g. they have different spectral (§2.4.2.1) characters, then this is easily accomplished. However, if noise is embedded within the observed signal (as is most often the case), this proves to be more complicated. In the frequency domain, useful information is extracted by specifying frequency components in the data to be accepted, i.e. passed, or

rejected. Depending on the frequencies to be passed or rejected, a filter is referred to as a low-pass, high-pass, band-pass, or notch filter.

Filters are characterized by their frequency responses – how they behave in the frequency domain at all frequencies. The frequency response, $R(f)$, of a low-pass filter is as follows: (after Buttkus, 2000)

$$R_l(f) = \begin{cases} 1 \text{ for} - f_c \le f \le f_c \\ 0 \text{ otherwise} \end{cases}$$

...(2.12)

where f_c is the cutoff frequency. For a high-pass filter:

$$R_h(f) = \begin{cases} 1 \text{ for } f_c < |f| \\ 0 \text{ for} - f_c \le f \le f_c \end{cases}$$

...(2.13)

Band-pass and notch filters operate by passing or rejecting frequencies between $f_{\min} = f_o - \frac{\Delta f}{2}$ and $f_{\max} = f_o + \frac{\Delta f}{2}$, where $\Delta f = f_{\max} - f_{\min}$. The frequency response of a band-pass filter is given by

$$R_b(f) = \begin{cases} 1 \text{ for } f_{\min} \le |f| \le f_{\max} \\ 0 \text{ otherwise} \end{cases}$$

...(2.14)

and that of a notch filter by

$$R_b(f) = \begin{cases} 0 \text{ for } f_{\min} \le |f| \le f_{\max} \\ 1 \text{ otherwise} \end{cases}.$$

...(2.15)

A potential field measurement taken at a single location is a composite of all subsurface sources. In other words, potential field data is broadband. Long-wavelength components of potential fields are usually associated with both large coherent bodies near the observational surface (e.g. sedimentary basins, batholiths) and deeply buried sources whose surface expression is a broad anomaly. Short-wavelength components are associated with relatively small near-surface mass distributions and noise.

This feature of potential fields allows sources to be discriminated by the wavelength of the anomaly they produce. Low-pass and high-pass filters distinguish the effects of deep, long-wavelength sources from shallow, short-wavelength sources. Low-pass filters applied to data sets in the frequency domain will pass the low-frequency (long-wavelength) components of the field unaltered. The high-frequency content will be suppressed contingent on the

specified cut-off frequency. Similarly, high-pass filters will pass the high-frequency (short-wavelength) content of a potential field and suppress the low-frequency signals. However, an abrupt cut-off frequency will result in ringing (Gibb's phenomenon) in the filtered data. Properly designed, a low-pass filter will smoothly attenuate the data values through the transitional range between values that are passed and those that are suppressed. A low-pass cosine roll-off filter was used here which smoothly attenuates the data within a 'roll-off' range. That is, frequencies less than the specified roll-off frequency (the frequency at which to begin attenuating the data), f_r, are passed unaffected and frequencies greater than the cut-off frequency, f_c, are eliminated. Data with frequencies between f_r and f_c are attenuated according to the function

$$\cos^n\left\{\frac{\pi}{2}\left(\frac{f-f_r}{f_c-f_r}\right)\right\} \qquad f_r \le f \le f_c$$

...(2.16)

where n is the degree of the cosine function; the lower the degree, the more gradual the attenuation will be. A degree of n=2 was used here to ensure as sharp a cutoff as possible while eliminating ringing.

To apply filters to a set of potential field data, it must be converted to the frequency domain using a fast Fourier transform algorithm. For transformation in Oasis Montaj, the gridded data must (1) be square (i.e. same number of data points in each of the two horizontal directions), (2) have no dummy values (i.e. no

absent data points), and (3) be periodic at its edges. This involves a series of preprocessing steps to prepare it for transformation. Trend removal followed by expansion of the gridded data and filling of the expanded area with extrapolated values will modify the data so it will meet these requirements.

Trend removal is a form of regional-residual separation in which a polynomial function or surface is fitted to the regional potential field. The degree of the function depends on what information is to be derived from the data. It can refer to the mean value of the field or an nth-order polynomial surface. The removal of a low-order polynomial surface removes the regional field. For example, removing a zeroth-order polynomial surface subtracts a mean value from the observed field. Removing the first-order polynomial surface will highlight the general strike of the potential field while the second-order polynomial surface will outline more specifically the trend of the field. The removal of higher-order polynomial functions will resolve the residual, near-surface features of the potential field. The trend to be removed is estimated from either the edge points at the margin of the potential field or all the data points defining the field. Using the edge points tends to yield a more accurate representation of the regional field. Trend removal is an important step. If left in the data, an appreciable trend will cause the expansion and filling processes to introduce a step function in the expanded area to make the data periodic and will contaminate the low-frequency estimates. This step function may produce ringing in the data upon transformation to the frequency domain.

A problem that arises when transforming the data is the appearance of a suspect periodicity which generates spurious fields near the edges of the data set (Parker, 1973). This is counteracted by adding a fringe of dummy values around the field to insulate it from these effects. To make the data smoothly periodic at its edges (and since the Fourier transform algorithm in Oasis Montaj does not accept dummy values) they are replaced by values extrapolated from the gridded data.

To isolate the long-wavelength gravitational effect of the Moho, a series of low-pass filters was applied to the data, each having a progressively lower cut-off frequency. This technique has been used by Agarwal, et al. (1995) to identify sources lying at Moho depth, Lefort and Agarwal (1996) to delineate undulations in the Moho beneath the Paris Basin related to the European Alpine orogen, and by Lefort and Agarwal (2000) to identify a lineated crustal bulge beneath Brittany, France.

The data was prepared for Fourier transformation by (1) removing the mean trend using edge points only, (2) expanding the grid to square dimensions, and (3) filling the expanded area with extrapolated values, allowing them to taper to 0 mGal over 25 km (i.e. 5 times the grid spacing). This was found to suppress ringing in the data. The data was low-pass filtered using cut-off wavelengths of 100, 150, 175, and 200 km to isolate progressively longer wavelength components of the field.

2.4.2.1 Depth Estimation

Using angular frequency $\omega = 2\pi f$, the Fourier transform of a function can be written complexly as

$$F(\omega) = A(\omega)\exp[i\Phi(\omega)] \qquad \ldots(2.17)$$

where $A(\omega)$ refers to the amplitude spectrum of the function and $\Phi(\omega)$ refers to its phase spectrum. The square of the Fourier amplitude spectrum is the power spectrum:

$$E = \left|A(\omega)\right|^2 \qquad \ldots(2.18)$$

Depth to causative mass distributions can be obtained by analyzing a plot of the logarithm of the power spectrum as a function of wavenumber (or frequency).

Spector and Grant (1970) devised a method of estimating the depth to subsurface sources by applying a basic principle of statistical mechanics to the power spectrum of magnetic fields. The underlying assumption of their hypothesis is that the subsurface is divided into a number of ensembles of right rectangular prisms and the observed magnetic field is a synthesis of the anomalies produced by each of the ensembles. Each prism is described by a set

of parameters including physical dimensions (e.g. length, width, thickness), depth, and magnetization (or density contrast). These parameters possess probabilities that are shared by the entire ensemble. Separation of the effects of individual ensembles is based on the statistical postulate that the ensemble average of the power spectrum is equal to its mathematical expectation value $\langle E \rangle$.

The expectation value of the power spectrum is expressed as the product of a depth extent factor, a depth factor, and a size factor. The depth extent factor, $(1-\exp(-tk))^2$ (where t is the depth extent of the ensemble) produces a peak in the spectrum. As the depth extent of the source ensemble increases, the peak shifts to smaller wavenumbers (Figure 2.3(a)). For an ensemble of prisms whose thickness is indiscernible, i.e. bottomless prisms, the peak occurs at $k=0$ and, in many cases, is not even visible. The depth factor, $\exp(-2\bar{h}k)$ (where $\bar{h}$ is the mean ensemble depth and $k=\sqrt{k_x^{\,2}+k_y^{\,2}}$) dominates the power spectrum since it determines the rate of decay of the power spectrum with increasing wavenumber. As the depth of the sources increases, the peak moves toward smaller wavenumbers. The size factor, $S^2(k)$, is a function of the length and width of the prismatic ensemble and attenuates the spectrum toward higher wavenumbers.

The amplitude of the spectrum at any wavenumber is finite and approaches zero exponentially with increasing wavenumber (Bhattacharyya, 1967). The power spectrum exhibits intervals of wavenumber in which the logarithm of power varies approximately linearly with wavenumber. That is, the logarithm of power

decreases linearly with increasing wavenumber within discrete segments of the spectrum. The slopes of these linear segments are proportional to the depths to the top of the prism ensembles.

Curvature of the power spectrum suggests that as many as five linear segments or ensemble depths can be identified (Connard, et al., 1983). The most commonly encountered situation is one in which there are two ensembles of sources - deep and shallow. These ensembles are recognizable by a change in the rate of decay of the power spectrum with wavenumber. As discussed above, the mean ensemble depth dominates the spectrum so a significant change in the depth of the ensembles results in a significant change in the rate of decay.

The power spectrum generally has two components arising from two source ensembles. The deeper ensemble of sources is manifested in the small-wavenumber end of the spectrum while the shallow ensemble manifests itself in the large-wavenumber end (Figure 2.3(b)). The tail of the spectrum is a consequence of high-wavenumber (high-frequency) noise.

Depth estimates in Oasis Montaj were calculated using the radially averaged power spectrum. This is obtained by averaging the power in all directions for each wavenumber. The ensemble depth is calculated using the formula

$$h = \frac{\log(E)}{4\pi k}. \qquad \ldots(2.19)$$

Since the slope of the logarithmic power spectrum is $\log(E)/k$, depth is obtained by dividing the slope by 4π.

2.4.3 Vertical Derivative

The gravitational effect of a subsurface distribution of mass varies as the inverse of the square of the distance between the mass and the observation point. The first vertical derivative varies as the cube of that distance; the second vertical derivative varies as the fourth power of the distance, and so forth. In this way, vertical derivatives tend to amplify the effects of shallow sources while attenuating the effects of deeper ones. This is evident in the calculation of vertical derivatives in the frequency domain. Given a potential field $f(x,y,z)$, the nth-order vertical derivative is calculated as follows,

$$\frac{\partial^n f(x,y,z)}{\partial z^n} = F^{-1}[|k|^n F(f(x,y,z))] \qquad \ldots(2.20)$$

where F refers to the Fourier transform operator, F^{-1} refers to the inverse Fourier transform operator and $|k| = \sqrt{k_x^2 + k_y^2}$ where k_x and k_y are the wavenumbers in the *x*- and *y*- directions, respectively. Clearly, multiplying the transformed potential field by $|k|$ to any power will magnify short-wavelength

features of the potential field typically associated with near-surface sources while attenuating long-wavelength components.

Higher order derivatives are unstable since they tend to amplify short-wavelength noise inherent in the potential field. First and second derivatives are the most commonly used. The first vertical derivative of the observed gravity field is required as input for the inversion algorithm used here.

2.5 INVERSION

The modelling procedure is performed in one of two modes: forward or inverse. With the forward method, an initial model of the source is constructed. The model anomaly is calculated and compared to the observed anomaly. If there is an unacceptable discrepancy between the two, the parameters of the model (i.e. geometry and/or density) are adjusted and the anomaly recalculated. The model parameters are adjusted after each comparison until there is reasonable agreement between the observed and calculated anomalies.

Inverse modelling is an automated procedure. Upon construction of an initial model and calculation of its anomaly, the fit between the observed and calculated anomalies is computed. The model is then automatically adjusted based on the misfit. This automated procedure is repeated until the error between the observed and calculated anomalies has been minimized. The initial model can be provided by the user or can be derived automatically from the observed field.

When modelling a gravitational field, the general equation to be solved is (Condi et al., 1999)

$$\vec{g} = \bar{A}\vec{\rho} \qquad \ldots(2.21)$$

where $\vec{g}$ is the vector of gravity field values, $\bar{A}$ is the matrix describing the geometry of the source, and $\vec{\rho}$ is the vector of source densities. In forward modelling, $\bar{A}$ and $\vec{\rho}$ are assumed and $\vec{g}$ is calculated and compared with the observed values. In inverse modelling, either $\vec{\rho}$ or $\bar{A}$ or both are unknown and must be determined from $\vec{g}$. If it is only $\vec{\rho}$ that is unknown, the inverse problem may be considered linear. If $\bar{A}$ or both $\bar{A}$ and $\vec{\rho}$ are unknown, the problem is non-linear.

Depending on the chosen inversion scheme, attributes such as non-uniqueness of the solution and uncertainty in the model at each step can be estimated - an advantage over forward modelling (Condi et al., 1999). Furthermore, using inversion rather than forward modelling significantly reduces the time required to fit the data to a model. A drawback of the inversion method is that it is essentially a mathematical procedure based on the 'goodness of fit' between the observed and calculated anomalies and may not yield a geologically significant solution.

Inversion methods can be divided into three categories (Condi et al., 1999): (1) iterative methods (Bott, 1960; Cordell and Henderson, 1968); (2) optimization methods (Li and Oldenburg, 1998; Barbosa et al., 1999; Condi et al., 1999); and (3) Fourier transform methods (Oldenburg (1974) based on Parker (1973); Gerard and Debeglia (1975); Chenot and Debeglia (1990)).

Iterative methods involve modelling the source as a distribution of polygonal (in two dimensions) or polyhedral (in three dimensions) bodies, calculating the expected anomaly and comparing it to the observed anomaly. This procedure is repeated until a suitable model is produced.

Optimization methods concentrate on optimizing the inversion process by modifying existing algorithms or designing new ones that try to mitigate some of the inadequacies inherent in inversion.

Fourier transform methods generally involve solution of the following equation:

$$F[\textit{updated source distribution}] = \frac{F[f(x,y,z)]}{A} - \sum^{n} \frac{(-|k|)^n}{n!} F[\textit{initial source distribution}] \quad \ldots(2.22)$$

where $f(x,y,z)$ is the potential field, F is the Fourier transform operator, and A is an expression describing the physical property (density) of the body. An initial estimate of the source distribution is substituted into the right-hand side of the equation and solved for a corrected model. The corrected model is then substituted in place of the initial model into the right-hand side of the equation and a more recent model calculated. This is repeated until a model is obtained

that is geologically sound and minimizes the error between observed and calculated anomalies.

There are two major problems inherent in gravity modelling: non-uniqueness of the solution and poor depth resolution. There are an infinite number of mass distributions that will produce a given gravitational field. An infinitesimally thin layer of material located immediately below the surface is one such distribution, implying that there is no depth resolution inherent in the gravity field (Li and Oldenburg, 1998). As well, resolution of subsurface sources is restricted to features whose wavelength is comparable in magnitude to the source-observational surface distance because short-wavelength signals decay quickly with distance from the source. It is, therefore, important to incorporate as much external geophysical and geological information as possible into the inversion procedure to constrain the model. Seismic refraction and reflection measurements, borehole information, and results from prior gravity and magnetic studies will reduce the number of models whose gravitational field matches the observed field and will ensure that the final model is geologically reasonable.

2.5.1 Inverse Modelling of Moho Topography

The inversion algorithm used here was developed by Chenot and Debeglia (1990). The algorithm models the observed gravity anomaly as a horizontal contrast interface between two media. Above the interface, the density distribution can be represented by an exponential function and below it by a

density contrast map. In this application, the contrast interface is the Moho. Above the Moho, an exponential density function was used to describe the crust, and below it, a constant density was assumed for the mantle.

The inversion is an iterative process that determines the topographic relief, $Z(x,y)$ (where (x,y) are surface coordinates coincident with gridded data points) of the interface by calculating the depth of the Moho at each grid point. Local deviations of depth, calculated at each step, are fitted until a suitable model is generated. The majority of the operations used in the inversion scheme are performed in the wavenumber domain. Gerard and Debeglia (1990) considered the use of this technique in the wavenumber domain to be advantageous since it reduced the number of iterations required to arrive at an acceptable model. Calculations performed in the wavenumber domain are also more rapid. The FORTRAN inversion program is given in Appendix B. The Fast Fourier Transform subroutine used in the program is taken from a compilation of United States Geological Survey Potential Field Geophysical Software (Cordell, et al., 1992).

Input data required for the depth inversion include the gravity anomaly field, the first vertical derivative field, the mean interface depth and the density contrast across the interface. The density contrast across the interface can be a constant or a one-, two-, or three-dimensional function. In this application, the density contrast, C, is a function of depth:

$$C = 2\pi G(\rho_2 - \rho_1(z))$$

...(2.23)

where G is the universal gravitational constant 6.672×10^{-11} $\mathrm{N \cdot m^2/kg^2}$, $\rho_1(z)$ is the exponential density function for the region above the interface and ρ_2 is the density of the region below the interface. Here,

$$\rho_1 = \rho_\infty[1 - \beta \exp(-\gamma Z_m)]$$

...(2.24)

where ρ_∞ is the asymptotic crustal density approaching mean Moho depth, Z_m, $\rho_\infty(1-\beta)$ is the surface density, i.e. the top of the crustal layer, and γ is the decay constant of crustal density with depth.

If P is the number of observed gravity values comprising the gravity field and, given the gravity field, G, the mean interface depth, Z_m, and the vertical gravity gradient field, M, then a transfer function, T_{Z_m}, can be calculated:

$$(T_{Z_m})_i = G_i + Z_m M_i \qquad i = 1,2,\ldots,P.$$

...(2.25)

T_{Z_m} is a first-order approximation to the downward continuation of the gravity field to the mean interface depth from which variations of depth about the mean are calculated:

$$Z_i = Z_m - (T_{Z_m})_i / C \qquad i = 1,2,\ldots,P$$

...(2.26)

where Z_i is the depth calculated at each observation point i . An initial model, $Z_{(0)}$, is calculated using this formula.

At each step of the inversion, the model gravity and vertical gravity gradient fields are calculated in the Fourier domain. The Fourier transform of the gravity field of the modelled interface can be expressed as the sum of (1) the effect ($G_1(k_x,k_y)$) due to the density contrast between the mantle and the crustal layer immediately above the interface having density equal to the asymptotic crustal density, and (2) the effect ($G_2(k_x,k_y)$) due to the density contrast between the crustal layer lying immediately above the interface and the main crustal unit whose density is described by an exponential function; i.e.,

$$\begin{aligned} G(k_x,k_y) &= G_1(k_x,k_y) + G_2(k_x,k_y) \\ &= \sum_P A_P(k_x,k_y)\{\rho_2 - \rho_\infty\}[(\exp(-2\pi f z_P)/2\pi f] \\ &\quad + \sum_P A_P(k_x,k_y)\rho_\infty \beta\,[(\exp(-(2\pi f + \gamma)z_P)/(2\pi f + \gamma)] \end{aligned}$$

...(2.27)

where k_x and k_y are wavenumbers of the field in the x- and y-directions, respectively, $f = \sqrt{k_x^2 + k_y^2}$ is the radial frequency, Z_P is the depth of the interface at data point P, β, γ, ρ_2, ρ_x and P are as defined earlier, and

$$A_P(k_x,k_y) = 2\pi G \frac{\sin \pi k_x P_x}{\pi k_x} \cdot \frac{\sin \pi k_y P_y}{\pi k_y} \exp(-2\pi i(k_x x + k_y y)).$$

...(2.28)

P_x and P_y refer to the grid spacing in the x- and y-directions, respectively. The Fourier transform of the gravity gradient field of the modelled interface is given as

$$M(k_x,k_y) = (\rho_2 - \rho_1) \sum_P A_P(k_x,k_y) \exp(-2\pi f z_P).$$

...(2.29)

Furthermore, residual functions ΔG and ΔM corresponding to the difference between the observed and most recently calculated gravity and gravity gradient fields, respectively, are calculated. Using the residual gravity and gravity gradient fields, a residual transfer function, ΔT_{N-1}, is calculated:

$$(\Delta T_{N-1})_i = (\Delta G_{N-1})_i + (Z_{N-1})_i (\Delta M_{N-1})_i \quad i = 1,2,....,P$$

...(2.30)

where N is an index referencing the inversion step, and $Z_{\backslash\ 1}$ are the most recently adjusted depth values. New adjustments to the depth values are made using the residual transfer function:

$$(Z_N)_i=(Z_{N-1})_i-(\Delta T_{N\ 1})_i/C \qquad i=1,2,....,P.$$

...(2.31)

At each iteration the root mean square (r.m.s.) error between the observed and calculated fields is determined. If (1) the r.m.s. error falls below a preset acceptable error, ε, or (2) the number of iterations exceeds a preset limit, then the inversion process stops.

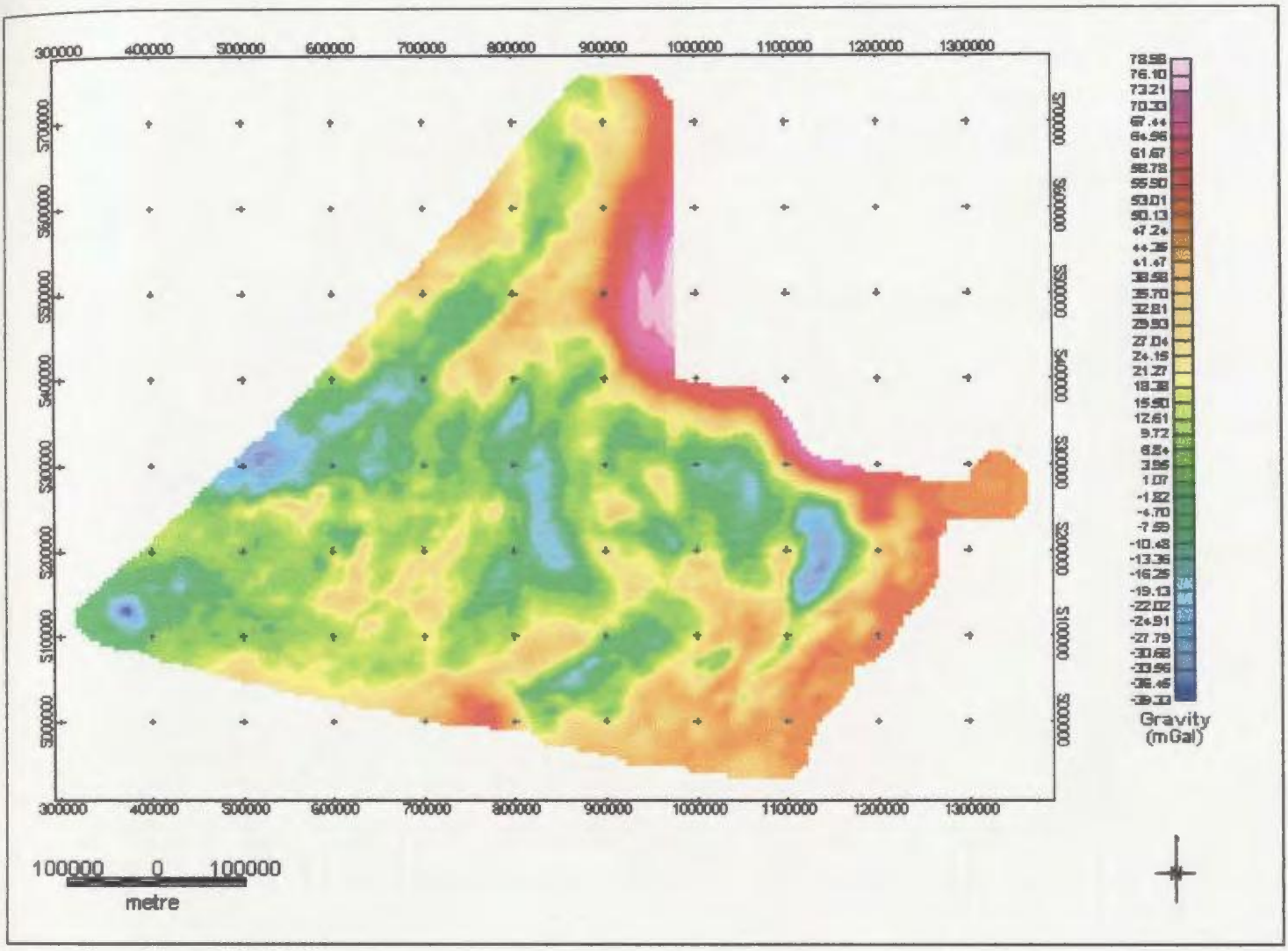

Figure 2.1. Bouger gravity anomaly map of the Avalon Terrane.

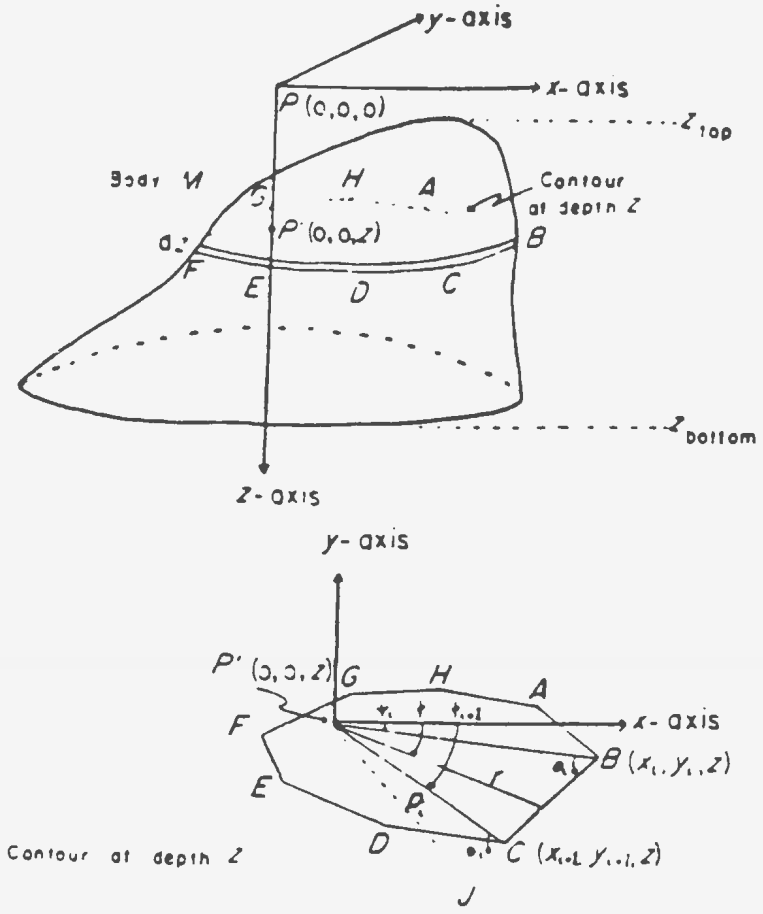

Figure 2.2 Geometrical elements involved in the computation of the gravity anomaly caused by a three-dimensional body. (From Talwani and Ewing, 1960).

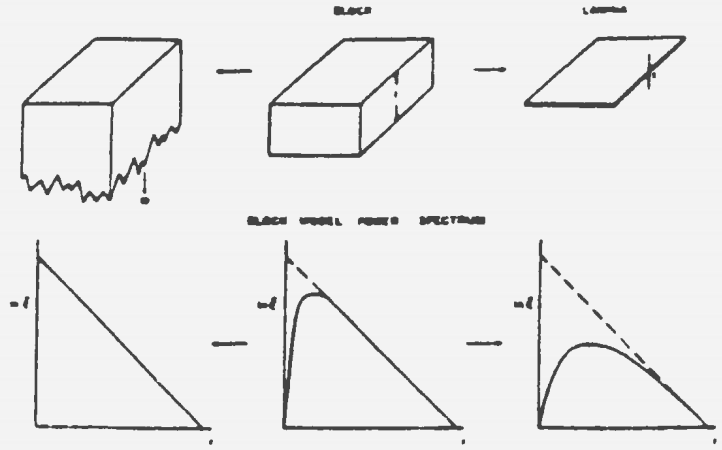

Figure 2.3(a) The effect of source thickness on the shape of the power spectrum. (From Spector and Grant, 1970)

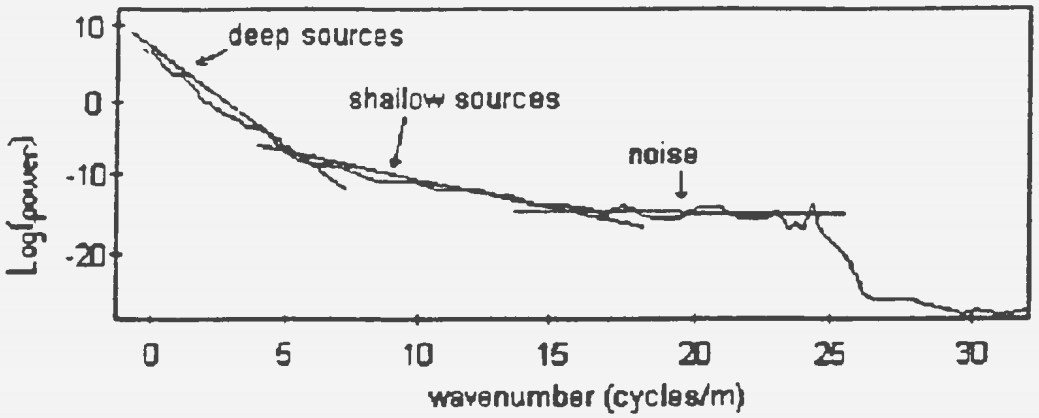

Figure 2.3(b) Sample power spectrum showing the differentiation of source ensembles into deep sources and shallow sources

CHAPTER 3: APPLICATION OF DATA PROCESSING STEPS

The gravity effects of the Carson, Horseshoe, Whale, and Jeanne d'Arc Basins were modelled using the method of Talwani and Ewing (1960) in which the basins were represented by a stack of horizontal polygonal laminae (§ 2.3.1). Estimation of the input parameter values for the modelling procedure, i.e. basin geometry and densities, are discussed in this chapter. The modelled gravity effect of the basins was removed from the observed gravity field to ensure that an unambiguous signal from below was obtained.

An ensemble average depth to sources at Moho depth was derived from spectral analysis of the field after the application of a series of low-pass filters. This depth was used in the determination of the input parameter values for the inversion algorithm.

Determination of the values used in the inversion program as well as a discussion of the pre-processing of the data prior to inversion are covered here. A synthetic data set was passed through the inversion program to evaluate its performance.

3.1 THE DATA

The Bouger anomaly map for the region is shown in Figure 3.1. The data were extracted from the National Gravity data base of the Geological Survey of Canada and interpolated onto a regular grid with 5 km spacing. The data were

then projected onto the map using the UTM Zone 21 North projection method using the North American Datum (1927).

The sedimentary basins are indicated on the map and are associated with negative anomalies. The positive northeastern edge of the field corresponds to the western margin of the East Newfoundland Basin.

3.2 MODELLING THE GRAVITY EFFECT OF SEDIMENTARY BASINS

To prevent the long-wavelength signal from the Mesozoic rift basins of the Grand Banks from masking that of the Moho, the gravitational attraction of each of the basins was modelled and subtracted from the observed field. The gravity effects of the Carson, Horseshoe, Whale and Jeanne d'Arc Basins were modelled and removed from the observed field to ensure that the remaining long-wavelength components of the field were originating from sources at depths comparable to Moho. As noted in Chapter 2, the modelling procedure is significantly improved by incorporating as much *a priori* information as possible. To effectively model the sedimentary basins, information regarding their density and geometry is necessary. The modelling procedure employed here (§ 2.3.1) models the basins as bodies comprised of stacked series of horizontal, polygonal laminae one kilometre thick (Talwani and Ewing, 1960). In some cases the basin has a second, less deep trough associated with it. These basins were modelled using two or more bodies that are themselves stacked; that is, they are vertically adjacent such that they replicate the shape of the basin.

3.2.1 Basin Geometry Contours

A map of depth to Lower Paleozoic basement compiled by Wade, et al. (1977) was used to obtain geometry information for each of the modelled basins. The map series, comprising a region from approximately 46° W to 86° W and 38° N to 64° N, covers all of eastern Canada from the Grand Banks of Newfoundland in the east to the Great Lakes in the west and from the northeastern United States in the south to Baffin Island and western Greenland in the north. Information gathered from deep seismic reflection profiles, some deep refraction surveys, high resolution seismic surveys, well cores, well sample cuttings, and marine gravity and magnetic studies was incorporated to produce the depth to basement contour map with a contour interval of one kilometre.

Figure 3.2 shows the portion of the depth to basement map used here. It indicates the locations of the Carson, Horseshoe, Whale, and Jeanne d'Arc Basins. The shape of each of the contour levels comprising a basin was digitized to produce a polygonal lamina. The latitude/longitude coordinates defining each contour line were converted to UTM coordinates in order to maintain the gravity anomaly field and basin geometry data sets at the same projection and coordinate system, thus co-registering the two data sets. When stacked, the laminae closely approximate the shape and volume of the basin.

3.2.2 Basin Densities

An empirical relationship exists between compressional velocity through marine sediments and sedimentary rocks and their porosity that allows for estimation of other parameters such as density and elastic constants characteristic of the medium (Nafe and Drake, 1957a). The path lengths of compressional waves through sediments are usually large and the frequencies of these waves low, so that calculated velocities tend to be averaged over large thicknesses of sediment (Nafe and Drake, 1963). The compressional velocities of near-surface sediments can be readily measured, however, at depth, the exact relationship between velocity and porosity becomes uncertain. It can only be estimated based on repeated observation and laboratory experimentation. Therefore, velocities are estimated, giving further uncertainty to density values thus derived. For this reason, density values for each basin were derived from density logs taken at representative wells.

The shallow structure of the Grand Banks has been investigated by at least 158 wells (DeSilva, 1999). Using the Schedule of Wells for the Newfoundland Offshore Area compiled by the Canada-Newfoundland Offshore Petroleum Board (C-NOPB) in 1995 and maps delineating the locations of these wells (e.g. Figure 6.1 of Grant and McAlpine, 1990), representative wells were chosen for each of the modelled basins (Figure 3.3). Density log information collected at these wells was used to assign an average density to each basin for input into the modelling program. For each well, the density log was sampled either every one metre or

10 feet, depending on the units used to measure depth on the log. Variations in the lithology result in variation in the observed density values so an average density, weighted by the thickness of rock exhibiting similar density values, was calculated for each kilometre of thickness, i.e.

$$\bar{\rho} = \frac{\sum_{i=1}^{n} \rho_i t_i}{\sum_{i=1}^{n} t_i} \qquad \ldots(3.1)$$

where ρ_i and t_i are the density and thickness if the i^{th} interval, respectively. The average density of each body comprising the basins was used for input into the modelling program. This requires that the density as a function of depth be known at each contour level, i.e. for each lamina. The contours from the depth to basement map (Wade, et al., 1977) were chosen to represent the configuration of the basin, not the stratigraphy. Therefore, the logical approach is to determine the average density.

There are very few wells that go to basement and the ones that do are on the edges of the basins therefore there is an inherent uncertainty in the densities used. Furthermore, a slight change in the assumed basin density results in a significant change in the calculated anomaly. The total drilled depths of the selected wells are considerably less than the thicknesses of the modelled basins so the density values at depth were extrapolated from the shallow densities

obtained from the logs. These factors combine to produce a significant uncertainty in the density value assigned to each basin. Where possible, density information was taken from multiple wells to fill any gaps that may have been present in the record. Variations in the observed well densities are indicative of changes in sampled lithology. The approach is to determine the average density in the basins based on a combination of an understanding of the stratigraphy and the density logs. Depths to the geologic tops of various stratigraphic sequences are referred to and correlation between wells is also briefly discussed.

3.2.3 Carson Basin

Carson Basin is a northeast-southwest trending basin located on the east-northeast Grand Banks at the edge of the shelf. The depocentre of the basin has a depth of approximately 5 km. Only one well, Osprey H-84, provided density information for Carson Basin (Figure 3.3). The total drilled depth is 3473.8 m (11 397 ft), approximately 1½ km less than the basin thickness. The well terminates in the Eurydice shale. Figure 3.4 shows the density-depth information for Carson Basin derived from analysis of the Osprey H-84 density log. Areas in which the log information was unintelligible are left blank. Aside from thin isolated areas of increased density, the density appears to be consistent between 2.1 and 2.2 g/cm^3. The geologic top of the Argo Formation occurs at approximately 1250 m depth. The top of the Eurydice Formation is marked by a sharp increase in density at approximately 3300 m depth. The average measured density of the

shale is 2.6 g/cm^3. The average density of shale is about 2.4 g/cm^3 (Telford, et al., 1990) so a higher measured density suggests some degree of compaction of the sediments at depth. Weighted average densities for each kilometre of thickness were calculated and are tabulated in Table 3.1. The densities were plotted as a function of associated depth range and extrapolated back to 5 km depth (Figure 3.5(a)) giving an average density for Carson Basin of 2.35 g/cm^3 with a density contrast of -0.32 g/cm^3 using the typical crustal density of 2.67 g/cm^3.

3.2.4 Horseshoe Basin

Horseshoe Basin is a northeast-southwest trending basin located west of Carson Basin with a depocentre 7 km deep. In Horseshoe Basin there is only one exploratory well, Bittern M-62. The total depth drilled is 4780.2 m (15 683 ft). As with Osprey H-84, Bittern M-62 terminates in Eurydice shale. Figure 3.6 shows the density-depth information for Horseshoe Basin derived from analysis of the Bittern M-62 density log. The density recorded in this well remains fairly consistent between 2.6 and 2.8 g/cm^3. The sharp decrease in density at about 4700 m depth coincides with the geologic top of the Argo salt Formation. The salt has a thickness of approximately 20 m here. This is followed by a significant increase in density marking the top of the Eurydice shale.

Weighted average densities for each one-kilometre slab are given in Table 3.1. This basin was divided into two separate but vertically adjacent bodies each

comprised of stacked polygons since there is a secondary depression associated with it. The first of the two Horseshoe Basin bodies extends to 4 km depth and was assigned an average density of 2.668 g/cm^3 giving a density contrast of -0.002 g/cm^3. The second body extends from 4 to 7 km depth and was assigned an average density of 2.73 g/cm^3. Note that this is based only on the density information in the last 0.78 km of the well log. With reference to the lithostratigraphic chart for the southern Grand Banks (Figure 1.3), the anomalously high density can be attributed to a layer of anhydritic dolomite and limestone (Iroquois Formation) extending from approximately 3470 m to almost 4700 m depth. Limestone densities range from 1.55 g/cm^3 to 2.75 g/cm^3, while those of dolomite fall between 2.72 g/cm^3 and 2.84 g/cm^3 (Olhoeft and Johnson, 1994). This high-density limestone-dolomite layer is also found in most of the other wells, as described below. The integrated average density over the whole of the log is approximately 2.67 g/cm^3, the average crustal density used for the Bouger correction, which explains the lack of a significant associated anomaly over the basin (see Figure 3.1). Therefore, a density contrast of 0 g/cm^3 was assigned to this basin.

3.2.5 Whale Basin

Whale Basin, another of the northeast-southwest trending basins on the Grand Banks, has a depocentre of about 7 km. As with Horseshoe Basin, Whale Basin was modelled using two vertically adjacent bodies: the first to 6 km depth; the

second extends from 6 to 7 km depth. There are four wells in Whale Basin that extend to such depths that significant density information was obtainable from them. They are: (1) Coot K-56 which has a total depth of 3535.7 m (11 600 ft) and terminates in the Eurydice shale Formation; (2) Gannet O-54 which has a total drilled depth of 3048 m (10 000 ft) and extends to basement; (3) Razorbill F-54 which has a total depth of 3135.2 m (10 286 ft) and extends to basement; and (4) Sandpiper 2J-77 which has a total depth of 3525.4 m (11 566 ft) and terminates in the Horton Formation. Figure 3.7 shows the density-depth information for Whale Basin from the Coot K-56, Gannet O-54, Razorbill F-54, and Sandpiper 2J-77 density wells.

The density log recorded from the Coot K-56 well shows alternating areas of high and low densities. Large portions of the record were incomprehensible. Densities taken from the Gannet O-54 well were highly variable. The Cenomanian unconformity occurs at approximately 1700 m. Basement rock is sampled beginning at approximately 2925 m. The Razorbill F-54 density plot shows an increasing trend of density with depth to about 2075 m. The Cenomanian unconformity is represented by a sharp decrease in density at approximately 1250 m depth. This is shallower than in the Gannet O-54 well to the southwest. The top of the Argo salt Formation is at approximately 2075 m depth and coincides with a significant drop in density from about 2.65 to 2.1 g/cm^3. The depth to basement in this well is approximately 2600 m. The Sandpiper 2J-77 densities are very oscillatory between 1200 (which marks the top of the Argo Formation) and 1500 m. Between 1500 and 3000 m density

fluctuates between 2.1 and 2.3 g/cm^3 but increases overall. The presence of Windsor evaporites is marked by the sharp increase in density at 3000 m depth. The drop in density at 3250 m coincides with the top of the Horton Formation. Tabulated averages for each well are found in Table 3.1.

A direct comparison of density with depth indicates poor agreement between wells. However, comparison of the formation densities from well to well reveals that there is remarkable agreement. The Petrel Member (of the Dawson Canyon Formation) densities recorded in the Gannet O-54 and Razorbill F-54 wells are practically the same (approximately 2.55 g/cm^3) as are the Eider Unit densities (approximately 2.4 g/cm^3). In both the Gannet O-54 and Sandpiper 2J-77 logs, the Windsor evaporites have high densities. The density of the Horton Formation in both of these wells has a median density around 2.55 g/cm^3. The density of the Iroquois Formation varies between 2.5 and 2.75 g/cm^3 in the Coot K-56, Razorbill F-54, and Sandpiper 2J-77 wells. For the Argo Formation, however, they all give the same low density (approximately 2.2 g/cm^3). The Eurydice Formation densities in the Coot K-56 and Sandpiper 2J-77 wells are also similar (approximately 2.5 g/cm^3). In general, the densities appear to remain steady between 2.6 and 2.7 g/cm^3.

For each kilometre of thickness, an average density was calculated using densities from each of the wells. Extrapolating back (Figure 3.5(b)), a density of 2.5 g/cm^3 was obtained for the first body giving a density contrast of -0.17 g/cm^3. A density of 2.65 g/cm^3 was obtained for the second body (i.e. from 6 to 7 km depth) giving a density contrast of -0.02 g/cm^3.

3.2.6 Jeanne d'Arc and East Newfoundland Basins

The shallow western edge of the East Newfoundland Basin is covered by the gravity data. Therefore, it was included in the modelling operation. Furthermore, density logs from the basin were examined to ensure a reliable density estimate was obtained for the entire Jeanne d'Arc-East Newfoundland Basin system.

The Jeanne d'Arc Basin on the northeast Grand Banks is a petroliferous basin and is host to a number of oil and gas discoveries including the Hibernia, Terra Nova, and White Rose oil fields. The vast majority of the exploratory, delineation, and development wells on the Grand Banks are located here. The basin trends northeast-southwest to north-south and has a depocentre of at least 12 km (as illustrated by Wade, et al., 1977; however, it is known that Jeanne d'Arc Basin is at least 15 km deep (Tankard, et al., 1989; Grant and McAlpine, 1990)). The East Newfoundland Basin, north of the Jeanne d'Arc Basin, is a broad basin on the northeast Newfoundland Shelf extending to about 15 km depth. Above about 9 km depth, the Jeanne d'Arc and East Newfoundland Basins coalesce into one large basin. For modelling purposes, the East Newfoundland-Jeanne d'Arc Basin system has been divided into three vertically adjacent bodies: (1) the Jeanne d'Arc Basin from 9 to 12 km depth; (2) the East Newfoundland and Jeanne d'Arc Basins from 6 to 9 km depth; and (3) the East Newfoundland and Jeanne d'Arc Basins to 6 km depth.

Wells from the Jeanne d'Arc Basin used to obtain density estimates are Bonanza M-71, Hibernia G-55A, and Spoonbill C-30 (Figure 3.8). The Bonanza M-71 exploratory well extends into basement with a total depth of 5294.7 m (17 367 ft). Densities taken from the Bonanza M-71 well exhibit an increase of density with depth. The Rankin limestone Formation is denoted by a significant rise in density at 4240 m depth. The Hibernia G-55A delineation well extends into basement with a total depth of 3460.1 m (11 349 ft). Densities in this well tend to increase between 1250 and 2200 m depth after which they stay fairly constant. At about 3400 m, density rises sharply corresponding to the presence of volcaniclastics. The Cenomanian unconformity is denoted by a decrease in density at about 1750 m. The Spoonbill C-30 exploratory well terminates in Paleozoic redbeds with a total depth of 2757.3 m (9046 ft). The densities observed in the Spoonbill C-30 well are quite variable. The Iroquois limestone and dolomite Formation corresponds to the thick zone between 900 and 1200 m with a density of 2.8 g/cm^3. The top of the Argo Formation is at approximately 1250 m and coincides with a sharp decrease in density. The high density peak at around 1550 m corresponds to a mafic sill, evidence of igneous activity during Mesozoic rifting. The increased density below 2500 m correlates to Paleozoic redbeds.

Wells located in the East Newfoundland Basin include Cumberland B-55, with a total depth of 4136.5 m (13 568 ft), and Linnet E-63, with a total depth of 4520.2 m (14 826 ft) (Figure 3.8). Both wells terminate in metasedimentary basement. Density in the Cumberland B-55 well increases with depth. The Cenomanian

unconformity occurs at about 3700 m depth, considerably deeper than in the Gannet O-54, Razorbill F-54, or Hibernia G-55A wells. It is marked by a distinct decrease in density values. In the Linnet E-63 well, densities oscillate between 2.0 and 2.25 g/cm^3 between 1000 and 2000 m depth. Beyond 2000 m, density tends to increase with depth. The geologic top of the Dawson Canyon Formation coincides with an increase in density at about 2500 m depth. The weighted average densities for each well are given in Table 3.1.

Figure 3.8 shows comparative density-depth information for the Jeanne d'Arc-East Newfoundland Basin from the Bonanza M-71, Hibernia G-55A, Spoonbill C-30, Cumberland B-55, and Linnet E-63 wells. Densities for the Dawson Canyon Formation are poorly correlated in the Cumberland B-55, Hibernia G-55A, and Linnet E-63 wells. Similarly, the Nautilus shale densities in the Hibernia G-55A and Linnet E-63 wells are in poor agreement. The high Iroquois Formation density recorded in Spoonbill C-30 (approximately 2.8 g/cm^3) corresponds to the high density observed for the same formation in the Coot K-56 well (approximately 2.75 g/cm^3). The Argo Formation density in this well is still relatively low. The density of the Eurydice Formation is higher (approximately 2.6 g/cm^3) than that found in Coot K-56 or Sandpiper 2J-77. It is evident from Figure 3.8 that density increases linearly with depth, at least to a depth of about 5300 m.

For each body in the Jeanne d'Arc-East Newfoundland Basin system, an average density was calculated using densities from each of the wells. Plotting these densities and extrapolating back (Figure 3.5(c)), the densities obtained for

each body are (with density contrast in brackets): (1) 2.65 g/cm^3 (-0.02 g/cm^3); (2) 2.64 g/cm^3 (-0.03 g/cm^3); and (3) 2.50 g/cm^3 (-0.17 g/cm^3).

These results are given in Table 3.2.

3.2.7 Removal of the Gravity Field of the Sedimentary Basins

Figures 3.9 through 3.11 show the gravity anomaly due to each of the Carson, Whale, and Jeanne d'Arc-East Newfoundland Basins, respectively, as calculated using the models based on depths and densities discussed above. Figure 3.12 shows the cumulative effect of all the basins. The noise generated by the modelling procedure is evident in this figure. To gauge the uncertainty in the gravity due to uncertainties in the estimated density contrasts, the variability of the basin gravity effects was examined by varying the contrasts by ±10% and ±25%. Ranges of uncertainty for Horseshoe Basin were estimated based on starting density contrasts of –0.002 g/cm^3 for the upper body (to a depth of 4 km) and +0.06 g/cm^3 for the lower body (4 to 7 km depth), which were the originally calculated values. Uncertainty ranges for each of the Carson, Whale and Jeanne d'Arc Basins are based on the average densities determined in sections 3.2.3, 3.2.5 and 3.2.6, respectively. Profiles were taken across the resultant gravity field maps to illustrate the variability of the gravity anomalies in response to these changes. The locations of these profiles are shown in Figure 3.12. Figures 3.13 and 3.14 show the gravity anomalies across profiles A-A' and B-B', respectively. Since only the basinal regions were modelled there should be no change in the

gravity anomaly over the platformal regions (e.g. between 175 and 300 km along A-A' and less than 25 km along B-B'). The greatest variability occurs above the depocentres of the basins. The northern portion of Horseshoe Basin is seen as the small near-zero anomaly located at about 240 km along profile A-A'. Perturbations in the assumed density contrast of this basin had very little effect on the amplitude of the calculated anomaly. Over Whale Basin (negative anomaly at about 100 km along profile A-A'; Figure 3.13) a change of ±25% in the density contrast produces a change in the anomaly of approximately ±20 mGal. This represents about 25% of the average anomaly. Over Carson Basin (negative anomaly centred at 330 km along A-A'; Figure 3.13) the response of the anomaly to changes of ±25% is also symmetric about the average value and is on the order of ±17 mGal, which is about 25% of the average anomaly. The calculated anomaly over the Jeanne d'Arc Basin (negative anomaly in Figure 3.14) varies by ±31 mGal (25%) in response to changes in the density contrast of ±25%. Given a ±10% change in the density contrast, the maximum change observed in the calculated anomalies is about ±12 mGal and occurs over Jeanne d'Arc Basin. Therefore, at its greatest, the uncertainty in the modelled basin effect is ±31 mGal. This is fairly large and will undoubtedly affect the uncertainty associated with the final model of Moho topography. Given the uncertainty in the raw data of ±2.5 mGal (§2.1) and the uncertainty in the modelled basin effect of ±31 mGal, then an r.m.s. error of less than 35 mGal in the inversion process would be acceptable.

Figure 3.15 shows the observed gravity field after the effect of the sedimentary basins calculated using the average model densities was removed. The presence of large positive anomalies over the Jeanne d'Arc and Carson Basins suggest that the Moho is drawn up beneath the basins, i.e. the mantle has warped upward to isostatically compensate for the depth of the basins. The anomaly associated with Whale Basin is significantly reduced. The large positive anomaly around UTM 950000 E, 5650000 N is the modelled edge of the East Newfoundland Basin. There was some concern that this artifact of the modelling procedure would affect the three-dimensional inversion process by creating an unrealistic step in the Moho topography function. Therefore, the northern extremity of the data was removed during the inversion. The portion of the field contained within the rectangle in Figure 3.15 was passed through the inversion algorithm.

3.3 WAVELENGTH FILTERING

Figure 3.16 shows the power spectrum of the observed gravity field. Figure 3.17 shows the power spectrum of the observed field with the gravitational effect of the sedimentary basins removed. There is no significant change in the character of the spectrum. This gravity field was low-pass filtered using a number of progressively lower cut-off frequencies to isolate sources at depths comparable to that of Moho.

Figure 3.18 shows the gravity field filtered to remove wavelengths less than 100 km. The effects of the Jeanne d'Arc and Carson Basins can still be seen, i.e. compare with the original field (Figure 3.15). The linear gravity low marking the Gander-Avalon Terrane boundary is also still very strong. Figure 3.19 shows the power spectrum calculated from the filtered field. There is a noticeable drop-off in energy around $k = 0.01$ km^{-1}. A depth of approximately 32 km was obtained for the source ensemble corresponding to the average Moho depth.

Figure 3.20 shows the gravity field filtered to remove wavelengths less than 150 km. The Jeanne d'Arc Basin anomaly is still prevalent which indicates that the crust is thinned below the basin. There are also significant positive anomalies over the Whale and Carson Basins. The power spectrum of the filtered field is shown in Figure 3.21. The decline in energy of the field is noticeable near $k = 0.007$ km^{-1}. The source ensemble gave an average depth of 33 km. The field was filtered further to ensure that the effects of shallower features were not visible.

Figure 3.22 shows the gravity field filtered to remove wavelengths less than 175 km. The effects of shallow structure have disappeared. The high associated with Whale Basin persists but this may not be a true feature of the field (Kane and Godson, 1985). The power spectrum of the field is shown in Figure 3.23. Around $k = 0.0057$ km^{-1} the energy drops off. The average depth is approximately 30 km, comparable to Moho depth. The field filtered with this cut-off wavelength is considered to be due primarily to the topographic relief of the Moho.

Figure 3.24 shows the observed field filtered to remove wavelengths less than 200 km. The associated power spectrum is given in Figure 3.25 showing the reduction in energy at about $k = 0.005$ km^{-1}. A depth of about 40 km was obtained for the source ensemble.

The ensemble average depths from each filtered field are given in Table 3.3.

Interpretation of wavelength filtered data is affected by the quality of the input data as well as the specifications of the filter. The data provided for this study are considered to be of reasonably high quality. However, the Moho cannot be reliably defined using analysis of the spectra of the filtered fields because the relief of the Moho is very small compared to its mean depth (Lefort and Agarwal, 1996). The results of this spectral analysis show a range of mean depths (Table 3.3). An unambiguous estimate of depth to Moho was not possible; therefore, the data was inverted using a variety of depths.

3.4 INVERSION

The gravity data were inverted using an algorithm of Chenot and Debeglia (1990) which models the Moho as a contrast interface above which the density is described by an exponential function and below by a constant density. The modelled gravity and vertical gradient fields are calculated in the wavenumber domain while iterative adjustments to the depth are calculated in the space domain.

Tsuboi (1979) presented a method of determining the condensed (i.e. concentrated on a horizontal plane) mass distribution from the observed gravity field by expressing both the gravity and mass distributions as Fourier series, $g(x,y)$ and $M(x,y)$, respectively. If the observed field is due to the undulation of an interface separating two media of different densities, ρ and ρ', then the function describing the amplitude of undulation, $h(x,y)$, is found by dividing $M(x,y)$ by the density contrast. However, Tsuboi's (1979) method assumes that the interface separates two isotropic and homogeneous media with two different but constant densities. The use of an upper layer density that varies exponentially with depth deviates from this assumption and is more consistent with observed density variations as determined from well logs. The method used in this thesis also attempts to deal with lateral density variations in the upper layer by correcting for the basin effects.

3.4.1 Model Parameters

The main parameters required for input into the inversion scheme are the mean Moho depth and densities of the layers above and below the Moho.

3.4.1.1 Estimation of Mean Depth to Moho

Mean Moho depth estimates were obtained from the interpretations of several deep seismic reflection and refraction profiles across the Grand Banks within the

data range (Figure 3.26) and from the spectral analysis discussed above. It is important to recognize that these seismic sections are dependent on the assumptions of the processors, particularly regarding the estimation of deep crustal seismic velocities. The objective here is not to re-process or critically assess the seismic data but rather to use the published interpretations (i) as a calibration tool to determine an average depth to Moho along profile, and (ii) for comparison with the gravity models derived here. The assumption is that the processing was critically assessed by the authors prior to publication and by the referees for the publications as part of the review process. The Moho depths along the seismic profiles were taken from the published sources; no time to depth conversion was undertaken as part of this thesis. As no estimate of the crustal velocity uncertainty is discussed by the source authors, one cannot assess the depth uncertainty in the seismic Moho depths. The depth of interpreted Moho on each of these lines was sampled at 5 km intervals along profile and then averaged. DeChassy, et al. (1990) provide a full set of deep seismic profiles across the conjugate margins of the North Atlantic Ocean from which depth to Moho along AGC reflection lines 84-3, 85-1, 85-3, and 85-4 was taken.

Reflection line 84-3 (Keen, et al., 1987a; Keen and de Voogd, 1988; DeChassy, et al., 1990) runs east-northeast sub-parallel to the Charlie-Gibbs Fracture Zone and crosses the broad Orphan Basin on the northeast Newfoundland Shelf. The data collected along line 84-3 was adversely affected by the presence of long-period water-bottom multiples. Therefore, the signal-to-

noise ratio, particularly from deep reflectors such as the Moho, is very low. For this reason, depth information could only be taken from the first 70 km of the profile at its western extreme since information from the remainder of the line was considered to be unreliable. The average depth measured on this portion of the line is 37.5 km.

Reflection line 85-1 (DeChassy, et al., 1990) is located on the southern Grand Banks where it runs southeast across the Whale and Horseshoe Basins and meets reflection line 85-2 on the South Bank High. Below the basins the deep reflections are heavily masked possibly due to the presence of thick sedimentary sequences which dampen the signal. For this reason, reliable depth estimates could only be taken along the first 40 km of the western end of the profile and the last 80 km at the eastern end, the latter of which is beyond the range of available gravity data. The average depth to Moho measured along this line is approximately 36.5 km.

Reflection line 85-3 (Keen and de Voogd, 1988; Keen, et al., 1989; DeChassy, et al., 1990) runs roughly east-northeast, sub-parallel to line 84-3 and passes across the northern Jeanne d'Arc Basin, Flemish Pass Basin, and Flemish Cap. Large thicknesses of sediment diminished the deep crustal reflectivity but reasonable measurements of depth to Moho were obtainable along the entire profile. On that portion of the line coincident with the gravity data (the western 300 km), the average depth to Moho was estimated to be 32 km.

Reflection line 85-4 (Keen and de Voogd, 1988; DeChassy, et al., 1990) strikes east-southeast and crosses the southern Jeanne d'Arc and Carson Basins on the

eastern Grand Banks. Only the western portion of the line gave significant depth estimates for the Moho. Offshore, beyond the continent-ocean boundary, Moho reflections were picked up more clearly but this is outside the range of available gravity data. An average Moho depth of 32 km was also estimated for this line.

Lithoprobe East refraction line 91-2 (Marillier, et al., 1994) is the only one of the selected seismic lines that lies entirely within the area covered by the gravity data. It lies parallel to the east coast of the Avalon Peninsula of the island of Newfoundland. The Moho depth measured along this line is 40 km and is constant along the entire region sampled by the survey.

All of the measured depths were summed and averaged to obtain a mean depth to Moho of 35 km with a standard deviation of 4 km. This value is limited by the fact that the seismic lines from which it was derived lie mainly along the periphery of the available data (Figure 3.26). Average depths derived from spectral analysis of the gravity field (Table 3.3) yield a more comprehensive estimate for the entire region than the depth derived from the sparse seismic coverage (Figure 3.26). The average ensemble depths to Moho obtained from spectral analyses of the wavelength filtered fields range from 30 to 40 km, which is comparable to the statistical estimate obtained from the seismic data. Since an unambiguous estimate of depth was not possible and since spectral analysis gave a range of depths, the data was inverted using depths ranging from 30 to 40 km with an increment of 2.5 km to assess the results.

3.4.1.2 Estimation of Density Parameters

In order to obtain the density of the crust, the densities at the top (surface density) and bottom (asymptotic density) of the crust and the density decay constant of the crustal unit must be estimated, as seen from inspection of equation (2.24). Of the wells selected to obtain density information for each of the Grand Banks basins (§ 3.2.1) six extended into crustal basement. Two more, Jaeger A-49, an exploratory well located on the South Bank High with a total depth of 938.5 m (3078 ft), and Blue H-28, an exploratory well on the northeast Newfoundland Shelf with a total depth of 6103.1 m (20 018 ft) were also used to assess the basement density. Figure 3.27 shows the locations of the wells used to estimate basement density. Table 3.4 gives the basement thickness sampled, the observed density range, and weighted average densities for each well. Basement density corresponds to surface density, i.e. atop the crustal unit.

Weighted according to thickness, the average surface density calculated from all the well logs is 2.62 g/cm^3. The density obtained from the Linnet E-63 well log does not agree well with the others and, if neglected, a surface density of 2.67 g/cm^3 is obtained, which is consistent with the average crustal density used in the Bouger reduction.

Direct evidence regarding the lithology of the lower crust comes from the investigation of ophiolite suites, xenoliths from volcanic rocks, and exposures of deep continental crust that include granulite facies metamorphic rocks and peridotite massifs (Wilshire, 1987; Nielson-Pike, 1987). From these direct

measurements of density can be made. In ophiolite suites, the lower crust is composed predominantly of gabbro (Wilshire, 1987) and according to Christensen (1994) the crust immediately above the mantle is chemically equivalent to gabbro. As well, exposures of deep continental crust have exhibited mafic granulite formed by metamorphosis of lower crustal mafics at granulite facies (Nielson-Pike, 1987). Indirect evidence of lower crustal lithology comes from wide-angle and deep refraction seismic studies, which compare *in situ* seismic velocities with laboratory measurements of velocity for a variety of materials. The deep crustal seismic velocities from a number of deep seismic profiles on the Grand Banks are given in Table 3.5. The locations of these lines are shown in Figure 3.28. The average velocity for the deep crust is 6.8 km/s. Using the Nafe-Drake curve (Nafe and Drake, 1957b) relating seismic velocity to density this corresponds approximately to a density of between 2.95 and 3.00 g/cm^3. This agrees well with the density for gabbro of 2.97 g/cm^3 (Olhoeft and Johnson, 1994) and the density range of 2.67 to 3.10 g/cm^3 for granulite (Olhoeft and Johnson, 1994). Therefore, 2.97 g/cm^3 was chosen for the asymptotic density, ρ_∞.

Given that $\rho_\infty(1-\beta)$ equals the surface density 2.67 g/cm^3 and substituting ρ_∞ into the expression, the factor β is found to be 0.1. Solving the general formula for exponential growth and decay,

$$\rho(z) = \rho(0)e^{\gamma z} \qquad \ldots(3.2)$$

using $\rho_x = \rho(35) = 2.97\,\mathrm{g/cm^3}$ and surface density = $\rho(0) = 2.67\,\mathrm{g/cm^3}$, gives the decay constant $\gamma = 0.003\,\mathrm{g/cm^3}$. Equation (2.24) can then be solved for the density of the crust at any depth.

A density of 3.33 g/cm^3 was selected for the mantle. This is a generally accepted value which agrees with densities of 3.33 g/cm^3 used by Watts and Fairhead (1999), 3.3 g/cm^3 used by Reid (1994), and 3.34 g/cm^3 used by Keen and Potter (1995) and Keen, et al. (1994).

R.m.s. errors, ε_1, of 2.5 mGal between the observed and calculated gravity fields and ε_2 of 2.5 mGal/km between the observed and calculated gravity gradient fields were chosen to be acceptable margins of error since the accuracy of the observed gravity values is no better than 2.5 mGal (§2.1). This is the best uncertainty one can expect to achieve in the final model. If the error between the original and modelled fields falls below these values or if the inversion does not converge after 10 iterations the inversion process ceases.

3.4.2 Pre-Processing

Before the data can be passed through the inversion scheme, it must be pre-processed to facilitate convergence. Pre-processing of the data was carried out using GEOSOFT's Oasis Montaj data processing software package.

The first vertical derivative of the gravity field was calculated from the observed gravity field (with the effect of the sedimentary basins removed) in the Fourier

domain. Prior to Fourier transformation, the data, excluding the portion associated with the edge of the East Newfoundland Basin, was expanded to rectangular dimensions (since the data set is fairly large and has a roughly rectangular shape) and the expanded area filled with extrapolated values.

The primary disadvantage of inversion algorithms of this type is that at high frequencies the process diverges, creating high-frequency oscillations in the generated model. This instability is due mainly to the presence of high-frequency noise generated by the use of the discrete or fast Fourier transform as well as the contribution to the field of shallow bodies in the subsurface which themselves generate high-frequency noise. Amplification of high frequencies (short wavelengths) is inherent in inversion (as well as in downward continuation). The amplitude of a short-wavelength anomaly (e.g. < 10 km) due to the undulation of a source interface at crustal depths (e.g. 30 – 40 km) is many times larger than that of a source interface located at or very near the surface. Consequently, it is very unlikely that the high-frequency (short-wavelength) content of the gravity anomaly field is related to undulations in the Moho (Marillier and Verhoef, 1989).

If the topography of the interface, $Z(x,y)$, has small local variations, $\Delta Z(x,y)$, then the inversion procedure will likely converge. Otherwise, the application of a low-pass filter to the data during pre-processing will eliminate high-frequency components and increase the chance of convergence. In general, successful convergence of the inversion procedure requires that the high-frequency components of the field be removed (Guspi, 1992). Care is needed because arbitrary filtering may produce over-filtered or under-filtered data, resulting in loss

of information or no significant loss of noise. Loss of high-frequency content prevents detailed modelling of short-wavelength anomalies. The trade-off is convergence toward a suitable model. A cut-off frequency of $0.4/\Delta Z_{\max}$ (Guspi, 1992), where $\Delta Z_{\max}$ is the maximum topographic variation of the interface, has been shown to give good results. Here, the maximum relief is estimated to be about 10 km, which gives a cut-off frequency of 0.04 km^{-1}. According to Guspi's (1992) formulation, this corresponds to a cut-off wavelength of approximately 150 km. Because of the uncertainties in the mean depth estimates, there are associated uncertainties in the values of maximum relief. Therefore, filters using cut-off wavelengths of 50, 100, 150, 200, and 250 km, were used on the data to assess the results.

3.4.3 Test Model

A synthetic data set of 60 x 60 data points was passed through the inversion procedure as a test. A depth map representing an area of upwarp or doming of the mantle, gridded at 2 km spacing is shown in Figure 3.29(a). The structure is 20 km wide, 100 km long, and has a mean depth of 29.6 km. The topographic relief of the body is 5 km. A constant density of 3.4 g/cm^3 was used for the mantle while an exponential density function, with $\rho_x = 2.97\,\mathrm{g/cm^3}$, $\beta = 0.1$, and $\gamma = 0.004\,\mathrm{g/cm^3/km}$, was used to describe the crust. The corresponding gravity field, covering an area of 120 x 120 km^2, is shown in Figure 3.30. The data was

low-pass filtered using a cut-off frequency of 0.1386 km^{-1} and a mean trend was removed. The vertical gravity gradient of the field is shown in Figure 3.31.

The inversion was allowed to proceed to achieve maximum r.m.s. errors between the synthetic and modelled fields of $\varepsilon_1 = 1\,\mathrm{mGal}$ and $\varepsilon_2 = 1\,\mathrm{mGal/km}$. After one iteration the inversion achieved an r.m.s. error between the original and modelled gravity fields for the inferred topography of 0.685 mGal and 0.007 mGal/km between the synthetic and modelled gravity gradient fields. Figure 3.29(b) shows the resultant depth map. The lobes at the sides of the structure are caused by inverting on the very small lobes produced by the low-pass filtering of the data prior to inversion (Kane and Godson, 1985).

In an effort to gauge the response of the inversion program to noise, noise in the range of ±1 mGal was added to the gravity data (Figure 3.32). Again, the inversion was successful after one iteration with no change in the r.m.s. error: 0.685 mGal between the synthetic and modelled gravity fields and 0.007 mGal/km between the synthetic and modelled gravity gradient fields. The resultant depth map is shown in Figure 3.29(c).

A profile was taken across each of the depth-to-structure maps perpendicular to strike (A-A' in Figures 3.29(a), 3.29(b), and 3.29(c)) to better gauge the agreement between the actual and inverted depths. Figure 3.33 shows these profiles. The almost perfect superposition of the inverted depth profiles illustrates the program's lack of response to high-frequency noise in the data set. There is a discrepancy of less than 2.5 km between the actual and inverted peak depths but this is less than 10% of the actual mean depth. The inversion does a

reasonable job of reproducing the geometry of the model. The maximum amplitude as measured from the minor flat area on the edge of the bump is consistent with the model but the absolute depth is not perfectly deduced in Figure 3.33.

It can be expected that, since a reasonable match was achieved between the actual depth distribution of the Moho and the modelled depth, a plausible model of the Moho topography will be obtained from inversion of the real data.

TABLE 3.1: DENSITY LOG INFORMATION BY WELL			
Well	Layer	Sampled Thickness (m)	Weighted Average (g/cc)
Osprey H-84	869.25-1000 m	127.7	2.364
	1000-2000 m	826.15	2.219
	2000-3000 m	988.41	2.153
	3000-3464.8 m	440.4	2.318
Bittern M-62	1464-2000 m	514.65	2.682
	2000-3000 m	964.78	2.664
	3000-4000 m	986.28	2.665
	4000-4782.4 m	739.55	2.730
Gannet O-54	1525-2000 m	438.4	2.368
	2000-3000 m	972.55	2.692
	3000-3043.9 m	43.9	2.700
Razorbill F-54	921.1-1000 m	78.9	2.128
	1000-2000 m	984.75	2.501
	2000-3000 m	661.45	2.499
	3000-3126.25	126.25	2.650
Sandpiper 2J-77	793-1000 m	207	2.444
	1000-2000 m	984.75	2.288
	2000-3000 m	876.15	2.210
	3000-3522.75 m	518.5	2.671
Coot K-56	1640.9-2000 m	215.75	2.676
	2000-3000 m	551.65	2.461
	3000-3534.95 m	534.95	2.271
Spoonbill C-30	860.1-1000 m	133.8	2.732
	1000-2000 m	951.2	2.511
	2000-2757.2 m	626.05	2.390
Hibernia G55-A	505-1000 m	220	2.790
	1000-2000 m	709	2.333
	2000-3000 m	969	2.418
	3000-3456 m	456	2.457
Bonanza M-71	3475-4000 m	579	2.249
	4000-5000 m	955	2.583
	5000-5300 m	275	2.680
Cumberland C-55	1311.5-2000 m	679.3	2.225
	2000-3000 m	958.5	2.375
	3000-4000 m	947.1	2.508
	4000-4141.29 m	138.24	2.657
Linnet E-63	975-1000 m	25	2.150
	1000-2000 m	991	2.109
	2000-3000 m	958	2.311
	3000-4000 m	923	2.561
	4000-4500 m	500	2.486

TABLE 3.2: DENSITIES USED TO MODEL SEDIMENTARY BASINS			
BODY	DEPTH RANGE	DENSITY (g/cc)	DENSITY CONTRAST (g/cc)
Carson Basin	2-5 km	2.35	-0.32
Horseshoe Basin	2-4 km	2.668	-0.002
Horseshoe Basin	4-7 km	2.73	0.06
Whale Basin	2-6 km	2.50	-0.17
Whale Basin	6-7 km	2.65	-0.02
Jeanne d'Arc Basin	9-12 km	2.65	-0.02
Jeanne d'Arc and East Newfoundland Basins	6-9 km	2.64	-0.03
Jeanne d'Arc and East Newfoundland Basins	2-6 km	2.50	-0.17

TABLE 3.3: MOHO DEPTHS FROM SPECTRAL ANALYSES OF THE FILTERED FIELDS	
Cut-off Wavelength (km)	Ensemble Average Depth (km)
100	32.7
150	32.8
175	30.5
200	39.8

TABLE 3.4: BASEMENT DENSITIES FROM WELL LOGS			
WELL	THICKNESS (m)	DENSITY RANGE (g/cc)	AVERAGE* DENSITY (g/cc)
Gannet O-54	115.9	no range	2.70
Razorbill F-54	503.3	2.60-2.65	2.63
Linnet E-63	300.0	2.4-2.625	2.41
Cumberland B-55	380.7	2.3-2.7	2.70
Blue H-28	236.0	2.6-2.675	2.68
Hibernia G-55A	41.0	no range	2.70
Jaeger A-49	36.6	2.575-2.675	2.65
Bonanza M-71	17.0	no range	2.75

* Weighted according to thickness

TABLE 3.5: DEEP CRUSTAL SEISMIC VELOCITIES		
LINE	VELOCITY (km/s)	REFERENCE
Refraction line 87-3	6.7	Reid, 1993
Refraction Line 84-1	6.5	Todd, et al., 1988
Refraction line 84-2	6.5	Todd, et al., 1988
Refraction line 84-3	7.5	Todd, et al., 1988
Refraction line 84-4	6.4	Todd, et al., 1988
Refraction line 84-5	6.4	Todd, et al., 1988
Refraction line 84-6	7.7	Todd, et al., 1988
Refraction line 84-14	7.0	Todd, et al., 1988
Refraction line 84-11	6.5	Reid, 1988
Refraction line 87-1	7.2	Reid and Keen, 1990
Refraction line 87-7	6.8	Reid, 1994
Refraction line 91-2	6.96	Marillier, et al., 1994
AVERAGE	6.8	

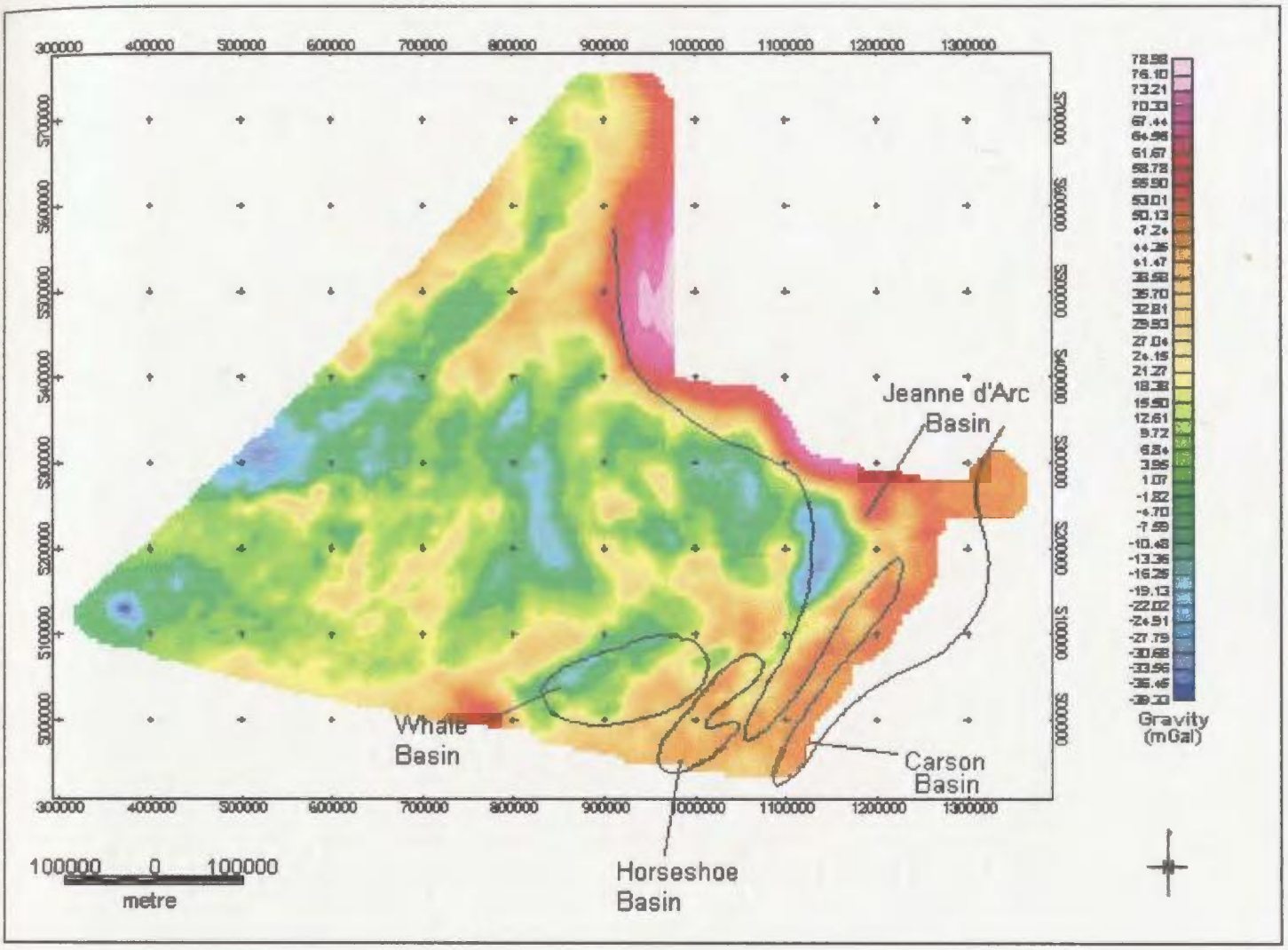

Figure 3.1. Bouger gravity anomaly map of the Avalon Terrane. The approximate locations and shapes of the Grand Banks basins are shown.

Figure 3.2. Depth to basement on the Grand Banks. The contour interval is 1 km. (From Wade, et. al., 1977).

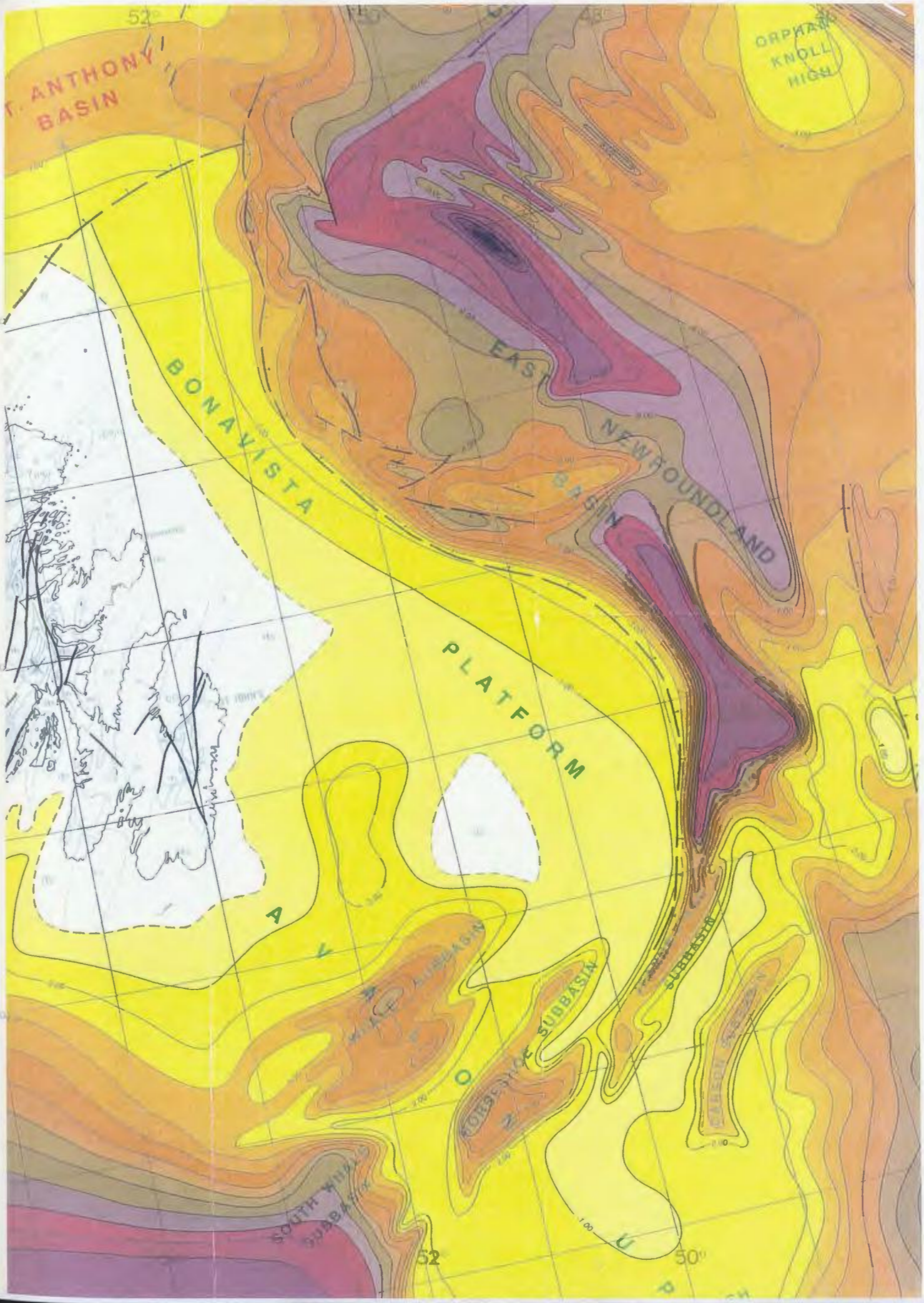
ST. ANTHONY BASIN
ORPHAN KNOLL HIGH
BONAVISTA PLATFORM
EASTERN NEWFOUNDLAND BASIN
AVALON UPLIFT
WHITE ROSE SUBBASIN
SOUTH TERRA NOVA SUBBASIN
52°
50°
48°
46°
44°

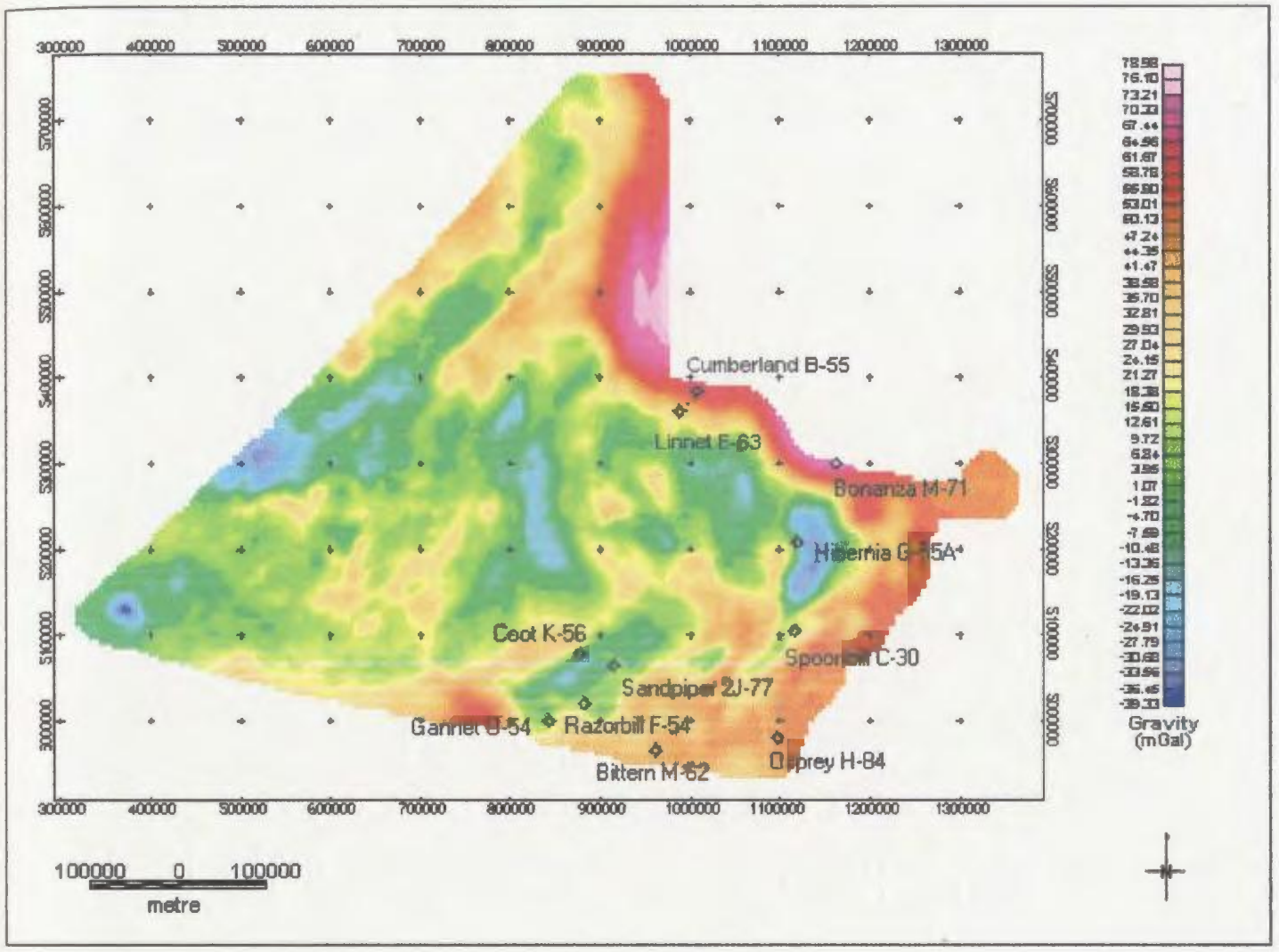

Figure 3.3. Locations of offshore exploratory wells used to determine basin density.

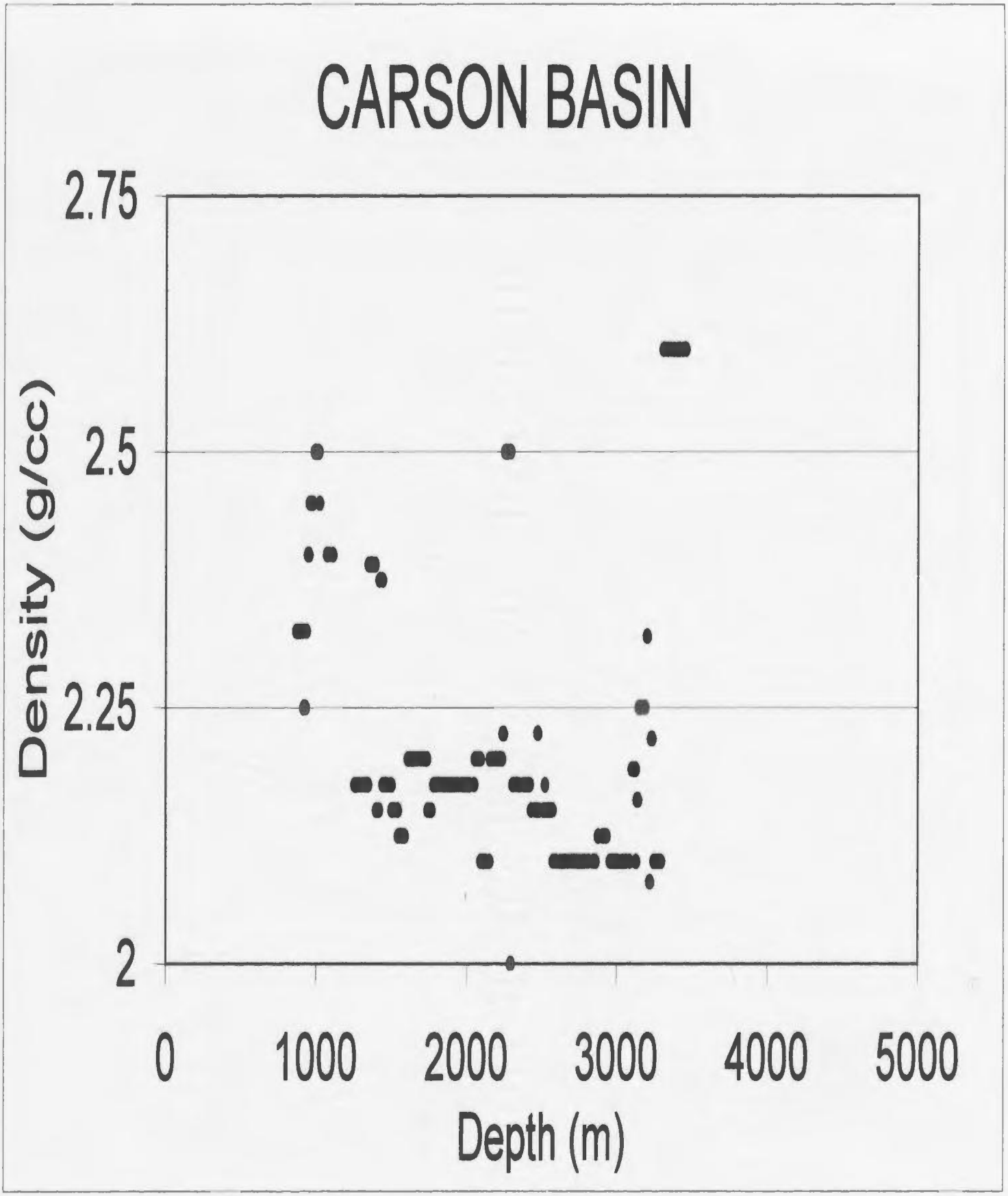

Figure 3.4. Density for Carson Basin from the Osprey H-84 well log.

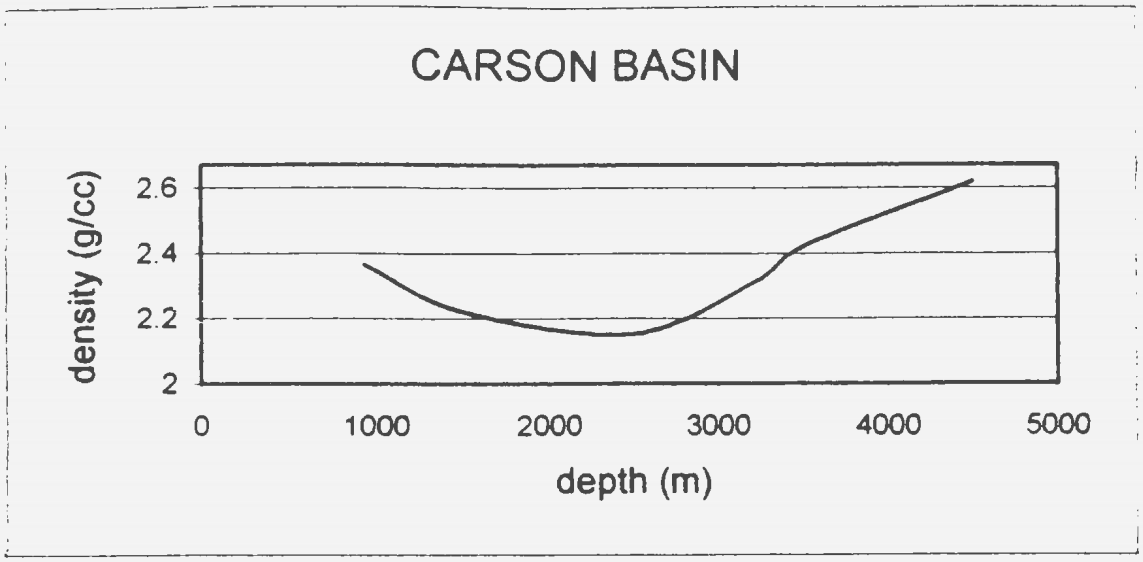

(a)

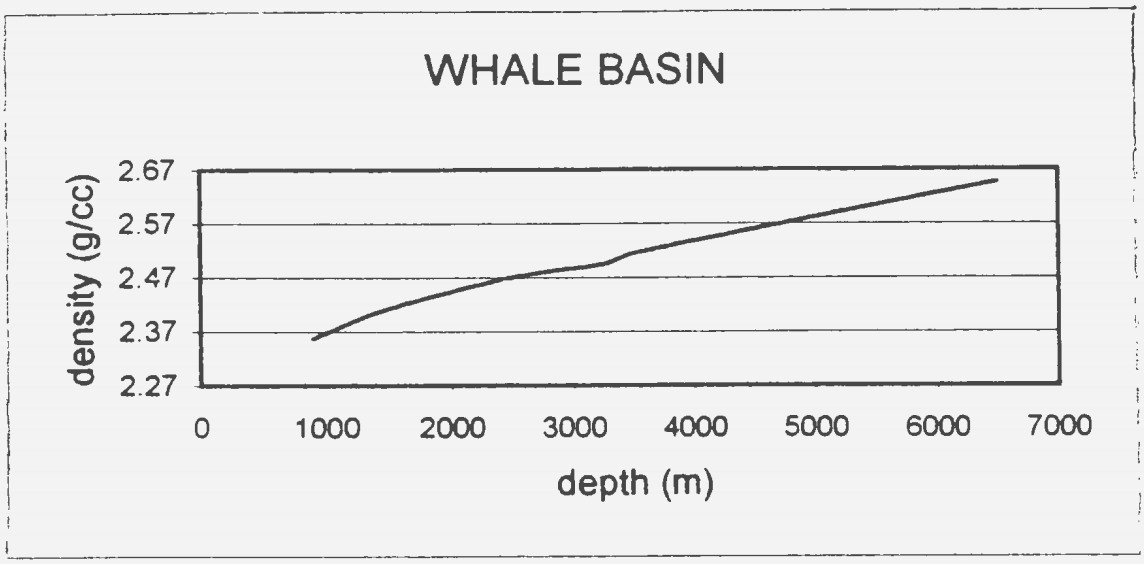

(b)

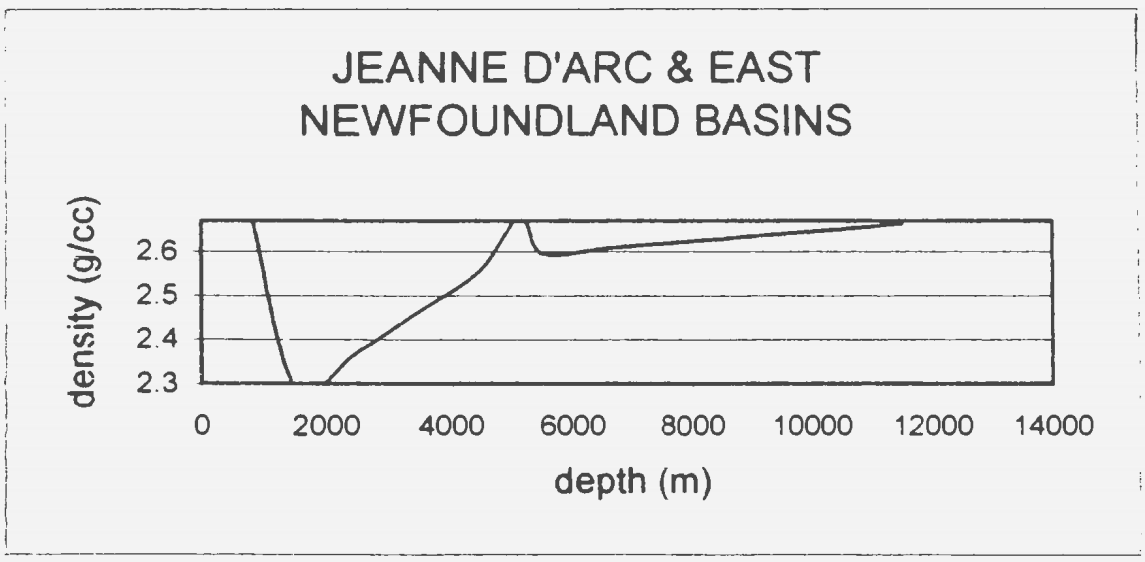

(c)

Figure 3.5. Density for Jeanne d'Arc-East Newfoundland Basins from the Bonanza M-71, Hibernia G-55A, Spoonbill C-30, Cumberland B-55, and Linnet E-63 well logs.

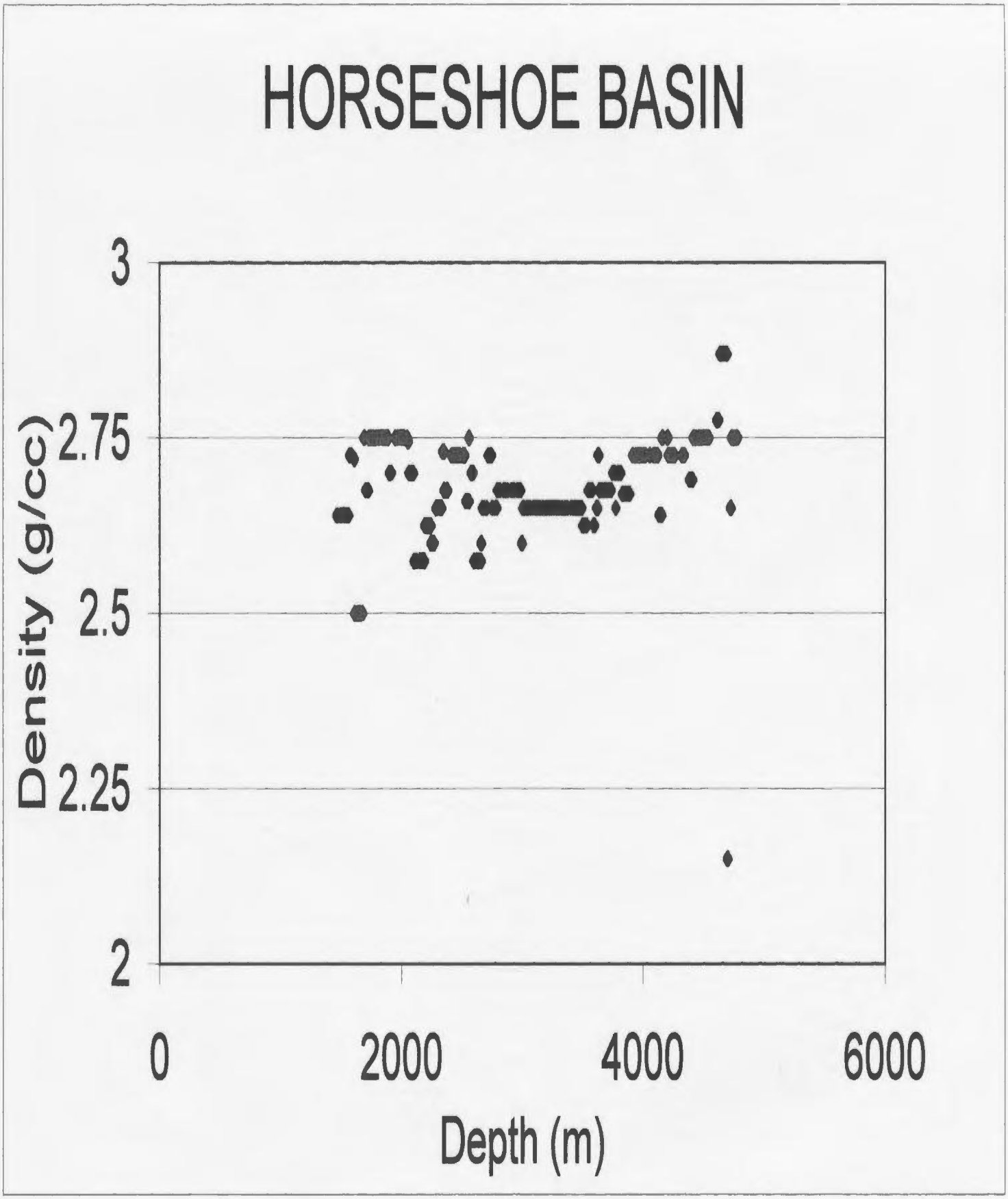

Figure 3.6. Density for Horseshoe Basin from the Bittern M-62 well log.

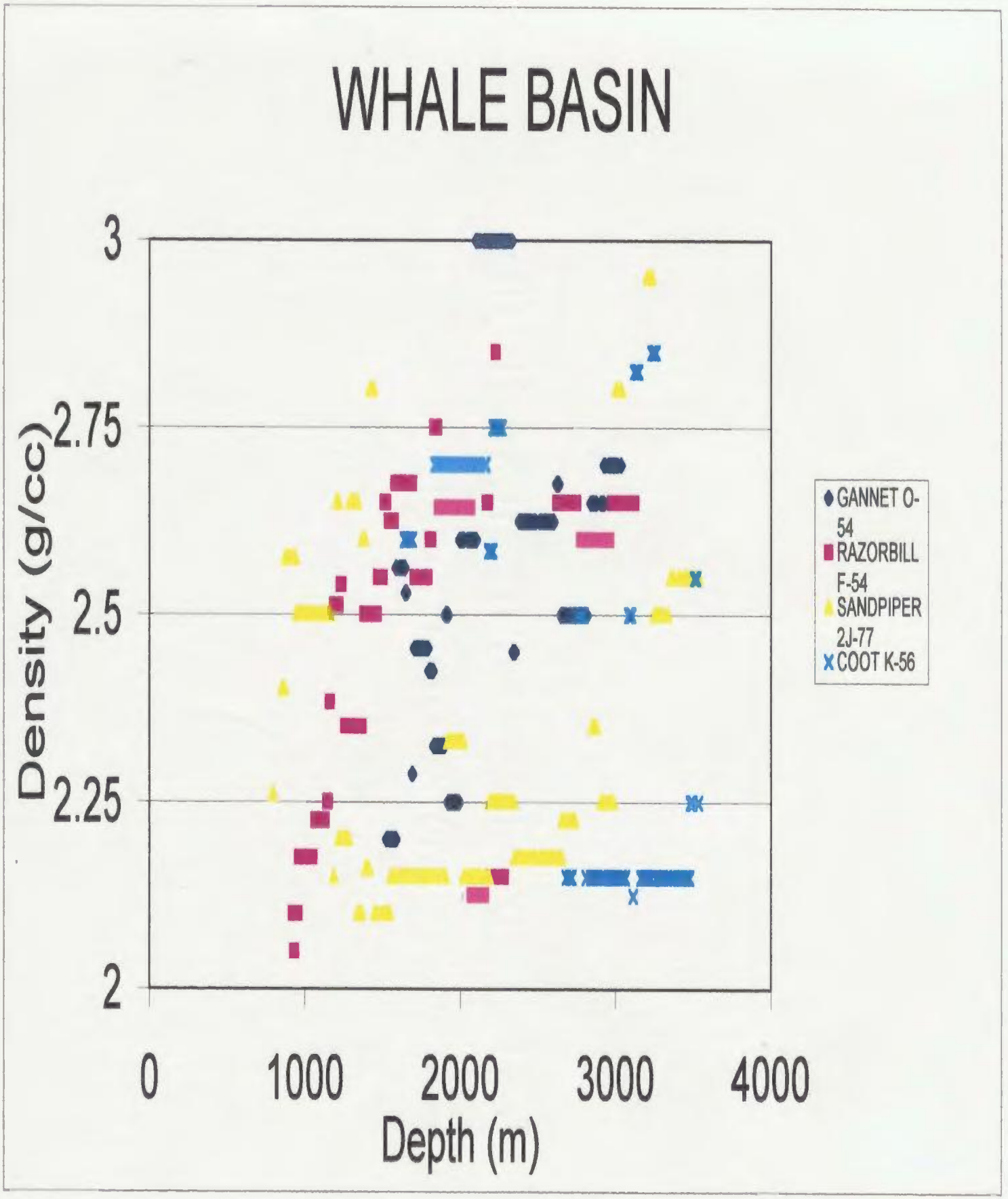

Figure 3.7. Density for Whale Basin from the Coot K-56, Gannet O-54, Razorbill F-54, and Sandpiper 2J-77 well logs.

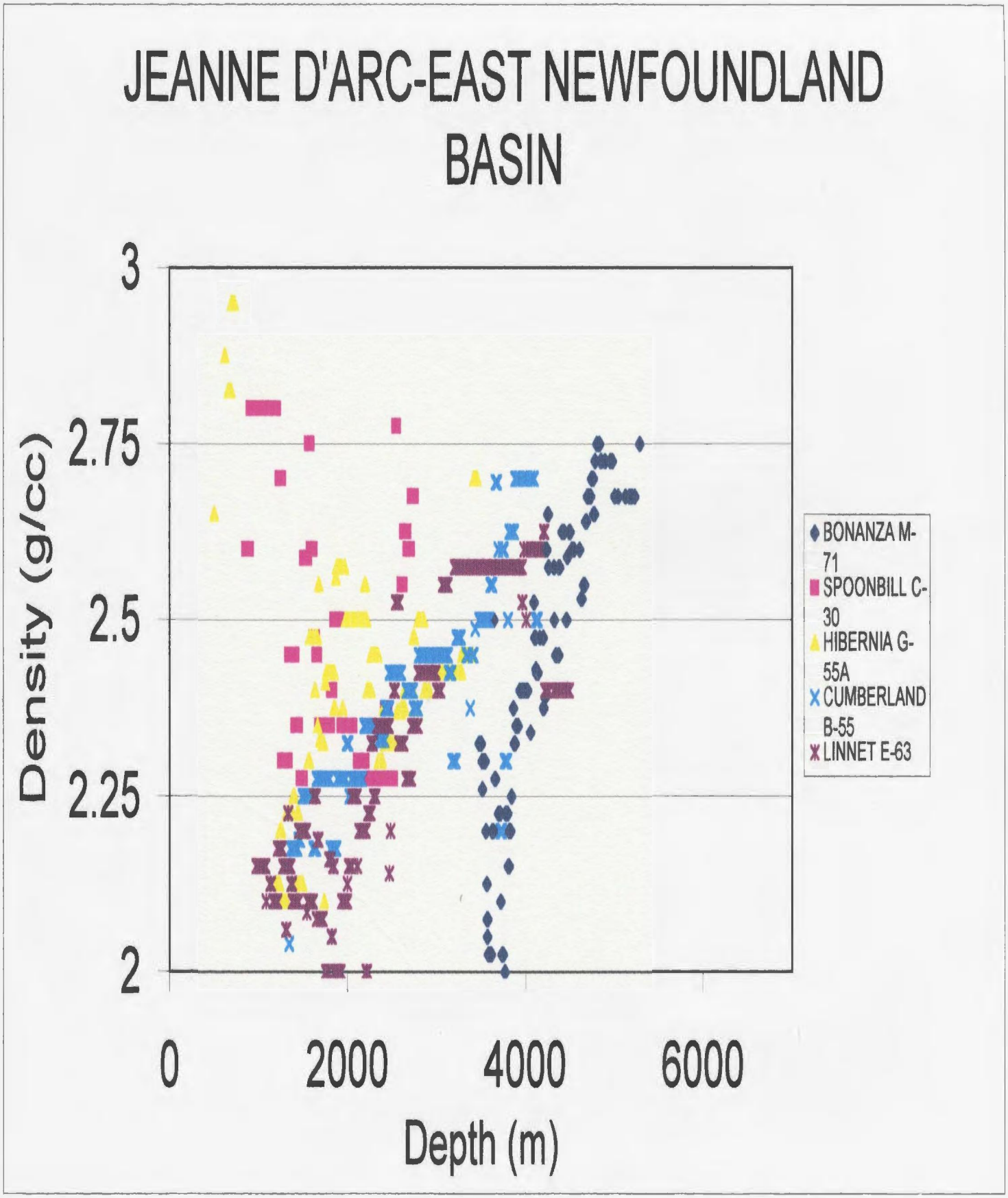

Figure 3.8. Density for Jeanne d'Arc-East Newfoundland Basins from the Bonanza M-71, Hibernia G-55A, Spoonbill C-30, Cumberland B-55, and Linnet E-63 well logs.

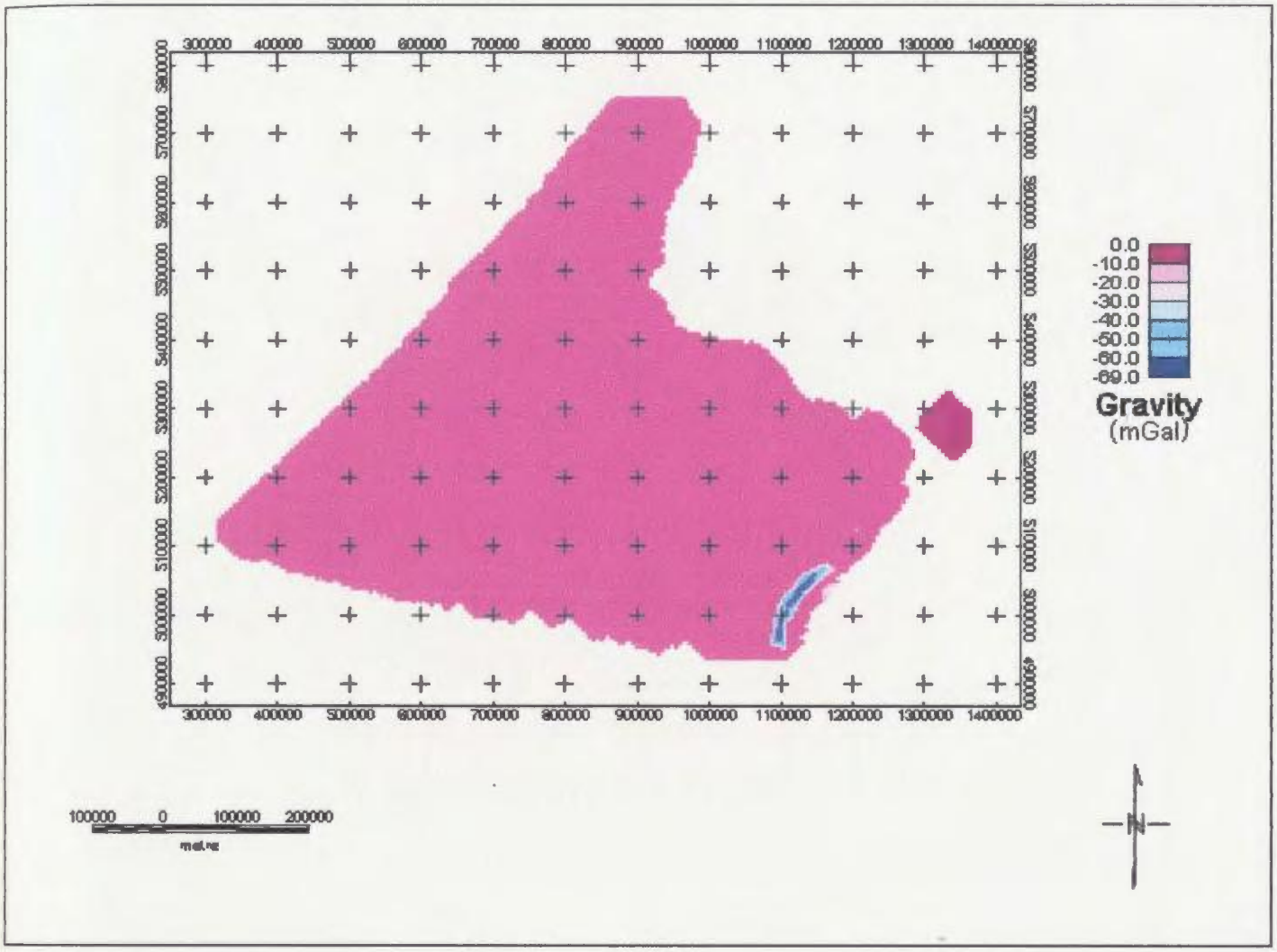

Figure 3.9. Modelled gravity anomaly field of Carson Basin.

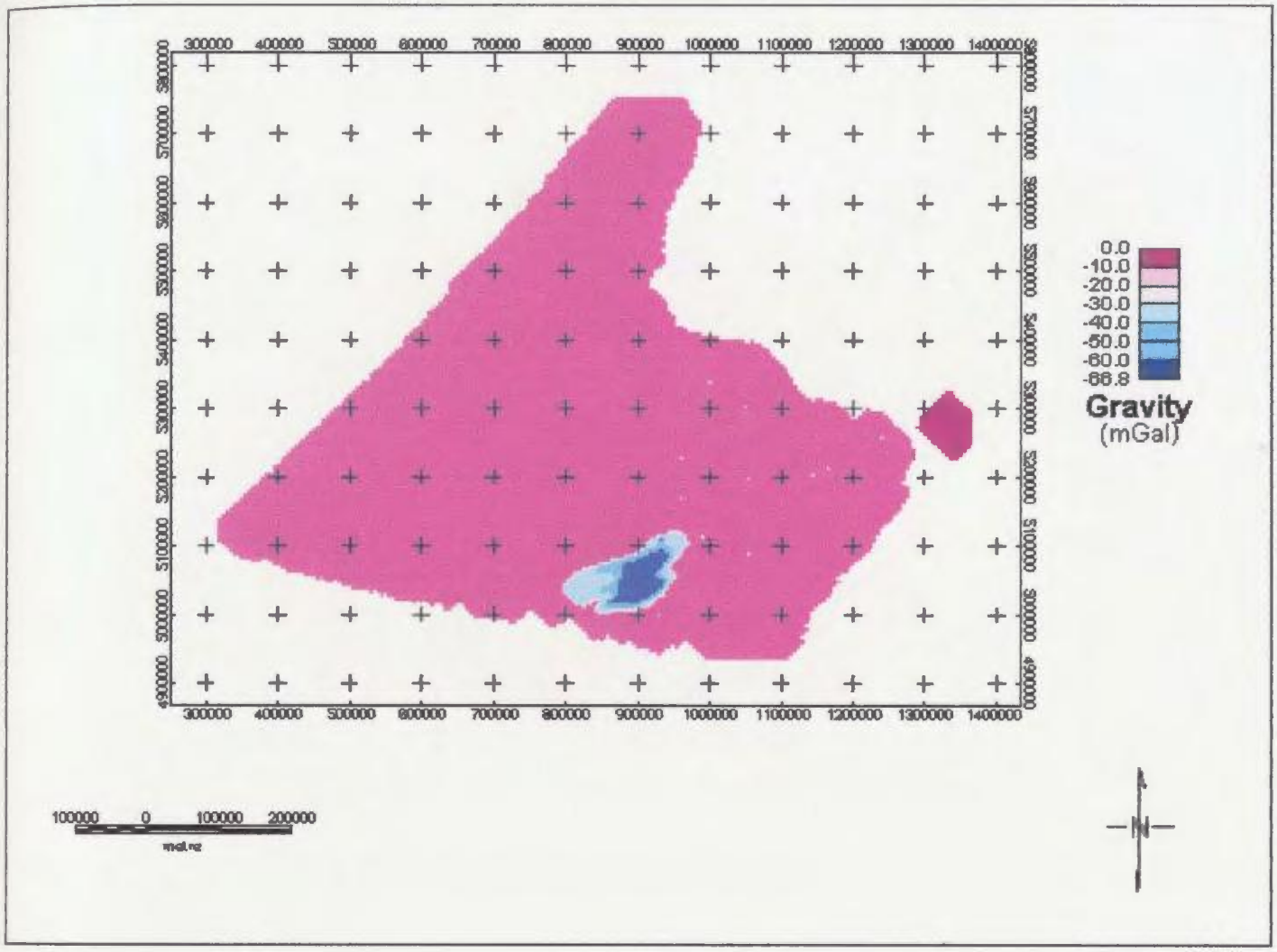

Figure 3.10. Modelled gravity anomaly field of Whale Basin.

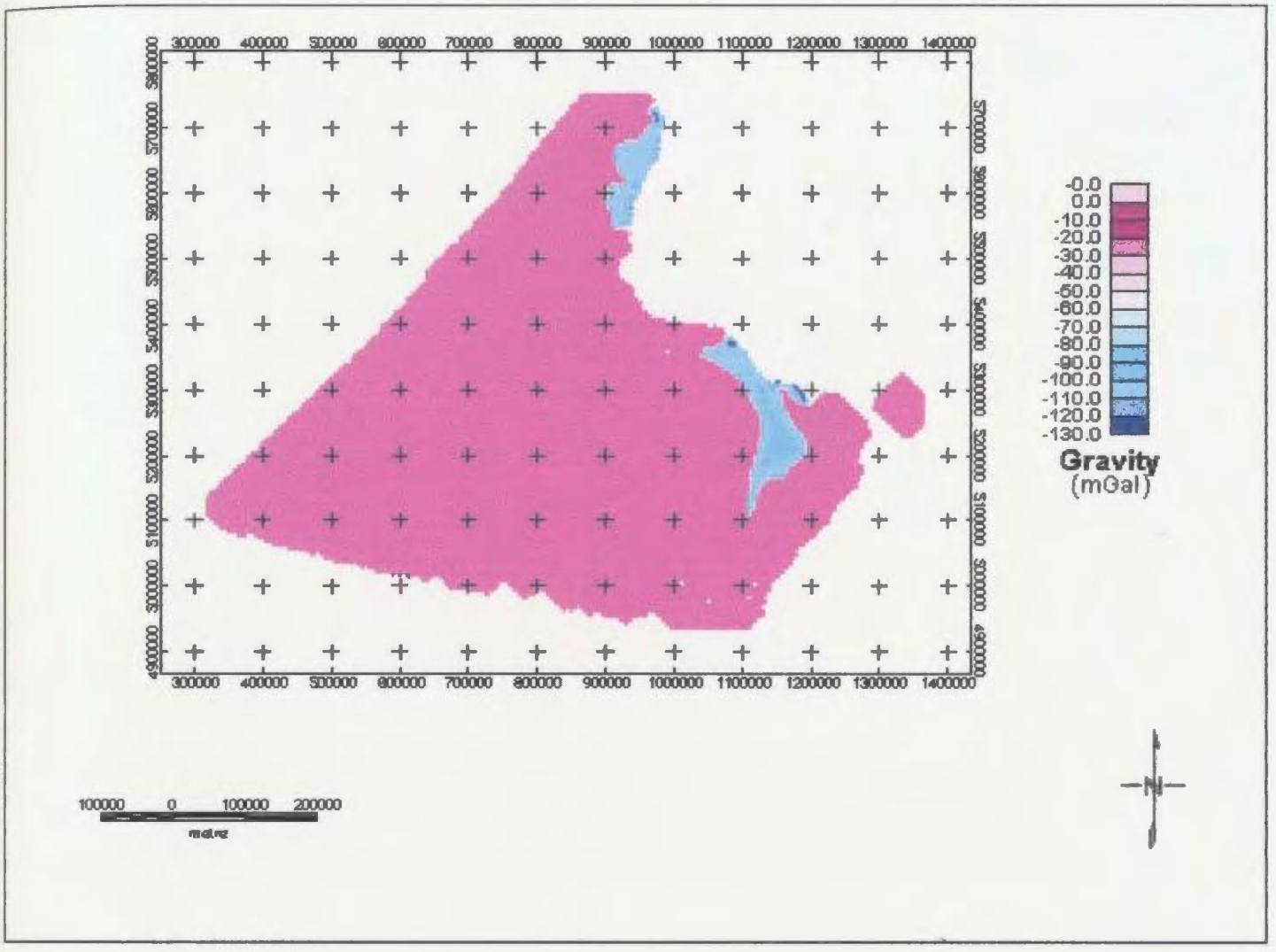

Figure 3.11. Modelled gravity anomaly field of Jeanne d'Arc-East Newfoundland Basins.

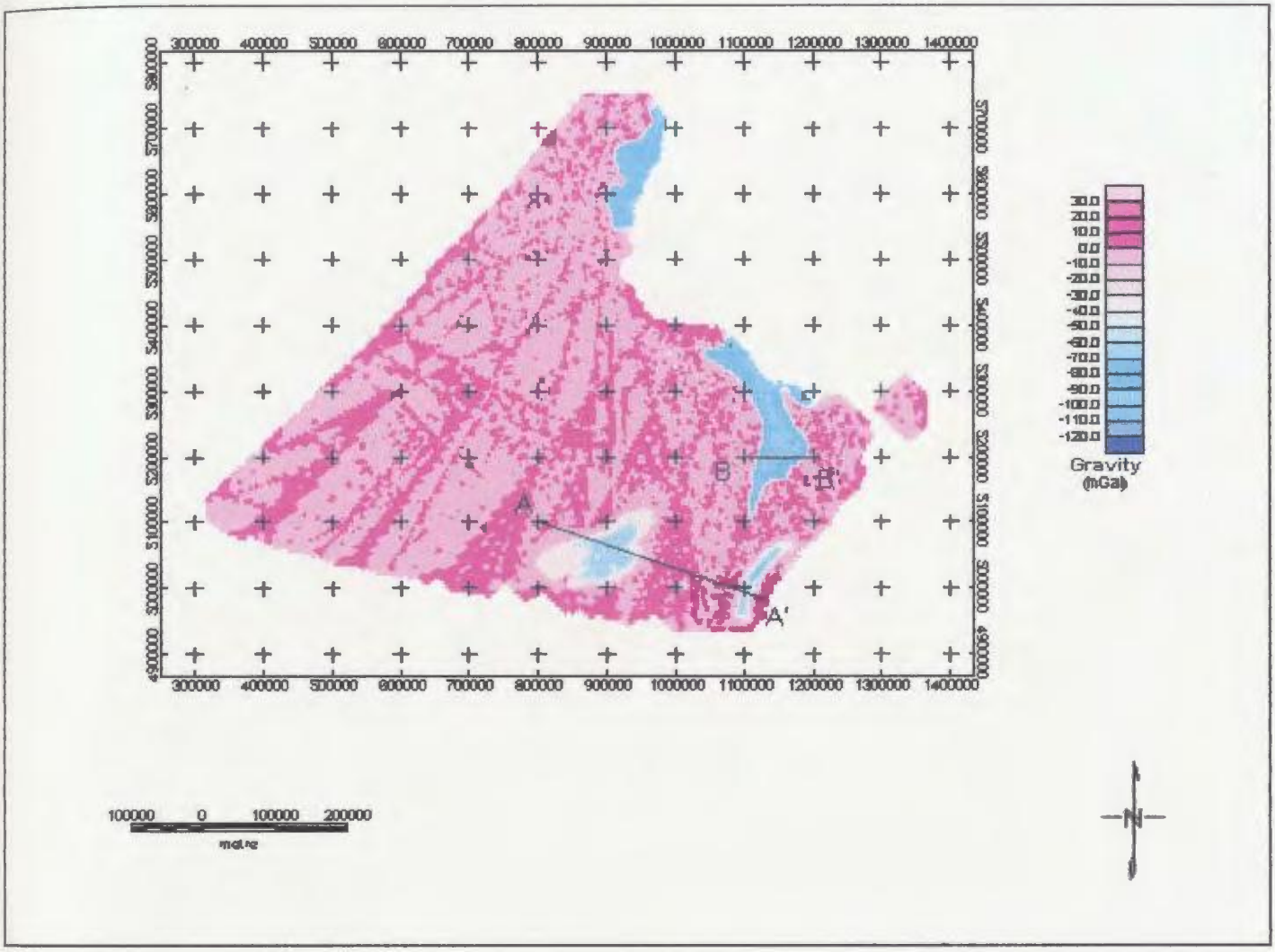

Figure 3.12. Total gravity anomaly field due to the Carson, Whale and Jeanne d'Arc-East Newfoundland Basins. The locations of profiles A-A' (across Whale, Horseshoe and Carson Basins) and B-B' (across Jeanne d'Arc Basin) are shown.

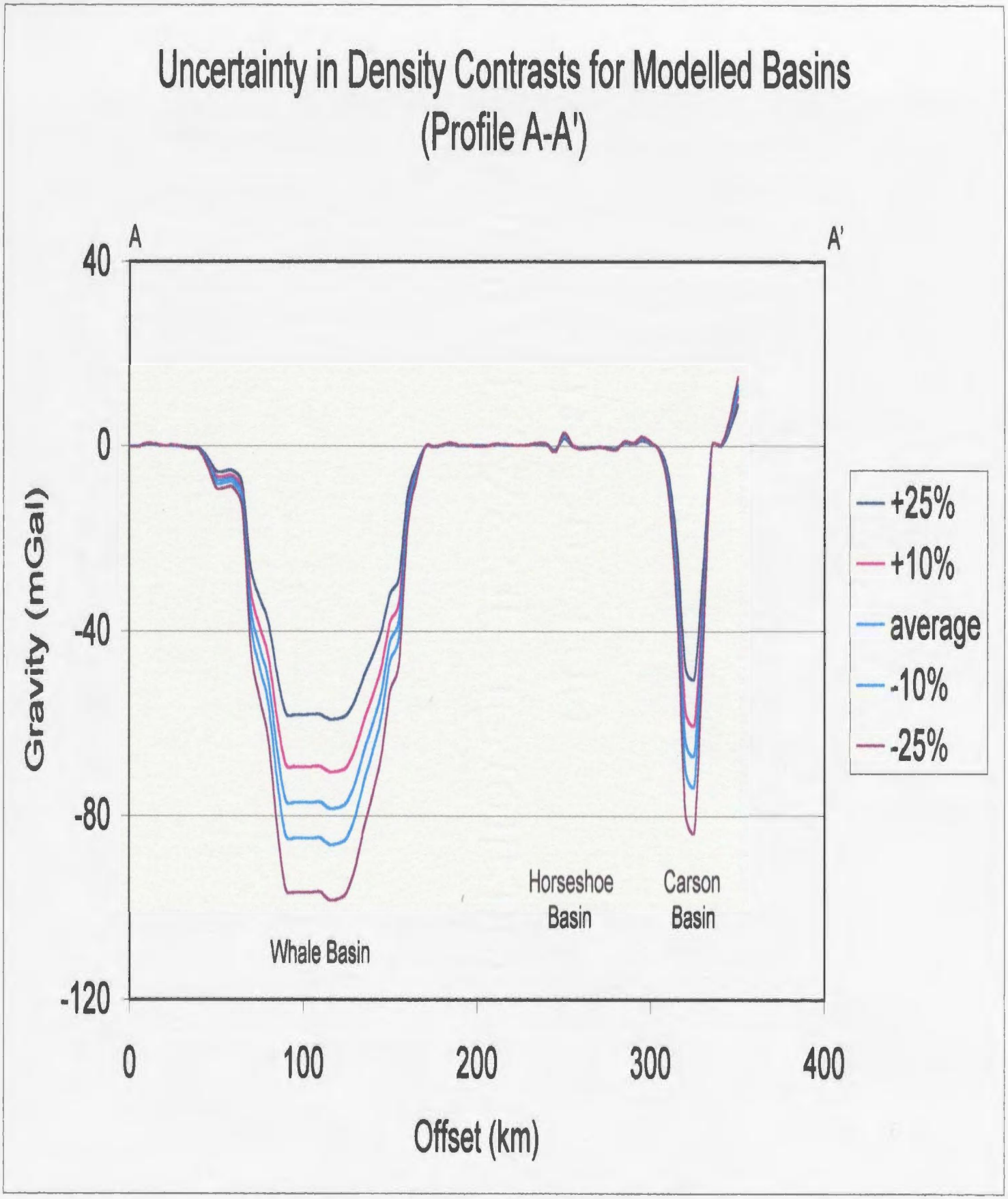

Figure 3.13. Uncertainty in the basin density contrasts along profile A-A' (across the Whale, Horseshoe, and Carson Basins).

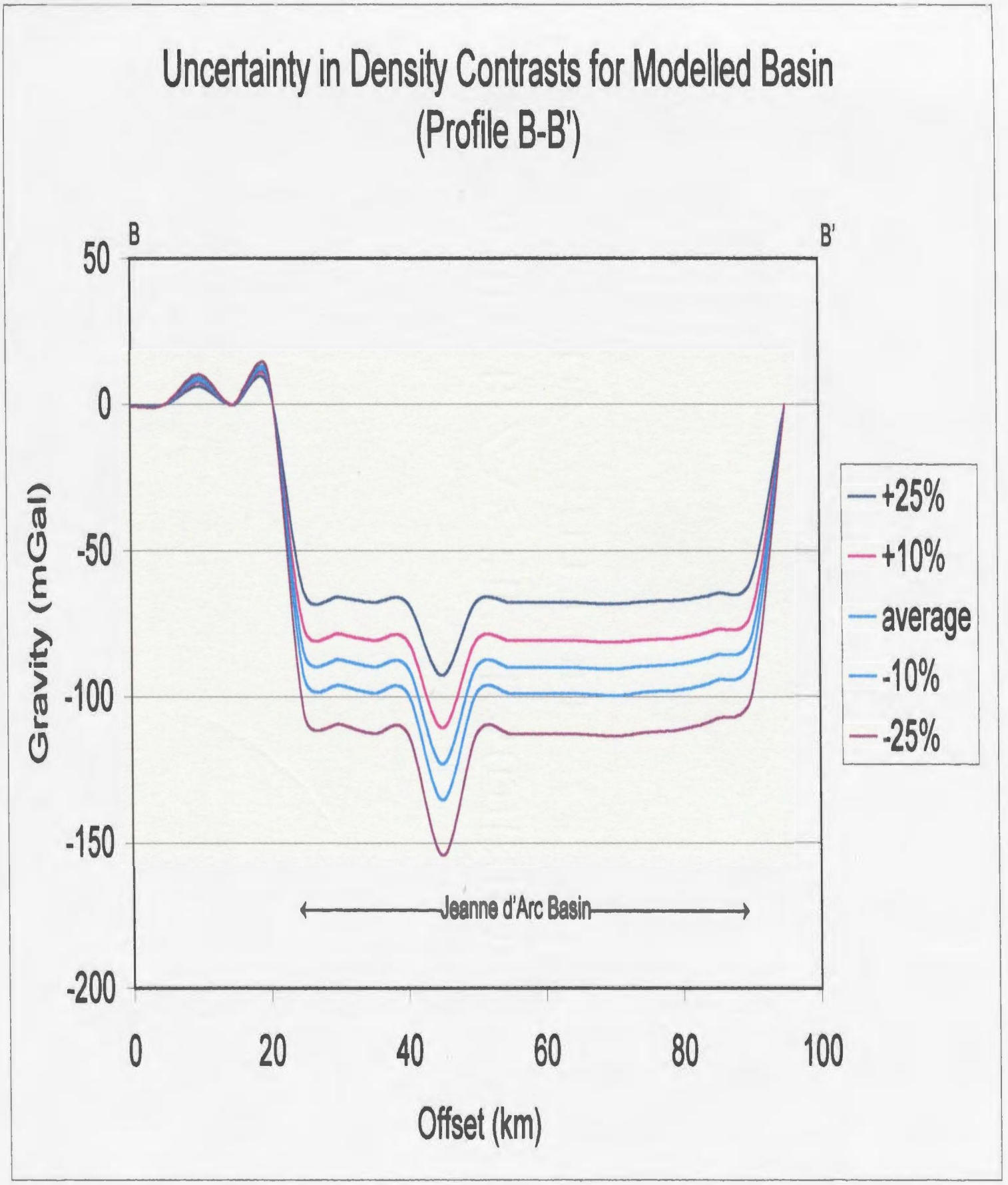

Figure 3.14. Uncertainty in the basin density contrasts along profile B-B' (across the Jeanne d'Arc Basin).

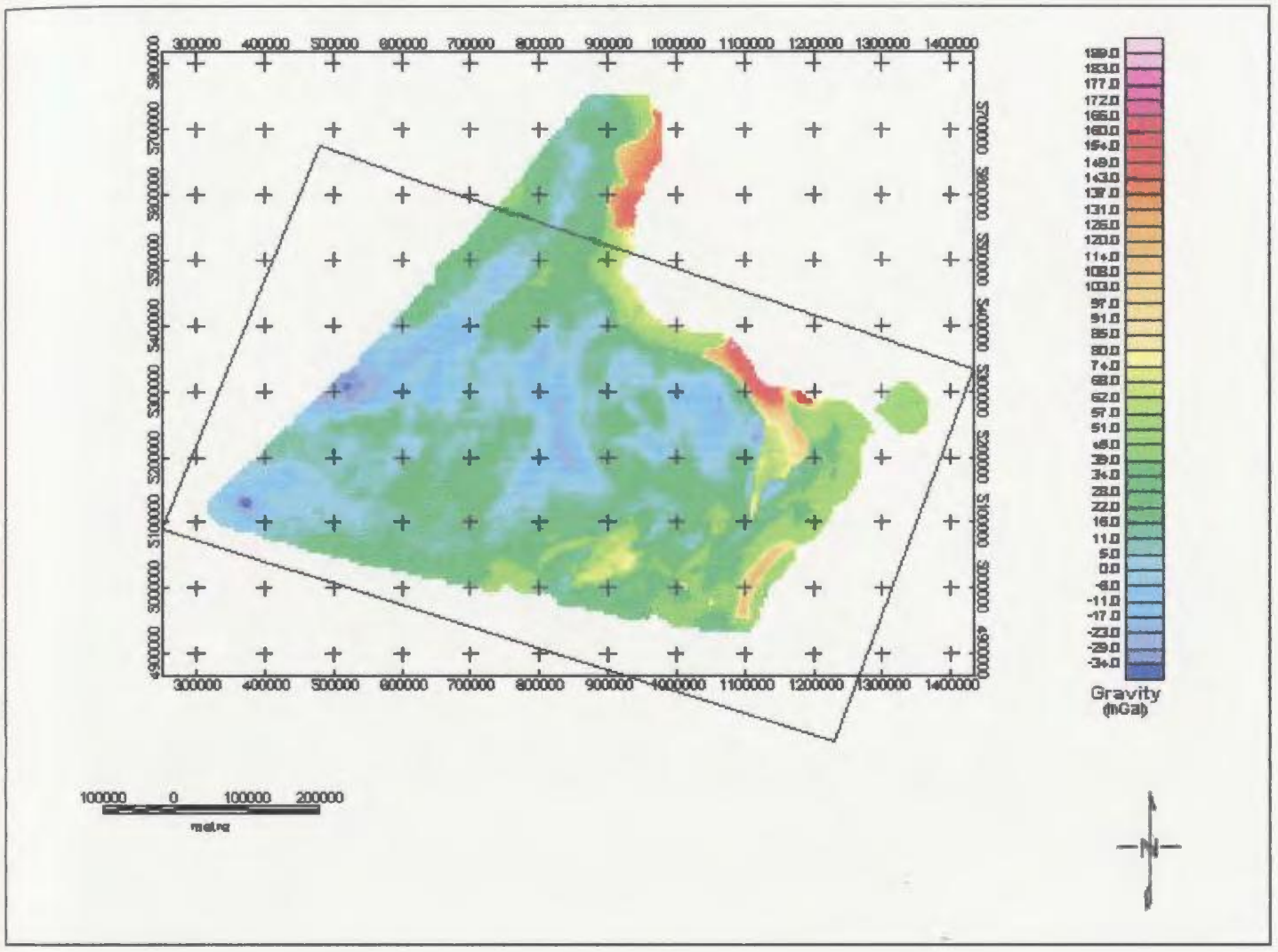

Figure 3.15. Gravity field of the Avalon Terrane with the effects of the sedimentary basins removed. The portion of the field contained within the rectangle was passed through the inversion program.

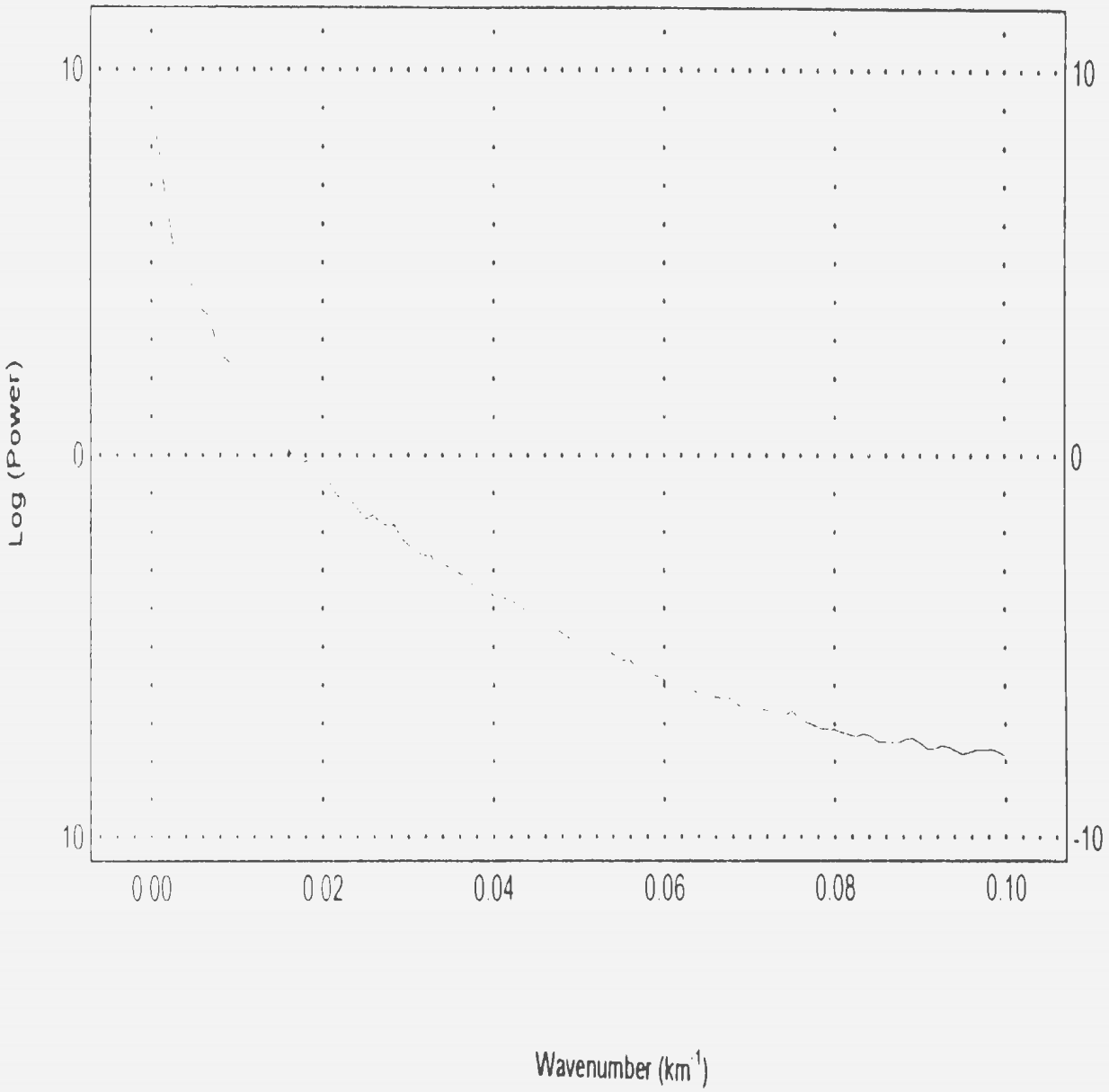

Figure 3.16. Power spectrum of observed gravity field.

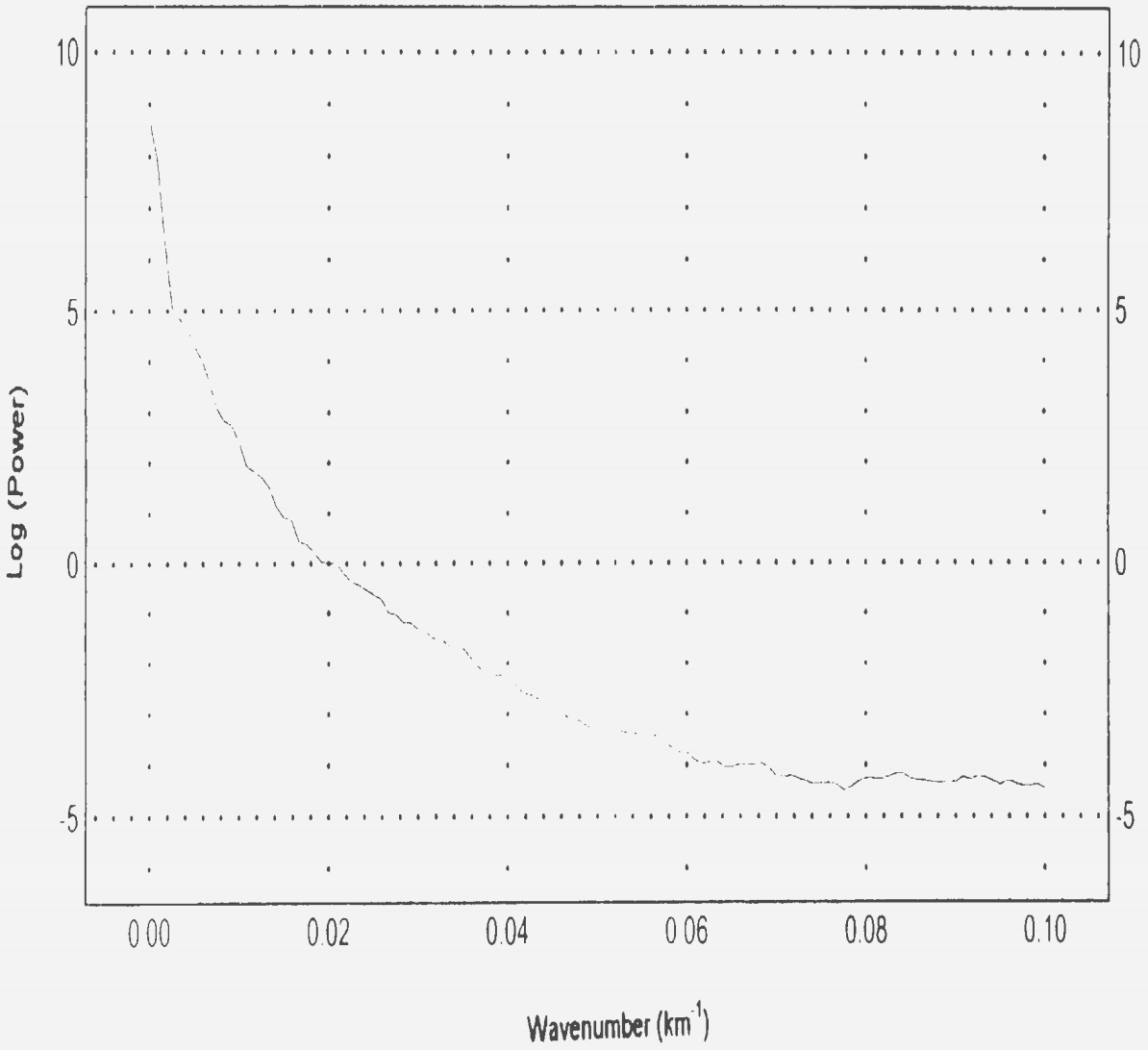

Figure 3.17 Power spectrum of observed gravity field after the effect of the sedimentary basins has been removed.

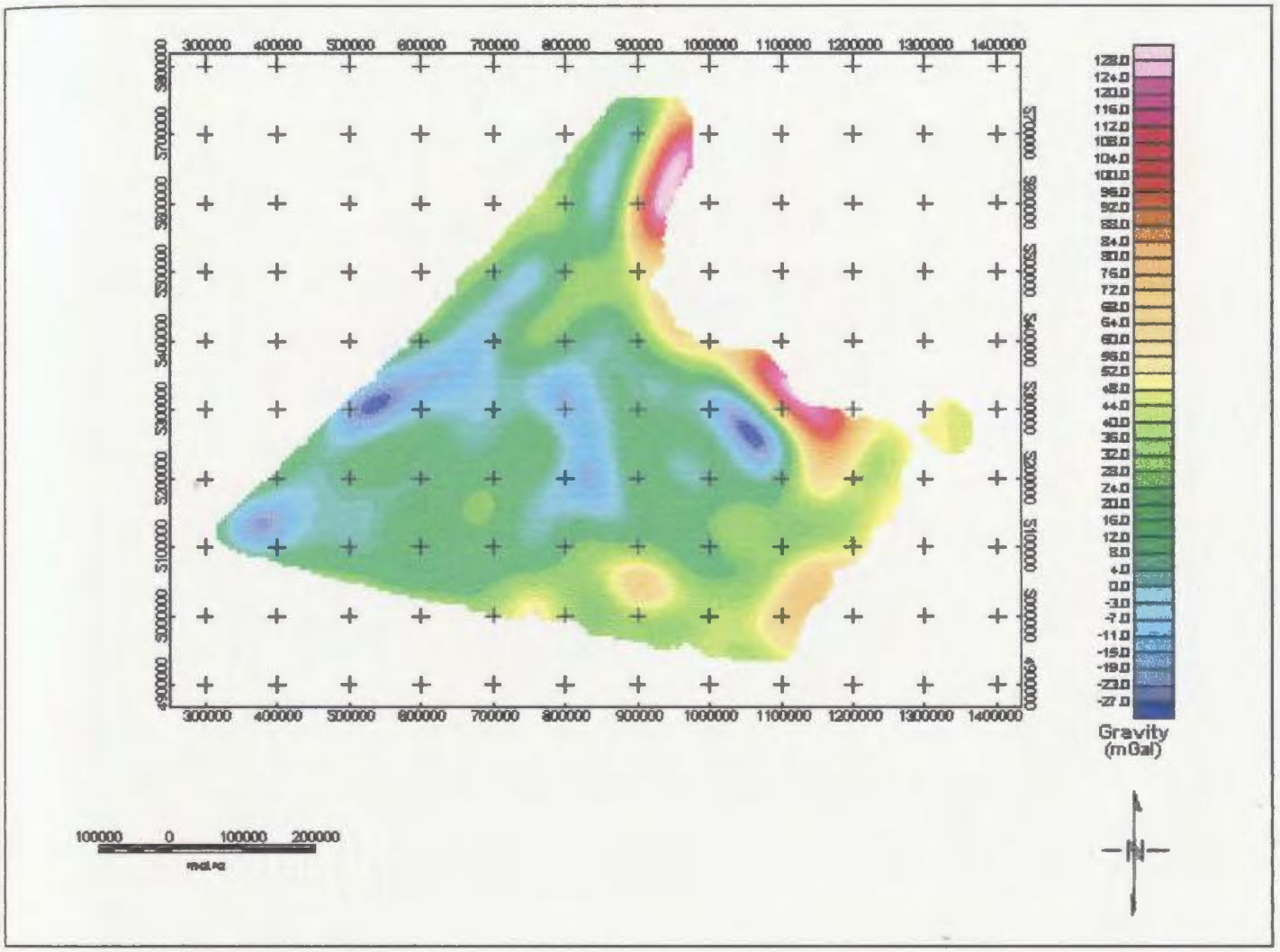

Figure 3.18. Observed gravity field, low-pass filtered to remove wavelengths less than 100 km.

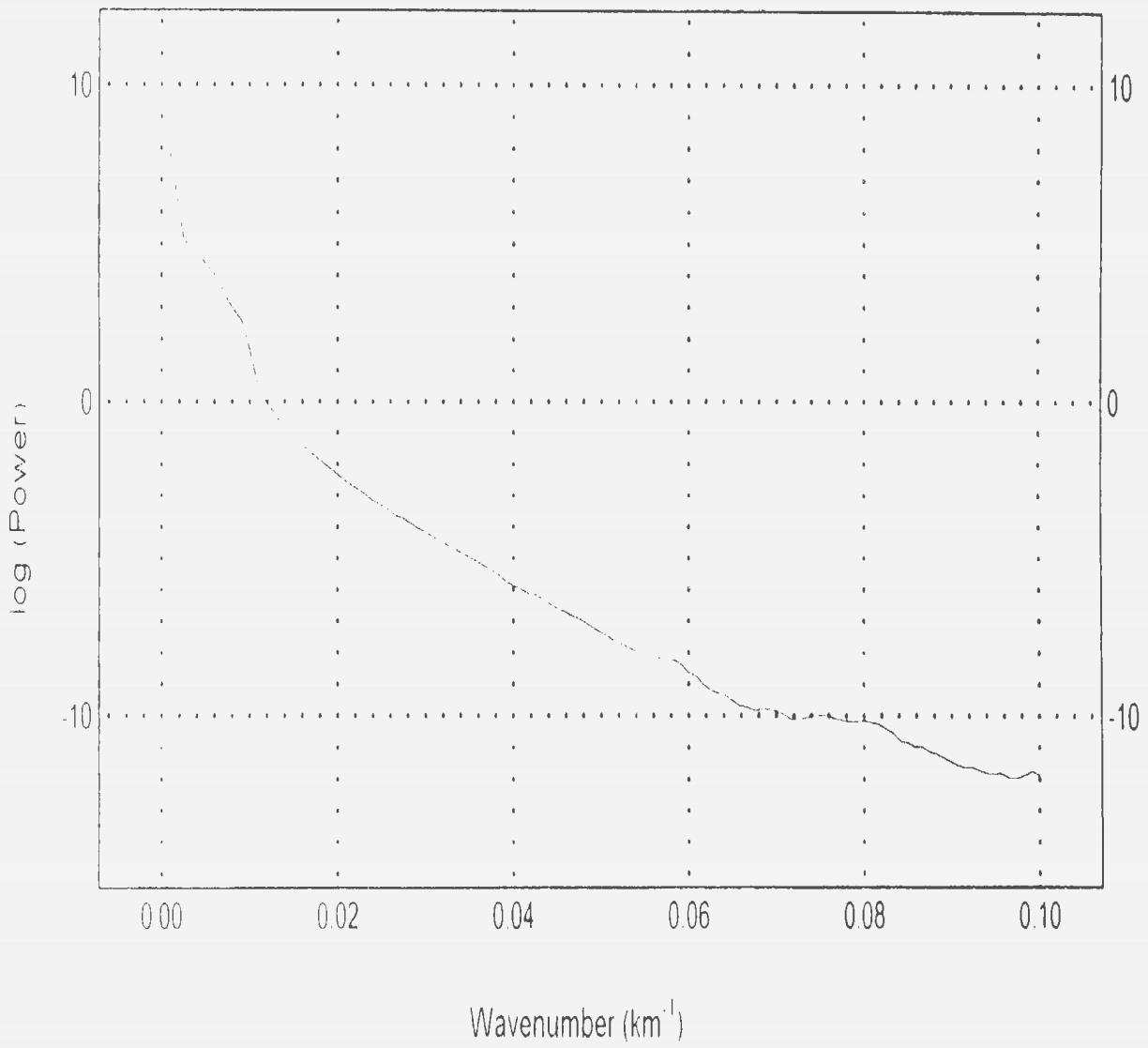

Figure 3.19 Power spectrum of gravity field filtered to remove wavelengths less than 100 km

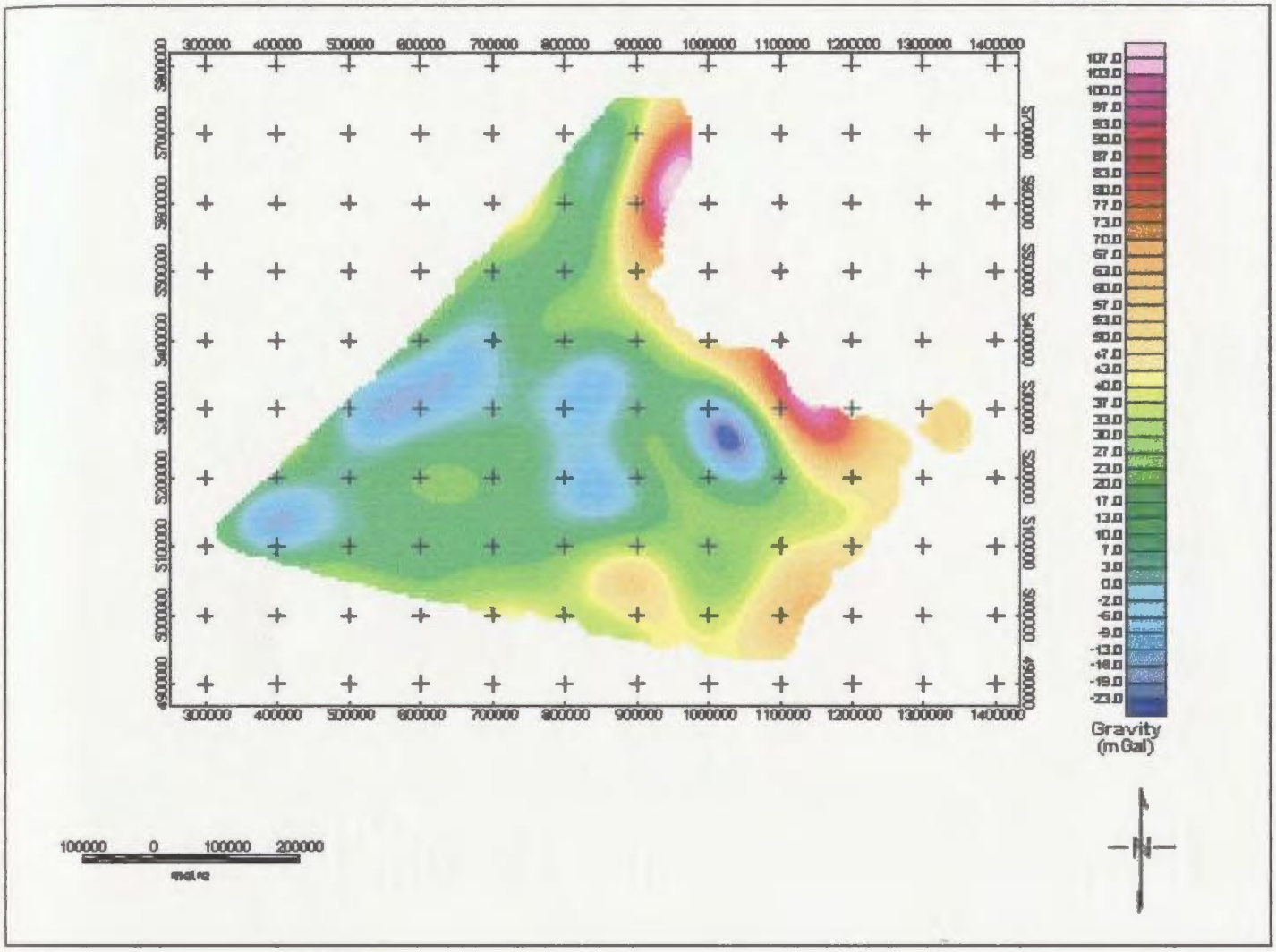

Figure 3.20. Observed gravity field, low-pass filtered to remove wavelengths less than 150 km.

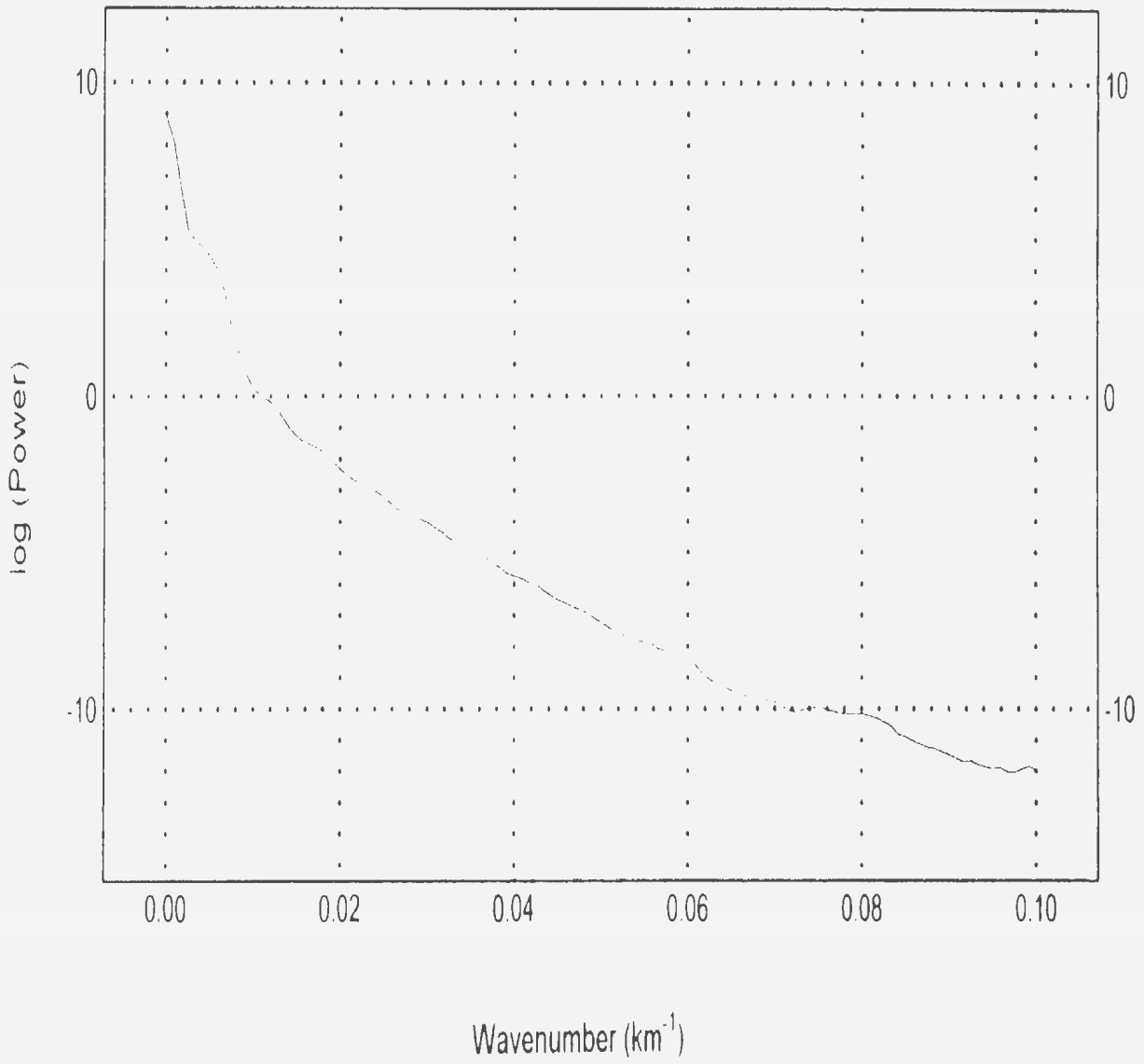

Figure 3.21 Power spectrum of gravity field filtered to remove wavelengths less than 150 km

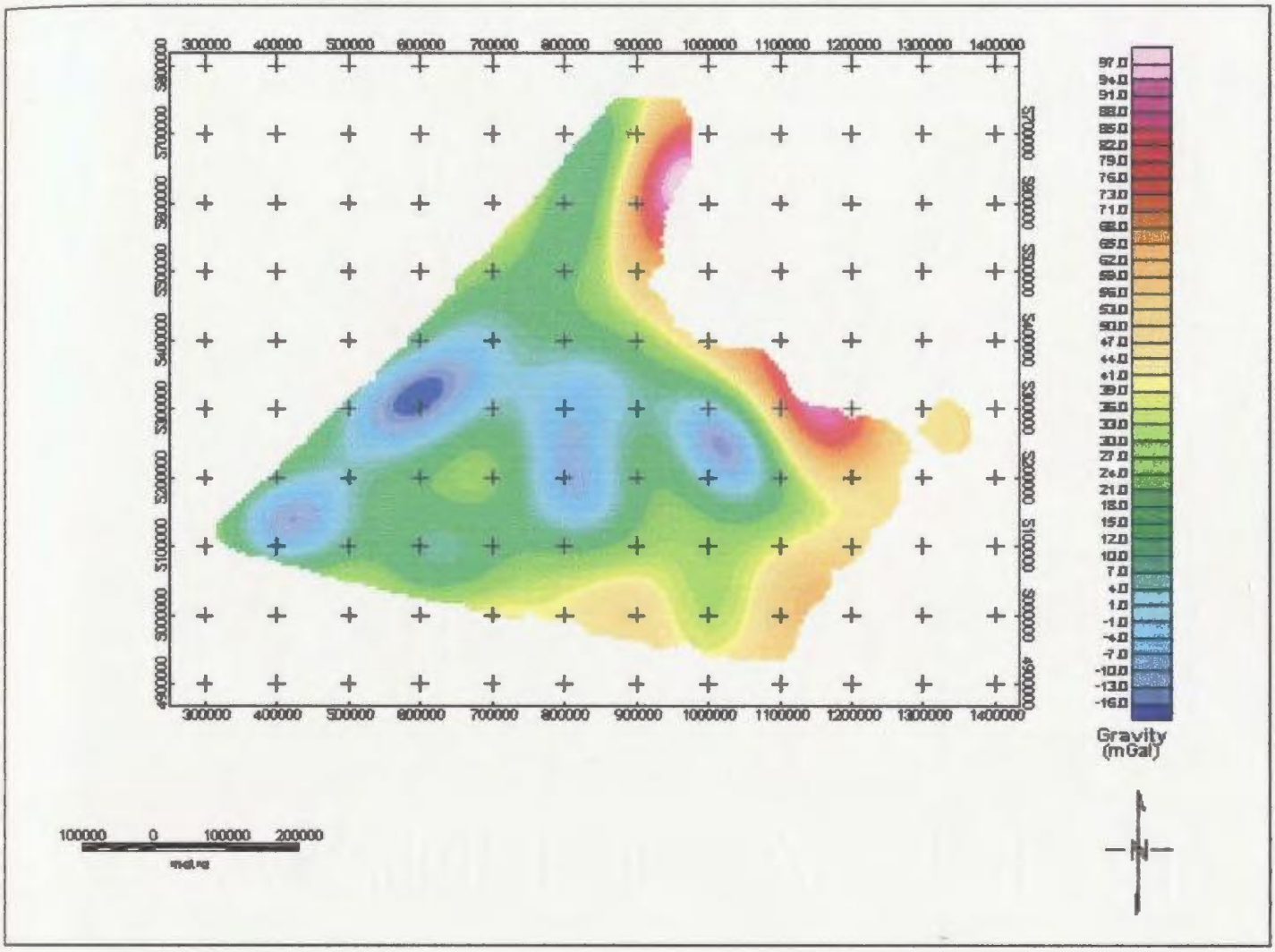

Figure 3.22. Observed gravity field, low-pass filtered to remove wavelengths less than 175 km.

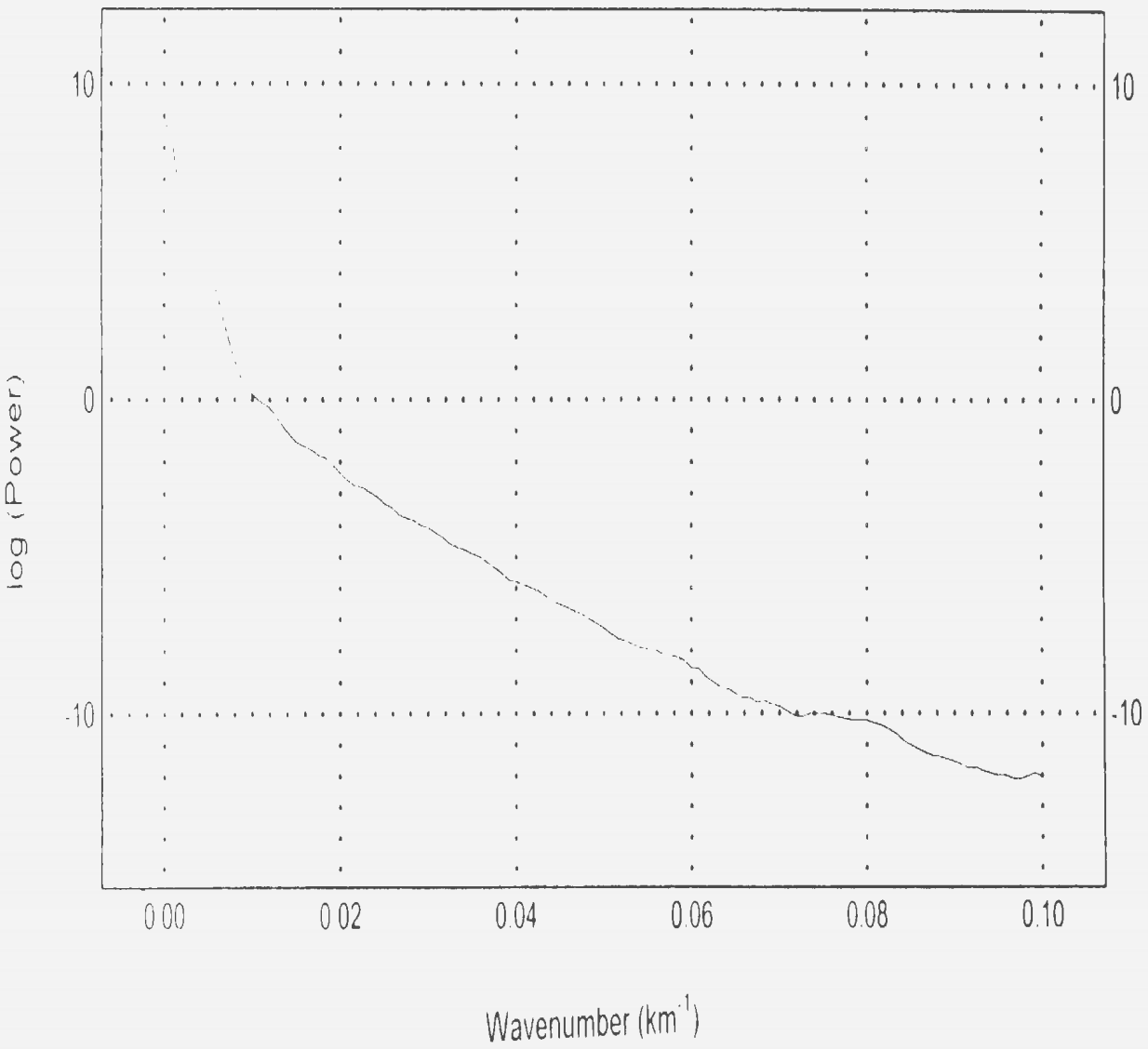

Figure 3.23 Power spectrum of gravity field filtered to remove wavelengths less than 175 km

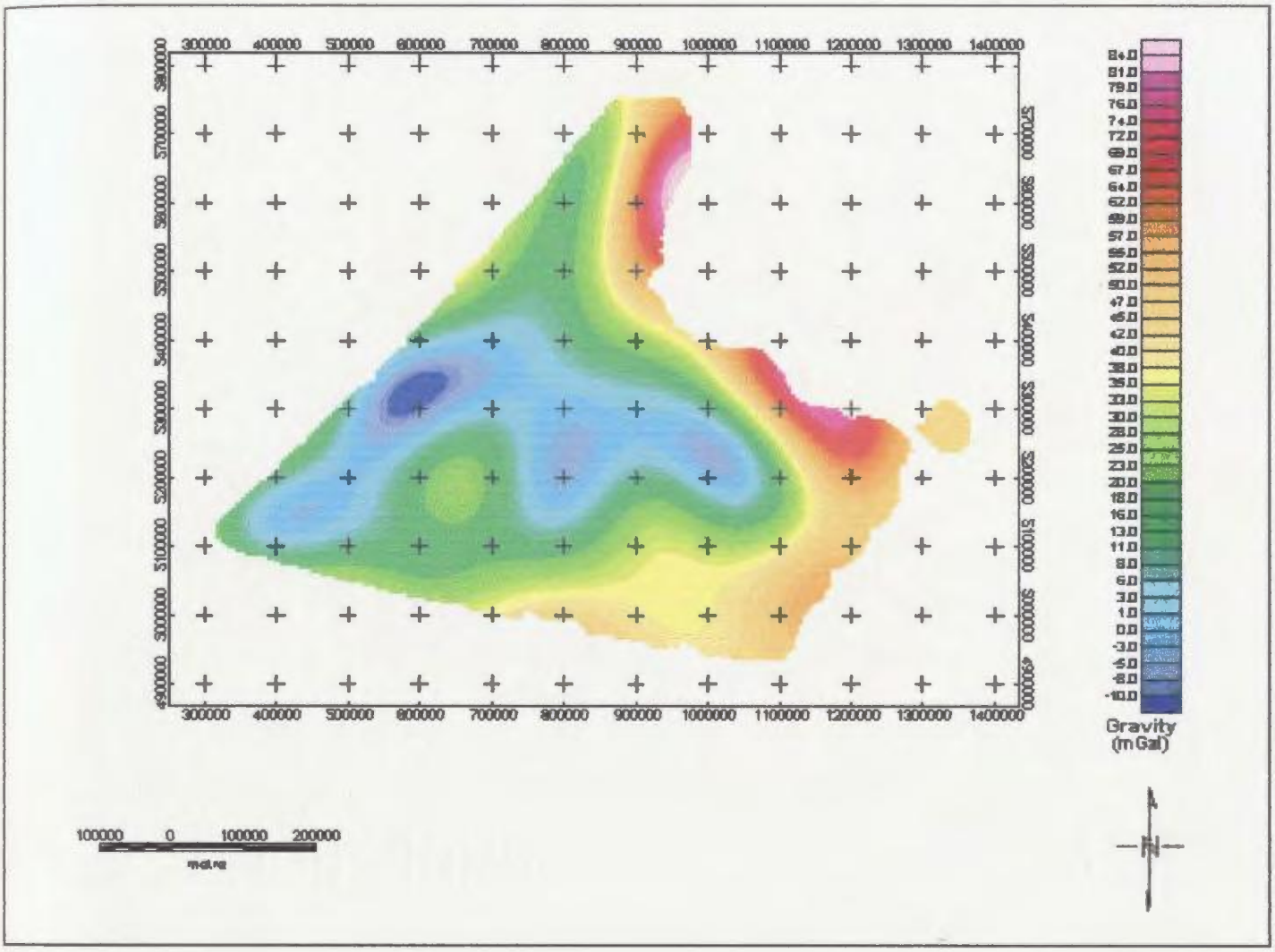

Figure 3.24. Observed gravity field, low-pass filtered to remove wavelengths less than 200 km.

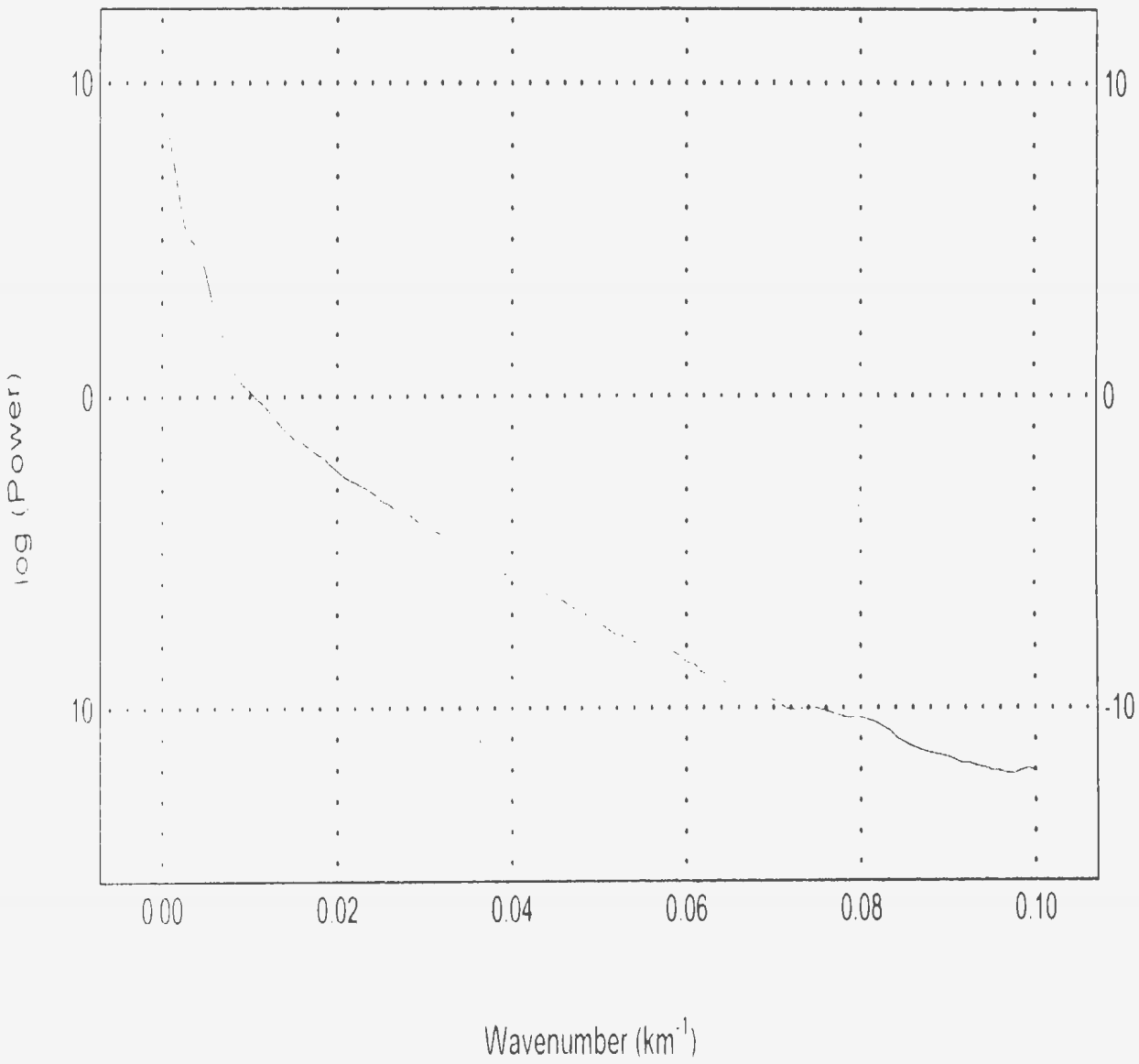

Figure 3.25 Power spectrum of gravity field filtered to remove wavelengths less than 200 km

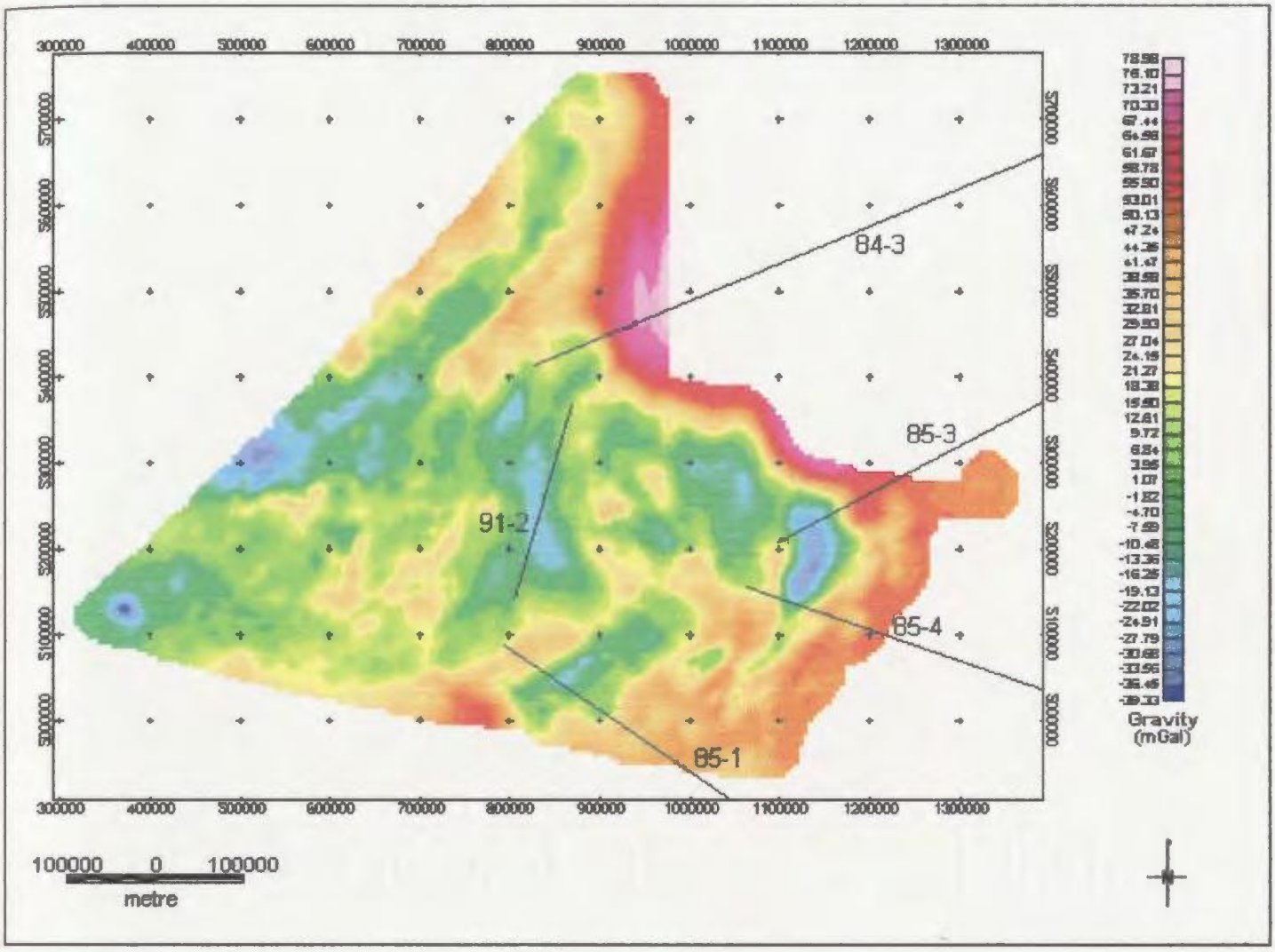

Figure 3.26. Location of seismic reflection and refraction lines used to determine mean depth to Moho on the Grand Banks.

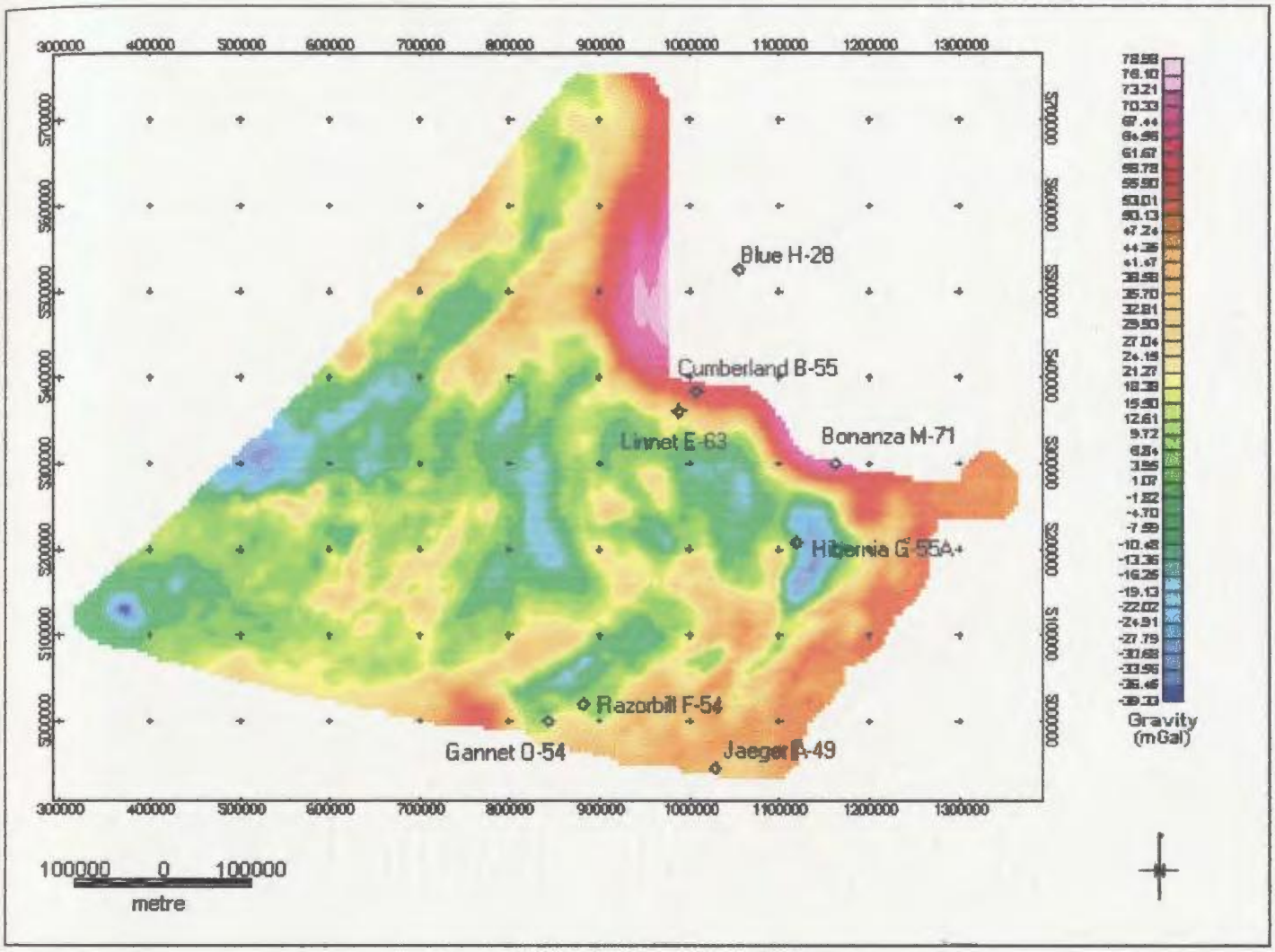

Figure 3.27. Location of exploration wells used to determine basement density.

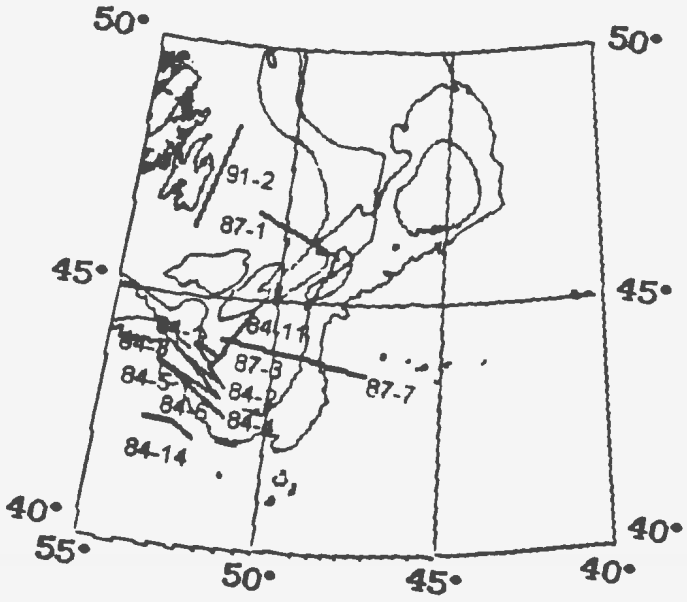

Figure 3.28. Location of seismic reflection and refraction lines used to determine deep crustal seismic velocity. (Modified from a Geological Survey of Canada web page containing an East Coast of Canada Refraction Catalogue for surveys between 1983 and 1992 inclusive; http://agc.bio.ns.ca/pubprod/ecref/index.html).

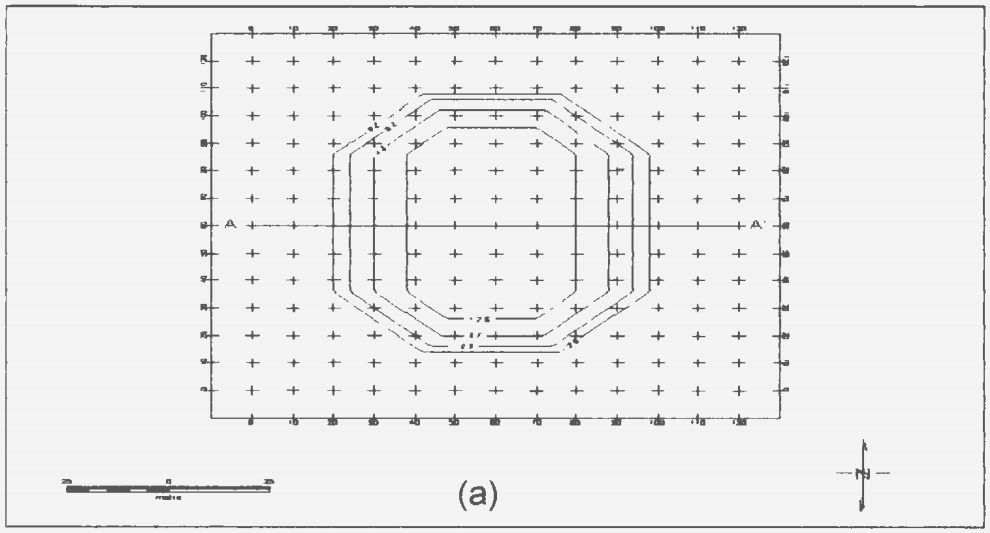

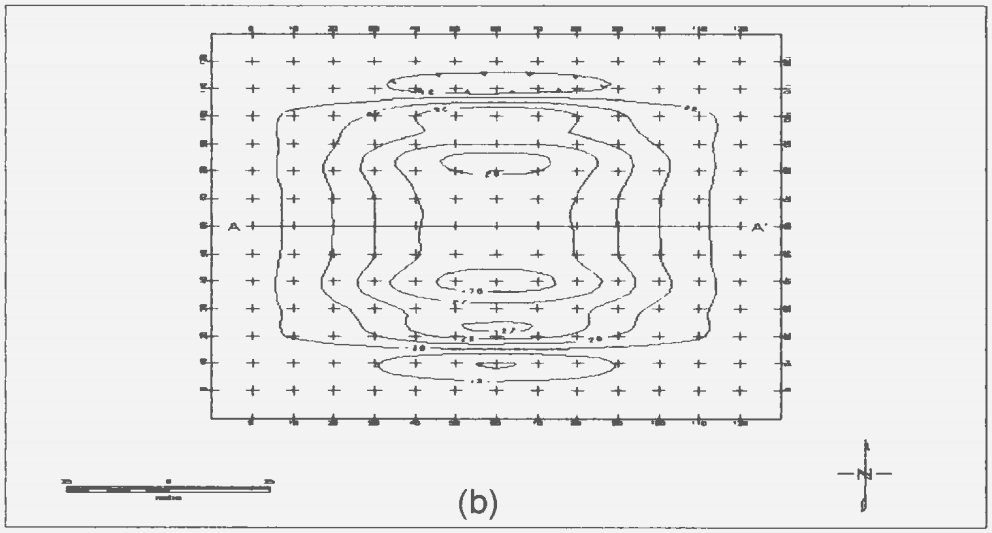

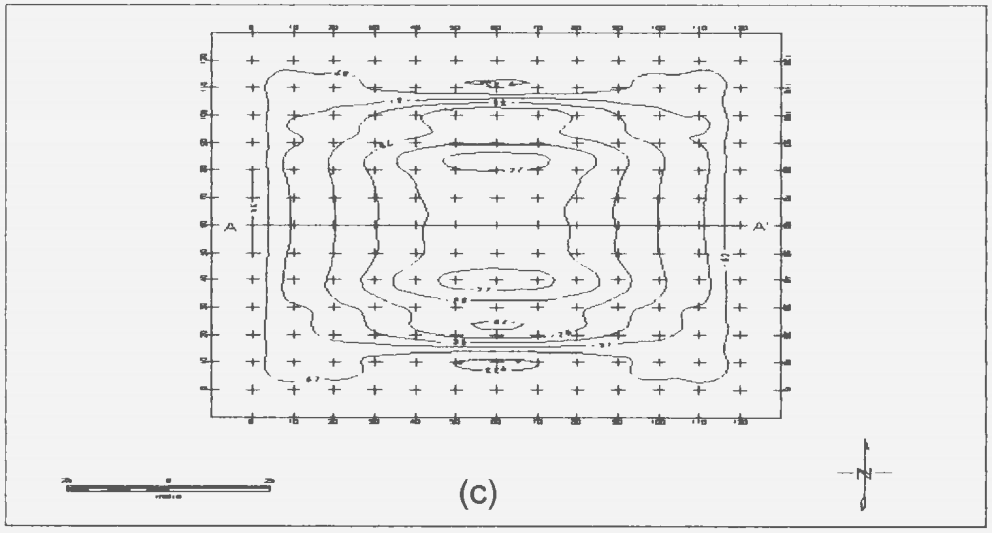

Figure 3.29. (a) Depth to Moho map of synthetic data set. (b) Modelled depth to Moho for the synthetic data set. (c) Modelled depth to Moho for the synthetic data set with noise (±1 mGal) added. The contour interval is 1 km.

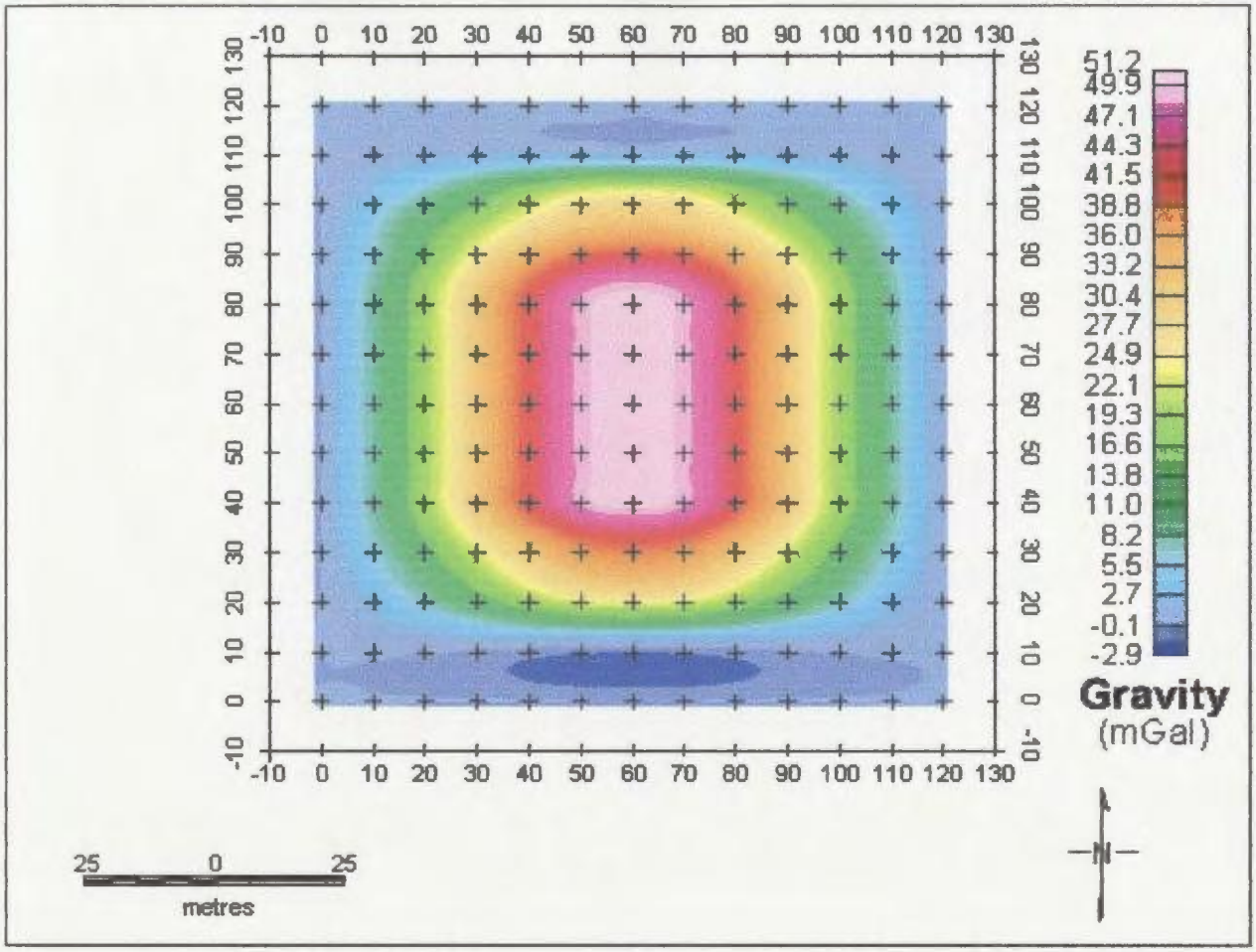

Figure 3.30. Gravity field of synthetic data set.

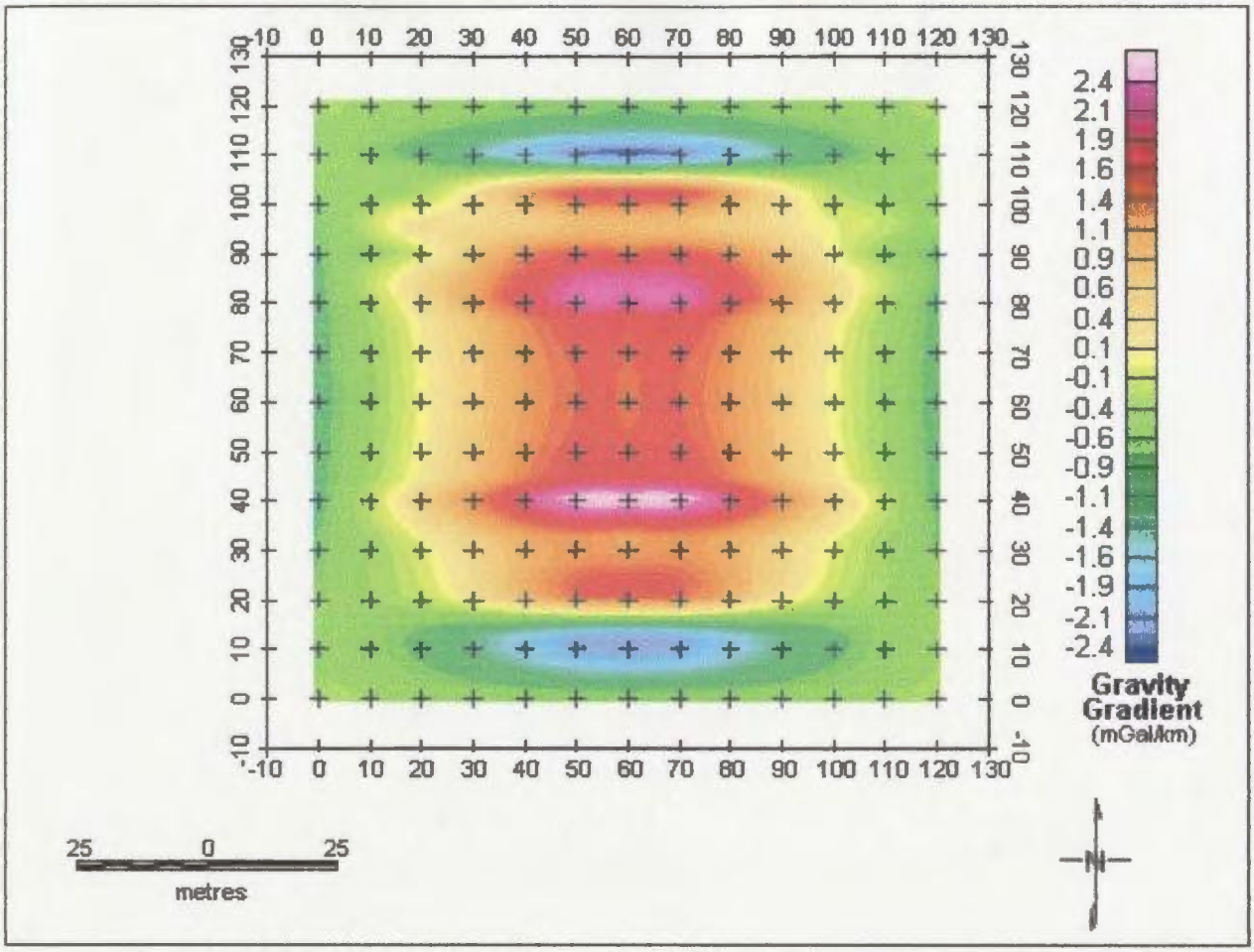

Figure 3.31. Vertical gravity gradient field of synthetic data set.

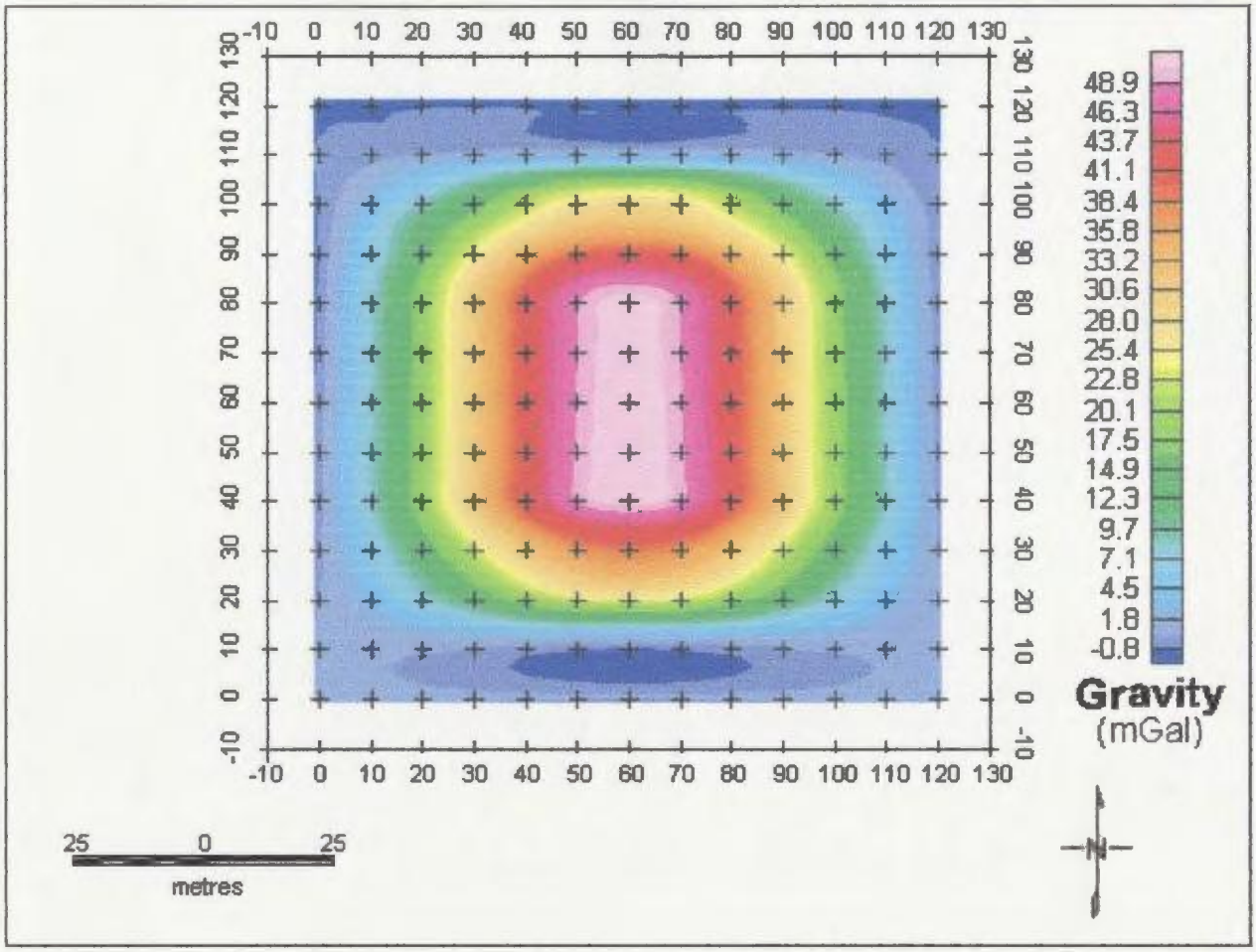

Figure 3.32. Gravity field of synthetic data set with noise (±1 mGal) added.

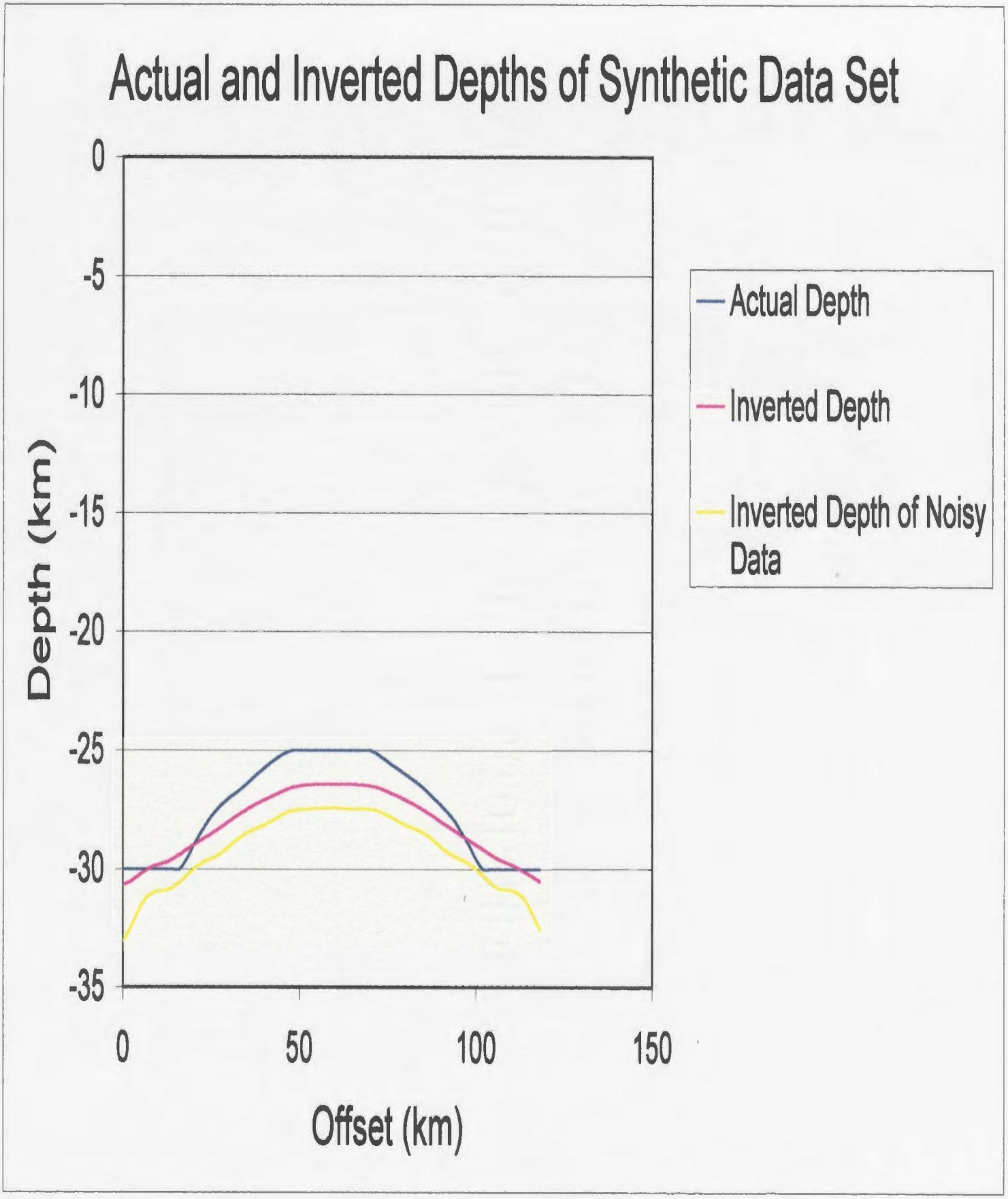

Figure 3.33. Depth profiles taken across the actual and modelled depth maps of the synthetic data set.

CHAPTER 4: INVERSION RESULTS

As discussed in section 3.4.1, the results obtained from the inversion depend on the following parameters: mean Moho depth, Z_m; crustal density, ρ_1, which is a function of surface density, $\rho_\infty(1-\beta)$ and the density decay constant, γ; and mantle density, ρ_2. Estimates of mean Moho depth were derived from spectral analysis of the wavelength filtered data as well as from seismic data collected in the region. Well logs around the Grand Banks yielded surface density estimates while the density decay constant was derived from both the surface density and the asymptotic density of the crust as it approached the Moho. The asymptotic density was obtained from deep seismic refraction measurements and compared with indirect geological information found in the literature (Christensen, 1994; Olhoeft and Johnson, 1994).

A sensitivity analysis was carried out on each of the parameters used in the inversion scheme.

As the input mean depth, Z_m, is increased, the calculated interface depth also increases and vice versa. This relationship between mean and modelled depths is evident in all of the inverted Moho topography profiles of Figures 4.1 through 4.5.

A 20% change in the values of γ and β had no significant effect on the modelled topography. However, a change in the mantle density, ρ_2, of ± 0.1 g/cm^3 resulted in a significant change (25%) in the r.m.s. error between the

observed and calculated gravity fields. No change in the misfit between the gravity gradient fields was observed when any of these parameters was changed.

As β and ρ_2 increase and/or as γ decreases, the density contrast, C, across the Moho increases. An increase in C reduces the modelled relief between the shallowest and deepest Moho topographies. Similarly, an increase in γ and/or a decrease in β and ρ_2 results in a reduced density contrast. A reduction in C increases the modelled relief.

Confidence in the final model can be gauged by assessing the control that each of the input parameters has on it.

4.1 COMPARISON OF GRAVITY AND SEISMIC MODELS

The gravity field was low-pass filtered using five different cut-off wavelengths: $\lambda_c = 50$, 100, 150, 200, and 250 km. For each set of filtered data passed through the inversion program, five different mean depths to Moho were used: $Z_m = 30$, 32.5, 35, 37.5, and 40 km. This was done for a number of reasons. (1) Examining the effects of a range of cut-off wavelengths ensured that the best filter was used. An appropriate filter will increase the likelihood of convergence by removing short-wavelength features of the field. Forcing the inversion operation to fit these short-wavelength features can slow the rate of convergence by increasing the number of iterations required to obtain a model or it can cause the procedure to diverge altogether. It also circumvents any problems caused by

over-filtering or under-filtering the data. (2) Calculating the modelled topography for a range of mean depths accounted for any discrepancy that occurred in estimating the mean depth initially (§ 3.4.1.1). This was done using seismic lines that lie mainly on the periphery of the data set and cross the ocean-continent boundary. This gives a somewhat inaccurate value for mean depth to Moho on the Grand Banks.

The inversion procedure produced an r.m.s. error of 14.3 mGal for the gravity fields and 0.4 mGal/km for the gravity gradient fields after one iteration. Considering the appreciable uncertainty in the gravity field associated with the calculation of the sedimentary basin effects in the modelling procedure, which may be as large as ±31 mGal as noted earlier (§3.2.7), and the inherent noise in the observed field (±2.5 mGal), the large r.m.s. error is within the realm expected. For each subsequent iteration, the calculated depths increased so dramatically that by the third iteration they were incomprehensibly large. The depths oscillated severely about the mean depth. When these depths were gridded (at 5 km spacing) and contoured, they produced 'bulls-eyes' about each grid point. That is, each grid point was surrounded by a closed contour owing to the severe oscillation in depth in all directions. Given this behaviour, the first inversion results were accepted.

Several techniques were tried to obtain better convergence. A mean trend was removed from the depth data, which was then low-pass filtered as discussed earlier. Since the gravity anomaly observed at a point is due to material below and adjacent to it, an attempt was made to smooth the calculated depth

adjustments over the surrounding data points. This failed to improve convergence. Downward continuation of the field to the mean interface (Moho) depth (Parker, 1973; 1974) or to a plane just above the topography (Parker and Huestis, 1974) is another way of improving convergence. This is accomplished through the transfer function of equation (2.25). However, at depths comparable to Moho downward continuation of the field is notoriously unstable.

The sensitivity analysis has shown that decreasing the mantle density, ρ_2, by 0.1 g/cm^3 will decrease the r.m.s. error between the observed and calculated gravity fields by as much as 25%. Reducing ρ_2 was examined as a way to improve convergence. It was found that to minimize the misfit, ρ_2 would have to be reduced to values much less than typical mantle densities. None of the techniques significantly reduced the r.m.s. error. Oscillations of modelled depth after few iterations is not uncommon so it was decided to cease after one iteration (H. Miller, pers. comm.). The best achievable uncertainty in the model is 14.3 mGal. The ideal uncertainty of 2.5 mGal (i.e. the uncertainty in the originating data set; §2.1, §3.4.1.2) was not obtained due to the large uncertainty in the correction for the sedimentary basin effects, which may be as large as ±31 mGal.

For each topographic contour map created from the inverted depths, profiles were extracted along the locations of deep seismic lines so a direct comparison could be made. Refraction line 91-2 and reflection lines 84-3, 85-1, 85-3, and 85-4 were used. Figures 4.1 through 4.5 show profiles comparing the Moho

topography obtained using different mean depths for each low-pass filter used and for each seismic line.

4.1.1 Seismic Control on Moho Depth

It is important to reiterate that the objective here is not to re-process the seismic data but to use the published interpretations for comparison with the resultant gravity models. The location of the Moho on each of these sections relies heavily on the assumptions of the processors of the original seismic data. Their published results are taken to be the best available.

Figure 4.6 shows the locations of the seismic refraction and reflection lines used to estimate mean Moho depth. These profiles were also used for comparison with the inverted gravity models. It is apparent that the regional coverage provided by these lines is very poor. Estimates of Moho depth obtained from these lines, therefore, are not representative of the entire region. For the most part, the seismic studies were conducted to investigate the character of the deep crust across the ocean-continent boundary of the Newfoundland passive margin. Gathering information regarding rift geometry, crustal thinning and extension, and the nature of the ocean-continent transition was the object of these studies. The majority of the region covered by the gravity data, i.e. the inner portion of the continental shelf, has not been investigated by deep seismic surveys (Figure 4.6) and hence, the control on seismic Moho here

is very poor. The poor control on Moho depth is mitigated to some extent by the ensemble average depths derived from spectral analysis (§3.4.1).

4.1.2 Refraction Line 91-2

Refraction line 91-2 (location shown in Figure 4.6) is the only deep seismic line located entirely within the data range. 150 km of Moho was sampled by this survey. The velocity structure along line 91-2 was obtained using five ocean bottom seismometers (OBS) (Marillier, et al., 1994). The upper crust here is typified by large velocity gradients whereas the lower crust is relatively uncomplicated and homogeneous. The Moho shows no topography and has a constant depth of 40 km.

Figures 4.1(a) through 4.1(e) show the seismic and gravity models of Moho topography along line 91-2 for each filtered data set. Models derived from data sets filtered to retain wavelengths greater than 50, 100, 200, and 250 km (Figures 4.1(a), 4.1(b), 4.1(d), and 4.1(e), respectively) show more variation of topography than for the models obtained from $\lambda_c = 150$ km (Figure 4.1(c)). The models for $\lambda_c =$ 150 km show almost no relief at all. With the exception of the $\lambda_c = 150$ km (Figure 4.1(c)) and $\lambda_c = 250$ km models (Figure 4.1(e)), they all show a deepening of the Moho at about 150 km offset. In the models calculated from the long-wavelength data sets ($\lambda_c = 200$ and 250 km; Figures 4.1(d) and 4.1(e)), topographies with alternating mean depths show comparable relief. In

Figure 4.1(d) ($\lambda_c = 200$ km), for example, Moho topography corresponding to 30, 35, and 40 km mean depth have the same appearance whereas models using $Z_m =$ 32.5 and 37.5 km exhibit similar relief.

The gravity model corresponding to $\lambda_c = 100$ km, $Z_m = 37.5$ km (Figure 4.1(b)) demonstrates the best agreement with seismic Moho. Interestingly, models calculated using $Z_m = 40$ km did not correlate with the seismic Moho at any wavelength.

4.1.3 Reflection Line 85-3

Reflection line 85-3 (location shown in Figure 4.6) crosses the northern Jeanne d'Arc and Flemish Pass Basins and the ocean-continent boundary northeast of Flemish Cap. West of Jeanne d'Arc Basin the crust is fairly thick (approximately 40 km) but thins to about 30 km beneath the basin (DeChassy, et al., 1990). The crust continues to thin as it approaches Flemish Pass attaining a thickness of approximately 25 km beneath Flemish Pass Basin. Below Flemish Cap, the crust thickens to about 30 km. Northeast of this continental fragment, the crust gradually thins to 10-15 km as it approaches the ocean-continent boundary.

Figures 4.2(a) through 4.2(e) show the Moho topography along line 85-3 computed from seismic and gravity modelling. Only the eastern 300 km of the line is used in order to match the length of the gravity profile. The seismic Moho shows the crustal thinning below the Jeanne d'Arc Basin (near 100 km offset) and Flemish Pass Basin (near 250 km offset).

When $\lambda_c = 50$ km and $\lambda_c = 100$ km (Figures 4.2(a) and 4.2(b)), the gravity models exhibit a similar topography as the seismic Moho but are displaced westward by as much as 50 km in places. In Figure 4.2(a), for example, there is an eastward dip in seismic Moho at about 150-175 km offset. In the gravity Moho, the dip occurs at about 100-125 km offset. There is virtually no agreement between the gravity and seismic Mohos for the $\lambda_c = 200$ km and $\lambda_c = 250$ km models (Figures 4.2(d) and 4.2(e)). The removal of wavelengths less than 200 km clearly results in a loss of detailed information. The gravity models corresponding to $\lambda_c = 150$ km (Figure 4.2(c)) exhibit the same general relief as the seismic Moho but the amplitudes of the undulations are greatly diminished. The modelled Mohos possess the same form for each input mean depth used, demonstrating the consistency of the inversion procedure.

4.1.4 Reflection Line 85-4

Reflection line 85-4 (location shown in Figure 4.6) traverses the Jeanne d'Arc and Carson Basins, then crosses the ocean-continent boundary east of the Grand Banks. The sediments of the Carson Basin reduce the transmission of seismic energy and as a result there is poor control on Moho topography beneath the continental slope east of the basin (Keen and de Voogd, 1988). Fortunately, this is outside the area covered by the gravity data. Below the Bonavista Platform (west of the Jeanne d'Arc Basin) the crust is almost 40 km thick. The

Moho beneath the basin is pulled up giving a local crustal thickness of about 30 km. Under Carson Basin, the crust thickens once again.

Figures 4.3(a) to 4.3(e) show seismic and gravity models of Moho topography along line 85-4 for each set of wavelength filtered gravity data. The rise of Moho beneath the Jeanne d'Arc Basin is seen on the seismic Moho at an offset of about 75 km. With the exception of the $\lambda_c = 50$ km model (Figure 4.3(a)), all of the gravity models exhibit a decrease in depth that roughly coincides with the decrease in Moho depth beneath Jeanne d'Arc Basin. The topographic models for $\lambda_c = 50$ km are nearly the reverse of the seismic model, i.e. a decrease in depth of the seismic Moho corresponds to an increase in that of the gravity Moho and vice versa.

In general, because the seismic Moho along line 85-4 exhibits long-wavelength relief, the models derived from the long-wavelength gravity fields ($\lambda_c \geq 150$ km (Figures 4.3(c), 4.3(d), and 4.3(e)) agree best. Of these models, the mean depth that is most compatible with the seismic Moho is $Z_m = 32.5$ km.

4.1.5 Reflection Line 84-3

The most prominent feature revealed on reflection line 84-3 (see Figure 4.6 for location) is a set of subhorizontal midcrustal reflections. They are interpreted as evidence of a zone of décollement between 6 and 10 km depth related to Mesozoic extension (Keen, et al., 1987a; Keen and de Voogd, 1988). Intense water-bottom multiples present in the data obscured the signal from deep crustal

reflectors including the Moho (Keen, et al., 1987a). Therefore, reliable depth estimates for the Moho were only obtained from the western 70 km of the line.

Figures 4.4(a) to 4.4(e) show the seismic and gravity models of Moho. The short section of seismic Moho appears to display a long-wavelength character. Progressing eastward, it steps from about 39 km to 37 km depth. This step is evident in all of the gravity models regardless of filter cut-off. The topographic profile produced using $Z_m = 35$ km most closely resembles the seismic Moho, particularly for the data filtered with $\lambda_c = 150$ km (Figure 4.4(c)).

4.1.6 Reflection Line 85-1

Reflection line 85-1 (location is shown In Figure 4.6) crosses both the Whale and Horseshoe Basins before meeting reflection line 85-2 on the southeastern Grand Banks. The upper crust is relatively non-reflective along this line whereas the lower crust adjacent to the basins is fairly reflective (DeChassy, et el., 1990). Below the basins, deep reflections are muted by the thick sedimentary wedges. Moho is imaged at the western end of the line where it climbs eastward from 37.5 km to 35 km. Definitive reflections from Moho are not picked up again until the far eastern end of the line which is beyond the extent of available gravity data.

Figures 4.5(a) through 4.5(e) show the topographic profiles derived from the gravity and seismic data. There is far too little seismic Moho to make a meaningful comparison. Most of the models did not even detect the increase in

Moho depth. However, $\lambda_c = 150$ km, $Z_m = 37.5$ km (Figure 4.5(c)) shows the most promise.

4.2 RESULTANT MOHO TOPOGRAPHY

The r.m.s. errors between the observed and calculated gravity and gravity gradient fields for all cut-off wavelengths and mean depths used are shown in Figures 4.7(a) and 4.7(b). The misfit between the observed and calculated gravity fields decreased with increasing mean depth, however, there was no change in this misfit as the cut-off wavelength varied. Misfit between the observed and calculated gravity gradient fields decreased with increasing cut-off wavelength but did not change with mean depth.

Overall, the models generated from the gravity field filtered with cut-off wavelength of 150 km showed the best agreement with the seismic models. Analysis of the misfit between observed and calculated gravity gradient fields (Figure 4.7(b)) reveals a local minimum at $\lambda_c = 150$ km. Although the r.m.s. error continues to decrease, the loss of information at higher cut-off wavelengths is too great. The compromise between the fitting of detailed Moho topography and minimizing the r.m.s. error is most acceptable using $\lambda_c = 150$ km.

Guspi (1992) showed that a low-pass cut-off frequency equal to $0.4/\Delta Z_{\max}$ improves the chance of convergence, where $\Delta Z_{\max}$ refers to the maximum topographic relief of the interface. Assuming a maximum relief of 10 km here, a

cut-off frequency of 0.04 km^{-1} is obtained. This corresponds to a cut-off wavelength of approximately 150 km. Therefore, removing wavelengths less than 150 km should improve convergence.

Gravity fields consisting of wavelengths less than 250 km generally show the effects of structures on a continental scale (Kane and Godson, 1985). In mapping undulations in the Moho beneath the Paris Basin, Lefort and Agarwal (1996) low-pass filtered the local gravity field using a cut-off wavelength of 150 km. They noted that the effects of shallow features were no longer observed and concluded that the long-wavelength signal was due primarily to Moho undulations.

Figure 4.7(a) suggests that the r.m.s. misfit decreases linearly with increasing mean depth. It would make sense then, to select a Moho topography model that used a large mean depth. Comparison of seismic and gravity topography models along reflection lines 84-3, 85-3, 85-4, and 85-1, i.e. lines that lie along the periphery of the data set, suggest a mean depth of 35 km. The modelled topography along refraction line 91-2 correlates best with a mean depth of 37.5 km. Therefore, Z_m = 37.5 km was chosen as the model that most closely represents Moho topography on the Grand Banks.

The largest source of uncertainty associated with modelling the Moho topography here is in the densities used to model the sedimentary basins. Using the parameters that gave the best model (i.e. λ_c = 150 km, Z_m = 37.5 km), the gravity field data derived from varying the basin density contrasts by ±10% and ±25% were inverted in an effort to estimate the uncertainty in the final model.

Figures 4.8 through 4.12 show the variability in Moho depth along profiles coinciding with each of the seismic refraction and reflection lines used for earlier comparison. The inverted Moho depth is very erratic in response to changes in density contrast along reflection line 85-1 (Figure 4.12). The remainder of the profiles show good agreement in both the amplitude and wavelength of the Moho topography. Reflection lines 85-3 and 85-1 (Figures 4.9 and 4.12), which lie directly over the Jeanne d'Arc and Whale Basins (see Figure 3.26 for location), respectively, show the most variability. The other lines, which either cross a rift basin at its edge (e.g. reflection lines 85-4 (Figure 4.10) and 84-3 (Figure 4.11)) or do not cross one at all (e.g. refraction line 91-2 (Figure 4.8)) show much less variation. The most apparent change is the lateral variation of Moho depth rather than the expected vertical variation. For example, Figure 4.10 shows that, at an offset along profile of 120 km, the present model indicates a depth to Moho of 36 km. Decreasing the density contrast in the underlying Jeanne d'Arc Basin by 10% changes the Moho depth at 120 km offset to 36.5 km, effectively shifting the Moho westward to 115 km offset. Similar variation in Moho depth is seen for all other changes in basin density contrast. The maximum uncertainty in the inverted Moho depths is 35 km laterally (as seen at 36.5 km depth on line 85-3; Figure 4.9) and 1 km vertically (as seen at 65 km offset on line 85-3; Figure 4.9). That is, the wavelength of the topography may be inaccurate by as much as 70 km while its amplitude is uncertain by about ± 1 km. This seems anomalously low considering that 1) the uncertainty assigned to the modelled basin gravity effect

is ±31 mGal and 2) the best achievable r.m.s. error for the inversion is 14.3 mGal.

Figure 4.13 shows the contour map of modelled depth to Moho for the Grand Banks region using a mean depth of 37.5 km and a wavelength filter of 150 km. This will be discussed further in Chapter 5. Figure 4.14 shows the residual gravity field for the region. This is the observed gravity field (corrected for the gravity effects of the sediments) minus the gravity effect computed for the Moho topography model obtained from the inversion. The three most conspicuous anomalies are the gravity minimum over the northern Jeanne d'Arc Basin (near 1150000 E, 5250000 N UTM), the positive region west of the Jeanne d'Arc Basin (about 1025000 E, 5250000 N UTM), and the moderate positive anomaly (60-70 mGal) above the Avalon Peninsula (from approximately 500000 to 700000 E, 5275000 to 5400000 N UTM). The positive gravity residual west of Jeanne d'Arc Basin results from inverting on a small flanking lobe created by the filtering process. It does not correspond to any real undulation in the Moho. The negative residual over the northern Jeanne d'Arc Basin is symptomatic of the poor control on basin density. The wells used to determine an average density for Jeanne d'Arc Basin (Bonanza M-71, Hibernia G-55A, Spoonbill C-30) are widely scattered around the basin's edges.

The majority of the residuals are between ±30 mGal. The r.m.s. error between the observed and calculated gravity fields obtained during the inversion process is 14.3 mGal. If the mean value is taken to be 0 mGal then, for large data sets, the standard deviation of the residual gravity field data is equivalent to the r.m.s.

error (Miller, 1978). In an normal, or Gaussian, distribution of data values 68% of the data lies within ±1 standard deviation of the mean while 95% of the values lie within ±2 standard deviations of the mean. Therefore, 95% of the gravity values lie within 30 mGal (i.e. twice the standard deviation) of the mean, that is, in the ±30 mGal range. This means that less than 5% of the residual gravity values exhibit an anomalously large residual. Note that this includes the most noticeable feature of the residual field, the positive anomaly associated with the flank of the Jeanne d'Arc Basin.

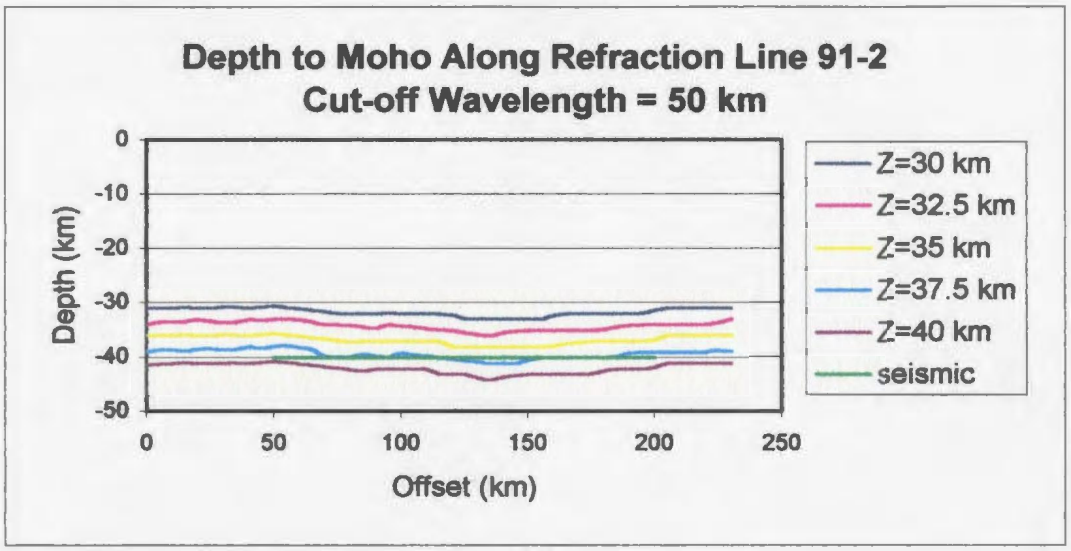

(a)

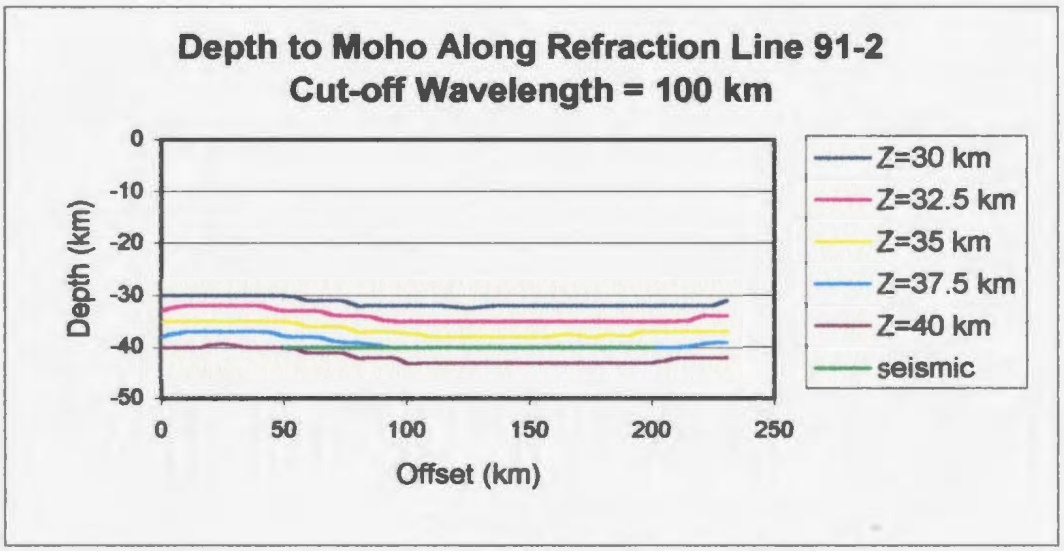

(b)

Figure 4.1. Modelled Moho topography along seismic refraction line 91-2 (line location is shown in Figure 4.6) from seismic and gravity data for a range of input mean depths. The gravity data was filtered to remove wavelengths less than (a) 50 km, (b) 100 km, (c) 150 km, (d) 200 km, and (e) 250 km.

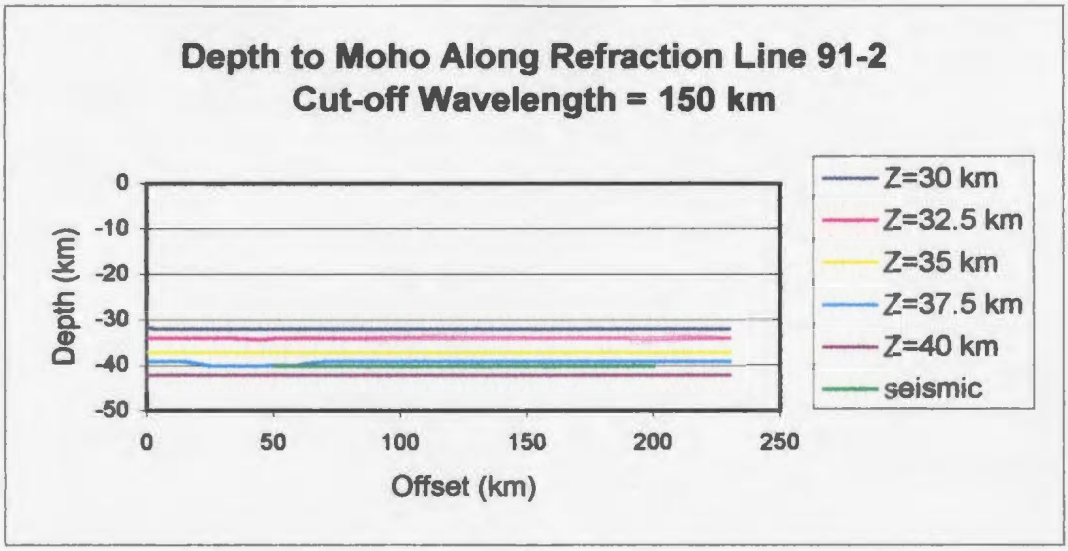

(c)

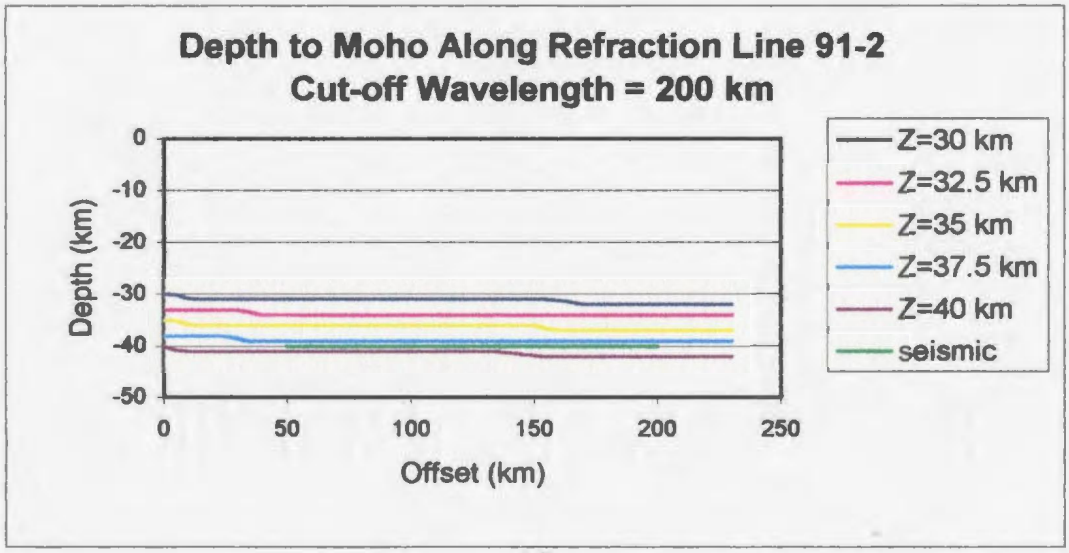

(d)

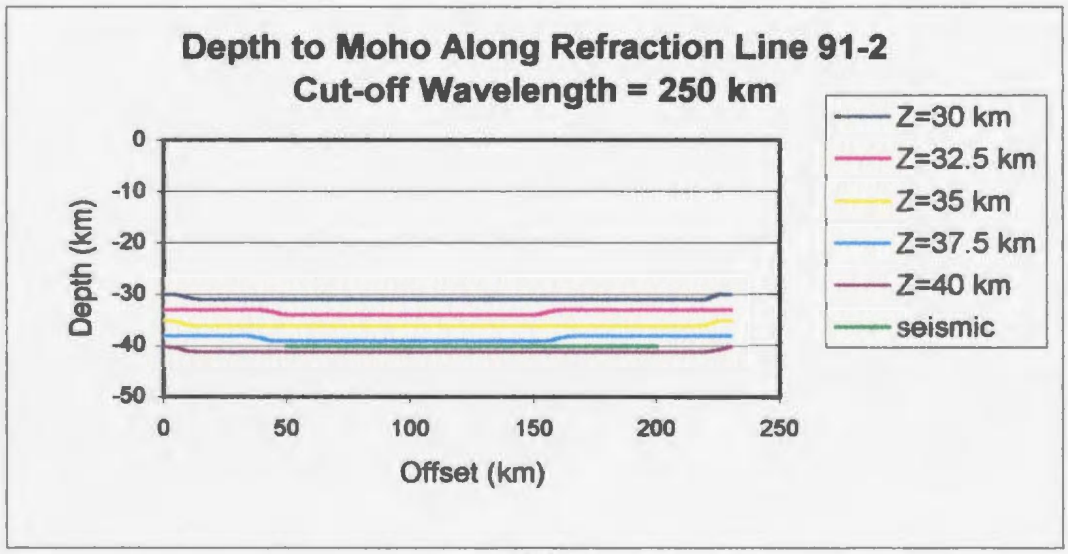

(e)

Figure 4.1. (continued).

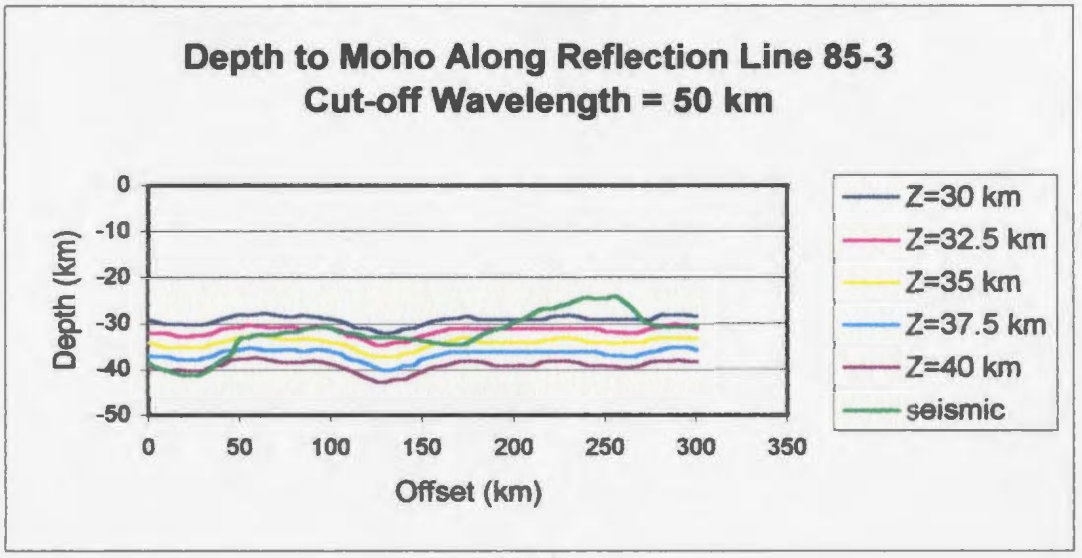

(a)

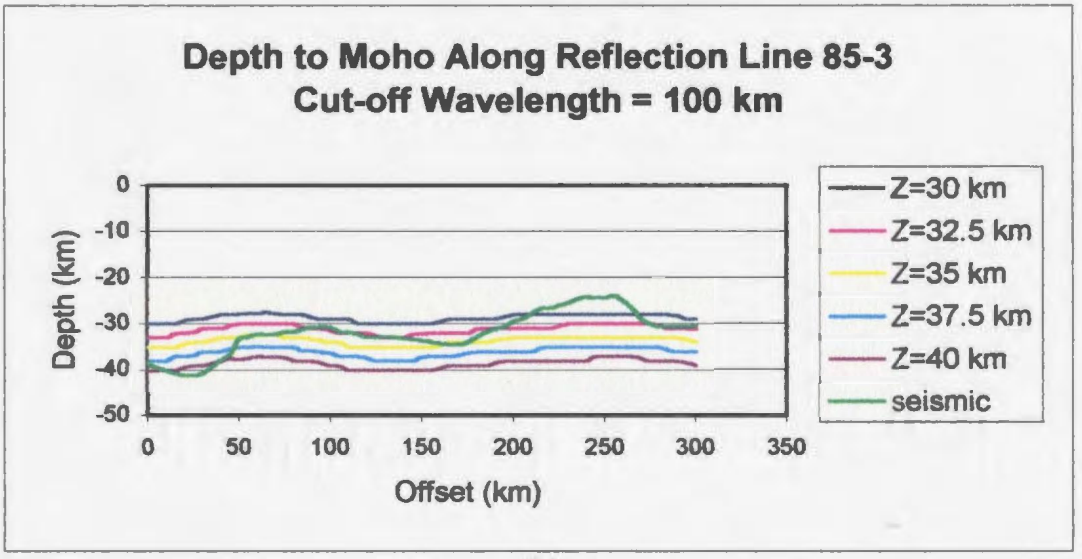

(b)

Figure 4.2. Modelled Moho topography along seismic reflection line 85-3 (line location is shown in Figure 4.6) from seismic and gravity data for a range of input mean depths. The gravity data was filtered to remove wavelengths less than (a) 50 km, (b) 100 km, (c) 150 km, (d) 200 km, and (e) 250 km.

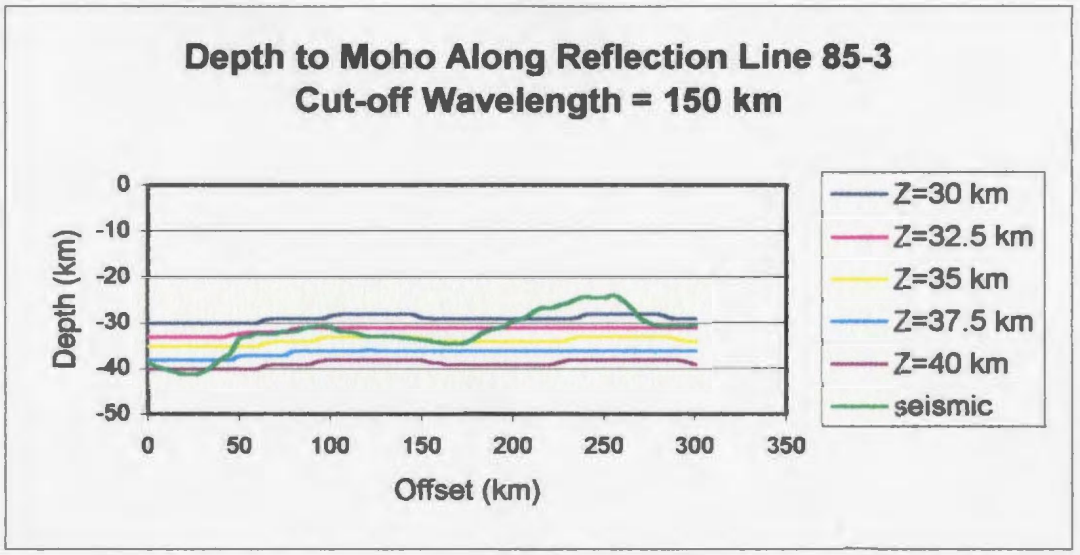

(c)

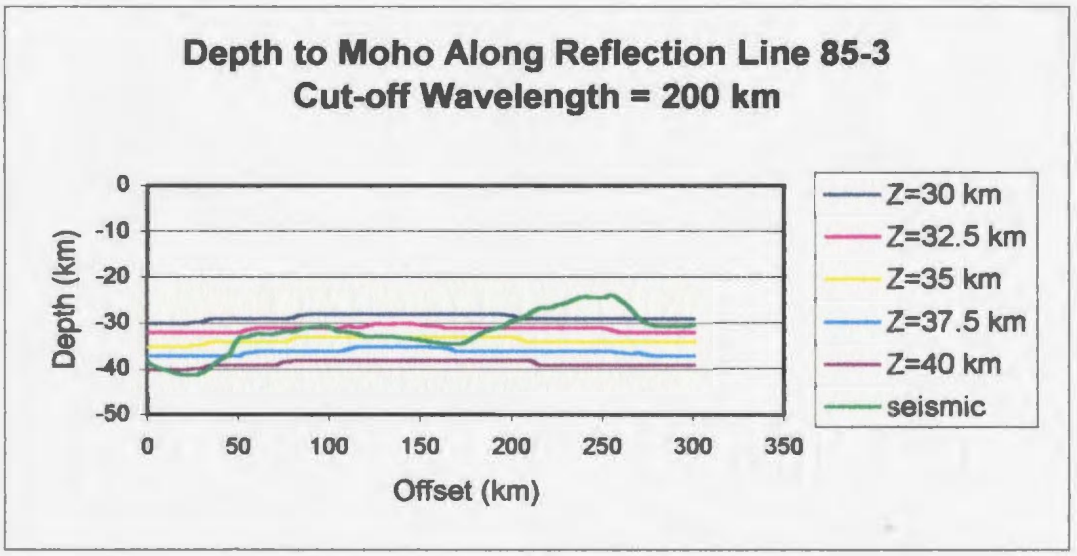

(d)

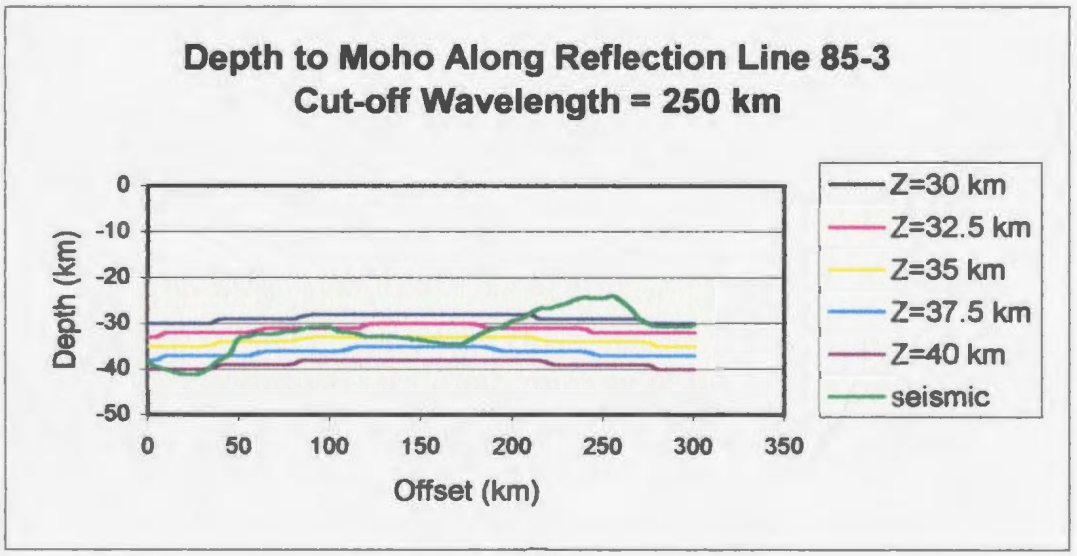

(e)

Figure 4.2. (continued).

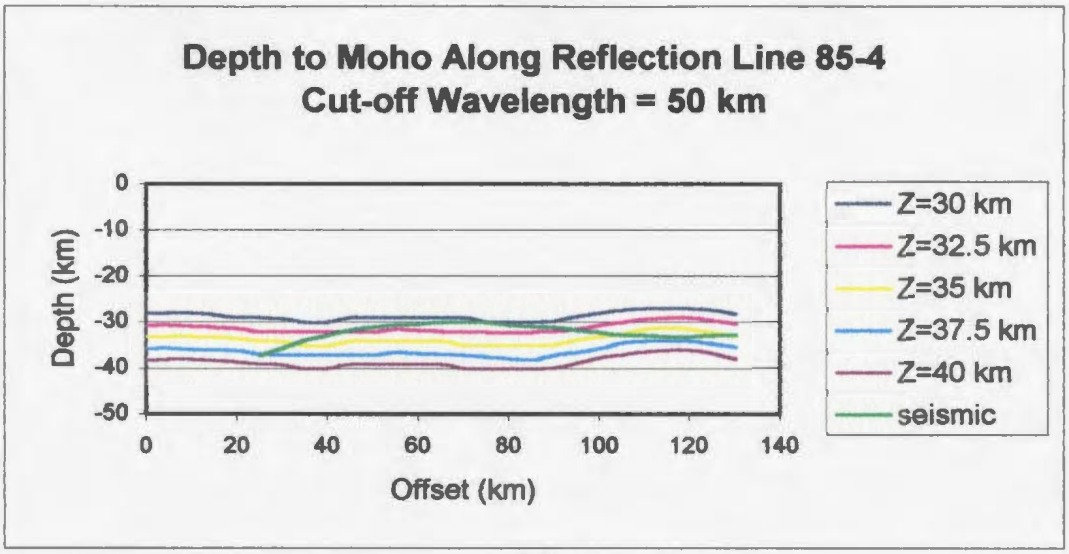

(a)

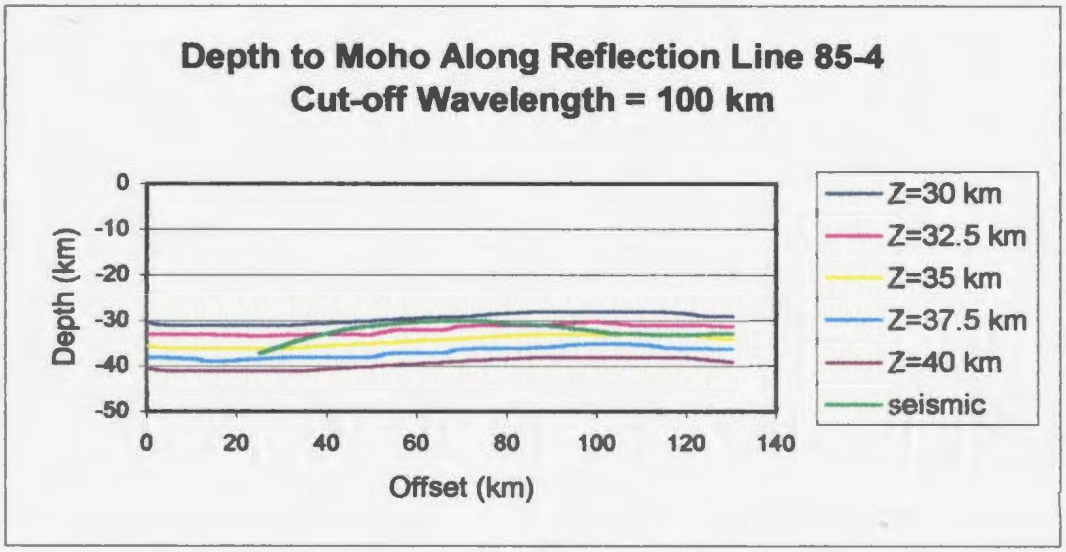

(b)

Figure 4.3. Modelled Moho topography along seismic reflection line 85-4 (line location is shown in Figure 4.6) from seismic and gravity data for a range of input mean depths. The gravity data was filtered to remove wavelengths less than (a) 50 km, (b) 100 km, (c) 150 km, (d) 200 km, and (e) 250 km.

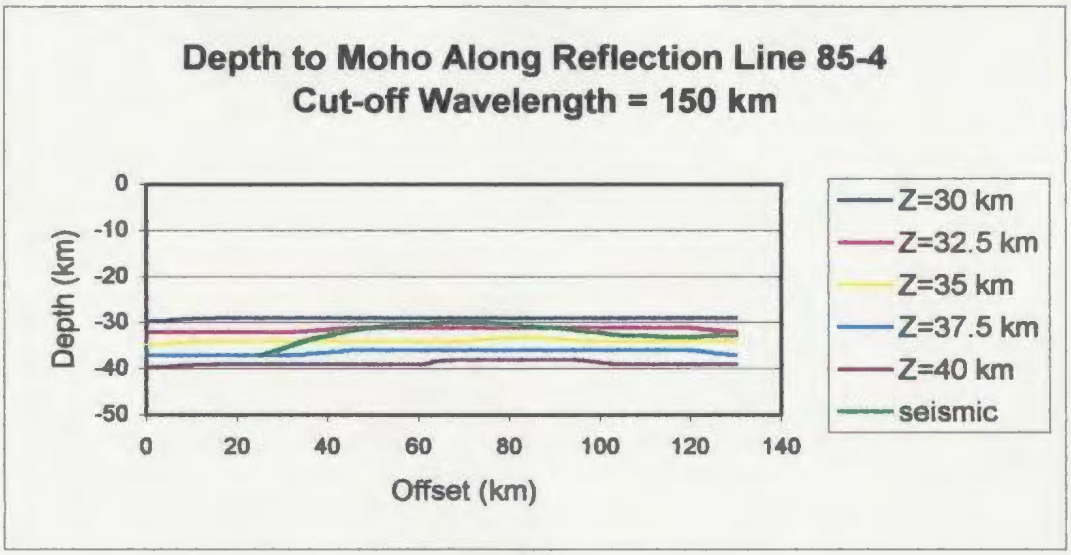

(c)

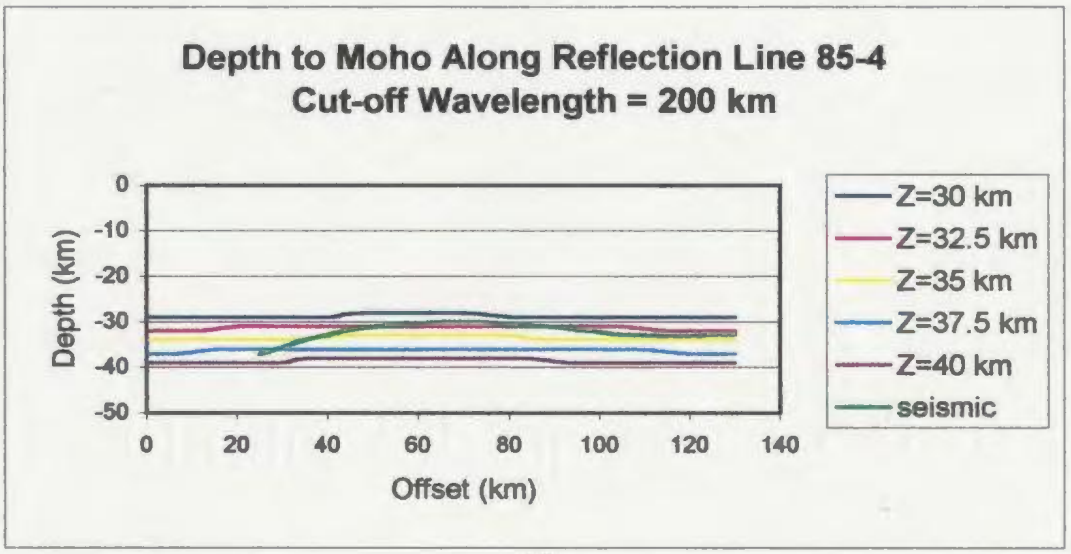

(d)

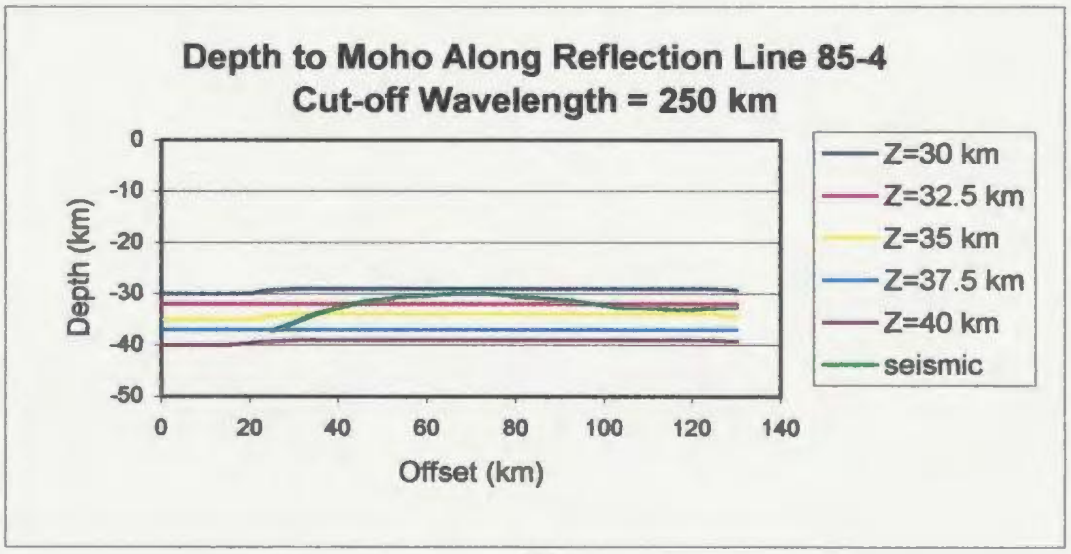

(e)

Figure 4.3. (continued).

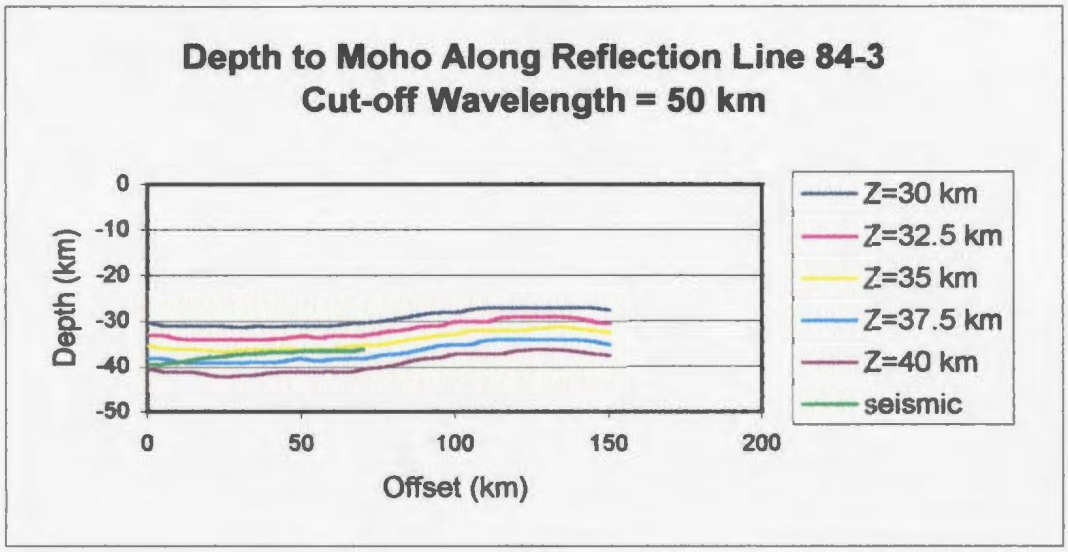

(a)

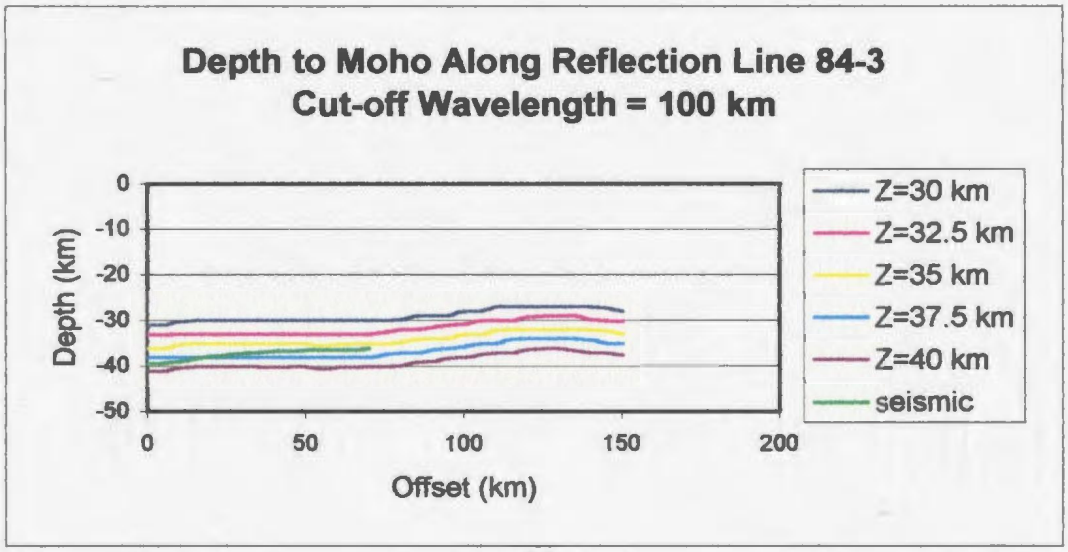

(b)

Figure 4.4. Modelled Moho topography along seismic reflection line 84-3 (line location is shown in Figure 4.6) from seismic and gravity data for a range of input mean depths. The gravity data was filtered to remove wavelengths less than (a) 50 km, (b) 100 km, (c) 150 km, (d) 200 km, and (e) 250 km.

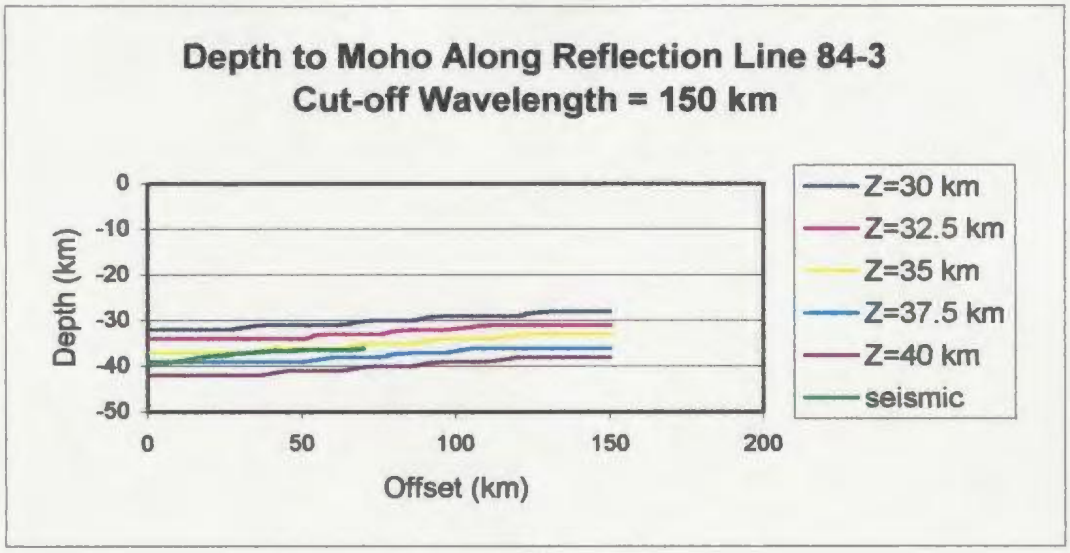

(c)

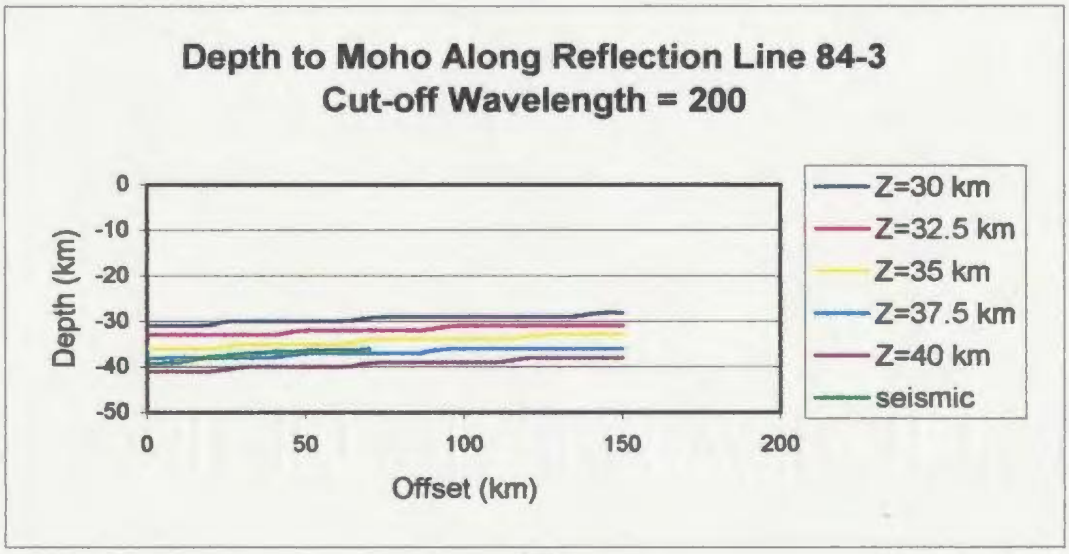

(d)

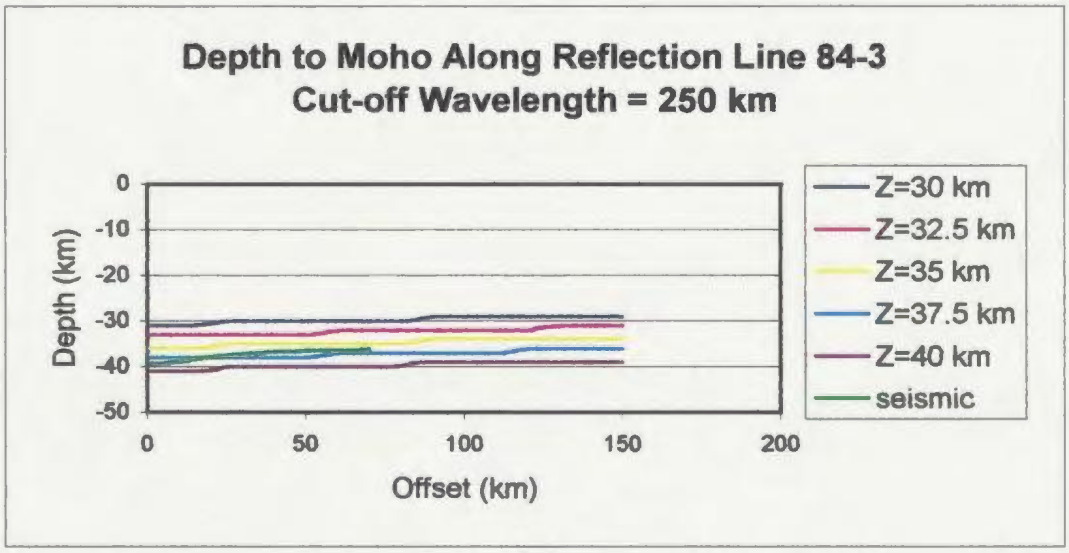

(e)

Figure 4.4. (continued).

(a)

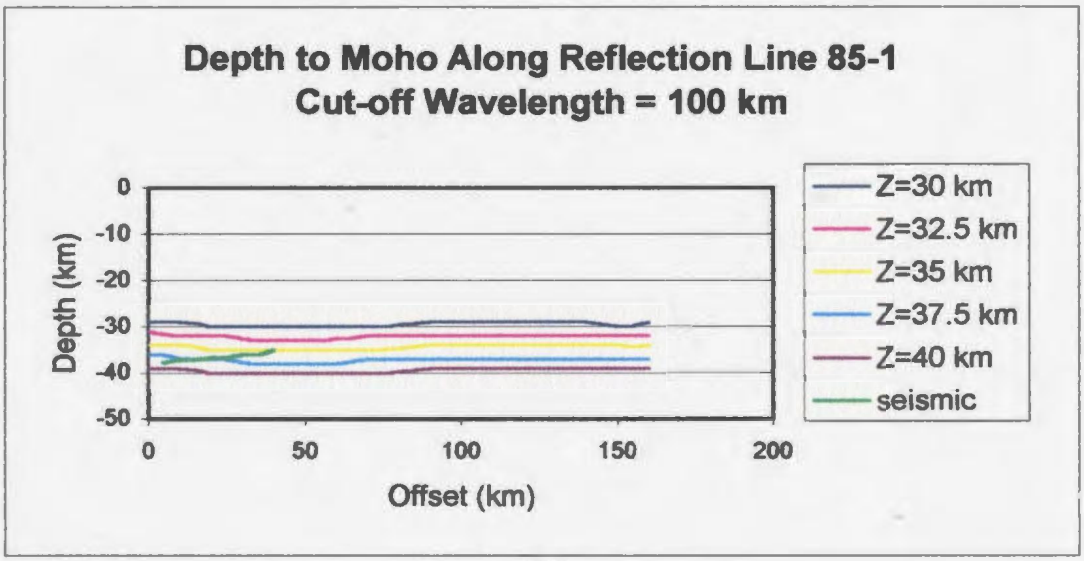

(b)

Figure 4.5. Modelled Moho topography along seismic reflection line 85-1 (line location is shown in Figure 4.6) from seismic and gravity data for a range of input mean depths. The gravity data was filtered to remove wavelengths less than (a) 50 km, (b) 100 km, (c) 150 km, (d) 200 km, and (e) 250 km.

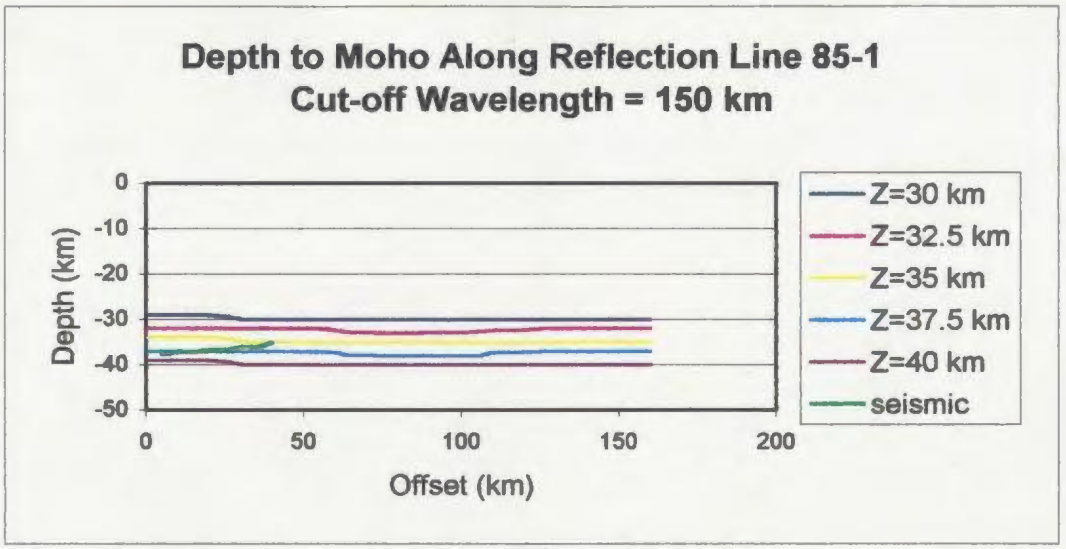

(c)

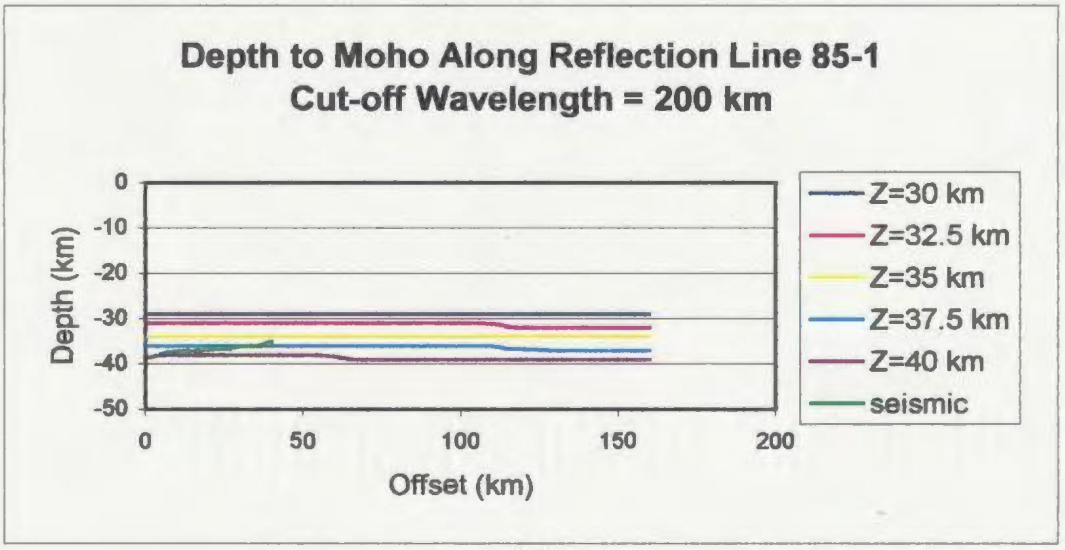

(d)

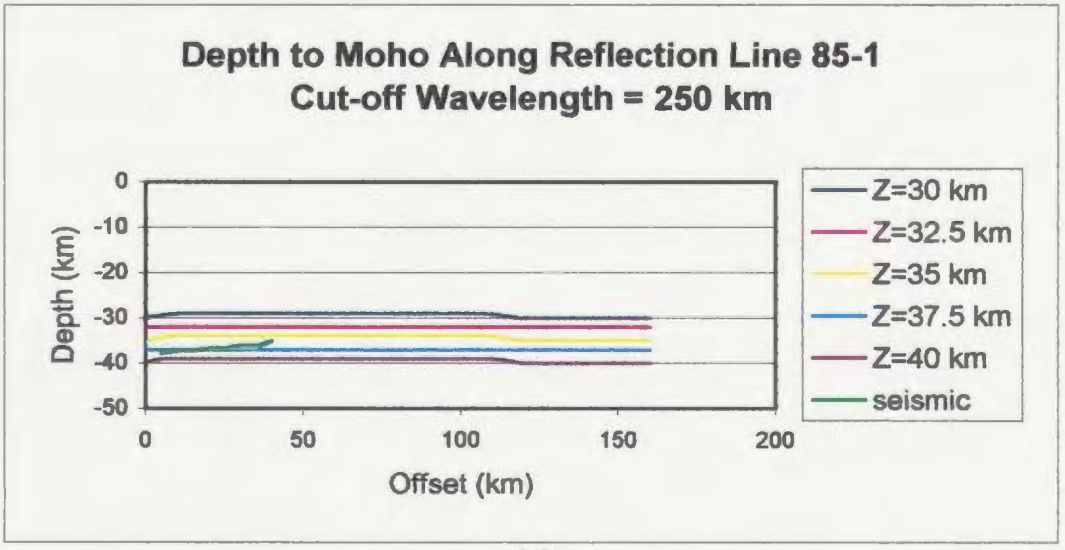

(e)

Figure 4.5. (continued).

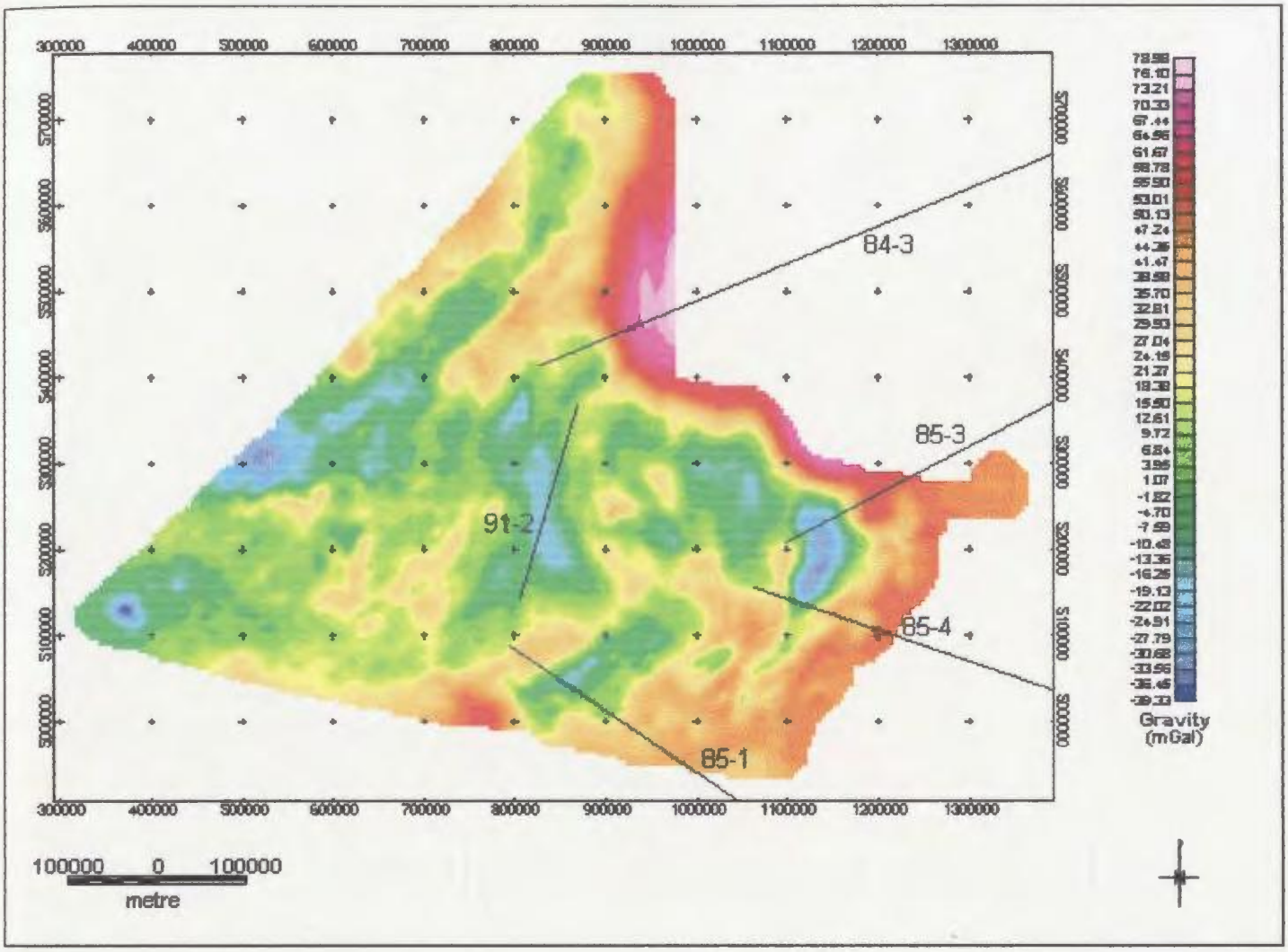

Figure 4.6. Location of seismic reflection and refraction profiles used in model comparison.

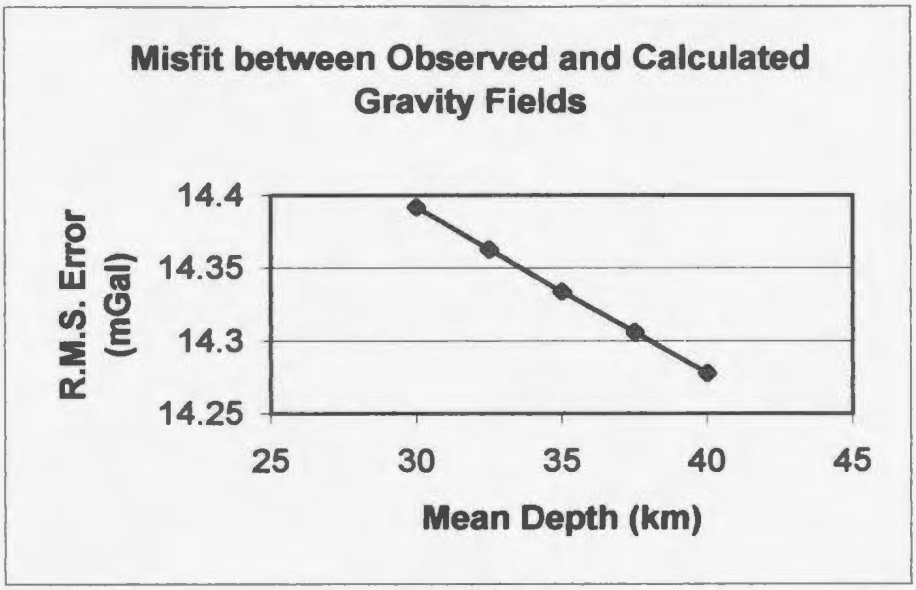

(a)

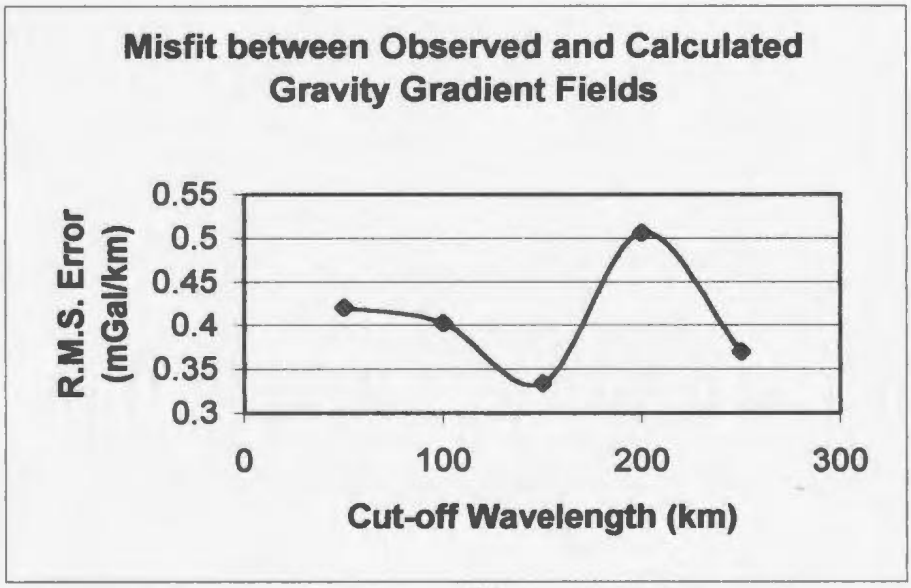

(b)

Figure 4.7. (a) Misfit between observed and calculated gravity fields for 3-D inversion program for all cut-off wavelengths. (b) Misfit between observed and calculated gravity gradient fields for 3-D inversion program for all mean depths.

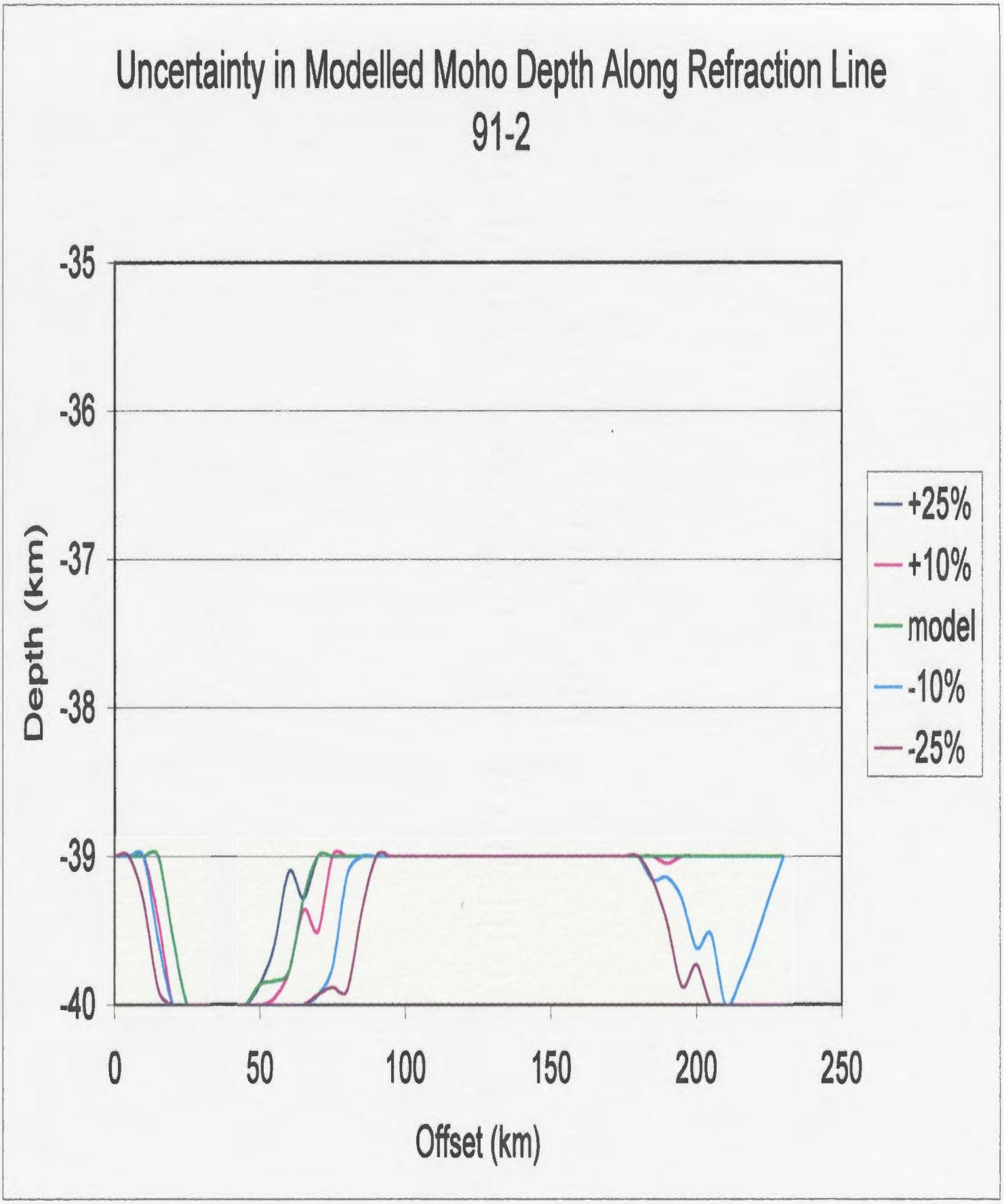

Figure 4.8. Uncertainty in modelled Moho depth along Refraction Line 91-2.

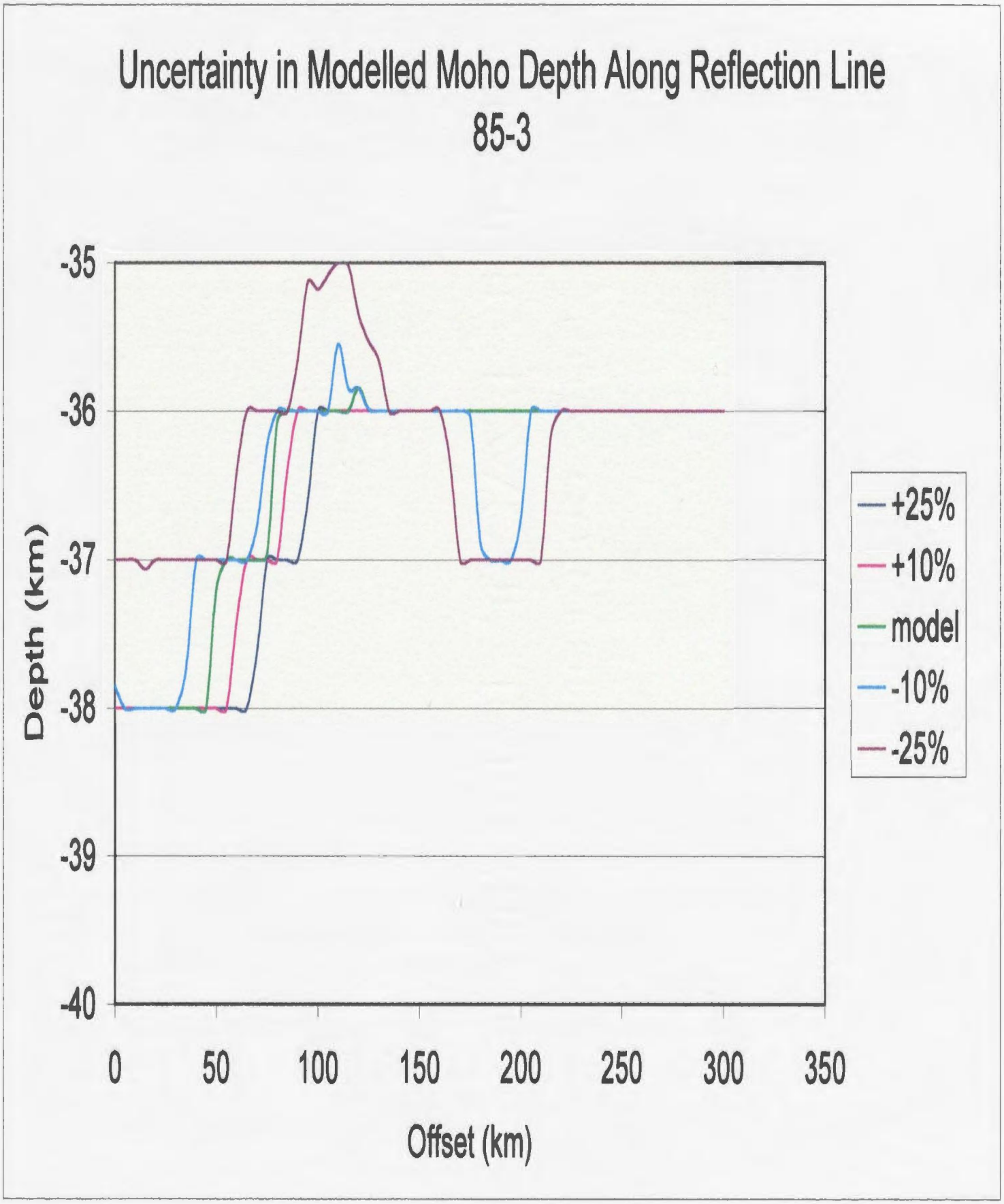

Figure 4.9. Uncertainty in modelled Moho depth along Reflection Line 85-3.

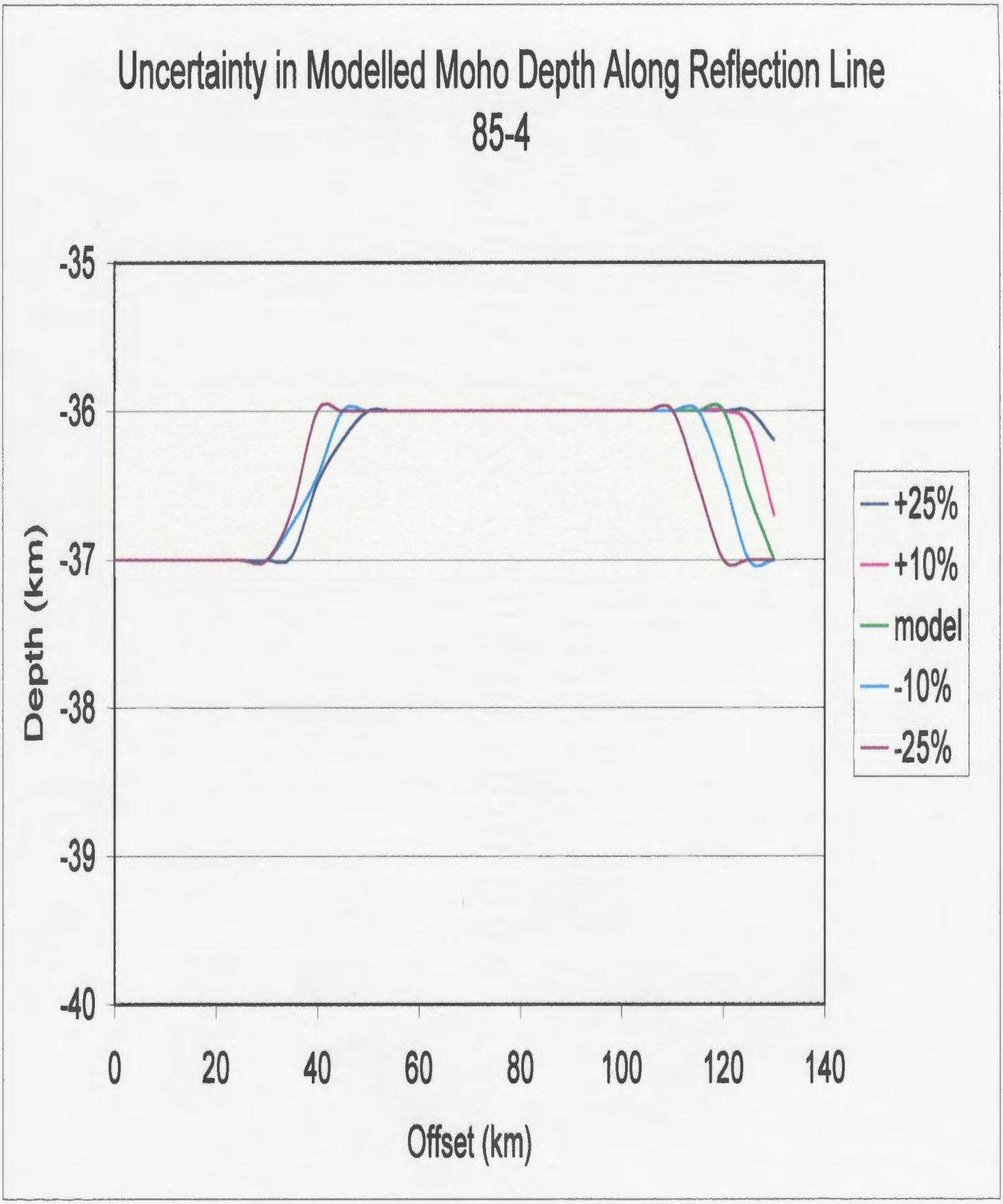

Figure 4.10. Uncertainty in modelled Moho depth along Reflection Line 85-4.

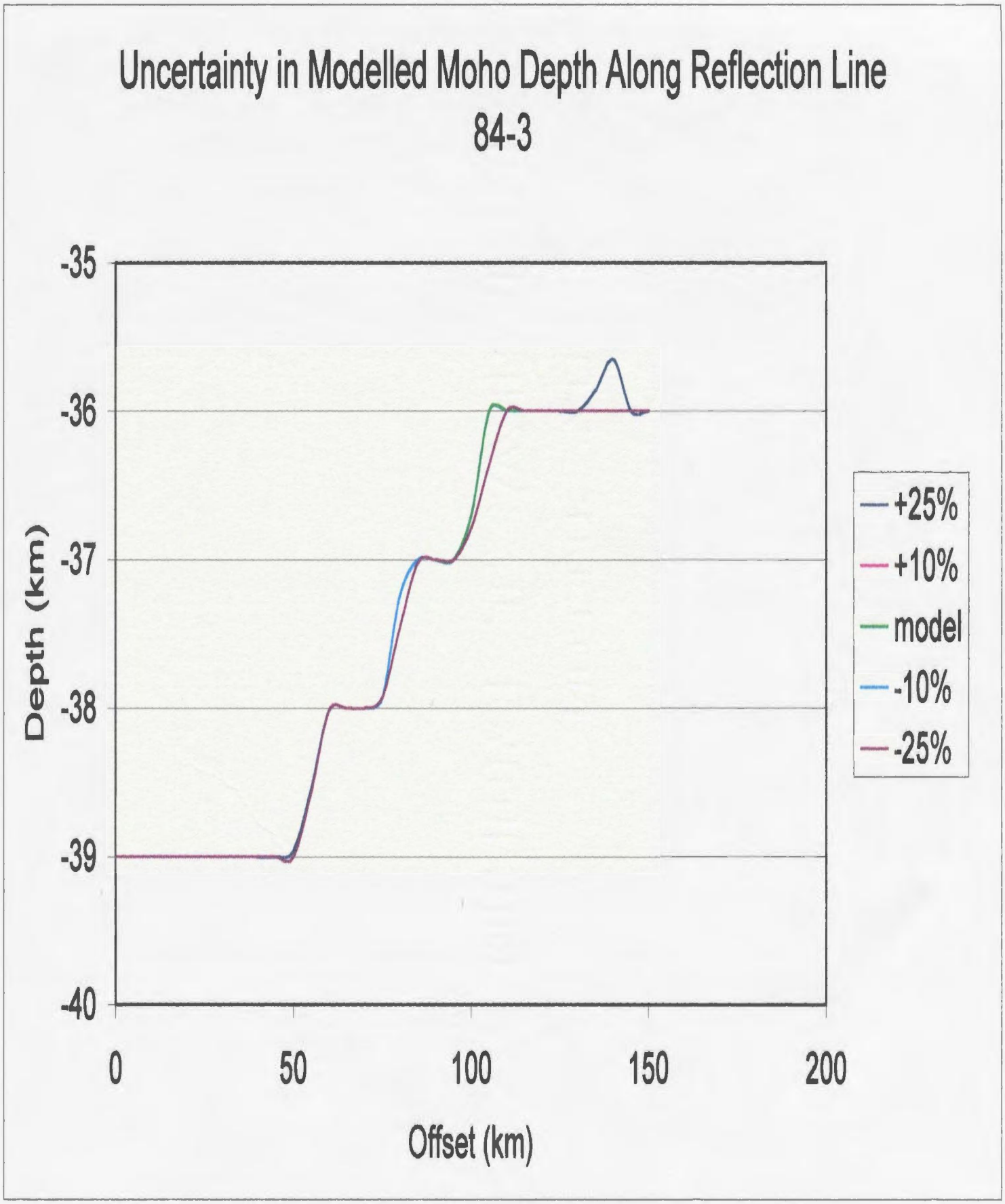

Figure 4.11. Uncertainty in modelled Moho depth along Reflection Line 84-3.

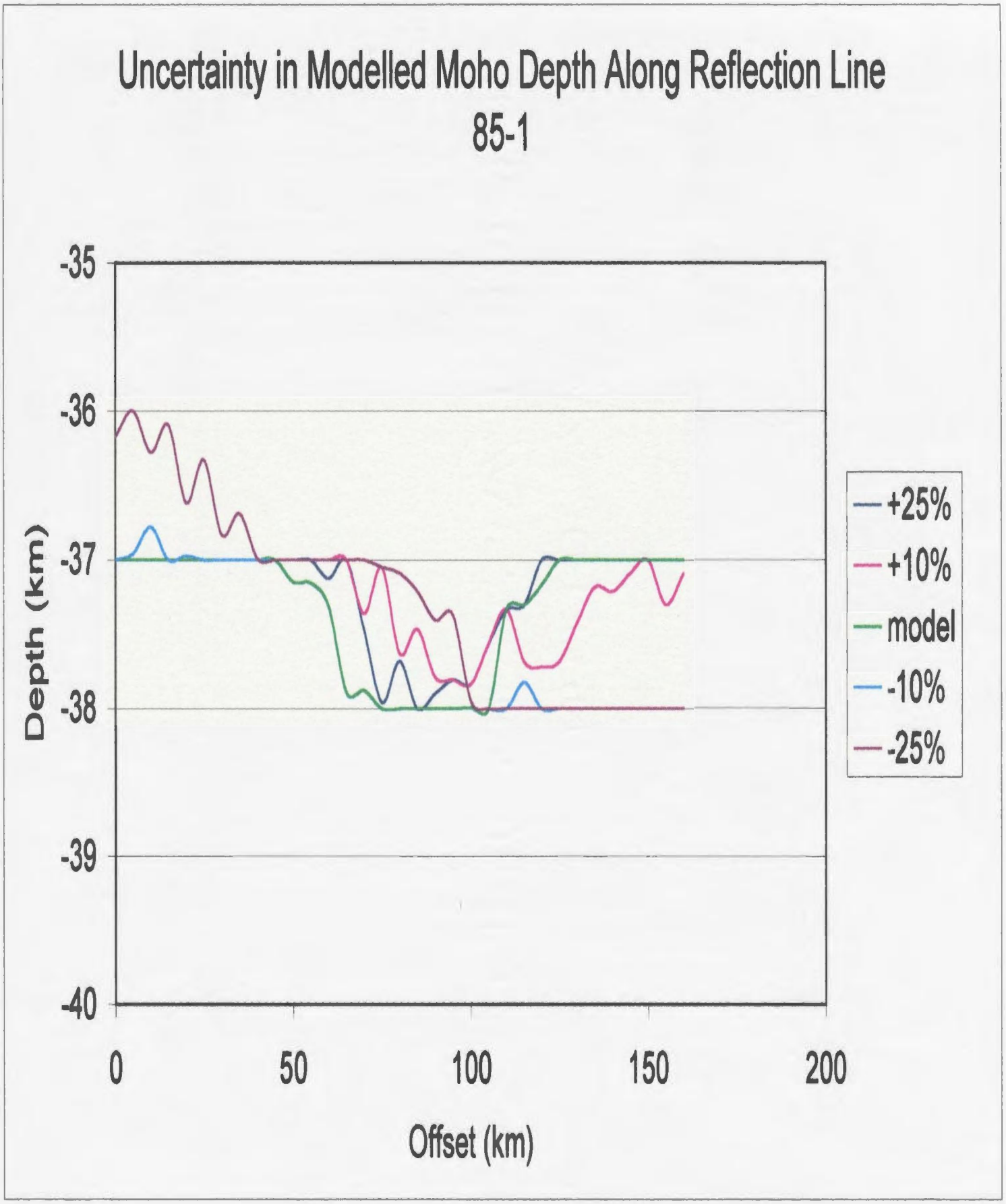

Figure 4.12. Uncertainty in modelled Moho depth along Reflection Line 85-1.

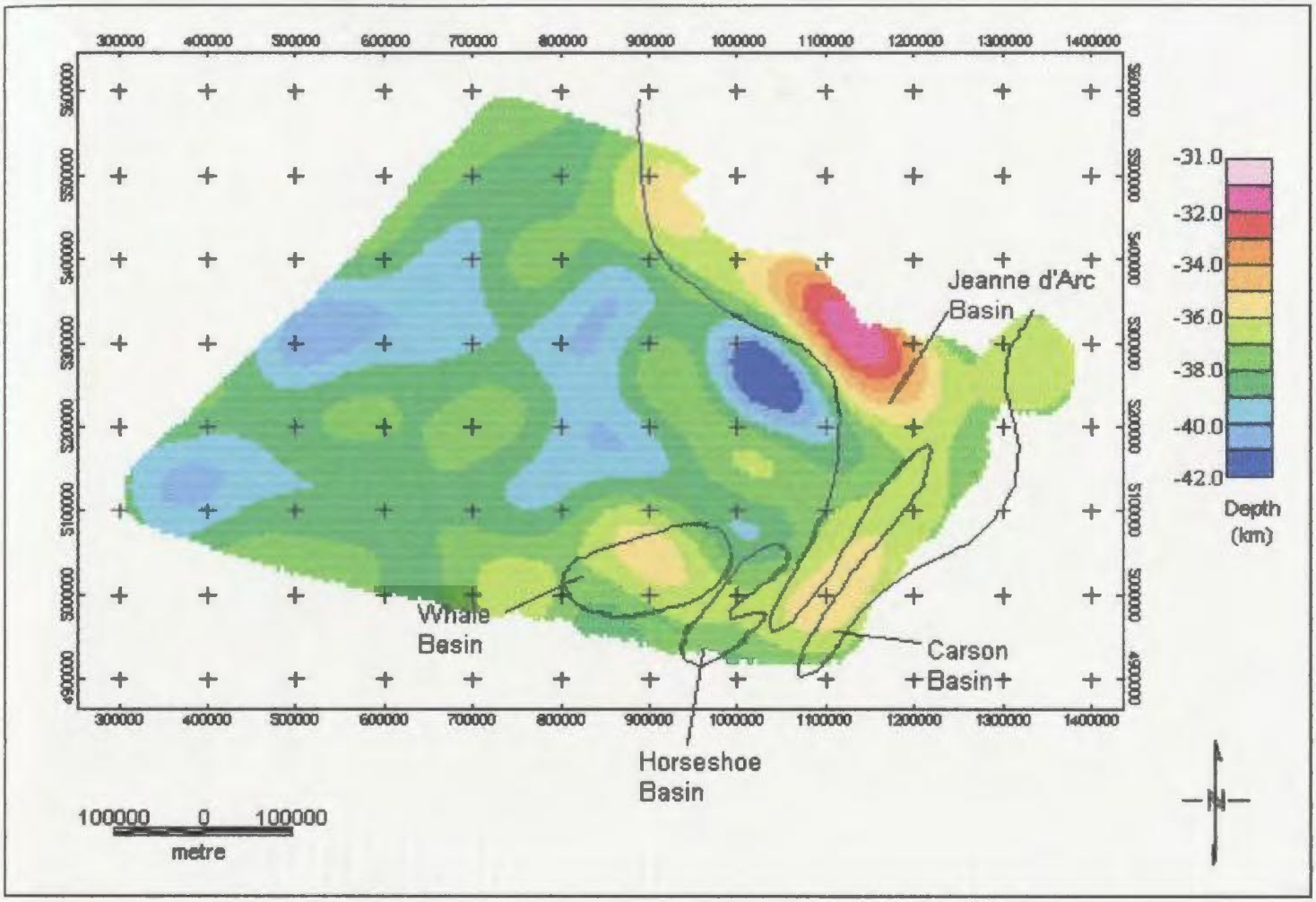

Figure 4.13. Modelled Moho topography of the Grand Banks region. The approximate locations and shapes of the Grand Banks basins are shown. The contour interval is 1 km.

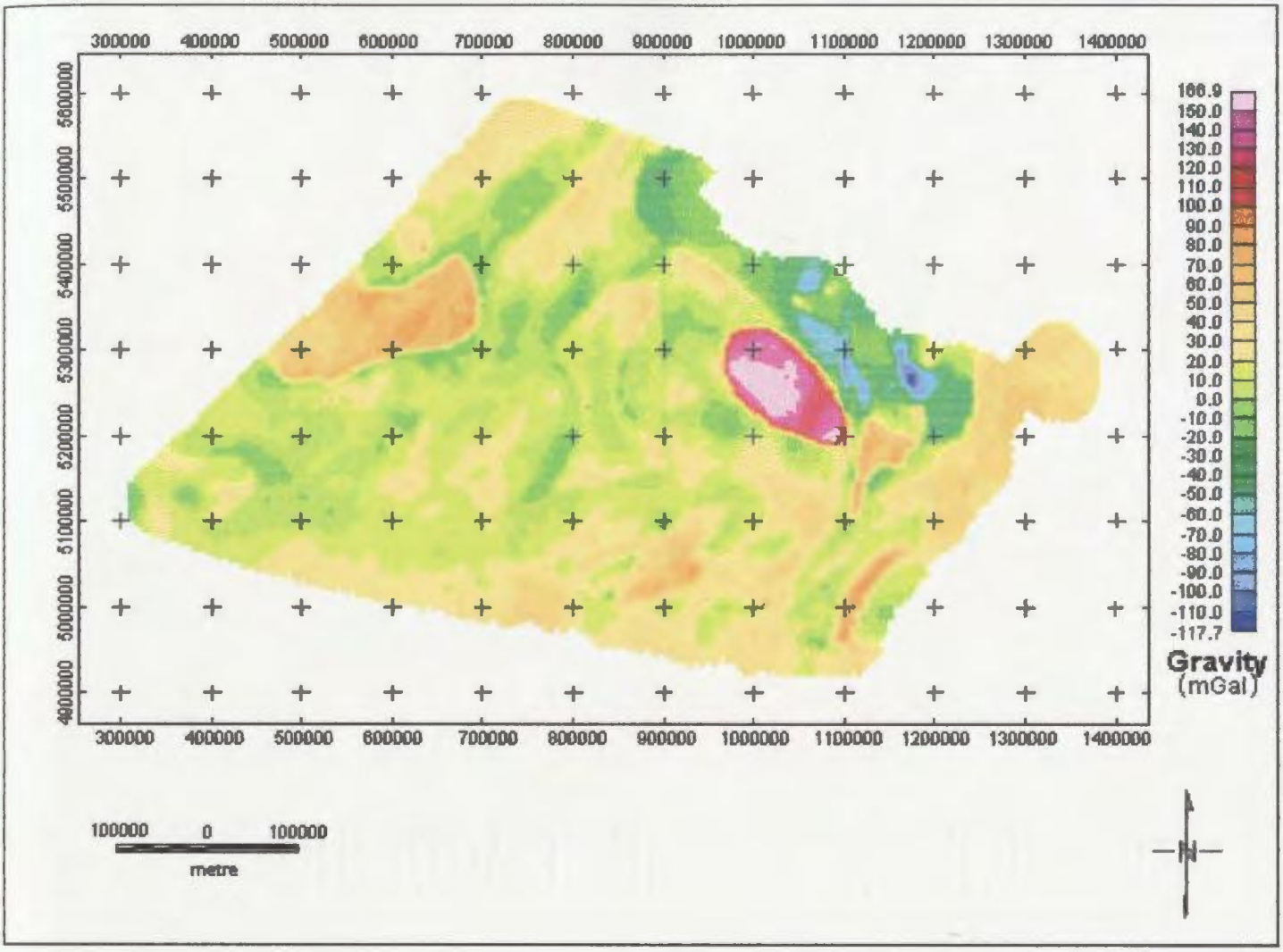

Figure 4.14. Residual gravity field between the observed gravity field (corrected for the gravity effects of the sediments) and the gravity effect computed for the Moho topography model obtained from the inversion.

CHAPTER 5: DISCUSSION AND CONCLUSIONS

5.1 DISCUSSION OF ERRORS

5.1.1 Modelling the Sedimentary Basins

The accuracy of the algorithm designed using the method of Talwani and Ewing (1960) depends on 1) the closeness of fit between the depth to basement contour line and its representative polygonal lamina, and 2) the choice of contour interval. The former becomes significant only when the distance between the lamina and the external point at which the gravity anomaly is calculated is relatively small – the maximum discrepancy occurring at the point of minimum separation – and then only to a maximum of less than one third of a percent of the total anomaly. The latter is negligible if an appropriate contour interval is chosen, i.e. one that ensures even coverage of the body. Given that the depocentres of the modelled basins range from 5 to 12 km, the contour interval of 1 km is reasonable.

Changes in the density of the sedimentary column and/or changes in its thickness may change the observed gravitational anomaly significantly. In this case, the depth to Paleozoic basement, i.e. the thicknesses of the Mesozoic sediments is fairly well known from seismic reflection and refraction surveys, potential field studies, and well logs. The densities, particularly at depth, are not as well constrained. The number of wells per basin is small, particularly for

Carson and Horseshoe Basins. The wells were very shallow in relation to the total thickness of the basins. The deepest of the wells, Bonanza M-71 in Jeanne d'Arc Basin, only extended to a depth of 5300 m compared with a maximum estimated depth of at least 15 km (Tankard, et al., 1989; Grant and McAlpine, 1990). With the exception of Whale Basin, the wells are located at the edges of the basins, where the sediments pinch out against the basin-bounding faults. Therefore, a large uncertainty in the calculated gravity effects (±31 mGal; §3.2.7) is associated with the uncertainties in the densities assigned to each basin due to both the averaging of the near-surface density log values and the extrapolation of densities to depth. The effects of sedimentary compaction have been addressed by assuming that basin densities increase with depth.

Uncertainty in the basin densities can be reduced as more accurate density information becomes available, particularly at depth.

5.1.2 Inversion of Gravity Field Data

Changes in the density of the crust or the mantle and/or changes in the thickness of the crust can change the observed gravitational anomaly significantly. Furthermore, a change in the thickness of the crustal layer (effected by a change in the depth of the Moho) will change the observed gravity anomaly by the same amount as a commensurate change in density contrast (effected by a change in crustal or mantle density). Choosing a range of depths from which several models were derived has mitigated uncertainties in the estimate of mean

depth to Moho. The surface density (2.67 g/cm^3) is well established, however, the asymptotic density (2.97 g/cm^3) is based on indirect evidence as discussed earlier.

The present model is limited by the assumption of a horizontally stratified crustal model. Horizontal layering of the crust changes the resultant average Moho depth but does not alter the modelled undulations greatly (Marillier and Verhoef, 1989). The methodology used here does not account for lateral variation of density within the crust aside from the Mesozoic sedimentary basins or the possible presence of anomalous bodies or structure, e.g. faults, folds, intrusions, or mafic layering or underplating which itself has a significantly large density that will not be reflected in the density-depth function. Furthermore, lateral variations of density in the mantle have not been addressed.

The Moho here is assumed to be a sharply defined interface between two media of differing densities. Contrary to this, Braile (1989) and Braile, et al. (1989) have suggested that the Moho may instead be characterized in places by a transition zone up to a few kilometres thick, across which seismic velocity changes. It is not unreasonable to expect that density would also vary across such a boundary.

A problem affecting the accuracy of the Moho topography model is the proximity of the region to the ocean-continent boundary. The crust thins as it approaches the boundary and this thinning is not reflected in the model because the distinctive gravity anomaly across it is not a part of the data set and was therefore not incorporated into the inversion scheme.

The broadband nature of the potential field itself can introduce uncertainty into the final model through the leakage of energy from broad, near-surface features into the power spectrum. These produce long-wavelength signals, which may have been misinterpreted as originating from undulations in the Moho. Although every effort has been made to remove the gravitational effect of the sedimentary basins, the modelling procedure can lead to residual energy that will appear in the spectrum.

With the removal of the long-wavelength gravity effects of the Mesozoic sedimentary basins in the region, the remaining long-wavelength gravity anomalies have been interpreted as due solely to the density contrast across the crust-mantle boundary. As noted above, this assumes an oversimplified view of crustal structure.

5.2 DISCUSSION

Geodynamic models of rift basin and continental margin formation have been proposed by Grant (1987), Keen, et al. (1987b), Tankard and Welsink (1987), Enachescu (1988); Keen and Dehler (1993), and Bassi, et al. (1993), among others, to explain the margin geometry of Newfoundland. The prevailing extensional model used to describe the evolution of rifted margins is as follows: Rifting produces extension in the lithosphere. The amount of extension, β, can vary throughout the rift zone. During rifting, the collapse of fault blocks causes lithospheric flexure, if the lower crustal lithosphere is strong. The crust is thinned

by the extension and the region vacated by the thinning is passively filled with asthenospheric material, raising the geothermal gradient and increasing heat flow. The surface topography is uplifted in response to the thermal expansion. This is offset by subsidence due to the upwelling of mantle material. Overall, subsidence, referred to as syn-rift subsidence, prevails. After extension, the lithosphere cools and thermal subsidence, also called post-rift subsidence, takes over. Although post-rift subsidence decays as thermal equilibrium is reached (approximately 200 m.y. for oceanic crust), subsidence continues due to sediment loading.

Different types or amounts of extension produce different rifted margin structure. The two end-members of the range of extensional styles are the pure shear model of McKenzie (1978) and the simple shear model of Wernicke (1985).

The symmetrical pure shear model of McKenzie (1978) proposes that the continental crust and lithosphere is thinned by an amount β (and consequently undergoes syn-rift subsidence). While ductile deformation takes place in the lower crust and mantle, brittle deformation occurs in the upper crust. The basin associated with pure shear extension forms above the zone of thinned crust. Depth-dependent extension models (Royden and Keen, 1980) propose layers with different stretching factors within the lithosphere.

The simple shear model of Wernicke (1985) proposes that lithospheric extension occurs along a detachment fault that cuts the lithosphere in its entirety. The amounts of thinning above and below the detachment fault may differ, e.g.

the crustal portion may be thinned by an amount β and the mantle lithosphere thinned by amount δ. The basin associated with simple shear extension develops proximal to the surface expression of the detachment fault. Lower layer thinning increases toward the distal end of the fault and upper layer thinning increases toward the proximal end.

A combination of pure and simple shear is most often used to describe margin structure, particularly for complex margins. A detachment fault in the crust, above which brittle deformation occurs, that soles out at Moho depths paired with ductile necking in the mantle lithosphere illustrates this type of combination model.

The delaminational model of Lister, et al. (1986) proposes a single shear zone throughout the lithosphere that is offset at different locations. A low-angle fault passes through the brittle upper layer, traverses an intra-crustal brittle-ductile transition, and dips down to sole out at or near the Moho.

Runaway lithospheric thinning (Buck, 1991) describes a pure shear extensional model where the thinned area cools and hardens. The area becomes stronger, preventing further thinning. Because extension concentrates in the weakest zone of the lithosphere, the deformation and thinning migrate laterally, widening the rift zone (Kuznir and Park, 1987). Rupture will normally occur in the weakest area, producing an asymmetric conjugate margin with a broad margin, evenly thinned, on one side of the rift and a narrow margin on the other. This asymmetry is usually interpreted as due to simple shear extension prior to rupture.

Lithospheric response to extension can be described as the sum of kinematic and isostatic components (Karner and Driscoll, 1993). Movement of fault blocks along detachment faults both thins the crust and lithosphere and creates structural 'holes' to be filled with sediments. Extension above a detachment fault or brittle-ductile transition zone must be balanced by a commensurate amount of extension below it. The loads placed on the crust during rifting (e.g. thermal uplift, magmatic underplating, sedimentation, subsidence) must be compensated. The flexural state of the lithosphere is determined by this compensation (Karner and Driscoll, 1993).

A response of the lithosphere to extension and stretching is flexural isostatic rebound of the flanks of the rift basins. The geometry of rift basin flanks is a consequence of regional isostatic compensation. Finite mechanical strength is required by extended lithosphere to accommodate this regional compensation. Flexural uplift in response to the creation of structural holes during rifting is centred below the hole. Uplifted rift flanks are transformed by the influx of seawater and sedimentation, which act to depress the topography. The magnitude of the uplift is decreased if the hole is filled with sediments but the wavelength of uplift remains constant. The compaction of sediments in very deep basins (e.g. Jeanne d'Arc Basin) means that the density of the sediments at depth approaches that of continental crust. The flexural uplift associated with the creation of these 'holes' is offset by the effect of the positive sediment load (Keen, et al., 1987b). Nonetheless, both the extension and subsidence processes will be manifested in the Moho topography below the region.

Changes in the topography of Moho beneath the region may be too subtle to be detected by inversion processes.

Figure 4.13 shows the modelled Moho depth for the Avalon Terrane of Newfoundland. The absence of any distinct discontinuity in the relief of the Moho suggests that the crust was extended via pure shear (McKenzie, 1978) extension or facilitated along detachment faults (Wernicke, 1985) that sole out at or near Moho, or both.

The Airy-Heiskanen hypothesis proposes that variations in crustal thickness support surface topography. Large topographic features with excess mass are compensated by mass deficiencies at depth, i.e. the downwarping of crustal material into the mantle, and those having a mass deficiency are compensated by an excess of mass at depth, i.e. upwarping of mantle material into the crust. Gravity anomalies of such compensating masses have long wavelengths and correlate negatively with long-wavelength surface topography. This is readily apparent in Figure 4.13, where the crust is thicker beneath the Newfoundland landmass and thins beneath the major basins, particularly beneath the northern Jeanne d'Arc Basin.

The average thickness derived for the crust is 38 km. The crust attains a maximum thickness of near 42 km adjacent to the Jeanne d'Arc Basin while the minimum thickness of less than 32 km occurs beneath the northern Jeanne d'Arc Basin. This gives a peak-to-trough amplitude of undulation of 11 km. The 42 km deep trough is a side-effect of inversion of the lobes flanking the Jeanne d'Arc Basin, therefore a more realistic value of the amplitude of undulation is nearer 4

or 5 km. Toward the Avalon Peninsula the crust thickens to approximately 38 km. Beneath the Jeanne d'Arc Basin the crust is thinned to less than 32 km. The undulation amplitude of the Moho is about 1 to 2 km in the western region of the data (i.e. west of 800000 E UTM) and about 4 to 5 km in the eastern region beneath the sedimentary basins. Considering the isostatic uplift of the Moho beneath the basins, the amplitudes are not unreasonable. The shallowest depths to the Moho correlate well with the positive gravity features observed on the long-wavelength (>150 km; Figure 3.20) gravity field and vice versa. This confirms that the general relief calculated for the modelling program is acceptable.

Seismic results show that the half-grabens of the Grand Banks are bounded by listric extensional faults (Keen and de Voogd, 1988; Reid and Keen, 1990; DeChassy, et al., 1990) that dip predominantly to the east at apparent angles of about 30° to 40° (Keen, et al., 1987b). These faults extend deep into the crust and flatten along or just above the Moho. Dipping reflectors seen on reflection line 85-1, which may be continuations of upper crustal faults, appear to graze the Moho (DeChassy, et al., 1990). If these basin-bounding faults sole out at or above the Moho rather than penetrate it, then the Moho should be fairly continuous beneath the basins. The present model of Moho topography, which does not show any discontinuities beneath the major Grand Banks basins, or elsewhere in the study region, supports this.

Refraction results from the Jeanne d'Arc Basin show that the deep crustal structure is fairly complex even though Moho is relatively smooth at between 35

and 37 km (Reid and Keen, 1990) depth. The crust is layered; in particular, there exists a lower crustal layer of constant thickness with a seismic velocity of 7.2 km/s. There is evidence of igneous activity on the Grand Banks during Mesozoic extension and rifting (Jansa and Pe-Piper, 1986; Grant and McAlpine, 1990). Therefore, the layer may be the result of magmatic underplating or intrusion. This layer is absent further south (Reid, 1988). At the southeastern Grand Banks the crust has a modelled thickness of 36 km. Refraction data collected at the southeastern (Reid, 1993) and southwestern (Reid, 1988) Grand Banks put the Moho at an average depth of 30 km. The refraction results from the southeast Grand Banks also show the presence of a high velocity (>7 km/s) layer in this region (Reid, 1993).

The modelled depth to Moho from the present study was compared to the map of crustal thickness compiled by Shih, et al. (1988) who used information collected from seismic refraction surveys, and free-air gravity, depth to basement, and bathymetric measurements to calculate crustal thickness. Their average crustal thickness is approximately 25 km, however this estimate includes the zones of thinned crust at the margin's edges. Crustal thickness at the southern Grand Banks is greater than 30 km, which differs from the present model by at least 6 km. Shih, et al. (1988) give a crustal thickness of over 35 km beneath the Jeanne d'Arc Basin while the modelled depth to Moho here is about 32 km. They show that landward of the Grand Banks the crust exceeds 35 km thickness which is comparable to the modelled thickness and covers the largest areal extent by far.

5.3 CONCLUSIONS

The main objective was to develop a technique to obtain the relative undulations in the Moho topography and their geographic locations throughout the region in order to supplement the present limited knowledge derived from seismic lines. This has been achieved. As observed in Chapter 4, the actual depth of the Moho and the Moho undulations are largely dependent on the mean depth used in the inversion program.

The study has demonstrated that an estimate of Moho topography for the area can be extracted from the Bouger gravity data following correction for the effects of the sedimentation in the basins and wavelength filtering. The Moho relief obtained is consistent with the limited seismic control. The present model approximates the Moho topography of the region sufficiently well to make conclusions regarding the general structure of the crust. The results show how regional surface topography, particularly sedimentary infilling and subsidence of the major Mesozoic basins of the Grand Banks, is sustained by variations in crustal thickness. The crust is thicker beneath the Avalon Peninsula and thins beneath the basins. The Jeanne d'Arc Basin is a particular example. The smoothness of the Moho topography in the region is suggestive of either a pure shear extensional mode of margin formation or extension via a combination of pure and simple shear facilitated along a detachment fault that soles out at or

above the Moho. This is consistent with the present knowledge of the geology and tectonics of the region.

The inversion used here was not intended to examine crustal thinning toward the ocean-continent boundary. Inclusion of a high density mafic layer such as interpreted by Reid and Keen (1990) and Reid (1993) would have increased the asymptotic density of the crust. This would result in a larger density for the crustal layer as a whole and a reduced contrast across the crust-mantle interface. Such a reduction in the contrast increases the amplitude of the modelled relief.

The algorithm created by Chenot and Debeglia (1990) was designed to model the interface between sedimentary basins and crustal basement, i.e. basement topography. This study has shown that it can be applied to modelling Moho topography. The inversion program could possibly be improved by applying optimization techniques.

The Moho relief inferred by this study could be improved if (1) more deep seismic information were available over a broader geographic area, and (2) density data were available for deeper portions of the basins. Given that both of these are expensive to obtain, the map of Moho topography presented here can be considered a successful first attempt at extracting the Moho topography from the gravity data.

REFERENCES

Agarwal, B.N.P., Das, L.K., Chakravorty, K., and Sivaji, Ch. 1995. Analysis of the Bouger anomaly over central India: A regional perspective. Mem. Geol. Soc. India, **31**: 469-493.

Barbosa, V.C.F., Silva, J.B.C., and Medeiros, W.E. 1999. Stable inversion of gravity anomalies of sedimentary basins with nonsmooth basement reliefs and arbitrary density contrast variations. Geophysics, **64**: 754-764.

Barnett, C.T. 1976. Theoretical modeling of the magnetic and gravitational fields of an arbitrarily shaped three-dimensional body. Geophysics, **41**: 1353-1364.

Bassi, G., Keen, C.E. , and Potter, P. 1993. Contrasting styles of rifting: Models and examples from the eastern Canadian margin. Tectonics, **12**: 639-655.

Bhattacharyya, B.K. 1967. Some general properties of potential fields in space and frequency domain: A review. Geoexploration **5**: 127-143.

Blakely, R.J. Potential Theory in Gravity and Magnetic Applications. Cambridge University Press: USA. 1995.

Bott, M.H.P. 1960. The use of rapid digital computing methods for direct gravity interpretation of sedimentary basins. Geophysical Journal of the Royal Astronomical Society, **3**: 63-67.

Braile, L.W. 1989. Seismic properties of the crust and uppermost mantle of the coterminous United States and adjacent Canada in Pakiser, L.C. and Mooney, W.D. (eds) Geophysical Framework of the Continental United States. Geological Society of America Memoir, **172**: 285-315.

Braile, L.W., Hinze, W.J., von Frese, R.R.B., and Keller, G.R. 1989. Crustal structure of the continental interior in Pakiser, L.C. and Mooney, W.D. (eds) Geophysical Framework of the Continental United States. Geological Society of America Memoir, **172**: 655-680.

Briggs, I.C. 1974. Machine contouring using minimum curvature. Geophysics, **39**: 39-48.

Buck, W.R. 1991. Modes of continental lithospheric extension. Journal of Geophysical Research, **96**: 20 161-20 178.

Chenot, D. and Debeglia, N. 1990. Three-dimensional gravity or magnetic

constrained depth inversion with lateral and vertical variation of contrast. Geophysics, **55**: 327-335.

Christensen, N.I. 1994. Seismic Velocities; Section VI in Carmichael, R.S. (ed.) Practical Handbook of Physical Properties of Rocks and Minerals. CRC Press: Boca Raton, Fla. pp. 429-546.

Coggon, J.H. 1976. Magnetic and gravity anomalies of polyhedra. Geoexploration, **14**: 93-105.

Condi, F.J., Zelt, C.A., Sawyer, D.S., and Hirasaki, G.J. 1999. Gravity inversion for rifted margin deep structure using extension and isostatic constraints. Geophysical Journal International, **138**: 435-446.

Connard, G. Couch, R. and Gemperle, M. 1983. Analysis of aeromagnetic measurements from the Cascade Range in central Oregon. Geophysics, **48**: 376-390.

Cordell, L. and Henderson, R.G. 1968. Iterative three-dimensional solution of gravity anomaly data using a digital computer. Geophysics, **33**: 596-602.

Cordell, L. and Grauch, V.J.S. 1982. Reconciliation of the discrete and integral Fourier transforms. Geophysics, **47**: 237-243.

Cordell, L., Phillips, J.D., and Godson, R.H. 1992. U.S. Geological Survey Potential Field Geophysical Software Version 2.0. (fourt.for)

DeChassy, A., Pinet, B., Keen, C.E., and Kay, W. 1990. Deep seismic profiles across conjugate margins and associated basins of the North Atlantic Ocean in Pinet, B. and Bois, Ch. (eds.) The Potential of Deep Seismic Profiling for Hydrocarbon Exploration. Technip, Paris, pp. 451-474.

Dehler, S.A. and Keen, C.E. 1993. Effects of rifting and subsidence on thermal evolution of sediments in Canada's east coast basins. Canadian Journal of Earth Sciences, **30**: 1782-1798.

DeSilva, N.R. 1999. Sedimentary basins and petroleum systems offshore Newfoundland and Labrador in Fleet, A.J. and Boldy, S.A.R. (eds.) Petroleum Geology of Northwest Europe: Proceedings of the 5th Conference. Geological Society, London, pp. 501-515.

Enachescu, M.E. 1987. The tectonic and structural framework of the northwest Newfoundland continental margin in Beaumont, C. and Tankard, A.J. (eds.) Sedimentary Basins and Basin-Forming Mechanisms. Canadian Society of Petroleum Geologists, Memoir **12**, pp. 117-145.

Enachescu, M.E. 1988. Extension modes and parameters for the Grand Banks of Newfoundland: Presented at the Joint Annual Meeting of the G.A.C./ M.A.C./C.S.P.G., Program with Abstracts, 13, A37.

Gerard, A. and Debeglia, N. 1975. Automatic three-dimensional modeling for the interpretation of gravity or magnetic anomalies. Geophysics, **40**: 1014-1034.

Gradstein, F.M., Grant, A.C., and Jansa, L.F. 1977. Grand Banks and J-Anomaly Ridge: a geological comparison. Science, **197**: 1074-1076.

Grant, F.S. and West, G.F. Interpretation Theory in Applied Geophysics. McGraw Hill: New York. 1965.

Grant, A.C. 1987. Inversion tectonics on the continental margin east of Newfoundland. Geology, **15**: 845-848.

Grant, A.C. and McAlpine, K.D. 1990. The continental margin around Newfoundland; Chapter 6 in Keen, M.J. and Williams, G.L. (eds.) Geology of the Continental Margin of Eastern Canada. Geological Survey of Canada, Geology of Canada, no. 2, pp. 239-292.

Guspi, F. 1992. Three-dimensional Fourier gravity inversion with arbitrary density contrast. Geophysics, **57**: 131-135.

Haworth, R.T. and Miller, H.G. 1982. The structure of Paleozoic oceanic rocks beneath Notre Dame Bay, Newfoundland in St-Julien, P. and Béland, J. (eds.) Major Structural Zones and Faults of the Northern Appalachians. Geological Association of Canada Special Paper, **24**: 149-173.

Haworth, R.T., Keen, C.E., and Williams, H. 1994. Transects of the ancient and modern continental margins of eastern Canada in Speed, R.C. (ed.) Phanerozoic Evolution of North American Continent-Ocean Transitions. Boulder, Colorado, Geological Society of America, DNAG Continent-Ocean Transect Volume.

Hodych, J.P. and Hayatsu, A. 1980. K-Ar isochron age and paleomagnetism of diabase along the trans-Avalon aeromagnetic lineament; evidence of Late Triassic rifting in Newfoundland. Canadian Journal of Earth Sciences, **17**: 491-499.

Jacobi, W. 1967. On the calculation of the gravity effect of arbitrarily shaped three dimensional masses with digital computers. Geophysics, **33**: 163-166.

Jansa, L.F. and Wade, J.A. 1975. Geology of the continental margin off Nova

Scotia and Newfoundland. Geological Survey of Canada Paper 74-30, pp. 51-105.

Jansa, L.F. and Pe-Piper, G. 1986. Geology and geochemistry of Middle Jurassic and Early Cretaceous igneous rocks on the eastern North American Continental Shelf. Geological Survey of Canada, Open File 1351, 104 p.

Kane, M.F. and Godson, R.H. 1985. Features of a pair of long-wavelength (>250 km) and short-wavelength (<250 km) Bouguer gravity maps of the United States in Hinze, W.J. (ed.) The Utility of Regional Gravity and Magnetic Anomaly Maps. SEG: Tulsa, Oklahoma, pp. 46-61.

Karner, G.D., Driscoll, N.W. 1993. Rift flank topography and extensional basin architecture; formation of Broken Ridge, Southeast Indian Ocean in Mantovani, M.S.M. and Flexor, J.M. (eds.) Contribution to the Study on the Composition, Structure and Dynamics of the Lithosphere. Anais da Academia Brasileira de Ciencias, 65, Suppl. 2, pp. 263-294

Keen, C.E., Stockmal, G., Welsink, H., Quinlan, G., and Mudford, B. 1987a. Deep crustal structure and evolution of the rifted margin northeast of Newfoundland: Results from LITHOPROBE East. Canadian Journal of Earth Sciences, **24**: 1537-1549.

Keen, C.E., Boutilier, B.B., de Voogd, B., Mudford, B., and Enachescu, M.E. 1987b. Crustal geometry and models of the rift basins on the Grand Banks off eastern Canada: constraints from deep seismic reflection data in Beaumont, C. and Tankard, A.J. (eds) Sedimentary Basins and Basin-Forming Mechanisms. Mem. Can. Soc. Pet. Geol., **12**: 101-115.

Keen, C.E. and de Voogd, B. 1988. The continent-ocean boundary at the rifted margin off eastern Canada: New results from deep seismic reflection studies. Tectonics, **7**: 107-124.

Keen, C., Peddy, C., de Voogd, B., and Matthews, D. 1989. Conjugate margins of Canada and Europe: Results from deep reflection profiling. Geology, **17**: 173-176.

Keen, C.E. and Dehler, S.A. 1993. Stretching and subsidence: Rifting of conjugate margins in the North Atlantic region. Tectonics, **12**: 1209-1229.

Keen, C.E., Potter, P., and Srivistava, S.P. 1994. Deep seismic reflection data across the conjugate margins of the Labrador Sea. Canadian Journal of Earth Sciences, **31**: 192-205.

Keen, C.E. and Potter, D.P. 1995. Formation and evolution of the Nova Scotian

rifted margin: Evidence from deep seismic reflection data. Tectonics, **14**: 918-932.

Keppie, J.D. 1985. The Appalachian collage in Dee, D.G. and Sturt, B. (eds.) The Caledonide Orogen: Scandinavia and Related Areas. Wiley, New York, pp. 1217-1226.

Keppie, J.D., Nance, R.D., Murphy, J.B., and Dostal, J. 1989. Northern Appalachians: Avalon and Meguma Terranes in Dallmeger, R.D. and Lécorché, J.P. (eds.) West African Orogens and Circum-Atlantic Correlations. Springer, Berlin.

King, L.H., Fader, G.B., Poole, W.H., and Wanless, R.K. 1985. Geological setting and age of the Flemish Cap granodiorite, east of the Grand Banks of Newfoundland. Canadian Journal of Earth Sciences, **22**: 1286-1298.

Kuznir, N.J. and Park, R.G. 1987. The extensional strength of continental lithosphere: Its dependence on geothermal gradient, and crustal composition and thickness in Coward, M.P., Dewey, J.F., and Hancock, P.L. (eds) Continental Extensional Tectonics. Geol. Soc. Spec. Publ., **28**: 35-52.

Lefort, J.P. and Agarwal, B.N.P. 1996. Gravity evidence for an Alpine buckling of the crust beneath the Paris Basin. Tectonophysics, 258: 1-14.

Lefort, J.P. and Agarwal, B.N.P. 2000. Gravity and geomorphological evidence for a large crustal bulge cutting across Brtittany (France): a tectonic response to the closure of the Bay of Biscay. Tectonophysics, 323: 149-162.

Li, Y. and Oldenburg, D.W. 1998. 3-D inversion of gravity data. Geophysics, **63**: 109-119.

Lister, G.S., Etheridge, M.A., and Symonds, P.A. 1986. Detachment faulting and the evolution of passive continental margins. Geology, **14**:246-250.

Marillier, F. and Verhoef, J. 1989. Crustal thickness under the Gulf of St. Lawrence, northern Appalachians, from gravity and deep seismic data. Canadian Journal of Earth Sciences, **26**: 1517-1532.

Marillier, F., Hall, J., Hughes, S., Louden, K., Reid, I., Roberts, B., Clowes, R., Coté, T., Fowler, J., Guest, S., Lu, H., Luetgert, J., Quinlan, G., Spencer, C., and Wright, J. 1994. Lithoprobe East onshore-offshore seismic refraction survey - constraints on interpretation of reflection data in the Newfoundland Appalachians. Tectonophysics, **232**: 43-58.

McKenzie, D. 1978. Some remarks on the development of sedimentary basins. Earth Planet. Sci. Lett., **40**: 25-32.

Miller, H.G 1970. A gravity survey of eastern Notre Dame Bay, Newfoundland. M.Sc. Thesis. Memorial University of Newfoundland. 84 p.

Miller, H.G. 1978. Three statistical tests for 'goodness of fit'. Canadian Journal of Earth Sciences, **15**: 171-173.

Miller, H.G. 1982a. Gravity and magnetic studies of crustal structure in Schenk, P.M. (ed) Newfoundland in Regional Trends in the Geology of the Appalachian-Caledonian-Hercynian-Mauritanide Orogen. D. Reidel Publishing Co. pp. 29-38.

Miller, H.G. 1982b. Geophysical constraints on the thickness of the Holyrood Pluton, Avalon Peninsula, Newfoundland. Maritime Sediments and Atlantic Geology, **18**: 75-85.

Miller, H.G., Goodacre, A.K., Cooper, R.V., and Halliday, D. 1985. Offshore extensions of the Avalon Zone of Newfoundland. Canadian Journal of Earth Sciences, **22**: 1163-1170.

Miller, H.G. 1987. A geophysical interpretation of the onshore and offshore geology of the southern Avalon Terrane, Newfoundland. Canadian Journal of Earth Sciences, **24**: 60-69.

Miller, H.G. and Singh, V. 1995. The Avalon Terrane of Newfoundland: geophysical correlations from onshore to offshore as evidence for Precambrian to Tertiary structural evolution. Tectonophysics, **242**: 183-197.

Mufti, I.R. 1975. Iterative gravity modelling by using cubical blocks. Geophysical Prospecting, **23**: 163-198.

Nafe, J.E. and Drake, C.L. 1957a. Variation with depth in shallow and deep water marine sediments of porosity, density and the velocities of compressional and shear waves. Geophysics, **22**: 523-552.

Nafe, J.E. and Drake, C.L. 1957b. Physical properties of crustal materials as related to compressional wave velocities; paper presented at Annual Meeting of Society of Exploration Geophysicists, 1957, Dallas, Texas (unpublished). Graph taken from Talwani, Sutton, and Worzel (1959).

Nafe, J.E. and Drake, C.L. 1963. Physical properties of marine sediments in M.N. Hill (ed) The Sea: Ideas and Observations on Progress in the Study of the Seas, Vol. 3. John Wiley & Sons: New York.

Nagy, D. 1966. The gravitational attraction of a right rectangular prism. Geophysics, **31**: 362-371.

Neilson-Pike, J.E. 1987. Character of the lower lithosphere: composition in Noller, J.S., Kirby, S.H., and Nielson-Pike, J.E. (eds.) Geophysics and Petrology of the Deep Crust and Upper Mantle - A Workshop Sponsored by the United States Geological Survey and Stanford University. U.S.G.S. Circular 956. pp. 9-12.

Oldenburg, D.W. 1974. The inversion and interpretation of gravity anomalies. Geophysics, **39**: 526-536.

Olhoeft, G.R. and Johnson, G.R. 1994. Densities of Rocks and Minerals; Section II in Carmichael, R.S. (ed.) Practical Handbook of Physical Properties of Rocks and Minerals. CRC Press: Boca Raton, Fla. pp. 139-176.

Parker, R.L. 1973. The rapid calculation of potential anomalies. Geophysical Journal of the Royal Astronomical Society, **31**: 447-155.

Parker, R.L. 1974. A new method for modelling marine gravity and magnetic anomalies. Journal of Geophysical Research, **79**: 2014-2016.

Parker, R.L. and Huestis, S.P. 1974. The inversion of magnetic anomalies in the presence of topography. Journal of Geophysical Research, **79**: 1587-1593.

Paul, M.K. 1974. The gravity effect of a homogeneous polyhedron for three dimensional interpretation. Pageoph, 112, III, pp.553-561.

Pederson, L.B. 1978. Wavenumber domain expressions for potential fields from arbitrary 2-, 2½-, and 3-dimensional bodies. Geophysics, **43**: 626-630.

Pe-Piper, G. and Jansa, L.F. 1986. Triassic olivine-normative diabase from Northumberland Strait, eastern Canada; implications for continental rifting. Canadian Journal of Earth Sciences, **23**: 1013-1021.

Peters, L.J. 1949. The direct approach to magnetic interpretation and its practical application. Geophysics, **14**: 290-320.

Rasmussen, R. and Pedersen, L.B. 1979. End corrections in potential field modeling. Geophysical Prospecting, **27**: 749-760.

Reid, I. 1988. Crustal structure beneath the southern Grand Banks: seismic refraction results and their implications. Canadian Journal of Earth Sciences, **25**: 760-772.

Reid, I.D. and Keen, C.E. 1990. Deep crustal structure beneath a rifted basin: results from seismic refraction measurements made across the Jeanne d'Arc Basin, offshore eastern Canada. Canadian Journal of Earth Sciences, **27**: 1462-1471.

Reid, I. 1993. Velocity structure of reflective lower crust beneath the Grand Banks of Newfoundland. Journal of Geophysical Research, **98**: 9845-9859.

Reid, I.D. 1994. Crustal structure of a nonvolcanic rifted margin east of Newfoundland. Journal of Geophysical Research, **99**: 15161-15180.

Royden, L. and Keen, C. 1980. Rifting processes and thermal evolution of the continental margin of eastern Canada determined from subsidence curves. Eart Planet. Sci. Lett., **51**:343-361.

Sheriff, R.E. Encyclopedic Dictionary of Exploration Geophysics. SEG: Tulsa, Oklahoma. 1973.

Shih, K.G., Kay, W., Woodside, J., Jackson, R., Adams, J., Drysdale, J., Bell, J.S., and Podrouzek, A.J. 1988. Crustal thickness, seismicity and stress orientations of the continental margin of eastern Canada. Map 1710A. Scale 1: 5 000 000. Geological Survey of Canada.

Spector, A. and Grant, F.S. 1970. Statistical models for interpreting aeromagnetic data. Geophysics, **35**: 293-302.

Sullivan, K.D. and Keen, C.E. 1977. Newfoundland Seamounts: petrology and geochemistry in Baragar, W.R.A., Coleman, L.C., and Hall, J.M. (eds.) Volcanic Regimes of Canada, Geological Association of Canada, Special Paper 16, pp. 461-476.

Talwani, M., Worzel, J.L., and Landisman, M. 1959. Rapid gravity computations for two-dimensional bodies with application to the Mendocino submarine fracture zone. Journal of Geophysical Research, **64**: 49-59.

Talwani, M., Sutton, G.H., And Worzel, J.L. 1959. A crustal section across the Puerto Rico Trench. Journal of Geophysical Research, **64**: 1545-1555.

Talwani, M. and Ewing, M. 1960. Rapid computation of gravitational attraction of three-dimensional bodies of arbitrary shape. Geophysics, **25**: 203-225.

Tankard, A.J. & Welsink, H.J. 1987. Extensional tectonics and stratigraphy of Hibernia Oil Field, Grand Banks, Newfoundland. Bull. Am. Assn. Petr. Geol. **71**: 1210-1232.

Tankard, A.J. and Welsink, H.J. 1988. Extensional tectonics and stratigraphy of the Mesozoic Grand Banks of Newfoundland in Manspeizer, W. (ed.)Triassic-Jurassic Rifting: Continental breakup and the origin of the Atlantic Ocean and passive margins, Part A, Developments in Geotectonics 22. Elsevier, pp. 129-165.

Tankard, A.J., Welsink, H.J., and Jenkins, W.A.M. 1989. Structural styles and stratigraphy of the Jeanne d'Arc Basin, Grand Banks of Newfoundland in Extensional Tectonics and Stratigraphy of the North Atlantic Margin. Tankard, A.J. and Balkwill, H.R. (eds.) AAPG Memoir, **46**: 265-282. 1989.

Tanner, J.G. 1967. An automated method of gravity interpretation. Geophysical Journal of the Royal Astronomical Society, **13**: 339-347.

Telford, W.M., Geldart, L.P., and Sheriff, R.E. Applied Geophysics, 2nd ed. Cambridge University Press: Cambridge. 1990.

Todd, B.J., Reid, I., and Keen, C.E. 1988. Crustal structure across the Southwest Newfoundland Transform Margin. Canadian Journal of Earth Sciences, **25**: 744-759.

Tsuboi, C. and Fuchida, T. 1937. Relations between gravity values and corresponding subterranean mass distribution. Earthquake Res. Inst. of the Tokyo Imperial Univ. Bulletin, **15**: 636-649.

Tsuboi, C. Gravity. George Allen & Unwin, Ltd: London. 1979.

Tucholke, B.E. & Ludwig, W.G. 1982. Structure and origin of the J-Anomaly ridge, Western North Atlantic Ocean. Journal of Geophysical Research, **87**: 9389-9407.

Wade, J.A., Grant, A.C., Sanford, B.V., and Barss, M.S. 1977. Basement Structure, Eastern Canada and Adjacent Areas. Map 1400A (SE). Scale 1: 2 000 000. Geological Survey of Canada.

Watts, A.B. and Fairhead, J.D. 1999. A process-oriented approach to modeling the gravity signature of continental margins. The Leading Edge, **18**: 258-263.

Weaver, D.F. 1967. A geological interpretation of the Bouger anomaly field of Newfoundland. Publ. Dominion Observatory, **35**: 223-250.

Weaver, D.F. 1968. Preliminary results of the gravity survey of the island of Newfoundland with maps No. 53, 54, 55, 56, 57. Earth Physics Branch, EMR, Ottawa.

Wernicke, B. 1985. Uniform-sense simple shear of the continental lithosphere. Canadian Journal of Earth Sciences, **22**: 108-125.

Williams, H. 1979. Appalachian Orogen in Canada. Canadian Journal of Earth Sciences, **16**: 792-807.

Williams, H., Colman-Sadd, S.P., Swinden, H.S. 1988. Tectonic-stratigraphic subdivisions of central Newfoundland in Current Research, Part B, Geological Survey of Canada, Paper 88-1B, pp. 91-98.

Wilshire, H.G. 1987. Character of the lower lithosphere: lithology in Noller, J.S., Kirby, S.H., and Nielson-Pike, J.E. (eds.) Geophysics and Petrology of the Deep Crust and Upper Mantle - A Workshop Sponsored by the United States Geological Survey and Stanford University. U.S.G.S. Circular 956. pp. 6-8.

Won, I.J. and Bevis, M.G. 1987. Computing the gravitational and magnetic anomalies due to a polygon: Algorithms and Fortran subroutines. Geophysics, **52**: 232-238.

Woodside, J.M. and Verhoef, J. 1989. Geological and tectonic framework of eastern Canada as interpreted from potential field imagery. Geological Survey of Canada Paper 88-26. 33 p.

APPENDIX A: FORTRAN PROGRAM FOR CALCULATION OF GRAVITATIONAL FIELD

```
C    GRAVITY.f
C    For calculating the 3D gravitational effect of a body whose coordinates are defined in the
C UTM projection. Modified from a program received from Hugh Miller.
     REAL X(20,50,2500),Y(20,50,2500),PX(2500),PY(2500),R(2500),RC
    &(2500),BM(2500),FT(2500),P(2500),Q(2500),V(20,50),VTOT(50),Z
    &(20,50),RHO(20),GDEL(20),DELG(20,50),THETA(20),GRAV1(20,50),
    &GRAV2(20,50),GRAV3(20,50),SGRAV(15000)
     INTEGER NCORD(20,2500),NHT(50),SLAT(15000),SLONG(15000),SZED
    &(15000),KSTN,NBLKS,NBLOC,COUNT
     CHARACTER*72 HELLO
     EXTERNAL COORD
     OPEN(1,FILE='/net/srvr07/public/janet/BASIN.DAT',STATUS=
    &'unknown')
     OPEN(6,FILE='/net/srvr07/public/janet/BASIN.XYZ',STATUS=
    &'unknown')
     PIE=3.1415927
     EROS=0.0
     READ(1,915)HELLO
     WRITE(6,915)HELLO
     READ(1,900)KSTN,NBLKS
     DO 42 K=1,KSTN
       READ(1,906)SLONG(K),SLAT(K),SZED(K)
  42 CONTINUE
C  Read in the block parameters
     DO 31 K=1,NBLKS
       READ(1,901)NBLOC,RHO(K),NHT(K)
       NH1=NHT(K)
       DO 31 J=1,NH1
         READ(1,903)Z(K,J),NCORD(K,J)
         NC1=NCORD(K,J)
         READ(1,904)(X(K,J,I),Y(K,J,I),I=1,NC1)
  29   CONTINUE
  31 CONTINUE
     COUNT=2
     DO 43 L=1,KSTN
       SGRAV(L)=0.0
       DO 150 K=1,NBLKS
         NH1=NHT(K)
         GDEL(K)=0.0
         DO 107 J=1,NH1
           VTOT(J)=0.0
           NC1=NCORD(K,J)
           DO 45 I=1,NC1
  45         CALL COORD(SLAT(L),SLONG(L),X(K,J,I),Y(K,J,I),PX(I),
     &PY(I),THETA(I))
           NCOR1=NC1+1
           PX(NCOR1)=PX(1)
           PY(NCOR1)=PY(1)
```

```
      STHETA=0.0
      DO 107 I=1,NC1
       R(I)=SQRT(PX(I)**2.0+PY(I)**2.0)
       R(I+1)=SQRT(PX(I+1)**2.0+PY(I+1)**2.0)
       RC(I)=SQRT((PX(I+1)-PX(I))**2.0+(PY(I+1)-PY(I))**2.0)
       BM(I)=(PY(I)*PX(I+1)-PY(I+1)*PX(I))/(R(I)*R(I+1))
       FT(I)=((PX(I)-PX(I+1))*PX(I+1)+(PY(I)-PY(I+1))*PY(I+1))/
     &(RC(I)*R(I+1))
       P(I)=((PY(I)-PY(I+1))*PX(I)-(PX(I)-PX(I+1))*PY(I))/RC(I)
       Q(I)=((PX(I)-PX(I+1))*PX(I)+(PY(I)-PY(I+1)*PY(I)))/(RC(I)*
     &R(I))
       STHETA=STHETA+THETA(I)
       S=1
       W=1
       IF(P(I))55,60,60
55      S=-S
60      IF(BM(I))65,70,70
65      W=-W
70      GK=6.67
       ALPHA=(PX(I)*PX(I+1)+PY(I)*PY(I+1))/(R(I)*R(I+1))
       BETA=Z(K,J)*Q(I)*S/SQRT(P(I)**2.0+Z(K,J)**2.0)
       GAMMA=Z(K,J)*FT(I)*S/SQRT(P(I)**2.0+Z(K,J)**2.0)
       IF(ABS(ALPHA)-1.0)92,92,91
91      ALPHA=1.0
92      IF(ABS(BETA)-1.0)94,94,93
93      BETA=1.0
94      IF(ABS(GAMMA)-1.0)96,96,95
95      GAMMA=1.0
96      V(I,J)=GK*RHO(K)*(W*ACOS(ALPHA)-ASIN(BETA)+ASIN(GAMMA))
       IF(ABS(STHETA-2*PIE)-0.0005)90,90,101
90      V(I,J)=V(I,J)+2*PIE*GK*RHO(K)
101     VTOT(J)=VTOT(J)+V(I,J)
107   CONTINUE
     NHT1=NHT(K)-2
     DO 150 J=1,NHT1
      GRAV1(K,J)=VTOT(J)*(Z(K,J)-Z(K,J+2))*(3*Z(K,J+1)-Z(K,J+2)-2*
     &Z(K,J))/(Z(K,J)-Z(K,J+1))
      GRAV2(K,J)=VTOT(J+1)*(Z(K,J)-Z(K,J+2))*(Z(K,J)-Z(K,J+2))*
     &(Z(K,J)-Z(K,J+2))/((Z(K,J+1)-Z(K,J+2))*(Z(K,J+1)-Z(K,J)))
      GRAV3(K,J)=VTOT(J+2)*(Z(K,J)-Z(K,J+2))*(3*Z(K,J+1)-Z(K,J)-2*
     &Z(K,J+2))/(Z(K,J+2)-Z(K,J))
     DELG(K,J)=(GRAV1(K,J)+GRAV2(K,J)+GRAV3(K,J))/6.0
     GDEL(K)=GDEL(K)+DELG(K,J)
     SGRAV(L)=SGRAV(L)+GDEL(K)
150   CONTINUE
    WRITE(6,910)SLONG(L),SLAT(L),SGRAV(L)
 43 CONTINUE
900 FORMAT(2I5)
901 FORMAT(I5,F10.3,I5)
902 FORMAT(2X,'FOR BLOCK #',I5,',THE DENSITY IS ',F10.3,' g/cc.')
903 FORMAT(F7.1,I5)
```

```
 904 FORMAT(9F8.0)
 906 FORMAT(I7,I8,I2)
 910 FORMAT(2X,I7,I8,F12.7)
 911 FORMAT(I5,F15.3,F10.3)
 912 FORMAT(2X,F10.3)
 915 FORMAT(A72)
 916 FORMAT('THE DEPTH OF CONTOUR ',I5,' IS ',F10.3,' km.')
 917 FORMAT('Line ',I4)
     STOP
     END
      SUBROUTINE COORD(SLAT,SLONG,X,Y,PX,PY,THETA)
     INTEGER SLAT,SLONG
     REAL X,Y,PX,PY,THETA
     PX=(SLONG-X)*2.5
     PY=(SLAT-Y)*2.5
     IF(PX.EQ.0)GOTO 10
     THETA=ATAN2(PX,PY)
     GOTO 20
  10 THETA=1.57079*SIGN(PY,1.0)
  20 CONTINUE
     RETURN
     END
```

APPENDIX B: FORTRAN INVERSION PROGRAM

```
C    INVERT.f
C ***************************************************************************
C * INVERT.f is a three-dimensional inversion program designed to construct a depth function *
C * Z(x,y) describing the topography of an interface separating two different media given 1) a  *
C * set of gridded gravity data, G(x,y), and 2) a density contrast across the interface. The    *
C * interface topography to be determined here is the Mohorovicic discontinuity (Moho)          *
C * between the crust and mantle. The algorithm used is that of Chenot and Debeglia (1990)     *
C * which allows for both vertical and lateral variation of the density contrast within the media *
C * and across the interface.                                                                   *
C ***************************************************************************
C
     REAL BETA,CNTRST,DEPTH(10,50000),ERRGRD,ERRGRV,FREQ(50000),GAMMA,
    &GRAD(50000),GRAV(50000),MEANZ,P,PX,PY,RHO1,RHO2,RHOAS,RGRAD(10,
    &50000),RGRAV(10,50000),RMSGRD,RMSGRV,RTRANS(10,50000),STORE(60000)
    &,SUMGRD,SUMGRV,TRANS(50000),U(50000),V(50000)
C
C  BETA = RHOAS(1-BETA) is the surface density
C  CNTRST = density contrast at the Moho (g/cc)
C  DEPTH(10,50000) = depth function at interface (km)
C  ERRGRD = maximum acceptable error between observed gradient field and
C           calculated gradient field
C  ERRGRV = maximum acceptable error between observed gravity field and
C           calculated gravity field
C  FREQ(50000) = radial frequency
```

```
C  GAMMA = decay constant of density in crust (g/cc km)
C  GRAD(10,50000) = expanded vertical gradient of gravity field (to
C                avoid appearance of Gibbs phenomenon)
C  GRAV(10,50000) = expanded gravity field (to avoid the appearance
C                of Gibbs phenomenon)
C  MEANZ = Mean depth to Moho (km)
C  P = number of data points (grid nodes) in gravity field
C  PX = spacing in the x-direction (km)
C  PY = spacing in the y-direction (km)
C  RHO1 = exponential density function of first layer (crust) (g/cc)
C  RHO2 = density of second layer (mantle) (g/cc)
C  RHOAS = asymptotic value of density in the crust (g/cc)
C  RGRAD(10,50000) = residual gradient function
C  RGRAV(10,50000) = residual gravity function
C  RMSGRD = r.m.s. error of calculated gradient values
C  RMSGRV = r.m.s. error of calculated gravity values
C  RTRANS(10,50000) = residual transferred field function
C  STORE(60000) = internal array used for data storage
C  TRANS(50000) = transferred field at depth MEANZ
C  U(50000) = wavenumber in the kx direction
C  V(50000) = wavenumber in the ky direction
C
     INTEGER N,NDIM,NN(2),NORDER,NX,NY,XCOORD(50000),YCOORD(50000)
C
C  N = inversion index
C  NDIM = dimension of fast Fourier transform
C  NN(2) = array of length NDIM containing the lengths of each dimension
C  NORDER = order of vertical derivative
C  NX = number of data elements in the S-N (y) direction
C  NY = number of data elements in the W-E (x) direction
C  XCOORD(50000) = x-coordinate (UTM) of gravity field data point (km)
C  YCOORD(50000) = y-coordinate (UTM) of gravity field data point (km)
C
     COMPLEX MGRAD(50000),MGRAV(50000),MGRAV1(50000),MGRAV2
    &(50000),TEMP1(50000),TEMP2(50000)
C
C  MGRAD(50000) = gradient of the modelled field
C  MGRAV(50000) = MGRAV1+MGRAV2 (modelled gravity field)
C  MGRAV1(50000) = effect of density of bottom layer compared to asymptotic
C                value of density
C  MGRAV2(50000) = effect of the difference between asymptotic density and the
C                'normal' density RHO1
C  TEMP1(50000) = temporary array containing residual gravity function (since
C               FOURN accepts only 1-D array)
C  TEMP2(50000) = temporary array containing residual gradient function (since
C               FOURN accepts only 1-D array)
C
     OPEN(1,FILE='/net/srvr08/public/janet/INVERT.DAT',STATUS=
    &'unknown')
     OPEN(7,FILE='/net/srvr08/public/janet/MODEL1.XYZ',STATUS=
    &'unknown')
```

```
      OPEN(8,FILE='/net/srvr08/public/janet/MODEL2.XYZ',STATUS=
     &'unknown')
      OPEN(9,FILE='/net/srvr08/public/janet/MODEL3.XYZ',STATUS=
     &'unknown')
      OPEN(10,FILE='/net/srvr08/public/janet/MODEL4.XYZ',STATUS=
     &'unknown')
      OPEN(11,FILE='/net/srvr08/public/janet/MODEL5.XYZ',STATUS=
     &'unknown')
      OPEN(12,FILE='/net/srvr08/public/janet/MODEL6.XYZ',STATUS=
     &'unknown')
      OPEN(13,FILE='/net/srvr08/public/janet/MODEL7.XYZ',STATUS=
     &'unknown')
      OPEN(14,FILE='/net/srvr08/public/janet/MODEL8.XYZ',STATUS=
     &'unknown')
      OPEN(15,FILE='/net/srvr08/public/janet/MODEL9.XYZ',STATUS=
     &'unknown')
      OPEN(16,FILE='/net/srvr08/public/janet/MODEL10.XYZ',STATUS=
     &'unknown')
      OPEN(20,FILE='/net/srvr08/public/janet/ERROR.XYZ',STATUS=
     &'unknown')
C
C  INVERT.DAT--file containing gravity data & inversion parameters (input)
C  MODEL1.XYZ--file containing initial interface topography model
C  MODEL2.XYZ--file containing second interface topography model
C  MODEL3.XYZ--file containing third interface topography model
C  MODEL4.XYZ--file containing fourth interface topography model
C  MODEL5.XYZ--file containing fifth interface topography model
C  MODEL6.XYZ--file containing sixth interface topography model
C  MODEL7.XYZ--file containing seventh interface topography model
C  MODEL8.XYZ--file containing eighth interface topography model
C  MODEL9.XYZ--file containing ninth interface topography model
C  MODEL10.XYZ--file containing tenth interface topography model
C  ERROR.XYZ--file containing r.m.s. error of the initial model and
C           each iteration
C
      PI=3.1415927
      G=6.67
      NDIM=2
C
C ************************PRE-PROCESSING*******************************
C * Read in the gravity and vertical gradient fields as well as the inversion parameters       *
C ***********************************************************************
      READ(1,900)P,NX,NY
900   FORMAT(F7.1,2I5)
      READ(1,902)MEANZ
 902  FORMAT(F10.3)
      READ(1,904)RHOAS,RHO2,BETA,GAMMA
 904  FORMAT(4F10.3)
      READ(1,905)ERRGRV,ERRGRD
 905  FORMAT(2F6.3)
      READ(1,906)PX,PY
```

```
906 FORMAT(2F7.1)
      DO 21 I=1,P
        READ(1,*)XCOORD(I),YCOORD(I),GRAV(I),GRAD(I)
 21   CONTINUE
      CLOSE(1)
903 FORMAT(2I5,F12.5)
      DO I=2,P-1
         U(I)=2*PI/(I*PX)
         V(I)=2*PI/(I*PY)
         FREQ(I)=SQRT(U(I)**2+V(I)**2)
      ENDDO
C
C*************************INITIAL MODEL************************************
C * Calculate the transferred field and use for the initial depth conversion. Derive the residual  *
C * functions and calculate error.                                                                  *
C ***************************************************************************
     SUMGRV=0.0
     SUMGRD=0.0
     NN(1)=NX
     NN(2)=NY
     RHO1=RHOAS*(1-BETA*EXP(-(GAMMA*MEANZ)))
     CNTRST=2*PI*G*(RHO2-RHO1)
     DO 41 I=1,P
      TRANS(I)=GRAV(I)+MEANZ*GRAD(I)
      DEPTH(1,I)=MEANZ-(TRANS(I)/CNTRST)
      WRITE(7,903)XCOORD(I),YCOORD(I),DEPTH(1,I)
41   CONTINUE
     DO 80 I=2,P-1
      MGRAV1(I)=2*PI*G*(SIN(PI*U(I)*PX)/(PI*U(I)))*(SIN(PI*V(I)*PY)/
     &     (PI*V(I)))*EXP(-(2*PI*CMPLX(0,1)*(U(I)*XCOORD(I)+
     &     V(I)*YCOORD(I))))*(RHO2-RHOAS)*EXP(-(2*PI*FREQ(I)*DEPTH
     &     (1,I)))/(2*PI*FREQ(I))
      MGRAV2(I)=(2*PI*G*(SIN(PI*U(I)*PX)/(PI*U(I)))*SIN(PI*V(I)*PY)/
     &     (PI*V(I)))*EXP(-(2*PI*CMPLX(0,1)*(U(I)*XCOORD(I)+
     &     V(I)*YCOORD(I))))*RHOAS*BETA*(EXP(-((2*PI*FREQ(I)+GAMMA)*
     &     DEPTH(1,I))))/(2*PI*FREQ(I)+GAMMA)
      MGRAV(I)=MGRAV1(I)+MGRAV2(I)
      MGRAD(I)=(2*PI*G*(SIN(PI*U(I)*PX)/(PI*U(I)))*(SIN(PI*V(I)*PY)/
     &     (PI*V(I)))*EXP(-(2*PI*CMPLX(0,1)*(U(I)*XCOORD(I)+
     &     V(I)*YCOORD(I)))))*(RHO2-RHO1)*EXP(-(2*PI*FREQ(I)*DEPTH
     &     (1,I)))
 80   CONTINUE
      DO I=2,P-1
       GRAV(I)=CMPLX(GRAV(I))
      ENDDO
      CALL FOURN(GRAV,NN,NDIM,-1,1,STORE)
      DO 42 I=2,P-1
        TEMP1(I)=GRAV(I)-MGRAV(I)
 42   CONTINUE
      CALL FOURN(TEMP1,NN,NDIM,1,1,STORE)
      DO 90 I=2,P-1
```

```
      TEMP1(I)=(TEMP1(I)/(NX*NY))
      RGRAV(1,I)=REAL(TEMP1(I))
      SUMGRV=SUMGRV+(RGRAV(1,I)**2)
      GRAD(I)=CMPLX(GRAD(I))
 90  CONTINUE
     CALL FOURN(GRAD,NN,NDIM,-1,1,STORE)
     DO 46 I=2,P-1
      TEMP2(I)=GRAD(I)-MGRAD(I)
 46  CONTINUE
     CALL FOURN(TEMP2,NN,NDIM,1,1,STORE)
     DO 91 I=2,P-1
      TEMP2(I)=(TEMP2(I)/(NX*NY))
      RGRAD(1,I)=REAL(TEMP2(I))
      SUMGRD=SUMGRD+(RGRAD(1,I)**2)
 91  CONTINUE
     RMSGRV=(1/(P-2))*SQRT(SUMGRV)
     RMSGRD=(1/(P-2))*SQRT(SUMGRD)
     WRITE(20,915)RMSGRV,RMSGRD
915 FORMAT('RMSGRV= ',F15.8,' ,RMSGRD= ',F15.8)
     IF (RMSGRV.LT.ERRGRV.AND.RMSGRD.LT.ERRGRD) GOTO 99
C
C**************************INVERSION*****************************************
C * If the error between the initial model and observed data does not fall below a predetermined *
C * acceptable error, proceed with iterative inversion.                                           *
C ************************************************************************************
 49  DO 51 N=2,10
     SUMGRV=0.0
     SUMGRD=0.0
     RMSGRV=0.0
     RMSGRD=0.0
     DO 61 I=2,P-1
      RTRANS(N-1,I)=RGRAV(N-1,I)+DEPTH(N-1,I)*RGRAD(N-1,I)
      DEPTH(N,I)=DEPTH(N-1,I)-(RTRANS(N-1,I)/CNTRST)
      WRITE(N+6,903)XCOORD(I),YCOORD(I),DEPTH(N,I)
      MGRAV1(I)=2*PI*G*(SIN(PI*U(I)*PX)/(PI*U(I)))*(SIN(PI*V(I)*
   &      PY)/(PI*V(I)))*EXP(-(2*PI*CMPLX(0,1)*(U(I)*XCOORD(I)+
   &      V(I)*YCOORD(I))))*(RHO2-RHOAS)*EXP(-(2*PI*FREQ(I)*DEPTH
   &      (N,I)))/(2*PI*FREQ(I))
      MGRAV2(I)=(2*PI*G*(SIN(PI*U(I)*PX)/(PI*U(I)))*SIN(PI*V(I)*
   &      PY)/(PI*V(I)))*EXP(-(2*PI*CMPLX(0,1)*(U(I)*XCOORD(I)+
   &      V(I)*YCOORD(I))))*RHOAS*BETA*(EXP(-((2*PI*FREQ(I)+GAMMA)
   &      *DEPTH(N,I))))/(2*PI*FREQ(I)+GAMMA)
      MGRAV(I)=MGRAV1(I)+MGRAV2(I)
      MGRAD(I)=(2*PI*G*(SIN(PI*U(I)*PX)/(PI*U(I)))*(SIN(PI*V(I)*
   &      PY)/(PI*V(I)))*EXP(-(2*PI*CMPLX(0,1)*(U(I)*XCOORD(I)+
   &      V(I)*YCOORD(I)))))*(RHO2-RHO1)*EXP(-(2*PI*FREQ(I)*DEPTH
   &      (N,I)))
 61  CONTINUE
     DO 62 I=2,P-1
      TEMP1(I)=GRAV(I)-MGRAV(I)
 62  CONTINUE
```

```
      CALL FOURN(TEMP1,NN,NDIM,1,1,STORE)
      DO 95 I=2,P-1
        TEMP1(I)=(TEMP1(I)/(NX*NY))
        RGRAV(N,I)=REAL(TEMP1(I))
        SUMGRV=SUMGRV+(RGRAV(N,I)**2)
        TEMP2(I)=GRAD(I)-MGRAD(I)
 95   CONTINUE
      CALL FOURN(TEMP2,NN,NDIM,1,1,STORE)
      DO 97 I=2,P-1
        TEMP2(I)=(TEMP2(I)/(NX*NY))
        RGRAD(N,I)=REAL(TEMP2(I))
        SUMGRD=SUMGRD+(RGRAD(N,I)**2)
 97   CONTINUE
      RMSGRV=(1/(P-2))*SQRT(SUMGRV)
      RMSGRD=(1/(P-2))*SQRT(SUMGRD)
      WRITE(20,916)N,RMSGRV,RMSGRD
916   FORMAT('N= ',I3,' RMSGRV= ',F15.8,' ,RMSGRD= ',F15.8)
      IF (RMSGRV.LT.ERRGRV.AND.RMSGRD.LT.ERRGRD) GO TO 99
 51   CONTINUE
 99   STOP
      END
C
C**************************FOURIER TRANSFORMATION**********************
      SUBROUTINE FOURN(DATA,NN,NDIM,ISIGN,IFORM,WORK)
c
c     the cooley-tukey fast fourier transform in usasi basic fortran
c
c     program by norman brenner from the basic program by charles rader,  june 1967.  the idea for
c     the digit reversal was suggested by ralph alter.
c
c     reference-- ieee audio transactions (june 1967), special issue on the fft.
c
      DIMENSION DATA(500),NN(2),IFACT(32),WORK(1000)
      DATA TWOPI/6.2831853071796/,RTHLF/0.70710678118655/
      IF(NDIM-1)920,1,1
1     NTOT=2
      DO 2 IDIM=1,NDIM
      IF(NN(IDIM))920,920,2
2     NTOT=NTOT*NN(IDIM)
c
      NP1=2
      DO 910 IDIM=1,NDIM
      N=NN(IDIM)
      NP2=NP1*N
      IF(N-1)920,900,5
c
c     is n a power of two and if not, what are its factors
c
5     M=N
      NTWO=NP1
      IF=1
```

```
      IDIV=2
   10  IQUOT=M/IDIV
      IREM=M-IDIV*IQUOT
      IF(IQUOT-IDIV)50,11,11
   11  IF(IREM)20,12,20
   12  NTWO=NTWO+NTWO
      IFACT(IF)=IDIV
      IF=IF+1
      M=IQUOT
      GO TO 10
   20  IDIV=3
      INON2=IF
   30  IQUOT=M/IDIV
      IREM=M-IDIV*IQUOT
      IF(IQUOT-IDIV)60,31,31
   31  IF(IREM)40,32,40
   32  IFACT(IF)=IDIV
      IF=IF+1
      M=IQUOT
      GO TO 30
   40  IDIV=IDIV+2
      GO TO 30
   50  INON2=IF
      IF(IREM)60,51,60
   51  NTWO=NTWO+NTWO
      GO TO 70
   60  IFACT(IF)=M
C
C     separate four cases--
C       1. complex transform or real transform for the 4th, 9th,etc. dimensions.
C       2. real transform for the 2nd or 3rd dimension.  method--transform half the data, supplying
C          the other half by conjugate symmetry.
C       3. real transform for the 1st dimension, n odd.  method--set the imaginary parts to zero.
C       4. real transform for the 1st dimension, n even.  method--transform a complex array of
C          length n/2 whose real parts are the even numbered real values and whose imaginary parts
C          are the odd numbered real values.  separate and supply the second half by conjugate
C          symmetry.
C
   70  ICASE=1
      IFMIN=1
      I1RNG=NP1
      IF(IDIM-4)71,100,100
   71  IF(IFORM)72,72,100
   72  ICASE=2
      I1RNG=NP0*(1+NPREV/2)
      IF(IDIM-1)73,73,100
   73  ICASE=3
      I1RNG=NP1
      IF(NTWO-NP1)100,100,74
   74  ICASE=4
      IFMIN=2
```

```
      NTWO=NTWO/2
      N=N/2
      NP2=NP2/2
      NTOT=NTOT/2
      I=1
      DO 80 J=1,NTOT
      DATA(J)=DATA(I)
80    I=I+2
c
c     shuffle data by bit reversal, since n=2**k.  as the shuffling can be done by simple
interchange,
c     no working array is needed
c
100   IF(NTWO-NP2)200,110,110
110   NP2HF=NP2/2
      J=1
      DO 150 I2=1,NP2,NP1
      IF(J-I2)120,130,130
120   I1MAX=I2+NP1-2
      DO 125 I1=I2,I1MAX,2
      DO 125 I3=I1,NTOT,NP2
      J3=J+I3-I2
      TEMPR=DATA(I3)
      TEMPI=DATA(I3+1)
      DATA(I3)=DATA(J3)
      DATA(I3+1)=DATA(J3+1)
      DATA(J3)=TEMPR
125   DATA(J3+1)=TEMPI
130   M=NP2HF
140   IF(J-M)150,150,145
145   J=J-M
      M=M/2
      IF(M-NP1)150,140,140
150   J=J+M
      GO TO 300
c
c     shuffle data by digit reversal for general n
c
200   NWORK=2*N
      DO 270 I1=1,NP1,2
      DO 270 I3=I1,NTOT,NP2
      J=I3
      DO 260 I=1,NWORK,2
      IF(ICASE-3)210,220,210
210   WORK(I)=DATA(J)
      WORK(I+1)=DATA(J+1)
      GO TO 230
220   WORK(I)=DATA(J)
      WORK(I+1)=0.
230   IFP2=NP2
      IF=IFMIN
```

```
240   IFP1=IFP2/IFACT(IF)
      J=J+IFP1
      IF(J-I3-IFP2)260,250,250
250   J=J-IFP2
      IFP2=IFP1
      IF=IF+1
      IF(IFP2-NP1)260,260,240
260   CONTINUE
      I2MAX=I3+NP2-NP1
      I=1
      DO 270 I2=I3,I2MAX,NP1
      DATA(I2)=WORK(I)
      DATA(I2+1)=WORK(I+1)
270   I=I+2
c
c     main loop for factors of two.  perform fourier transforms of length four, with one of length
two
c     if needed.  the twiddle factor w=exp(isign*2*pi*sqrt(-1)*m/(4*mmax)).  check for
c     w=isign*sqrt(-1) and repeat for w=w*(1+isign*sqrt(-1))/sqrt(2).
c
300   IF(NTWO-NP1)600,600,305
305   NP1TW=NP1+NP1
      IPAR=NTWO/NP1
310   IF(IPAR-2)350,330,320
320   IPAR=IPAR/4
      GO TO 310
330   DO 340 I1=1,I1RNG,2
      DO 340 K1=I1,NTOT,NP1TW
      K2=K1+NP1
      TEMPR=DATA(K2)
      TEMPI=DATA(K2+1)
      DATA(K2)=DATA(K1)-TEMPR
      DATA(K2+1)=DATA(K1+1)-TEMPI
      DATA(K1)=DATA(K1)+TEMPR
340   DATA(K1+1)=DATA(K1+1)+TEMPI
350   MMAX=NP1
360   IF(MMAX-NTWO/2)370,600,600
370   LMAX=MAX0(NP1TW,MMAX/2)
      DO 570 L=NP1,LMAX,NP1TW
      M=L
      IF(MMAX-NP1)420,420,380
380   THETA=-TWOPI*FLOAT(L)/FLOAT(4*MMAX)
      IF(ISIGN)400,390,390
390   THETA=-THETA
400   WR=COS(THETA)
      WI=SIN(THETA)
410   W2R=WR*WR-WI*WI
      W2I=2.*WR*WI
      W3R=W2R*WR-W2I*WI
      W3I=W2R*WI+W2I*WR
420   DO 530 I1=1,I1RNG,2
```

```
      KMIN=I1+IPAR*M
      IF(MMAX-NP1)430,430,440
  430 KMIN=I1
  440 KDIF=IPAR*MMAX
  450 KSTEP=4*KDIF
      IF(KSTEP-NTWO)460,460,530
  460 DO 520 K1=KMIN,NTOT,KSTEP
      K2=K1+KDIF
      K3=K2+KDIF
      K4=K3+KDIF
      IF(MMAX-NP1)470,470,480
  470 U1R=DATA(K1)+DATA(K2)
      U1I=DATA(K1+1)+DATA(K2+1)
      U2R=DATA(K3)+DATA(K4)
      U2I=DATA(K3+1)+DATA(K4+1)
      U3R=DATA(K1)-DATA(K2)
      U3I=DATA(K1+1)-DATA(K2+1)
      IF(ISIGN)471,472,472
  471 U4R=DATA(K3+1)-DATA(K4+1)
      U4I=DATA(K4)-DATA(K3)
      GO TO 510
  472 U4R=DATA(K4+1)-DATA(K3+1)
      U4I=DATA(K3)-DATA(K4)
      GO TO 510
  480 T2R=W2R*DATA(K2)-W2I*DATA(K2+1)
      T2I=W2R*DATA(K2+1)+W2I*DATA(K2)
      T3R=WR*DATA(K3)-WI*DATA(K3+1)
      T3I=WR*DATA(K3+1)+WI*DATA(K3)
      T4R=W3R*DATA(K4)-W3I*DATA(K4+1)
      T4I=W3R*DATA(K4+1)+W3I*DATA(K4)
      U1R=DATA(K1)+T2R
      U1I=DATA(K1+1)+T2I
      U2R=T3R+T4R
      U2I=T3I+T4I
      U3R=DATA(K1)-T2R
      U3I=DATA(K1+1)-T2I
      IF(ISIGN)490,500,500
  490 U4R=T3I-T4I
      U4I=T4R-T3R
      GO TO 510
  500 U4R=T4I-T3I
      U4I=T3R-T4R
  510 DATA(K1)=U1R+U2R
      DATA(K1+1)=U1I+U2I
      DATA(K2)=U3R+U4R
      DATA(K2+1)=U3I+U4I
      DATA(K3)=U1R-U2R
      DATA(K3+1)=U1I-U2I
      DATA(K4)=U3R-U4R
  520 DATA(K4+1)=U3I-U4I
      KDIF=KSTEP
```

```
      KMIN=4*(KMIN-I1)+I1
      GO TO 450
  530 CONTINUE
      M=M+LMAX
      IF(M-MMAX)540,540,570
  540 IF(ISIGN)550,560,560
  550 TEMPR=WR
      WR=(WR+WI)*RTHLF
      WI=(WI-TEMPR)*RTHLF
      GO TO 410
  560 TEMPR=WR
      WR=(WR-WI)*RTHLF
      WI=(TEMPR+WI)*RTHLF
      GO TO 410
  570 CONTINUE
      IPAR=3-IPAR
      MMAX=MMAX+MMAX
      GO TO 360
c
c     main loop for factors not equal to two.  apply the twiddle factor w=exp(isign*2*pi*sqrt(-
c     1)*(j1-1)*(j2-j1)/(ifp1+ifp2)), then perform a fourier transform of length ifact(if), making use
c     of conjugate symmetries.
c
  600 IF(NTWO-NP2)605,700,700
  605 IFP1=NTWO
      IF=INON2
      NP1HF=NP1/2
  610 IFP2=IFACT(IF)*IFP1
      J1MIN=NP1+1
      IF(J1MIN-IFP1)615,615,640
  615 DO 635 J1=J1MIN,IFP1,NP1
      THETA=-TWOPI*FLOAT(J1-1)/FLOAT(IFP2)
      IF(ISIGN)625,620,620
  620 THETA=-THETA
  625 WSTPR=COS(THETA)
      WSTPI=SIN(THETA)
      WR=WSTPR
      WI=WSTPI
      J2MIN=J1+IFP1
      J2MAX=J1+IFP2-IFP1
      DO 635 J2=J2MIN,J2MAX,IFP1
      I1MAX=J2+I1RNG-2
      DO 630 I1=J2,I1MAX,2
      DO 630 J3=I1,NTOT,IFP2
      TEMPR=DATA(J3)
      DATA(J3)=DATA(J3)*WR-DATA(J3+1)*WI
  630 DATA(J3+1)=TEMPR*WI+DATA(J3+1)*WR
      TEMPR=WR
      WR=WR*WSTPR-WI*WSTPI
  635 WI=TEMPR*WSTPI+WI*WSTPR
  640 THETA=-TWOPI/FLOAT(IFACT(IF))
```

```
      IF(ISIGN)650,645,645
  645 THETA=-THETA
  650 WSTPR=COS(THETA)
      WSTPI=SIN(THETA)
      J2RNG=IFP1*(1+IFACT(IF)/2)
      DO 695 I1=1,I1RNG,2
      DO 695 I3=I1,NTOT,NP2
      J2MAX=I3+J2RNG-IFP1
      DO 690 J2=I3,J2MAX,IFP1
      J1MAX=J2+IFP1-NP1
      DO 680 J1=J2,J1MAX,NP1
      J3MAX=J1+NP2-IFP2
      DO 680 J3=J1,J3MAX,IFP2
      JMIN=J3-J2+I3
      JMAX=JMIN+IFP2-IFP1
      I=1+(J3-I3)/NP1HF
      IF(J2-I3)655,655,665
  655 SUMR=0.
      SUMI=0.
      DO 660 J=JMIN,JMAX,IFP1
   659 SUMR=SUMR+DATA(J)
  660 SUMI=SUMI+DATA(J+1)
      WORK(I)=SUMR
      WORK(I+1)=SUMI
      GO TO 680
  665 ICONJ=1+(IFP2-2*J2+I3+J3)/NP1HF
      J=JMAX
      SUMR=DATA(J)
      SUMI=DATA(J+1)
      OLDSR=0.
      OLDSI=0.
      J=J-IFP1
  670 TEMPR=SUMR
      TEMPI=SUMI
      SUMR=TWOWR*SUMR-OLDSR+DATA(J)
      SUMI=TWOWR*SUMI-OLDSI+DATA(J+1)
      OLDSR=TEMPR
      OLDSI=TEMPI
      J=J-IFP1
      IF(J-JMIN)675,675,670
  675 TEMPR=WR*SUMR-OLDSR+DATA(J)
      TEMPI=WI*SUMI
      WORK(I)=TEMPR-TEMPI
      WORK(ICONJ)=TEMPR+TEMPI
      TEMPR=WR*SUMI-OLDSI+DATA(J+1)
      TEMPI=WI*SUMR
      WORK(I+1)=TEMPR+TEMPI
      WORK(ICONJ+1)=TEMPR-TEMPI
  680 CONTINUE
      IF(J2-I3)685,685,686
  685 WR=WSTPR
```

```
      WI=WSTPI
      GO TO 690
686   TEMPR=WR
      WR=WR*WSTPR-WI*WSTPI
      WI=TEMPR*WSTPI+WI*WSTPR
690   TWOWR=WR+WR
      I=I
      I2MAX=I3+NP2-NP1
      DO 695 I2=I3,I2MAX,NP1
      DATA(I2)=WORK(I)
      DATA(I2+1)=WORK(I+1)
695   I=I+2
      IF=IF+1
      IFP1=IFP2
      IF(IFP1-NP2)610,700,700
c
c     complete a real transform in the 1st dimension, n even, by conjugate symmetries.
c
700   GO TO (900,800,900,701),ICASE
701   NHALF=N
      N=N+N
      THETA=-TWOPI/FLOAT(N)
      IF(ISIGN)703,702,702
702   THETA=-THETA
703   WSTPR=COS(THETA)
      WSTPI=SIN(THETA)
      WR=WSTPR
      WI=WSTPI
      IMIN=3
      JMIN=2*NHALF-1
      GO TO 725
710   J=JMIN
      DO 720 I=IMIN,NTOT,NP2
      SUMR=(DATA(I)+DATA(J))/2.
      SUMI=(DATA(I+1)+DATA(J+1))/2.
      DIFR=(DATA(I)-DATA(J))/2.
      DIFI=(DATA(I+1)-DATA(J+1))/2.
      TEMPR=WR*SUMI+WI*DIFR
      TEMPI=WI*SUMI-WR*DIFR
      DATA(I)=SUMR+TEMPR
      DATA(I+1)=DIFI+TEMPI
      DATA(J)=SUMR-TEMPR
      DATA(J+1)=-DIFI+TEMPI
720   J=J+NP2
      IMIN=IMIN+2
      JMIN=JMIN-2
      TEMPR=WR
      WR=WR*WSTPR-WI*WSTPI
      WI=TEMPR*WSTPI+WI*WSTPR
725   IF(IMIN-JMIN)710,730,740
730   IF(ISIGN)731,740,740
```

```
731   DO 735 I=IMIN,NTOT,NP2
735   DATA(I+1)=-DATA(I+1)
740   NP2=NP2+NP2
      NTOT=NTOT+NTOT
      J=NTOT+1
      IMAX=NTOT/2+1
745   IMIN=IMAX-2*NHALF
      I=IMIN
      GO TO 755
750   DATA(J)=DATA(I)
      DATA(J+1)=-DATA(I+1)
755   I=I+2
      J=J-2
      IF(I-IMAX)750,760,760
760   DATA(J)=DATA(IMIN)-DATA(IMIN+1)
      DATA(J+1)=0.
      IF(I-J)770,780,780
765   DATA(J)=DATA(I)
      DATA(J+1)=DATA(I+1)
770   I=I-2
      J=J-2
      IF(I-IMIN)775,775,765
775   DATA(J)=DATA(IMIN)+DATA(IMIN+1)
      DATA(J+1)=0.
      IMAX=IMIN
      GO TO 745
780   DATA(1)=DATA(1)+DATA(2)
      DATA(2)=0.
      GO TO 900
c
c     complete a real transform for the 2nd or 3rd dimension by conjugate symmetries.
c
800   IF(I1RNG-NP1)805,900,900
805   DO 860 I3=1,NTOT,NP2
      I2MAX=I3+NP2-NP1
      DO 860 I2=I3,I2MAX,NP1
      IMIN=I2+I1RNG
      IMAX=I2+NP1-2
      JMAX=2*I3+NP1-IMIN
      IF(I2-I3)820,820,810
810   JMAX=JMAX+NP2
820   IF(IDIM-2)850,850,830
830   J=JMAX+NP0
      DO 840 I=IMIN,IMAX,2
      DATA(I)=DATA(J)
      DATA(I+1)=-DATA(J+1)
840   J=J-2
850   J=JMAX
      DO 860 I=IMIN,IMAX,NP0
      DATA(I)=DATA(J)
      DATA(I+1)=-DATA(J+1)
```

```
860   J=J-NP0
c
c     end of loop on each dimension
c
900   NP0=NP1
      NP1=NP2
910   NPREV=N
920   RETURN
      END
C
C************************REFERENCES*****************************************
C *1. Blakely, Richard J. 1995. Potential Theory in Gravity & Magnetic Applications.  *
C *    Cambridge University Press: Cambridge.                                          *
C *2. Chenot, D. and Debeglia, N. 1990. Three-dimensional gravity or magnetic constrained  *
C *    depth inversion with lateral and vertical variation of contrast. Geophysics, 55: 327-335.  *
C *3. Cordell, L., Phillips, J.D., and Godson, R.H. 1992. U.S. Geological Survey Potential  *
C *    Field Geophysical Software Version 2.0. (fourt.for)                             *
C ********************************************************************************
```